Production of strangeness in partonic interactions at the LHC

Matonoha, Oliver

2023

Document Version:
Publisher's PDF, also known as Version of record

Link to publication

Citation for published version (APA):
Matonoha, O. (2023). *Production of strangeness in partonic interactions at the LHC*. Lund University.

Total number of authors:
1

Production of strangeness in partonic interactions at the LHC

OLIVER MATONOHA
DEPARTMENT OF PHYSICS
FACULTY OF NATURAL SCIENCES | LUND UNIVERSITY

Production of strangeness in partonic interactions at the LHC

Production of strangeness in partonic interactions at the LHC

by Oliver Matonoha

LUND
UNIVERSITY

Thesis for the degree of Doctor of Philosophy
Thesis advisors: Dr. David Silvermyr, Prof. Peter Christiansen,
Dr. Alice Ohlson
Faculty opponent: Prof. Michael Murray

To be presented, with the permission of the Faculty of Natural Sciences of Lund University, for public criticism in the Rydberg lecture hall (Rydbergsalen) at the Department of Physics on Friday, the 9th of June 2023 at 13:15.

Production of strangeness in partonic interactions at the LHC

by Oliver Matonoha

LUND
UNIVERSITY

Cover picture: Artistic interpretation of a collision of two protons generated using the Midjourney AI model.

Thesis part pictures: Artistic interpretation of a collision of two protons generated using the Midjourney AI model (Part I, III, and IV), Photo of the ALICE Detector (Part II, image credit: CERN)

Funding information: The thesis work was financially supported by the Swedish Research Council.

Faculty of Natural Sciences, Department of Physics

ISBN: 978-91-8039-739-1 (print)
ISBN: 978-91-8039-740-7 (pdf)

Printed in Sweden by Tryckeriet E-huset LTH, Lund University, Lund 2023

To myself,

my parents,

lovers and loved ones,

and my niece,
who is born at the same time
as this thesis.

Abstract

The strong interaction is responsible for nearly all observable baryonic matter in the Universe. Quantum Chromodynamics, which describes interactions between quarks and gluons, however, cannot be solved analytically in the non-perturbative regime, involving low momentum transfers. In this regime, interesting phenomena occur, such as the formation of colour-neutral hadrons from constituent quarks and in extreme conditions, the transition of hadronic matter to a plasma of deconfined quarks and gluons. This quark-gluon plasma (QGP) is believed to have comprised the Universe in the first several microseconds after the Big Bang and can be recreated in laboratory conditions, such as in collisions of ultra-relativistic heavy nuclei at the Large Hadron Collider (LHC).

The QGP exhibits certain signatures whose strength varies with the multiplicity of particles produced in the collisions, which is directly linked to the number of colliding nucleons in the collision and the energy density in the initial state. In the last decade, contrary to expectations, it has been discovered that pp collisions and pA collisions also exhibit QGP-like behaviour, including an increase in the production of strange particles and an increase in the ratio of neutral strange hadrons, Λ to K^0_S, at intermediate transverse momentum p_T. However, in pp collisions, it is challenging to link particle multiplicity to the initial state.

This dissertation aims to investigate the origin of QGP-like behavior in pp collisions by analyzing the production of K^0_S and Λ particles and their dependence on event shape and sub-structure. Specifically, measurements are performed using the ALICE detector at the LHC for pp collisions at $\sqrt{s} = 13\,\mathrm{TeV}$. For the first time ever, observables quantifying the event shape geometry, the transverse spherocity $S_\mathrm{O}^{p_\mathrm{T}=1.0}$, and the magnitude of the underlying event activity, the R_T, $R_\mathrm{T,min}$, and $R_\mathrm{T,max}$, are employed to investigate their effect on the production of K^0_S and Λ particles. These observables allow for a more differentiated understanding of the collision dynamics and help access the number of colliding quarks and gluons (partons). The results of this study will contribute to the understanding of the QGP-like behaviour in pp collisions and help further the understanding of the strong interaction at low momentum transfers.

Popular summary in English

Do you ever contemplate what the Universe is made of? What are the most fundamental building blocks of reality, and how do they interact? At the smallest scales, everything we see around us consists of atoms, which are composed of even smaller particles called protons, neutrons, and electrons. But what are protons and neutrons made of? In the world of particle physics, these particles are composed of even smaller, fundamental particles called *quarks*, which cannot be broken down into smaller parts.

Fundamental particles, such as quarks and electrons, interact with each other through forces. There are four fundamental forces in the universe: the gravitational force (which keeps us on Earth), the electromagnetic force (which makes electric charges attract or repel), the weak force (which is responsible for forms of radioactivity), and the strong force. The interactions occur through the exchange of a *mediating* particle, such as the photon in the case of electromagnetism.

The strong force, which is focused on in this thesis, is responsible for holding protons and neutrons together. It is similar to the electromagnetic force in that it acts between particles with a charge. However, instead of electric charge, the strong force acts on objects with a ”strong” charge, which is called *colour* and the mediating particle is called a *gluon*. Furthermore, the strong force is the strongest of all fundamental forces, about 100 times stronger than the electromagnetic force. However, it is also much more complex. While the electromagnetic force only has one type of charge (electric), the strong force has three, known as red, green, and blue. Additionally, the strong force only acts over very short distances.

The *strong force* is essential for several reasons. One of them becomes apparent when considering its binding of quarks with gluons inside protons and neutrons. The energy of these binding interactions is equivalent to mass (using the famous Einstein mass-energy equivalence equation $E = mc^2$). In this case, the sum of masses of the three quarks in a proton is only around 1% of the proton mass! This implies that the rest comes from this binding energy. Therefore, without the strong force, the Universe would look drastically different.

However, there is still much that is not known about the strong force, and mathematical theories describing it based on first principles have severe limitations. That is why scientists study it experimentally by *colliding two protons* or nuclei at high speeds in particle accelerators, such as the LHC at CERN. This collision breaks them apart, and the insides can be studied. One way to study the strong force (among hundreds of others) is by looking at the number of produced particles containing the so-called *strange quark*, and its dependence on how many particles got produced in the collision overall, which can be related to how “violent” the collision was.

This dissertation introduces new methods for studying the strong force. Instead of just looking at the number of particles produced, we study the overall geometric shape of the collection of produced particles and also the number of particles coming from a less energetic component of the collision called the underlying event. These techniques help us better understand how the strong force behaves on a microscopic level and how many individual quarks and gluons (together called *partons*) took part in the collision. Moreover, they provide insights into the creation of *quark-gluon plasma*, an extreme state of matter that existed in the early Universe. This, in turn, can help us understand the origins of the Universe and how it evolved over time.

Therefore, to conclude, by studying the strong force, we are not only expanding our understanding of the fundamental building blocks of matter and the origin of 99% of the mass we see around us, but also gaining insight into the infant stages of the Universe itself.

Populärvetenskaplig sammanfattning på svenska

Funderar du någonsin på vad universum består av? Vilka är de mest grundläggande byggstenarna i vår värld, och hur samverkar de? Allt vi ser omkring oss är uppbyggt av atomer, som är sammansatta av ännu mindre partiklar som kallas protoner, neutroner och elektroner. Vad består då protonerna och neutronerna av? I partikelfysikens värld är dessa partiklar sammansatta av ännu mindre, fundamentala partiklar som kallas *kvarkar*, som inte kan brytas ner i mindre delar.

Fundamentala partiklar, såsom kvarkar och elektroner, växelverkar med varandra genom krafter. Det finns fyra grundläggande krafter i universum: gravitationskraften (som håller oss jordnära), den elektromagnetiska kraften (som gör att elektriska laddningar attraherar eller repellerar), den svaga kraften (som är ansvarig för vissa former av radioaktivitet) och den starka kraften . Växelverkan sker genom utbyte av en *kraftförmedlande* partikel, såsom fotonen vid elektromagnetism.

Den starka kraften, som fokuseras på i denna avhandling, är ansvarig för att hålla ihop protoner och neutroner. Den liknar den elektromagnetiska kraften genom att den verkar mellan partiklar med en laddning. Men istället för elektrisk laddning verkar den starka kraften på föremål med en “starkladdning, som kallas *färg* och den förmedlande partikeln kallas *gluon*. Dessutom är den starka kraften den starkaste av alla grundläggande krafter, cirka 100 gånger starkare än den elektromagnetiska kraften. Den är dock också mycket mer komplex. Medan den elektromagnetiska kraften bara har en typ av laddning (elektrisk), har den starka kraften tre, känd som röd, grön och blå. Dessutom verkar den starka kraften bara över mycket korta avstånd.

Den *starka kraften* är högst väsentlig av flera anledningar. En av dem blir uppenbar när man betänker att den binder kvarkar samman med gluoner inuti protoner och neutroner. Denna bindningsenergi är ekvivalent med massa (med Einsteins berömda mass-energiekvivalensekvation $E = mc^2$). I det här fallet är summan av massorna av de tre kvarkarna i en proton bara cirka 1% av protonmassan! Detta innebär att resten kommer från denna bindningsenergi. Därför, utan den starka kraften, skulle universum se drastiskt annorlunda ut.

Det finns dock fortfarande mycket som inte är känt om den starka kraften, och de matematiska teorier som beskriver den har allvarliga begränsningar. Det är därför som forskare studerar den starka kraften experimentellt genom att *kollidera två protoner* eller kärnor med höga hastigheter i partikelacceleratorer, som LHC vid CERN. Denna kollision bryter isär protonerna, och deras beståndsdelar kan studeras. Ett sätt (bland hundratals andra) att studera den starka kraften är att titta på antalet producerade partiklar som innehåller den så kallade *sär-kvarken*, och dess beroende av hur många partiklar som producerades i kollisionen totalt, vilket kan relateras till hur

”våldsam”kollisionen var.

Denna avhandling introducerar nya metoder för att studera den starka kraften. Istället för att bara titta på antalet producerade partiklar, studerar vi den övergripande geometriska formen av alla producerade partiklar tillsammans och även antalet partiklar som kommer från en mindre energetisk komponent i kollisionen som kallas den underliggande händelsen. Dessa tekniker hjälper oss att bättre förstå hur den starka kraften beter sig på mikroskopisk nivå och hur många individuella kvarkar och gluoner (tillsammans kallade *partoner*) som deltog i kollisionen. Dessutom ger de insikter i skapandet av *kvark-gluon plasma*, ett extremt tillstånd av materia som fanns i det tidiga universum. Detta kan i sin tur hjälpa oss att förstå universums ursprung och hur det utvecklades över tiden.

Därför, som en sammanfattning: genom att studera den starka kraften utökar vi inte bara vår förståelse av materiens grundläggande byggstenar och ursprunget till 99% av massan vi ser omkring oss, utan vi får också insikt i det tidiga Universum.

Contents

6 Transverse spherocity **91**

7 Underlying event activity **113**

Preface

A word from the author

I would like to start this thesis with some personal and, maybe overly candid, words. I started my journey in particle physics ten years ago. Weighed down by the seemingly crushing expectations of choosing a career, a realisation eventually crystallised: I want to be a knower, a solver, and a pioneer. In the most fundamental natural science there is. Advancing humanity's knowledge, that was to be my impact on this world, and my *ikigai*.

These ten years have been a winding, trying journey. I have met people, moved countries, travelled the world, and made memories. I also fell in and out of love with physics and with academic work countless times. I have had moments of disillusionment, doubting if doing the "ant's work" that such fundamental research involves is what I envisioned for myself. I have questioned if what we do makes sense and if what I chose is actually good and healthy for my existence. And I have questioned if there is a place for me. I believe many early career researchers can relate.

Having said that, I am grateful to some of the people who have inspired me and helped shape my path. Specifically, people who manage to choose love, happiness, and lust for life over hopelessly surrendering to the weights of this field's rigours. It has not always been easy to find role models who spoke to me and my experience, but they are here.

The truth is, I tend to realise, that knowing the world is an incredibly fulfilling feeling. Quenching that juvenile curiosity and *just understanding*, that can be, without exaggerations, intoxicating. Figuring out the peculiarities of the Universe and our existence can be a very satiating diet to a person hungry for life. This is one of the truths on the other side of the coin, one that I now cherish deeply and which makes me appreciate my journey.

And it can be oh-so fun. I will not speak for other disciplines, but studying the physics of hadronic collisions and quark-gluon plasma is an incredible game to play. There are hundreds of observables and hundreds of measurements, each trying to fit a small puzzle piece into a larger mosaic of something so ridiculously extreme. And when the puzzle piece fits, and things start making sense, or maybe even stop again, that is entertainment.

In the final stages of my doctorate, I found myself continuously toyed with by my research. It has sometimes been doing with me what it wants. Often, I did not feel like working. But then I opened my notepad, sat behind the computer, and noticed that one work is not ready, and the other one hopeless. And so I stayed with it for a while and, suddenly, realised that the night had come already. And in this way, every morning, I allowed myself to be pleasantly abused by my work, which enabled me to play this game of satisfying my curiousity and fitting puzzle pieces, eventually giving life to this love letter.

With that said, I would like to present this dissertation. It is the product of my doctoral studies at Lund University in Sweden. Entitled "Production of strangeness in partonic interactions at the LHC", its aim is to experimentally measure the production of neutral strange particles K^0_S and Λ in collisions of protons, using specific observables which allow us to get a firmer grasp on the number and properties of partonic interactions.

Outline of the thesis

The thesis is divided into three parts: fundamental theory, experimental setup and methodology, and author's measurements. The first part provides an overview of relevant physics and a summary of important measurements, giving context to the dissertation. It describes the theory of the strong interaction, quantum chromodynamics, and discusses the interactions of quarks and gluons, with an emphasis on multiple partonic interactions in proton-proton (pp) collisions and the physics of quark-gluon plasma (QGP) formation in nuclei-nuclei (AA) collisions. The part also provides a detailed account of observed evidence for QGP formation in smaller systems, such as pp.

The second part explains the technical specifications and operating principles of the detector apparatus ALICE and the particle accelerator Large Hadron Collider (LHC), located at CERN. It describes the detector systems used to measure hadron collisions and gives an overview of the data collection and data preparation process that is carried out within the ALICE collaboration, such as track reconstruction, to allow its members to conduct physics analyses.

The final part introduces the author's own contributions. It begins by laying out the techniques used to identify yields and transverse momentum spectra of the K^0_S and Λ particles in the collected data from pp collisions at $\sqrt{s} = 13\,\mathrm{TeV}$. The methodology for applying corrections to the results and estimating their systematic uncertainties is also explained. The part then describes the observable transverse spherocity $S_\mathrm{O}^{p_\mathrm{T}=1.0}$, which is a measure of the event topology, and explains its experimental application. This observable allows for a more differential insight into the dynamics of partonic interactions than using event activity observables, such as multiplicity. The results of the analysed K^0_S and Λ based on this observable are presented and discussed. Similarly, the same is done for the R_T, $R_\mathrm{T,min}$, and $R_\mathrm{T,max}$ observables, which quantify the magnitude of the underlying event and are a clean proxy for estimating the number of multiple partonic interactions.

Finally, the key results of the two measurements are highlighted, discussed, compared and contextualised with other findings in the field. Additional information about this thesis can be found at the end, including a list of cited references, a list of all used acronyms, and other supplementary material. Figures taken from or based on a cited reference are indicated by a citation in the figure caption. Moreover, in various parts of the text, a sketch is included to illustrate the behaviour of a function formula. These sketches serve as a visual aid to the reader, rather than providing a detailed quantification.

Author's contributions

All figures and tables presented in this dissertation without citations and all body text are the author's own, unless explicitly specified otherwise.

The author developed the experimental use of observables $S_\mathrm{O}^{p_\mathrm{T}=1.0}$ and R_T together with a few close collaborators (listed below as publication co-authors). All work, including data management, operation of computational resources, testing the observables' experimental definition, production of theoretical predictions from simulations, and communicating the results to a broader audience, was shared equally. The other collaborators used these observables in their individual measurements of different particles such as π, K, p, Ξ, ϕ, and in the case of $S_\mathrm{O}^{p_\mathrm{T}=1.0}$, also K^*, each requiring specific treatment, such as reconstructing their transverse momentum spectra, applying corrections, and determining systematic uncertainties. The author solely and fully analysed the particles K^0_S and Λ. Moreover, the author solely developed the experimental use of observables $R_\mathrm{T,min}$ and $R_\mathrm{T,max}$, also presented in this thesis.

The author is a member of the ALICE experiment, a collaboration of approximately two thousand members. Common data collection and preparation processes, many of which are listed in Chapter 4, are developed centrally. ALICE members contribute to the functioning of the collaboration by detailed participation in its internal review process of publications, taking shifts operating the detector during data collection, and very importantly, a service task. In the author's case, it was miscellaneous work related to the Run 3 upgrade of the ALICE TPC detector using GEM read-outs, particularly disassembling the previous front-end read-out system and testing the GEM operation in the TPC data taking during commissioning periods.

These are the publications with the author's contribution, in chronological order:

- J. Adolfsson *et al.* The upgrade of the ALICE TPC with GEMs and continuous readout. JINST **16** (2021) no.03, P03022, [arXiv:2012.09518 [physics.ins-det]].
  Summary paper of the TPC upgrade by the ALICE TPC collaboration, of which the author is a member, as part of his student service task.

- O. Matonoha. Light-flavour hadron production as a function of the underlying event. *ARISF* 2021, p. 277. Available at *https://cds.cern.ch/record/2758268*.
  Proceedings of the 55th Rencontres de Moriond on QCD conference.

- J. Adolfsson, *et al.* QCD challenges from pp to A–A collisions, Eur. Phys. J. A **56** (2020) no.11, 288 [arXiv:2003.10997 [hep-ph]]
  Summary paper to the 3rd International Workshop on QCD Challenges from pp to A–A, 2019, presenting main ideas discussed during the workshop, where the author actively participated and helped review the final document.

- ALICE Collaboration. Production of pions, kaons and protons as a function of the transverse event activity in pp collisions at $\sqrt{s} = 13$ TeV. Accepted by JHEP, preprint [arXiv:2301.10120 [nucl-ex]].
  The first publication of the author and his collaborators on the R_{T} measurements. The author was one of four members of the Paper Committee (with O. Vazquez, A. Nassirpour, P. Christiansen), which together developed the analysis techniques and the use of the observable R_{T}. The publication presents the use of this observable as well as particle spectra of π, K, and p, which were reconstructed by O. Vazquez.

- ALICE Collaboration. Light-flavor particle production in high-multiplicity pp collisions at $\sqrt{s} = 13$ as a function of transverse spherocity. Publication currently undergoing the internal review process of ALICE.
  Publication of the author and his collaborators on the $S_O^{p_T=1.0}$ measurements, including results presented in this dissertation. The author was one of six members on the Paper Committee (with O. Vazquez, A. Nassirpour, P. Christiansen, R. Rath, S. Basu), which together developed the analysis techniques and the use of the observable $S_O^{p_{\mathrm{T}}=1}$. The publication presents the use of this observable as well as spectra of π, K, p, Ξ, ϕ, K^*, and the author's $\mathrm{K}^0_{\mathrm{S}}$ and Λ.

ALICE publications are subjected to an extensive internal review process, often taking several years. The Paper Committee in ALICE is the group of collaborators responsible for conducting the actual data analysis, producing the figures, and writing of the final publication.

The K^0_S and Λ measurements as a function of R_T, $R_\mathrm{T,min}$, and $R_\mathrm{T,max}$ presented in this thesis have not been published yet but are planned for publication in the near future.

Acknowledgements

Firstly, I would like to express my sincere gratitude to my brilliant, patient, and always kind advisors, David, Peter, and Alice. David, you have provided me with steady support, helped me lay out the overall structure of my studies and research plans, and navigate the university process as well as the collaboration. You also relieved a lot of pressure by taking care of the logistics of the thesis printing and defense planning. You are immensely considerate and have always had my back. Peter, you have an incredible mind for physics and your leadership skills set a high bar for my future bosses. You have the ability to boost spirits and are unafraid to befriend your students, but also work hard alongside them. Alice, you have been a very joyful addition to my advisors, and I thank you for your compassionate approach when dealing with people and always very valuable feedback and contributions in discussions.

Furthermore, I would like to acknowledge the rest of the (former) Division of Particle Physics. I was always impressed by the level of professionalism and kindness that my colleagues treated me and each other with. I appreciate every Fredagsfika and after-work gathering. I would like to specifically mention Florido, who provided excellent technical and computational support, and Bozena, who always helped me with administrative matters and, as a fellow Slav, made me feel a little more at home. I also want to thank the former PhD students with whom I shared my office for several years and travelled the world: Adrian, Omar, and Jonathan; other PhD students who I wish the best of luck to: Alex, Lara, Joey, Joachim, Kaare, Roman, and Sten; as well as other ALICE colleagues: Vytautas and Sumit.

My sincere thanks also belong to my parents, who have always doubtlessly and unconditionally supported me on my path, as well as to my partner, who has lovingly stood by my side and who makes my life fuller.

I would also like to express my gratitude to all who helped and provided feedback on my thesis, including Else, my three advisors, and Zuzana. I also want to thank Trine and Anna, who gave me feedback on some sketches and visual aspect of the thesis.

Regarding the work and figures presented in this dissertation, credit should be given to the following individuals: P. Christiansen, who measured the Ξ spectra used for feeddown corrections and provided the MC predictions for $R_\mathrm{T,min}$ and $R_\mathrm{T,max}$; O. Vazquez, who measured the pions and charged kaons that the results in this thesis

are compared with, as well as unfolded the $S_{\mathrm{O}}^{p_{\mathrm{T}}=1.0}$ distributions and produced their plots; A. Nassirpour, who determined the experimental bias values in the $S_{\mathrm{O}}^{p_{\mathrm{T}}=1.0}$ measurements, produced the plots of ratios of integrated yields as a function of $S_{\mathrm{O}}^{p_{\mathrm{T}}=1.0}$, and provided a script skeleton for producing the ratio-to-pions plots in the $S_{\mathrm{O}}^{p_{\mathrm{T}}=1.0}$ analysis; R. Rath, who provided a script skeleton for producing the plots of particle yields and average momenta in the $S_{\mathrm{O}}^{p_{\mathrm{T}}=1.0}$ analysis; S. Basu, who assisted with simulating the various MC predictions, and T. Poulsen, who created the sketch of the factorisation theorem.

Part I

Fundamental theory

Chapter 1

Introduction to quantum chromodynamics

This chapter serves as an introduction to particle physics, QCD, and phenomenology of high energy QCD interactions, with the focus on multiple partonic interactions and string formations. Furthermore, it introduces the physics of QCD matter and the deconfinement of hadrons.

1.1 Standard Model of elementary particles

The Standard Model (SM) of particle physics is a set of theories that describe *elementary* constituents of matter and their interactions via fundamental forces of the Universe. It has been formulated in the 1970s, combining frameworks of quantum field theory (QFT), gauge symmetries, and spontaneous symmetry breaking.

Matter particles in the SM are classified into two main categories: quarks and leptons. Quarks come in six flavours (*up, down, charm, strange, top, and bottom*) and form hadrons, i.e. *baryons* (qqq) and *mesons* ($q\bar{q}$). The lepton sector also comprises six flavours (*electron, muon, tau*, and their corresponding *neutrinos*). Quarks and leptons are fermions with an intrinsic spin $1/2$. Furthermore, matter particles in the SM also come with associated antiparticles, which have opposite quantum numbers but the same mass.

The interactions between matter particles in the SM are mediated by an exchange of gauge bosons. There are three fundamental forces in the SM, described by four types of vector bosons (ordered by their typical strength):

1. *Strong force*, mediated by the gluon.
2. *Electromagnetic force*, mediated by the photon.
3. *Weak force*, mediated by the massive bosons $W^{\pm}$ and Z^{0}.

Moreover, the interactions are associated with local gauge symmetries, which determine their mathematical structure. The symmetry group for the SM is $\mathrm{SU}(3) \times \mathrm{SU}(2) \times \mathrm{U}(1)$, corresponding to the strong and the electroweak sector. [1]

In addition, the SM also includes the scalar Higgs boson, which is responsible for giving mass to other elementary particles. This is achieved via the Higgs mechanism [2, 3], which involves the spontaneous breaking of the electroweak symmetry in the early universe. The Higgs boson was discovered experimentally at the Large Hadron Collider (LHC) in 2012 by the ATLAS [4] and CMS [5] collaborations, confirming a key prediction of the SM.

Nevertheless, the SM has several limitations, including its inability to account for dark matter, explain why the particle masses span over several orders of magnitude, and the CP violation problem related to the observed matter-antimatter asymmetry in the Universe. These are actively investigated in Beyond Standard Model (BSM) theories.

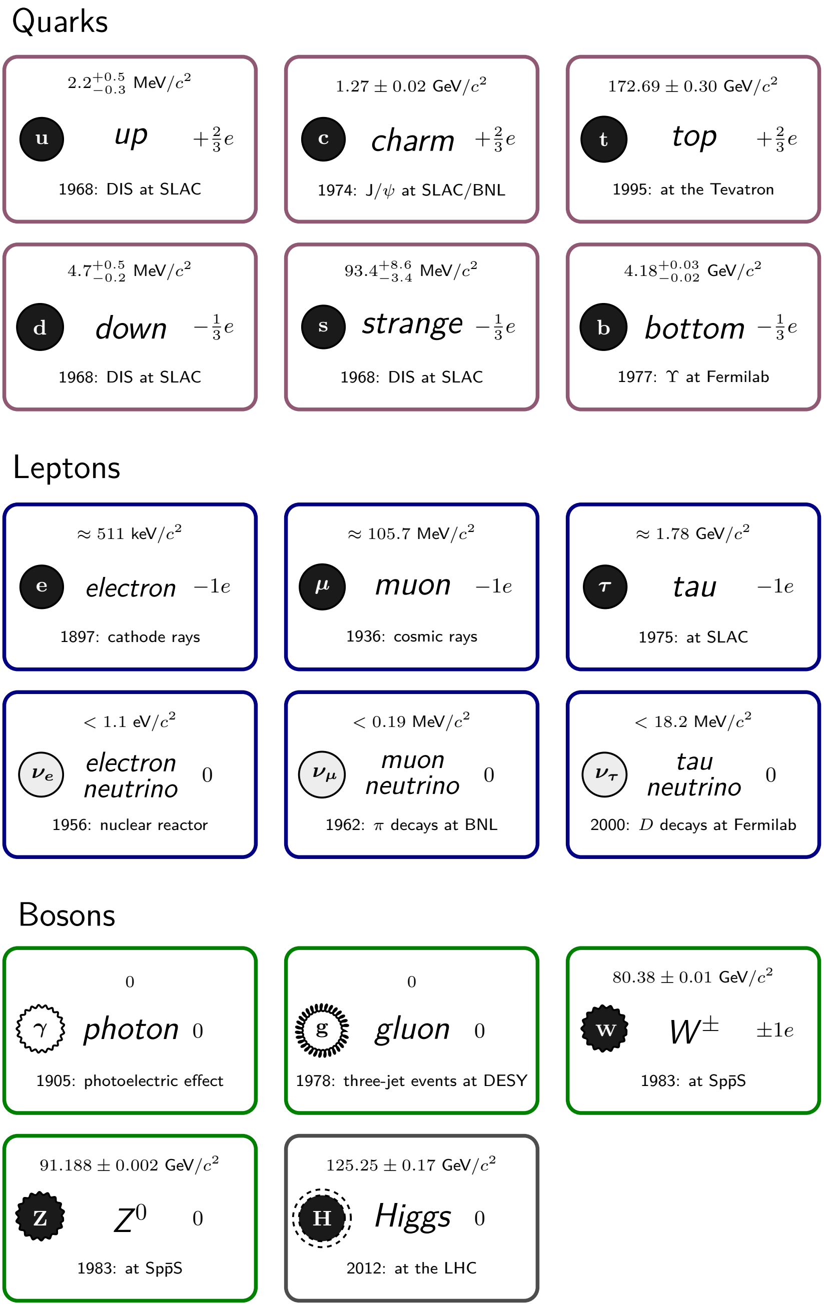

Figure 1.1: Particle of the Standard Model, listed together with their mass, electric charge, and the year and means of discovery or location (going clockwise from the top). The mass values are taken from Ref. [6].

1.2 Coordinate systems and kinematic observables

Particles in HEP processes are described by their Lorentz-invariant four-vectors, $\boldsymbol{x} = (ct, x, y, z)$ and $\boldsymbol{p} = (E/c, p_x, p_y, p_z) = (E/c, \vec{p_\mathrm{T}}, p_z)$, where $|\vec{p_\mathrm{T}}| \equiv \sqrt{p_x^2 + p_y^2}$. In LHC experiments, the coordinate system is defined such that the x-axis points in the direction of the centre of the LHC, the z-axis points in the direction of the beam, and the y-axis points, perpendicularly, up, as shown in Fig. 1.2. In addition to the standard Cartesian coordinates, two observables, ϕ (azimuthal angle) and η (pseudo-rapidity), are used to describe the position and momentum of particles relative to the nominal interaction point (IP), which is located at $x = y = z = 0$. Pseudorapidity is defined as a function of the polar angle θ, where

$$\eta = -\ln(\tan(\theta/2)) \quad . \tag{1.1}$$

For high-momentum particles ($E \simeq pc$), pseudorapidity is an approximation of the rapidity relative to the beam, given by

$$y = \frac{1}{2} \ln \frac{E + p_z c}{E - p_z c} \quad . \tag{1.2}$$

Rapidity is a convenient quantity to use because it transforms additively under Lorentz boosts, unlike velocity. In these coordinates, the following relations hold:

$$p_x = |\vec{p_\mathrm{T}}| \cos\phi\,, \qquad p_y = |\vec{p_\mathrm{T}}| \sin\phi\,, \qquad p_z = |\vec{p}\,| \sinh\eta\,. \tag{1.3}$$

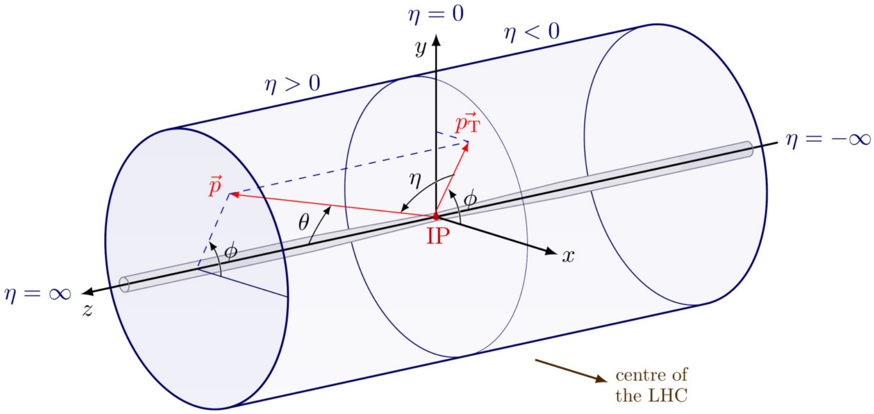

Figure 1.2: Coordinate system of an LHC experiment, with the interaction point in the centre. Schematic inspired by I. Neutelings.

1.3 Quantum electrodynamics, electrons, and photons

In many aspects, QCD is a very similar theory to the simpler and better explored theory QED. In QFT, dynamics of particles can be provided in terms of its Lagrangian density $\mathcal{L}$, from which equations of motions can be derived and which is also used to calculate interaction probabilites. The QED theory with a local U(1) symmetry has its $\mathcal{L}_{\text{QED}}$ defined as:

$$\mathcal{L}_{\text{QED}} = \bar{\psi}(i\not{\partial} - m)\psi - \frac{1}{4}F_{\mu\nu}F^{\mu\nu} - e\bar{\psi}\not{A}\psi \quad , \tag{1.4}$$

where ψ is the electron field with mass m and electric charge e, A_μ the electromagnetic vector field associated with the photon, $F_{\mu\nu}$ the field-strength tensor, and Feynman slash notation is employed. The first part describes the dynamics of the electron fields, the second part describes the dynamics of the electromagnetic field, and the last part describes the interaction of electrons and photons with a coupling strength e. Using Feynman diagrams, they can be visualised as:

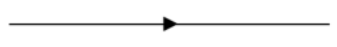

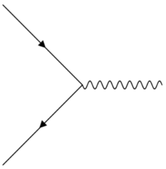

In QED interactions, each vertex depicted in the Feynman diagrams contributes to the probability of the process with a coefficient α (to the matrix elements as $\sqrt{\alpha}$), which is the coupling constant defined as $\alpha = e^2/4\pi$. This constant is generally small, which allows for interactions to be calculated using perturbation theory as an expansion series in α. The contributions to the series correspond to different Feynman diagrams representing the possible interaction processes, and they are ordered in powers of α based on the complexity of the diagrams.

Contributions from higher orders, such as the electron loop depicted below, lead to "screening" of the effective charge at large distances/small momenta, which leads to a re-definition of the coupling constant and becoming dependent on the scale of the process μ. For example, at low energies corresponding to atomic scales, $\alpha \approx 1/137$, but at scales of the Z^0 boson mass, $\alpha \approx 1/127$ [7]. The *running* of this coupling is given by the β function, $\beta(\alpha) \equiv \frac{\partial\alpha}{\partial \log \mu^2}$, and it can be calculated by quantifying the effective coupling strengths at various orders of perturbation theory and using renormalisation group tools [8], although renormalisation is a more general concept.

In QED, the screening leads to a positive sign in β calculated at lowest order, which means that when solving for α by integrating, α grows with the energy scale[1].

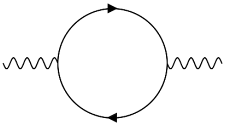

Renormalisation is also used when calculating physical quantities where loop contributions lead to divergences, which are then absorbed into the parameters of the theory. The success of these procedures and the QED theory as a whole is validated by excellent prediction power for experimental measurements, such as the magnetic moment of the electron [9].

1.4 Quantum chromodynamics, quarks, and gluons

In QCD, particles have an additional quantum number called colour charge: red, green, and blue. Thus, there are three quarks of each flavour and eight gluons mediating the interactions. Gluons also carry colour charges, which allows them to interact with each other, making the theory non-Abelian. The QCD Lagrangian is symmetric under local SU(3) transformations and takes the shape of:

$$\mathcal{L}_{\mathrm{QCD}} = \sum_{f}^{n_f} \overline{\psi}_i^{(f)} (i\not{D}_{ij} - m_f \delta_{ij}) \psi_j^{(f)} - \frac{1}{4} \sum_{a}^{8} F_a^{\mu\nu} F_{\mu\nu}^a \quad , \tag{1.5}$$

$$D_{ij}^{\mu} \equiv \partial^{\mu} \delta_{ij} + i g_s t_{ij}^a A_a^{\mu} \quad , \tag{1.6}$$

$$F_{\mu\nu}^a \equiv \partial_\mu A_\nu^a - \partial_\nu A_\mu^a - g_s f_{abc} A_\mu^b A_\nu^c \quad , \tag{1.7}$$

where ψ are the quark fields of n_f different flavours with mass m_f and colours i, j, D_{ij}^{μ} the covariant derivative with the coupling strength g_s and eight SU(3) generators given by matrices t_{ij}^a, and A_a^{μ} are the gluon fields [10]. Lastly, $F_{\mu\nu}^a$ is the field-strength tensor with f_{abc} being structure constants. The Lagrangian now also contains terms with interactions between gluons. In the representation of Feynman diagrams, for the interactions, there is:

---

[1] The scale at which QED eventually breaks down due to this increase is well above the Plack mass.

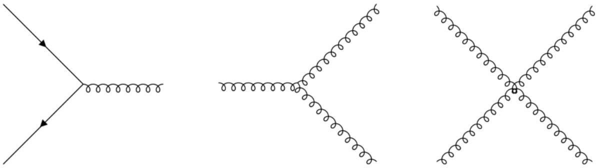

Similarly to the QED case, the strong coupling constant can be defined as $\alpha_s = g^2/4\pi$. However, when considering its modifications due to virtual corrections, in addition to the quark loop, there is also a gluon loop:

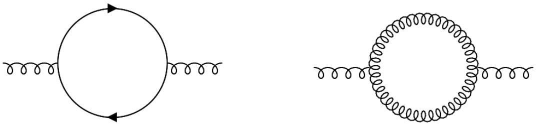

The gluon loop contributes to the β function in an opposite and larger way than the quark loop, and so overall, there is an *anti-screening* effect instead and a negative sign in the calculated one-loop β function. The running of the coupling can be calculated as:

$$\alpha_s(\mu) = \frac{1}{b_0 \log(\mu^2/\Lambda^2_{\mathrm{QCD}})} \quad , \tag{1.8}$$

where b_0 is a constant computed from the loop calculations, $b_0 = \frac{11-\frac{2}{3}n_f}{4\pi}$ [11]. The introduced Λ_{QCD} is a scale parameter of the theory corresponding to the energy where the coupling becomes infinite, and depends on the definition of α_s and the number of available quark flavours n_f [10]. It ranges between 200 and 300 MeV [12].

From the running, it is evident that the coupling strength decreases with increasing energy, which is known as *asymptotic freedom* [11, 13] and corresponds to the fact that strong interaction is short-ranged. On the other hand, at low values, α_s diverges, which is related to the fact that quarks are bound to hadrons – *quark confinement*. The evolution of α_s also limits the applicability of perturbation theory at low energy regimes; calculations from perturbative QCD (pQCD) are relevant at leading orders starting typically from $1-2$ GeV/c of transferred momentum. The measured $\alpha_s(\mu)$ is shown in Fig. 1.3, and at scales of the Z^0 boson mass is approximately 0.1185 ± 0.0006 [6, 14].

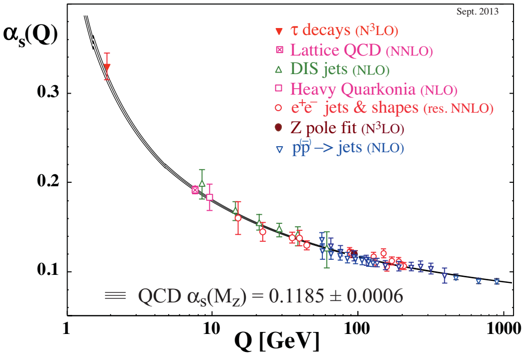

Figure 1.3: Strong coupling constant determined at different energy scales through various measurements and numerical calculations (data points) and compared with theoretical predictions from QCD. [14]

1.5 From partons to hadrons

1.5.1 Initial and Final State Radiation

In QFT, charged particles are surrounded by a cloud of virtual particles, which can be thought of as fluctuations in the particles' field. For example, the electron state can be described as a superposition of the bare electron plus additional massless bosons:

$$|\mathrm{e}\rangle_{\mathrm{phys}} = |\mathrm{e}\rangle + |\mathrm{e}\gamma\rangle + |\mathrm{e}\gamma\gamma\rangle + \dots \tag{1.9}$$

and, at higher orders, pairs of virtual electrons. The fluctuations continuously form and recombine, with their lifetime depending on their energy and momentum. Specifically, the lifetime of a fluctuation with energy ω and transverse momentum k_{T} can be approximated as:

$$\tau \approx \frac{\omega}{k_{\mathrm{T}}} \quad . \tag{1.10}$$

This implies that fluctuations with smaller-k_{T} live longer. [15]

As illustrated in Fig. 1.4, the undisturbed, coherent mixed state of the bare charge and the field fluctuations can be disrupted by the presence of an interaction. Intuitively, this interaction can change the energy and momentum of the fluctuations, their formation and recombination, and lead to the emission of radiation in two ways:

1. a fluctuation is kicked on-shell by the interaction and part of the field continues in its original direction, which leads to Initial State Radiation (ISR);

2. as a result of the field of the scattered particle rearranging itself , which can be a source of Final State Radiation (FSR).

In both of the cases, a larger momentum transfer implies more radiation. *For hard, wide angle emissions, cross sections can be calculated perturbatively at fixed orders.*

Soft and collinear emissions, however, lead to infra-red divergences ($\propto \frac{1}{\omega}$,$\propto \frac{1}{k_{\mathrm{T}}^2}$) and thus, need to be factorised away from the amplitudes or the cross sections and then described using resummation techniques. Without any emissions, the probabilities of finding electrons and photons of fractional momentum x with respect to the whole system are:

$$f_{\mathrm{e}}(x) = \delta(1-x)\,, \qquad f_{\gamma}(x) = 0\,, \tag{1.11}$$

When considering the emissions above some scales parametrised by the resolution parameter Q^2, these probabilities, however, evolve according to the DGLAP equation [16] :

$$\frac{\partial}{\partial \ln Q^2} \begin{pmatrix} f_e(x,Q^2) \\ f_\gamma(x,Q^2) \end{pmatrix} = \frac{\alpha_{\mathrm{em}}}{2\pi} \int_x^1 \frac{dz}{z} \begin{pmatrix} P_{ee}(z) & P_{e\gamma}(z) \\ P_{\gamma e}(z) & P_{\gamma\gamma}(z) \end{pmatrix} \begin{pmatrix} f_e\left(\frac{x}{z}, Q^2\right) \\ f_\gamma\left(\frac{x}{z}, Q^2\right) \end{pmatrix} \quad , \tag{1.12}$$

where $P_{ij}(z)$ are the splitting probability functions of a particle i emitting a particle j.

In QCD, the behaviour is analogous, with $\alpha_{\mathrm{em}} \to \alpha_s$, $e \to q$, and $\gamma \to g$. [15]

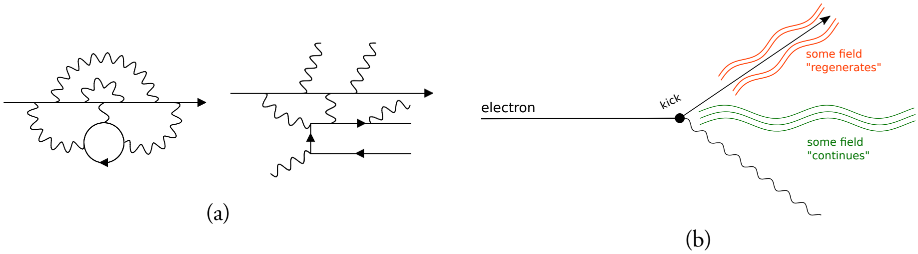

Figure 1.4: **(a)** Illustration of the field fluctuations before and after the state coherence gets disturbed by an external actor. **(b)** Illustration of emmisions of radiation in a scattering process.

1.5.2 Factorisation theorem

The evolution equation (1.12) implies that the probabilities of observing emissions with a fractional momentum x depend on the resolution Q^2. In QCD,

1. when applied to the initial state, they are known as parton distribution functions (PDFs) f_i^A and determine the probabilities of finding partons[2] i in the composite hadronic state A.
2. When applied to the final state, they are called fragmentation functions, and determine the probabilities of measuring fragments of the outgoing particles.

This leads to the factorisation theorem [17] for processes involving collisions of two hadrons, which separates the perturbatively calculable partonic cross section from the non-perturbative partonic evolution and hadronisation. The theorem can be expressed as follows:

$$\sigma = f_i^A(x_i, \mu_F) f_j^B(x_j, \mu_F) \otimes \hat{\sigma}_{ij\to n}(\mu_F, \mu_R) \otimes D_{n\to n'} \, . \tag{1.13}$$

Here, i and j are the initial partons, $\hat{\sigma}_{ij\to n}$ is the partonic cross section, $D_{n\to n'}$ is the process-specific fragmentation function for evolving the partons n into the particles' final state n', and μ_F and μ_R are the factorisation and renormalisation scales, respectively. The factorisation scale, μ_F, determines the scale below which the emissions are absorbed into the PDFs. The theorem is depicted in Fig. 1.5.

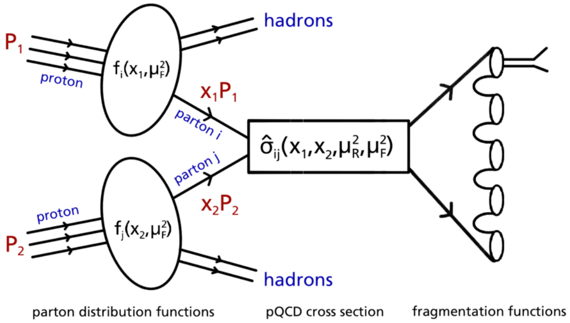

Figure 1.5: Illustration of the factorisation theorem. Sketch drawn by T. Poulsen.

1.5.3 Parton distribution functions

The PDFs defining the probabilities of finding quarks and gluons in nucleons can be determined experimentally at hadron-electron colliders such as HERA [18]. They are determined from measurements of deep inelastic scatterings in a range of energies and momentum transfers. They are displayed in Fig. 1.6 as a function of the fractional momentum x (also called Björken x).

---

[2] Partons refer to the valence quarks, sea quarks, and gluons inside hadrons.

According to collider kinematics, $x \propto \frac{1}{\sqrt{s}\cdot e^{y}}$, therefore, the partonic composition of ultra-relativistic hadrons is dominated by gluons. Following unitarity principles and the Balitsky-Kovchegov evolution equation [19], it is expected that gluons start recombining and the gluonic content saturates as $x \rightarrow 0$. This is actively researched [20], however, not explicitly measured yet. Additionally, it should be noted that in ultra-relativistic heavy nuclei, the partons are modified in the contracted nuclear environment and the PDFs there are referred to as nPDFs.

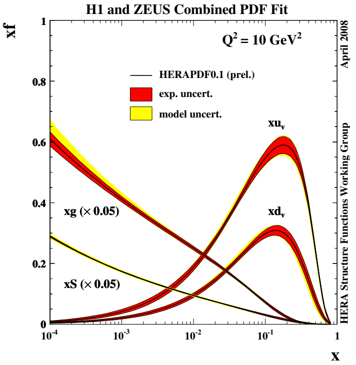

Figure 1.6: Parton distribution functions determined in ep scatterings at HERA as a function of the fractional momentum for the up, down, sea quarks, and gluons. [18]

1.5.4 Parton fragmentation and the Lund string

After the scattering process, the produced partons continue to fragment by emitting more partons in a process called the parton shower. Since the coupling strength in QCD increases with decreasing the energy scale of the splitting, this leads to the production of many soft, collimated emissions known as jets. The partonic evolution continues until the virtuality of the partons reaches the hadronization scale ($\approx \Lambda_{\mathrm{QCD}}$). There are multiple frameworks within QCD to describe the evolution of partons into their final state, such as using the DGLAP equations or the so-called dipole formalism.

Once the partonic final state is reached, the partons hadronise into the observable mesons and baryons. The hadronisation process is not calculable in QCD and requires phenomenological models to describe it. One such model is the Lund string model [21], which describes hadronisation as the breaking of a colour string between the quarks in the final state. In this model, the energy stored in the color string is converted into the mass of new hadrons.

According to confinement, hadronisation should involve at least two partons with complementary colours. In QCD, the $q\bar{q}$ potential takes the shape of

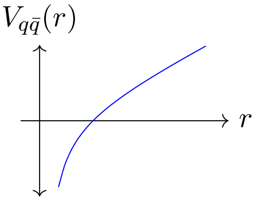

$$V_{q\bar{q}}(r) \approx -\frac{4}{3}\frac{\alpha_s \hbar c}{r} + \kappa r \quad , \tag{1.14}$$

where κ is a parameter with value around 1 GeV/fm. In the non-perturbative regime (long distances), the potential is dominated by the linear part, which is reminiscent of a system bound by a string with tension κ. This is taken advantage of by the Lund string model – a q and $\bar{q}$ pair separated by distance Δx is bound by a colour field (string) with energy $\kappa \Delta x$.

If the q and $\bar{q}$ continue separating as a result of the scattering, the energy stored in the colour field increases. At some point, it can become energetically favourable to produce a new $q\bar{q}$ pair out of vacuum, which is a quantum mechanics tunnelling phenomenon characterised by the probability:

$$\frac{\mathrm{d}P}{\mathrm{d}m_\mathrm{T}} \propto \exp\left(-\frac{\pi m_\mathrm{T}^2}{\kappa}\right) \quad , \tag{1.15}$$

where m_T is the transverse mass of the produced quarks. Otherwise, the $q\bar{q}$ system starts contracting and oscillates with a period $T = 2E_\mathrm{kin}/\kappa$, where E_kin is its maximum kinetic energy. The produced q and $\bar{q}$ then connect by new colour fields to the original pair. This process repeats itself resulting in a cascade of many $q\bar{q}$ pairs connected by many colour strings. In this description, baryons can also be created by double tunnelling of a $qq\bar{q}\bar{q}$ pair. The process of string breaking is illustrated in Fig. 1.7.

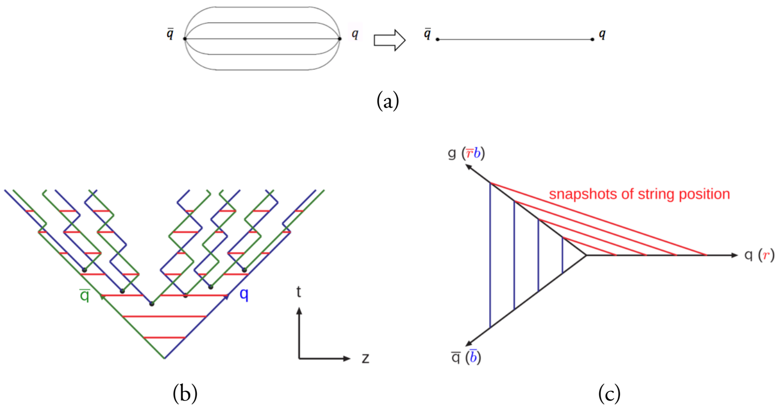

(a)

(b)

(c)

Figure 1.7: **(a)** Illustration of the colour field between two quarks and its simplified representation with a string [21]. **(b)** Illustration of the string splitting by producing new $q\bar{q}$ in the $t-z$ plane [21]. **(c)** Visualisation of the treatment of gluons in the Lund string model [22].

Equation (1.15) also implies that production of strange quarks is suppressed by a factor of

$$\rho = \exp\left(-\frac{\pi(m_s^2 - m_{u,d}^2)}{\kappa}\right) \quad . \tag{1.16}$$

This parameter is typically tuned to data, as substituting constituent masses (e.g., in baryons, $m_s \approx 0.5\,\mathrm{GeV}/c^2$, $m_{u,d} \approx 0.33\,\mathrm{GeV}/c^2$) versus current masses ($m_s \approx 0.1\,\mathrm{GeV}/c^2$, $m_{u,d} \approx 0$) leads to considerable differences underestimating and overestimating data, respectively.

For a $q\bar{q}g$ system, in this model, the gluon connects to the quark and antiquark and is effectively treated as a "kink" on the colour field, adding energy and momentum to the $q\bar{q}$ string (stretching it in its direction), as visualised in Fig. 1.7.

It should be noted that in the paradigm of AA collisions, hadron production can be alternatively modelled by hadronisation at the QGP's phase boundary by *coalescing* free quarks.

1.6 Multiple partonic interactions

Results from Sp$\bar{\text{p}}$S in the 1980s sparked motivations for considering interactions of multiple partons between the two composite protons. For example, the AFS experiment observed an abundance of 4-jet events, displayed in Fig. 1.8, that could not be explained by calculations considering a double gluon bremsstrahlung from a single partonic scattering [23]. Furthermore, UA5 measurements studying energy dependence of multiplicity distributions P(N_{ch}) saw the so-called KNO scaling [24], where P(N_{ch})/$\langle N_{\mathrm{ch}}\rangle$ does not depend on energy, but revealed a broadening in high-multiplicity events with increasing $\sqrt{s}$ [25, 26], which was not reproducible in the context of N_{ch} being produced from a single string [27]. This further suggested the presence of multiple production sources.

These findings prompted further development of Regge theory and approaches that incorporated multiple pomerons, which were successful in describing the N_{ch} distributions. However, this approach is fully decoupled from descriptions of the perturbative primary scattering. Subsequently, much of the phenomenology related to multiple partonic interactions was developed within the framework of the Pythia MC event generator, which is discussed individually in Chapter 2 [27]. However, nowadays, the relevance of the concept of MPIs in hadronic collisions extends beyond this generator. A scattering with double partonic interactions is illustrated in Fig. 1.9.

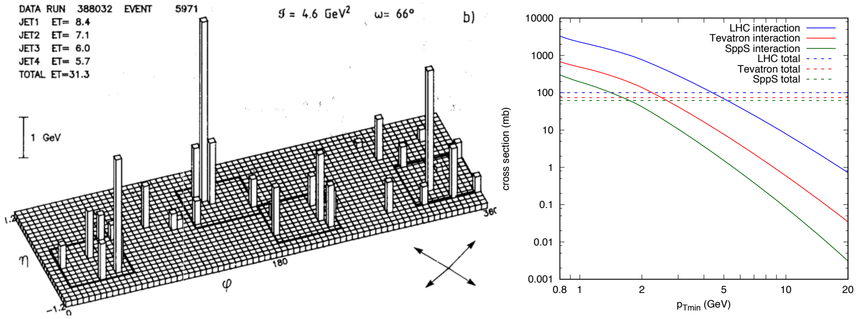

(a) (b)

Figure 1.8: **(a)** Event display of an event with a 4-jet, where the pillars correspond to transverse energy deposits. [23] **(b)** Dependence of the integrated parton-parton cross section on the cutoff parameter $k_{\perp\mathrm{min}}$ for $\mathrm{Sp\bar{p}S}$ at $\sqrt{s} = 0.63\,$TeV, Tevatron at $\sqrt{s} = 1.96\,$TeV, and the LHC at $\sqrt{s} = 13\,$TeV, modelled with Pythia. [27]

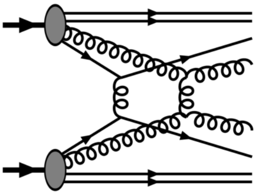

Figure 1.9: Diagram showing a double partonic interaction, a case of $n_{\mathrm{MPI}} = 2$. [15]

In the Pythia approach, MPI are treated as additional perturbative scatterings. In QCD, the $2 \to 2$ cross section (dominated by the gluon exchange t-channel) diverges as $\propto \alpha_S^2(k_\perp^2)/k_\perp^4$, so a cutoff parameter $k_{\perp\mathrm{min}}$ must be introduced, and using (1.13) leads to:

$$\frac{d\sigma}{dk_\perp^2} = \sum_{ij} \int dx_1 dx_2 f_i(x_1, \mu_F^2) f_j(x_2, \mu_F^2) \frac{d\hat{\sigma}_{ij}^H}{dk_\perp^2}\,, \tag{1.17}$$

$$\sigma_{\mathrm{int}}(k_{\perp\mathrm{min}}) = \int_{k_{\perp\mathrm{min}}^2}^{s/4} \frac{d\sigma}{dk_\perp^2} dk_\perp^2\,. \tag{1.18}$$

The choice of cutoff can be tuned to experimental data, and for the $\mathrm{Sp\bar{p}S}$ energy of $\sqrt{s} = 630\,$GeV, a value of around $1.6\,\mathrm{GeV}/c$ was typical [27]. The dependence of this parton-parton scattering cross section is shown in Fig. 1.8.

The total pp cross-section, which is of the order of 100 mb at $\sqrt{s} = 13\,$TeV, is given by

$$\sigma_{\mathrm{pp}} = \sigma_{\mathrm{elastic}} + \sigma_{\mathrm{single\,dif.}} + \sigma_{\mathrm{double\,dif.}} + \sigma_{\mathrm{non-dif.}} \quad , \tag{1.19}$$

where the inelastic cross sections $\sigma_{\text{inel}} \approx \sigma_{\text{double dif.}} + \sigma_{\text{non-dif.}}$ corresponds to approximately 60% of the total. The mean number of MPIs, $\langle n_{\text{MPI}} \rangle$, can be estimated using:

$$\langle n_{\text{MPI}} \rangle (k_{\perp,\text{min}}) = \frac{\sigma_{\text{int}}(k_{\perp,\text{min}})}{\sigma_{\text{inel}}} \tag{1.20}$$

However, the actual treatment is more complex and involves considerations of other parameters such as the dampening factor $k_\perp^0$ to account for the confinement nature of partons, modifications of multiparton PDFs, energy-momentum conservation effects, x-dependent source geometry, and the intertwinedness of partonic evolutions.

In summary, MPIs represent several subcollisions that take place in an average pp collision with p_{T} scales of a few GeV. They are colour-connected to the beam remnants, which in the Lund model are represented by strings. Since a string with $\kappa = 1\,\text{GeV/fm}$ yields, as a rule of thumb, approximately one hadron per unit rapidity, and the average, minimum bias (MB), pp collision at the LHC at $\sqrt{s} = 13\,\text{TeV}$ has $\langle \text{d}N_{\text{ch}}/\text{d}y \rangle \approx 6$, the typical number of partonic interactions is around six [27].

Finally, the observation of QGP-like phenomena in pp collisions at the LHC has renewed interest in MPI phenomenology, as discussed in the following chapter. Such observations do not contradict the concept of MPIs; rather, they suggest the possibility of incorporating collective behavior among the MPIs, such as interactions between strings, local modifications of string tensions, or, alternatively, the formation of a multipartonic state with QGP-like properties.

1.6.1 Colour reconnection

The incorporation of MPIs improved the description of the N_{ch} distributions and their dependence on $\sqrt{s}$. However, there were also observations of $\langle p_{\text{T}} \rangle (N_{\text{ch}})$ increasing as a function of N_{ch}, which could not be explained. More MPIs lead to more strings, which in turn leads to the production of more particles, but the p_{T} is mostly unaffected. This would predict a weaker dependence of $\langle p_{\text{T}} \rangle$ on N_{ch}, contrary to the data [27]. The issue was resolved by implementing a possible colour reconnection (CR) mechanism, which rearranges the colour fields between partons.

One can envision the following process:

$$e^+e^- \to W^+W^- \to q_1\bar{q}_2q_3\bar{q}_4.$$

In this scenario, a colour reconnection mechanism could rearrange the colour-connected $q_1\bar{q}_2$ and $q_3\bar{q}_4$ into $q_1\bar{q}_4$ and $q_3\bar{q}_2$ if it were energetically favourable, depending on

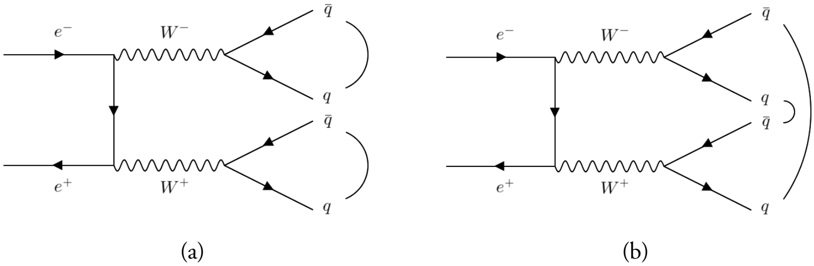

Figure 1.10: Illustration of the $e^+e^- \to W^+W^- \to q_1\bar{q}_2q_3\bar{q}_4$ process **(a)** before colour reconnection (CR) and **(b)** its possible correction after CR. The bent lines between quarks indicate the colour fields.

the phase-space configurations. This is illustrated in Fig. 1.10. Measurements at LEP [28] of this process have indeed shown that such final-state corrections must be taken into account to explain the data on W masses and widths. They also reported that the reconnection probabilities for such events are on the order of 50%, further indicating that colour reconnection is an important factor to consider.

Pythia implements CR by minimizing the total length of strings in the system, analogous to minimising potential energy [29]. This mechanism, illustrated in Fig. 1.11, explains the rising trend of $\langle p_\mathrm{T} \rangle$ as a function of N_ch: shorter strings imply fewer hadrons to split the transverse boost across, and the more MPI, the bigger this effect. Moreover, CR also helped describe the absolute value of $\langle p_\mathrm{T} \rangle$. With this approach, no further modifications of fragmentation parameters were necessary, in line with the concept of jet universality. However, it should be noted that there are various CR implementations and all rely on parameters obtained from tuning to data.

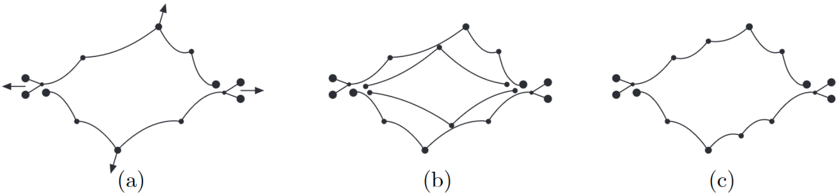

Figure 1.11: Depiction of the CR process: **(a)** in a hard parton subcollision, the outgoing gluons are connected to the beam remnants through colour. Additional gluon kinks may occur through initial state radiation, which are ordered by rapidity. **(b)** A second hard scattering should theoretically result in two new strings connected to the remnants. **(c)** In order to minimise the total string length, gluons are colour reconnected. [30]

It is also worth noting that the p_T boost acquired through colour reconnection may depend on mass and whether a hadron is a baryon or meson, which somewhat mimics the hydrodynamic signatures of collective flow observed in AA collisions [31].

1.7 Underlying event

The underlying event (UE) in high-energy collisions refers to the additional hadronic activity that accompanies the primary hard scattering process, but is not directly related to it. This includes the fragmentation products of the beam remnants, ISR and FSR, as well as the effects of the previously discussed MPIs, and is visualised in Fig. 1.12. The UE (with its name coined at Tevatron [32]) is typically characterised by a distribution of softer particles around and far outside of the hard process and was first observed at Sp$\bar{\text{p}}$S in the 1980s [33]. These measurements saw a constant plateau of transverse energy E_{T} outside of the jet core, with its height independent of the jet energy.

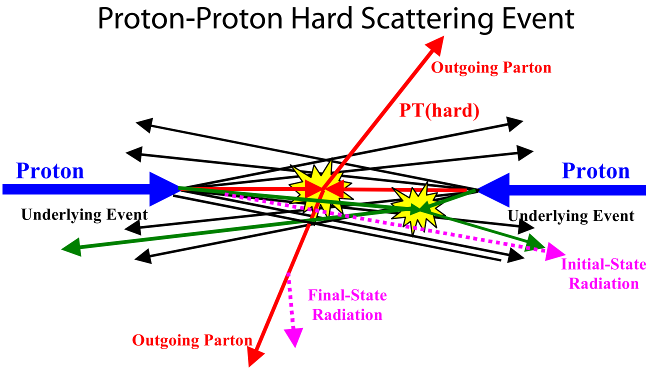

Figure 1.12: Cartoon illustrating a pp collision and its components: the hard scattering process, beam remnants, initial/final state radiation, and the MPIs. The last three contribute to the underlying event. [32, 34]

It is important to note that particle production in UE is different from the MB production, as it is biased by the presence of hard scattering. Additionally, the magnitude of the UE can fluctuate significantly from event to event.

1.8 From hadrons to partons: deconfined QCD matter

A simple argument can be made that confinement of quarks inside hadrons cannot be sustained when the density of partons is too large compared to that inside ordinary hadrons. Or alternatively, when the partonic kinetic energies are much larger than the confining part of the $q\bar{q}$ potential in (1.14). The following sections introduce some theoretical frameworks predicting the deconfinement of quarks and gluons. The calculations presented use natural units ($\hbar = c = k_B = 1$).

1.8.1 Bag model of hadrons

In this very naive approach [35, 36], hadrons are treated as spherical cavities ("bags") with radius R of free massless quarks. These cavities exist in the non-perturbative QCD vacuum, which exerts a confining pressure B. The lowest-energy solution of the Dirac equation for the quarks, which in this case is $\not{p}\psi = 0$, is the $s_{1/2}$-state given by:

$$\psi(r,t) = N \begin{pmatrix} j_0(\omega r)U \\ i\sigma \cdot \hat{r} j_1(\omega r)U \end{pmatrix} \exp(-i\omega t) \quad , \tag{1.21}$$

where N is a normalisation constant, j_0 and j_1 are spherical Bessel functions, ω is the quark energy, and U the two-component spinor. The assumption that quarks are confined within the cavity volume represents the boundary conditions that the quark scalar density $\psi\bar{\psi}$ becomes zero at $r = R$, which is equivalent to $j_0(\omega R) = j_1(\omega R)$:

$$j_0^2(\omega R) - \vec{\sigma} \cdot \hat{r}\vec{\sigma} \cdot \hat{r} j_1^2(\omega R) = 0 \tag{1.22}$$

$$j_0(\omega R) = j_1(\omega R) \quad , \tag{1.23}$$

which happens when $\omega \approx \frac{2.04}{R}$. Thus, the energy of the system can be given by

$$E(R) \approx n_q \cdot \frac{2.04}{R} + \frac{4\pi}{3} B R^3 \quad . \tag{1.24}$$

Here, the first term represents the kinetic energy of n_q quarks in the cavity and the second term is the cavity volume energy. Gluon solutions should also be considered but are neglected in this approach. The first term acts to expand the cavity, whereas the second term acts to contract it. Finding an optimum of this energy with respect to R leads to

$$B^{1/4} \approx \left(\frac{2.04 n_q}{4\pi} \right)^{1/4} \frac{1}{R} \quad . \tag{1.25}$$

Finally, assuming values for a proton, $R \approx 0.8$ fm, and three valence quarks $n_q = 3$, the confining pressure can be approximated as $B^{1/4} \approx 206$ MeV. [35]

To relate the confining pressure to a critical temperature at which deconfinement occurs, T_c, one can assume a gas of relativistic massless fermions and bosons with energy density ρ [37, 38]. Using Stefan-Boltzmann law, the equation of state is,

$$P = \frac{1}{3}(d_b + \frac{7}{8} d_f)\rho = (d_b + \frac{7}{8} d_f)\frac{\pi^2}{90} T^4 \tag{1.26}$$

where d_b and d_f are the degeneracy numbers for bosons and fermions, in this case gluons and quarks, respectively. Summing together possible colours, polarisations, and flavours for particles and antiparticles, one gets $d_b = 16$ and $d_f = 24$. Inserting the cavity pressure B value calculated in (1.25), T_c can be estimated as approximately 145 MeV.

1.8.2 Lattice QCD

Lattice QCD (LQCD) is a technique allowing calculation of processes involving the strong interaction in the non-perturbative regime, from first principles, without phenomenological assumptions. In this approach, the space-time continuum is discretised into a four-dimensional lattice, which allows QCD path integrals to be solved numerically. The smallest squares on the lattice are called *plaquettes*, with the lattice links representing gluon fields and lattice sites representing quark fields. [39]

Lattice calculations are computationally extremely intensive[3], thus, a sufficiently coarse lattice spacing must be chosen to reduce computational costs and make the approach feasible. Often, simulations are also performed with unphysical quark masses (e.g., $m_q \sim m_\pi$), for the same reason. The results are then extrapolated using highly complex methods. Another limitation in LQCD is the so-called *sign problem*, discussed in detail for instance in Ref. [41], which arises when evaluating highly oscillatory complex integrals in finite-density environment.

Despite its challenges, LQCD has been successful in various predictions, notably, the *ab initio* calculation of the mass of the neutron (uud) using the mass of Ω (sss) as an input [42]. Furthermore, it allows for the calculation of thermodynamics of QCD matter and predicts its equation of state, as well as a phase transition at $T_c \approx 150$ MeV [43, 44], which is usually identified with the formation of quark-gluon plasma QGP, discussed in Chapter 2. The dependence of energy density and pressure on temperature can be seen in Fig. 1.13.

---

[3] In fact, in the past, LQCD was among some of the most important drivers of the advancement of GPU computing and it is also used as benchmark in high-performance computing [40].

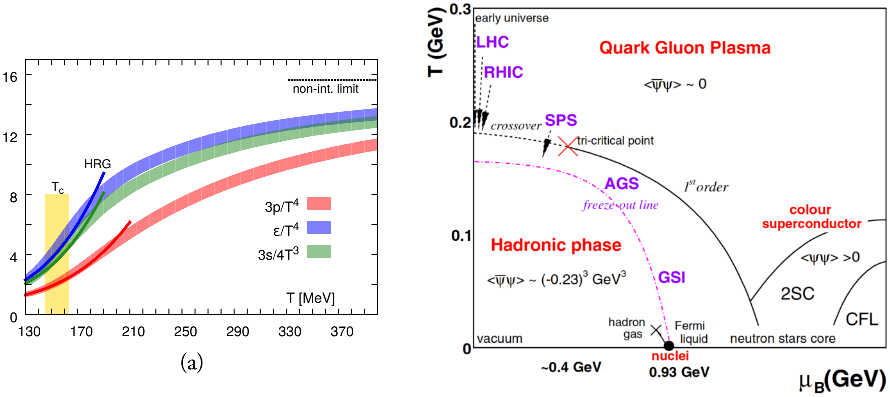

(a)

(b)

Figure 1.13: **(a)** Dependence of the pressure (red), energy density (blue), and entropy density (green) on temperature, determined with LQCD. [44] **(b)** Phase diagram of QCD matter. [45]

1.8.3 QCD phase diagram, chiral symmetry restoration

Phase transitions of QCD matter are investigated to explore the QCD phase diagram with respect to temperature T and baryon chemical potential μ_B, which corresponds to the net baryon density. Figure 1.13 visualizes the different areas of the QCD phase diagram probed by various experiments [45]. Measurements of Pb-Pb collisions at the LHC access high T and almost zero μ_B, as the nucleons of ultrarelativistic Pb nuclei escape the interaction volume before the plasma develops, and the high energy subsequently leads to a sizable baryon production balanced by anti-baryons due to conservation laws. Experiments studying collisions of slower and heavier nuclei reach higher μ_B regions.

Furthermore, looking back at the QCD Lagrangian in (1.5) and neglecting quark current masses ($m_{u,d} \to 0$), it can be seen that it is invariant when switching the up and the down quark, corresponding to a SU(2) isospin symmetry. This allows the fermion fields to be rewritten in terms of their left and right chiralities and the QCD Lagrangian then exhibits a larger *chiral symmetry*.

However, it is known that the vacuum expectation value of a $q\bar{q}$ state is much larger than the current masses $m_{u,d}$:

$$\langle 0|q\bar{q}|0\rangle = \langle 0|u\bar{u} + d\bar{d}|0\rangle \approx (250\,\mathrm{MeV})^3 \quad , \tag{1.27}$$

where the value is taken from average masses of light flavour mesons. This means that the QCD vacuum spontaneously breaks the chiral symmetry. [46]

It can be expected that in the plasma of deconfined quarks and gluons, chiral symmetry is *restored* [47, 48]. This is actively studied in AA collisions, for example in searches of the so-called chiral magnetic effect [49] or degeneracy of normally chiral partners [50], such as the ρ ($J^P = 1^-$) and a_1 ($J^P = 1^+$) states.

Chapter 2

QCD phenomena in high-energy hadronic collisions

The aim of this chapter is to give an introduction to the physics of heavy-ion collisions and the various phenomena related to the quark-gluon plasma QGP. Furthermore, a detailed summary of the findings of QGP phenomena in small systems, i.e., pp and pA collisions, is given. Lastly, some Monte Carlo event generators based on phenomenological modelling of hadronic collisions relevant to this dissertation are summarised.

2.1 Collisions of heavy nuclei

2.1.1 Collision geometry, centrality, multiplicity

Collisions of heavy nuclei, composed of many nucleons with fluctuating positions, may occur under various initial state configurations. Some quantities used to describe them are the impact parameter b, defined as the distance between the two nuclei centers, number of participating (scattered) nucleons $N_{\rm part}$, and the number of binary nucleonic collisions $N_{\rm coll}$.

Determining these quantities is important because:

1. Soft processes, such as light flavor particle production, are expected to scale with the interaction volume, which $\propto N_{\rm part}$.

2. Hard processes, such as jet and heavy flavor production, are expected to scale with the number of large momentum transfer interactions given by N_{coll}.
3. b, disregarding the fluctuations of nucleonic positions, defines the shape and anisotropy of the overlap region, which are important initial state conditions.

Since these quantities cannot be directly measured, they need to be modelled. The charged particle *multiplicity* is commonly used for this purpose, as $\langle N_{\text{ch}} \rangle$ is expected to increase monotonically with N_{part}, N_{coll}, and decreasing b. Multiplicity N_{ch} can be measured experimentally, e.g., with tracking detectors. The concept of *centrality* is also used, which is defined as quantiles of the total nuclear cross-section. For example, a centrality of $0 - 5\%$ refers to low b values and the top $\sim 5\%$ quantile of N_{ch} values (central events), while $95 - 100\%$ centrality refers to high b values and the bottom $\sim 5\%$ quantile of N_{ch} values (peripheral events). Centrality can also be inferred from other *event activity* classifiers, such as amplitudes of scintillators at forward rapidity, transverse energy measured in calorimeters, or energy from beam remnants in zero-degree-calorimeters.

In AA collisions, these relationships are well-defined, and thus the models perform well. The most popular model is the MC Glauber model [51]. Other models include MC-KLN [52] and IP Glasma [53].

2.1.2 MC Glauber model

The MC Glauber model [51] is based on a very simple albeit powerful approach. The two nuclei are simulated in three dimensions in a way that satisfies their respective nuclear density profiles, usually modelled by sampling the positions of nucleons from the Woods-Saxon distribution:

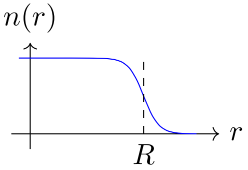

$$n(r) = \frac{1}{1 + \exp((r - R)/a)} \quad , \tag{2.1}$$

where R is the nuclear radius and a the nuclear skin thickness.

The nucleonic densities can be represented by uniform disks, or more accurately by Fermi-distributions or Gaussian profiles to account for fluctuations of their densities. The nucleon parameters are left free and tuned to the data.

Subsequently, a random impact parameter is chosen or sampled. The collision is then treated as a sequence of independent binary nucleon-nucleon collisions, where

1. nucleons remain travelling in straight lines,
2. the inelastic nucleon-nucleon cross section $\sigma_{\rm NN}$ does not depend on the number of interactions,
3. two nucleons are considered to interact if their transverse relative distance $d \leq \sqrt{\sigma_{\rm NN}/\pi}$.

Figure 2.1 illustrates an example of a Glauber Monte Carlo event for a Au+Au collision. By simulating numerous collisions, the average $N_{\rm part}$ and $N_{\rm coll}$ are determined[1], and their relations to centrality and event activity observables are evaluated by fitting to experimental data.

Recent studies have extended the MC Glauber model to include sub-nucleonic structures. Such efforts show that the production of charged hadrons at mid-rapidity scales linearly with the number of participating partons. Comparisons with LHC data at $\sqrt{s_{\rm NN}} = 5.02\,\text{TeV}$ suggest that the number of sub-nucleonic degrees of freedom ranges from 3 to 5 [54].

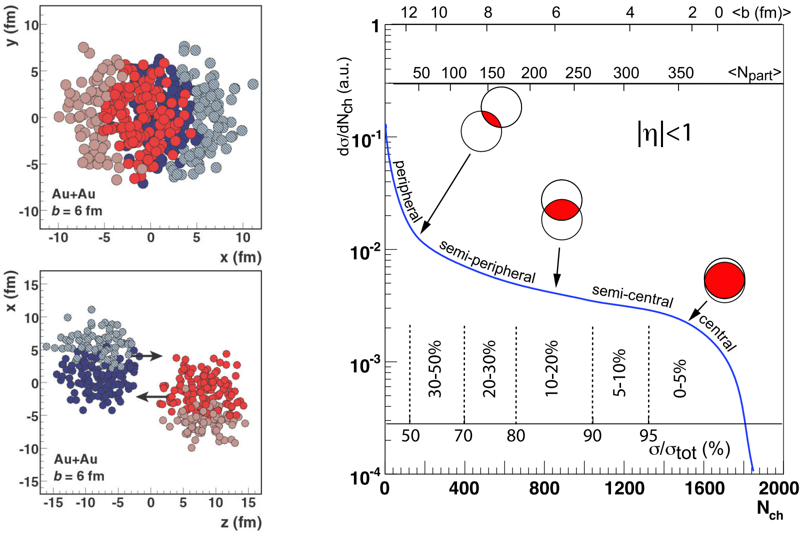

(a) (b)

Figure 2.1: **(a)** Glauber Monte Carlo event of a Au+Au collision at $\sqrt{s_{\rm NN}} = 200\,\text{GeV}$ shown in the transverse plane (top panel) and along the beam axis z (bottom panel). The darker circles represent participating nucleons and their area corresponds to $\sigma_{\rm NN}$. **(b)** Illustrative diagram of the dependence of final-state event multiplicity on the initial-state quantities, number of participants $N_{\rm part}$ and impact parameter b. [51]

---

[1] It also shows the scaling between the numbers of participants and binary collisions, which is approximately $N_{\rm coll} \approx 0.35 N_{\rm part}^{4/3}$.

2.2 Quark-gluon plasma

In agreement with lattice QCD predictions [55], the QGP has been measured in ultra-relativistic collisions of heavy nuclei at RHIC [56, 57], LHC [58], and even SPS [59]. Although it cannot be observed directly, a wealth of evidence from three decades of research combining various observables reveals the effects of the produced QGP medium. Whilst somewhat context-dependent, the following features make QGP the most extreme phenomenon observed in terms of its:

- *Temperature*: QGP temperatures reach values on the order of hundreds of MeV, which corresponds to approximately 2×10^{12} K.[2] [60]
- *Viscosity*: the shear viscosity to entropy density ratio η/s approaches the minimum quantum limit of $1/4\pi$ (for water at room temperature, $\eta/s \approx 8$), making it an almost perfect liquid. [45]
- *Vorticity*: in semi-peripheral collisions, the rotating plasma reaches a vorticity of approximately 9×10^{21} s^{-1}. [61]
- *Magnetic field*: in non-central collisions, the magnetic fields in the system may peak at $\sim 10^{19}$ T. [62]

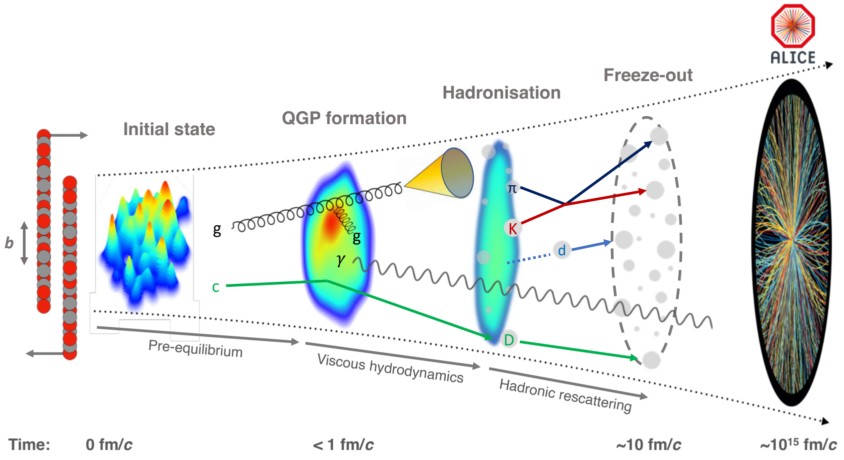

Figure 2.2: Evolution of heavy nuclei collisions at LHC energies, depicting the different stages. [63]

---

[2] Contrasting some of the lowest temperatures required for the super-conducting magnets of the LHC, $T \approx 1.9$ K.

Figure 2.2 illustrates the common paradigm for the different stages of a collision between heavy nuclei:

1. The Lorentz-contracted heavy nuclei approach each other at ultra-relativistic speeds ($v \approx c$).
2. *Pre-hydrodynamisation stage* ($\tau \equiv \sqrt{t^2 - z^2} \leq 1$ fm/c): "hard" particles are produced in scatterings with the highest momentum transfer Q^2. Produced matter expands rapidly in the longitudinal direction and starts expanding in the radial direction.
3. *Hydrodynamisation* ($1 \leq \tau \leq 10$ fm/c): abundantly produced partons create a deconfined medium, which can be described by hydrodynamic equations.
4. *Chemical freeze-out* ($\tau \sim 10$ fm/c): the system cools down and hadronises. The produced hadrons then stop interacting inelastically and the system's chemical content is stabilised.
5. *Kinetic freeze-out* ($\tau \lesssim 20$ fm/c): hadrons no longer interact elastically and their kinematics stabilize.
6. Long-lived particles can be directly measured in the detector volume.

The following subsections outline some of the essential phenomena related to the production of QGP.

2.2.1 Quarkonium dissociation and sequential suppression

Heavy quarkonia are vector meson states consisting of $c\bar{c}$ or $b\bar{b}$. They include J/ψ, ψ(2S), Υ(1S), Υ(2S), Υ(3S), which can be relatively easily measured in LHC experiments via their di-lepton decay channels. They are created solely in the first phases of the collision and experience the entire evolution of the QGP medium:

$$t^{Q\overline{Q}}_{\text{creation}} < t^{\text{QGP}}_{\text{creation}} < t^{\text{QGP}}_{\text{lifetime}} \ll t^{Q\overline{Q}}_{\text{lifetime}} \quad . \tag{2.2}$$

Additionally, due to their large binding energies, their radii may remain smaller than the plasma screening radius $r_{\text{D}}(T)$, and thus, survive the dissociation. For instance, considering their in-vacuum radii determined from the $q\bar{q}$ potential, $r_{\Upsilon(1\text{S})} \sim 0.14$ fm, $r_{\Upsilon(2\text{S})} \sim 0.28$ fm, $r_{\Upsilon(3\text{S})} \sim 0.39$ fm, which contrast the $r_{\pi} \sim 0.7$ fm [64]. This implies that different temperatures result in the dissociation of different states, and measuring the production of different states can help infer the QGP temperature, as illustrated in Fig. 2.3 [65, 66].

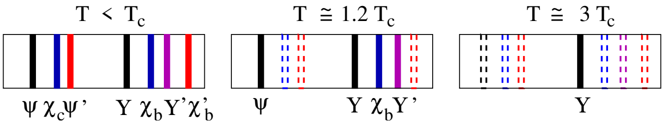

Figure 2.3: Spectral lines corresponding to various charmonium and bottomonium states for different medium temperatures , relative to the QGP critical temperature. [66]

The production of heavy quarkonia in AA collisions is compared to that in pp collisions (scaled by the average number of binary collisions) through the nuclear modification factor, R_{AA}. This quantity is widely used in various other measurements and is defined as:

$$R_{\mathrm{AA}} = \frac{\mathrm{d}N_{\mathrm{AA}}/\mathrm{d}p_{\mathrm{T}}}{\langle N_{\mathrm{coll}} \rangle \, \mathrm{d}N_{\mathrm{pp}}/\mathrm{d}p_{\mathrm{T}}} \quad . \tag{2.3}$$

R_{AA} can take on the following values:

1. $R_{\mathrm{AA}} = 1$: The result one would expect if the AA collision is a mere superposition of nucleon-nucleon collisions. There is no net effect on the production, corresponding to the absence of the QGP medium and other nuclear effects, or their mutual cancellation.

2. $R_{\mathrm{AA}} < 1$: The production is overall suppressed, for example, due to dissociation.

3. $R_{\mathrm{AA}} > 1$: The plasma and nuclear effects systematically enhance the measured production.

At LHC energies, the abundance of charm quarks in the QGP is high enough that charmonia can be formed after dissociation, which somewhat complicates the interpretation of charmonia suppression. However, the $\Upsilon(3\mathrm{S})$ bottomonium has R_{AA} consistent with zero at $\sqrt{s_{\mathrm{NN}}} = 5.02$ TeV, as shown in Fig. 2.4 [60]. This complete suppression is a clear signature of the QGP and can be used together with models to estimate the QGP temperature at these energies as $T \approx 630$ MeV [67].

2.2.2 Strangeness enhancement

In the production of hadrons in vacuum, strangeness is suppressed relative to light quarks not only due to the higher current mass of the strange quark ($m_s \approx 0.1$ GeV/c^2), but also due to the much higher constituent mass ($m_K \approx 0.5$ GeV/c^2). However, in

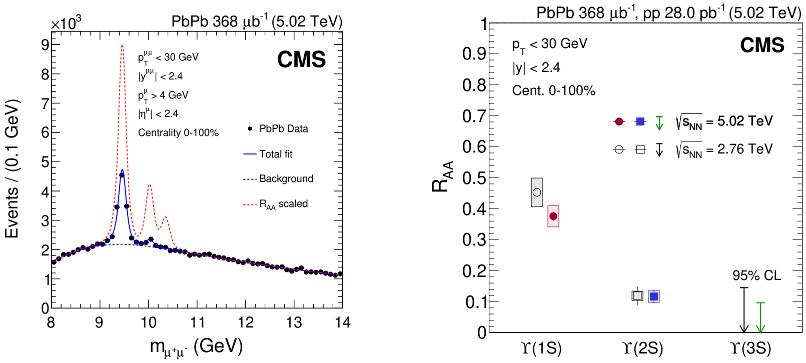

(a)

(b)

Figure 2.4: **(a)** Muon invariant mass distributions in Pb-Pb collisions at $\sqrt{s_{\mathrm{NN}}} = 5.02$ TeV, also showing a scaled result from pp collisions at same energies (red dashed line). **(b)** Nuclear modification factors of the three bottomonium states. [60]

the QGP, due to the high gluon densities and $T \sim m_s$, strangeness production may equilibrate with u and d quarks through gluon fusion:

$$gg \rightarrow s\bar{s} \quad .$$

This phenomenon was proposed as one of the first signatures of QGP observation in colliders [68, 69]. Indeed, an enhancement in the production of strange hadrons is observed in AA collisions, which is dependent on the event activity and increases with increasing strangeness content of the hadron [70]. Figure 2.5 displays these results.

Furthermore, the yields of hadrons measured in AA collisions can be accurately described by statistical models [71, 72] which, generally, assume that the dense system is in thermal and chemical equilibrium at the point of freezing out. In these models, strangeness is assumed to be conserved on average, which corresponds to a grand-canonical ensemble with a strange chemical potential μ_S.

In small systems, the conservation of strangeness must be taken into account for each interaction, locally. This necessitates the use of a canonical ensemble and introducing a parameter, V_0, to describe the volume of this locality requirement [73]. With this approach, strangeness enhancement can be reproduced by increasing V_0 and transitioning from the canonical ensemble in small systems to the grand-canonical ensemble in AA collisions, as depicted in Fig. 2.5.

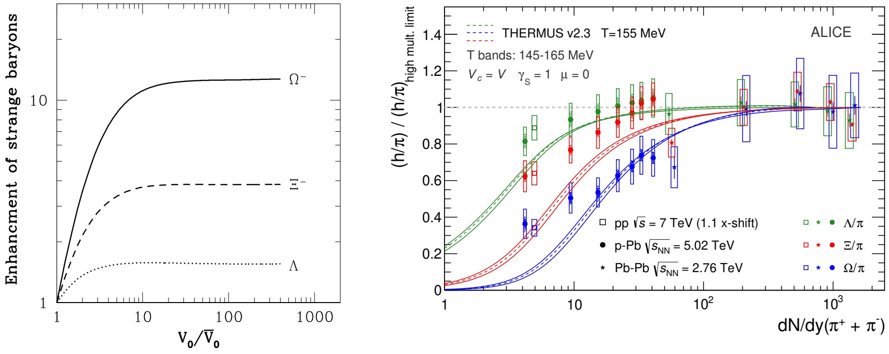

(a) (b)

Figure 2.5: **(a)** Dependence of strange baryon densities on the parameter V_0 characterising the volume where strangeness is locally conserved in models describing strangeness suppression in small systems as canonical suppression. The volume is normalised to a typical AA value of $\overline{V}_0 = 7.4$ fm^3. [73]. **(b)** Ratios of yields of strange baryons to pions in pp, p-Pb, and Pb-Pb collisions as a function of the pion multiplicity normalised to the high-multiplicity limit in $0 - 60\%$ most central Pb-Pb collisions. The results are compared with a statistical model combining the canonical and grand-canonical approach. [70, 72]

2.2.3 Collective flow

The strongly interacting plasma exhibits a collective expansion which can be described by hydrodynamic equations, since the mean free paths of the constituents are much smaller than the system size ($\lambda \ll L$). The non-uniform energy density in the initial state results in varying pressure gradients, which drive this expansion. Since the centre of the plasma has greater pressure than its outside regions, common expansion velocity field develops, which results in the so-called *radial flow*. Similarly, the medium also translates the directionally-dependent anisotropies in the initial state, which stem from the ellipsoid-shape geometry of the collision overlap region as well as nucleonic fluctuations in position, to the final-state. This is the so-called *anisotropic flow*.

Together with hadronic re-scattering, the flows are reflected in the kinematics of the final-state hadrons. When comparing p_T spectra in central AA collisions to those in peripheral or in pp collisions, a broadening as well as a momentum boost can be observed (see Fig. 2.6), caused by the radial expansion as well as the less important thermal motion [74, 75, 76]. The expansion effect depends on the mass of the hadrons, as the amount of additional p_T acquired is proportional to their mass and the collective expansion velocity field, $\Delta p \approx \gamma m \beta c$. A notable exception to this trend is the ϕ quarkonium; although comparable with the proton ($m_\phi \approx 1.02\,\text{GeV}/c^2 \sim m_p$), its hadronic scattering cross-section is much smaller [77].

The p_{T} spectra influenced by radial flow can be described by the Blast-Wave parametrisation [78]. In this approach, the radial expansion is accounted for as a common velocity field profile $\beta(r)$ affecting thermal spectra,

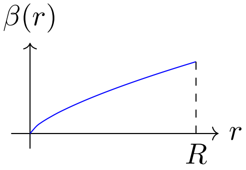

$$\beta(r) = \beta_s(\frac{r}{R})^n \quad , \tag{2.4}$$

where β_s, R, and n are the expansion velocity on the surface of the plasma, its radius, and an extra parameter usually in the range $0.7 - 1.0$ in central collisions [74], respectively. The effects of radial flow can also be reproduced in AA collisions with hydrodynamic models using an equation of state from LQCD and hadronic re-scattering [77], and in pA collisions with the EPOS3 model, which also incorporates hydrodynamic evolution in QGP droplets [79].

Ratios of baryons to mesons, such as p/π or $(\Lambda + \overline{\Lambda})/(2\mathrm{K}^0_\mathrm{S})$, as a function of event activity are often used to demonstrate the effect of radial flow, as shown in Fig. 2.6. In these ratios, the modification of p_{T} spectra results in the following effects on the high-event-activity ratios:

1. The peak in the ratio is shifted to higher p_{T} by up to 1.5 GeV/c,
2. there is an enhancement of baryons in the intermediate p_{T} ($1.5 < p_{\mathrm{T}} < 6$ GeV/c) region,
3. and a corresponding depletion of baryons at low p_{T}.

Figure 2.7 shows a typical shape of the initial state with its azimuthal anisotropy and the resulting pressure gradients. Anisotropic flow can be quantified by decomposing the azimuthal particle distribution into its Fourier expansion [80]:

$$\frac{dN}{d\varphi} \propto 1 + 2\sum_{n=1}^{\infty} v_n e^{in(\varphi - \Psi_n)} \, , \qquad v_n = \langle \cos[n(\phi - \Psi_n)] \rangle \, , \tag{2.5}$$

where Ψ_n is the symmetry plane of the n-th harmonic and v_n is the Fourier coefficient corresponding to that harmonic, also known as the flow coefficient. In this context, a finite initial state ellipticity ϵ_2 leads to a finite *elliptic flow* v_2, a triangularity ϵ_3 leads to a *triangular flow* v_3, and so forth [81, 82].

The flow coefficients can be experimentally extracted using various methods, including two-particle azimuthal correlations (as shown in Fig. 2.7), and are typically studied as a function of event multiplicity. It is important to note that these azimuthal

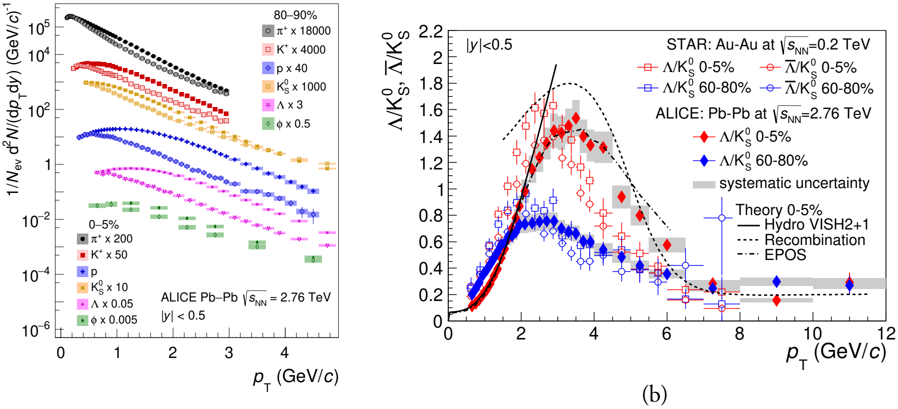

(a)

(b)

Figure 2.6: **(a)** Transverse momentum spectra of light-flavour hadrons in central $0-5\%$ and peripheral $80-90\%$ Pb-Pb collisions scaled by arbitrary factors to enhance the visibility. [63, 74, 75, 76] **(b)** Λ to K^0_S ratios of transverse momentum spectra in Pb-Pb collisions at the LHC and Au-Au collisions at RHIC for central $0-5\%$ events (red) and peripheral $60-80\%$ events (blue). [75]

correlations between particles due to anisotropic flow are long-range, i.e., present consistently across the entire pseudorapidity range $\Delta\eta$ (the so-called "ridge") [83], which makes them distinguishable from similarly appearing "non-flow" short-range correlations coming from jet fragmentation and resonance decays.

Moreover, measurements of v_2 in AA collisions for different particle species reveal a mass dependence in the low-p_T region, and a baryon/meson dependence in the intermediate p_T region, with baryons having approximately 1.5 times higher values [84]. This suggests that the flow of hadrons is built up from its deconfined constituents.

2.2.4 Jet quenching

In AA collisions, partons produced in hard scattering processes interact with the colour charges in the quark-gluon plasma, resulting in the loss of energy through collisions and gluon bremstsstrahlung. This phenomenon is known as jet quenching and modifies or even "quenches" the parton shower [86, 87]. In the factorisation theorem in Eq. (1.13), this corresponds to the medium-modification of the fragmentation functions. Studies of parton energy loss and jet quenching often use the transport coefficient $\hat{q}$, which describes the average p_T loss of a parton per a mean free path length in the plasma and corresponds to the medium opacity.

Jet quenching is one of the most important probes into the structure and dynamical properties of the QGP, since the hard partons experience its entire evolution, similarly

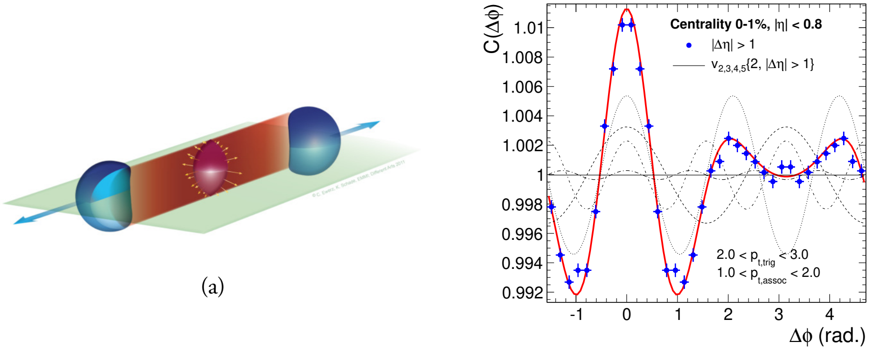

(a)

(b)

Figure 2.7: **(a)** Illustration of a collision of ultra-relativistic heavy nuclei and the overlapping region with pressure gradients (yellow). [85] **(b)** Correlation function of the relative azimuthal angle between a trigger particle and an associated particle, separated by a pseudorapidity gap, measured in central Pb-Pb collisions. The contributions from the elliptical, triangular, quadrupolar, and pentapolar harmonics are shown as different dashed lines. [82]

to the case of heavy quarkonia discussed in Sec. 2.2.1. It can also be compared with a large body of sound theoretical calculations [88] and MC simulations [89] based on QCD. Experimentally, jet quenching can manifest as a suppression of the jet yield or even its complete disappearence, due to the energy loss of partons in the medium and their re-scattering. [63]

Figure 2.8 displays such an AA event with a large jet imbalance and juxtaposes it with a pp event, where the leading and the recoil jet need to be balanced in azimuth due to conservation laws. Further effects and fields of study of jet quenching include the modification of jet substructures and shapes.

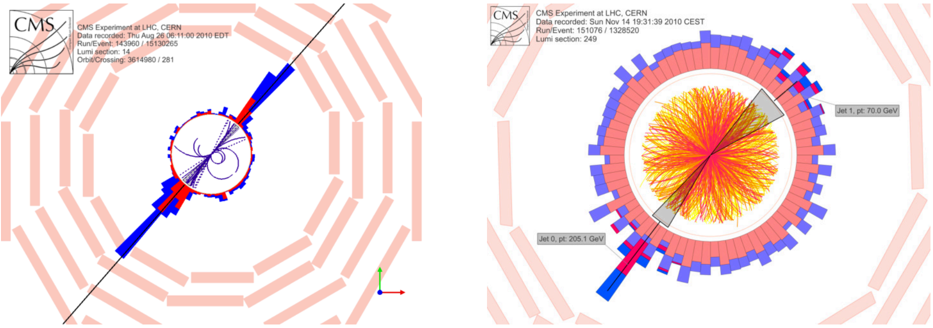

(a)

(b)

Figure 2.8: Event displays from CMS in azimuthal plane showing a collision of **(a)** pp and **(b)** Pb-Pb with a dijet. The red and blue columns correspond to energy deposits in the detector calorimeters. [58, 90]

2.2.5 Cold nuclear matter effects

It should be noted that apart from the QGP, other effects come into play due to the fact that the collision involves two nuclei instead of two protons. These effects are important caveats to bear in mind and include:

1. Nuclear (anti-)shadowing: Reflects the modification in production due to differences in nPDFs and PDFs. [91]
2. Cronin effect: Describes the initial parton energy loss due to scatterings in the nuclear medium and broadens measured p_{T} spectra. [92]
3. Nuclear absorption: Describes the dissociation of particles due to their interactions with the passing-by nuclear remnants [37]. It is generally negligible at LHC energies.
4. Co-mover absorption: This is the effect of inelastic interactions with the hadron gas. [93]

These effects can be isolated and quantified in pA or very peripheral AA collisions.

2.3 QGP phenomena in small systems

Measurements within the last decade have shown that certain QGP phenomena can also be observed in high-multiplicity events of pp collisions at LHC energies, which challenges the traditional assumption that QGP is only produced in AA collisions. This has sparked debates about the existence of QGP in pp collisions and, to a lesser degree, about the absence of QGP in AA collisions, despite the extensive experimental evidence.

Furthermore, the observed behavior of these phenomena indicates that the role of event multiplicity N_{ch} may be more significant than the collision system size. This has led to ongoing efforts to establish a consistent and seamless link between the paradigms of pp and AA collisions.

Strangeness and charm enhancement

ALICE measurements on Λ/π, Ξ/π, and Ω/π ratios demonstrate that the production rates of particles containing strange quarks increase faster with multiplicity than those containing only u and d quarks [94]. This also depends on the strangeness content – the effect is the strongest for Ω and vanishes for protons. Furthermore, the evolution to larger systems seems to be continuous with respect to N_{ch}. The measurements can be seen in Fig. 2.9 [63].

To contrast the strangeness measurements with charm, the $J/\psi\ /\pi$ ratio also shows a clear increase in yield with increasing N_{ch} in pp collisions, as is shown in Fig. 2.9 [95, 96]. However, this comes with an important caveat: high-multiplicity events are biased to have enhanced hard processes, as discussed further in Chapter 7. Moreover, the evolution of this phenomenon is also not continuous with N_{ch} when going from pp collisions at $\sqrt{s} = 13\,\mathrm{TeV}$ to $\sqrt{s_{\mathrm{NN}}} = 5.02\,\mathrm{TeV}$, which can also be explained by the fact that charm quarks are produced solely in hard scattering processes, the rates of which depend on the collision system and center-of-mass energy.

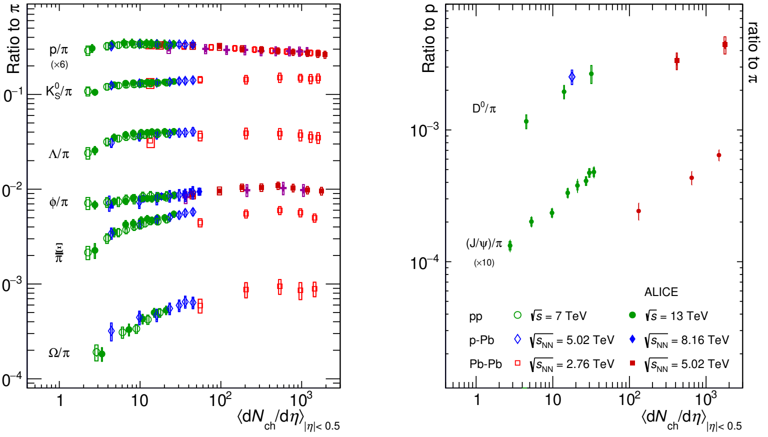

(a)

(b)

Figure 2.9: Ratios of integrated yields of **(a)** various light-flavour hadrons [94] and **(b)** charm mesons [95, 96] to pions as a function of multiplicity in pp, p-Pb, and Pb-Pb collisions. [63]

Anisotropic flow

Azimuthal correlations and anisotropic flow measurements in small collision systems exhibit features similar to those observed in AA collisions, hinting at the presence of collective expansion [97]. However, in small systems, these measurements are particularly challenging due to their large sensitivity to non-flow effects, such as jet fragmentation or resonance decays, which can mimic the features of collective flow.

While models using hydrodynamic-like descriptions seem to be able to describe v_2 results (despite the fact that their assumption $\lambda \ll L$ is not valid) [98], especially at high multiplicities, the interpretation of the results in small systems is still under investigation. The values of elliptic flow v_2 seem to be comparable to those in low-multiplicity Pb-Pb collisions, although the evolution of v_2 across different system sizes does not appear to be smooth. The measurements from CMS displaying a clear ridge in high-multiplicity events [97] and the v_2 results from ALICE [99] can be seen in Fig. 2.10.

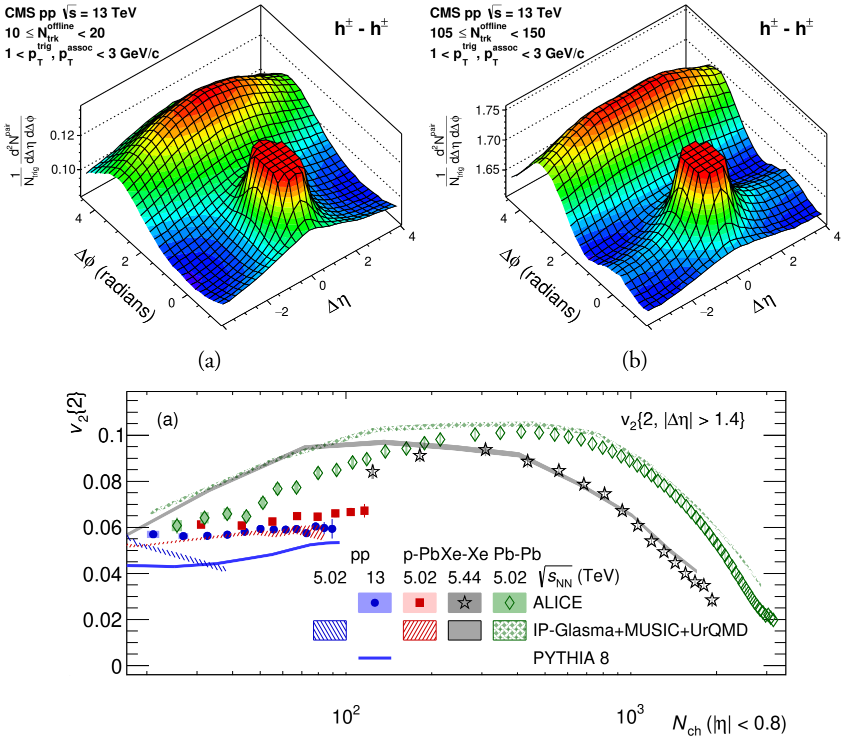

(a) (b)

(c)

Figure 2.10: **(a, b)** Two-dimensional two-particle correlation functions of charged hadrons in low (left) and high (right) multiplicity events of pp collisions at $\sqrt{s} = 13\,\mathrm{TeV}$. [97] **(c)** Elliptic flow measured using two-particle cumulants with a pseudorapidity separation in pp, p-Pb, Xe-Xe, and Pb-Pb collisions as a function of multiplicity. [99]

Radial flow

Measurements of the ratio of Λ to K^0_S p_T spectra ratio were also studied in pp collisions with differing N_ch, see Fig. 2.11 [100]. The boost of a collectively expanding system, as expected in the context of radial flow, should have a greater impact on heavier hadrons, leading to an enhancement of the baryon-to-meson ratio at intermediate p_T. This enhancement is observed in the $\Lambda/\mathrm{K}^0_\mathrm{S}$ ratio, its magnitude increases with increasing N_{ch} and its peak position shifts towards higher values of p_{T}, consistent with the hydrodynamic picture. The increase at intermediate momenta due to the momentum boost leads to a corresponding depletion at low p_{T}. High-p_{T} (as well as integrated) $\Lambda/\mathrm{K}^0_{\mathrm{S}}$ ratios exhibit essentially no (or minor) multiplicity dependence. These observations also apply to proton-to-pion ratios.

Recent studies have also investigated the charmed baryon-to-meson ratio Λ_c/D^0, with similar findings, although measurements with smaller uncertainties are still required. Fig. 2.11 presents the corresponding results.

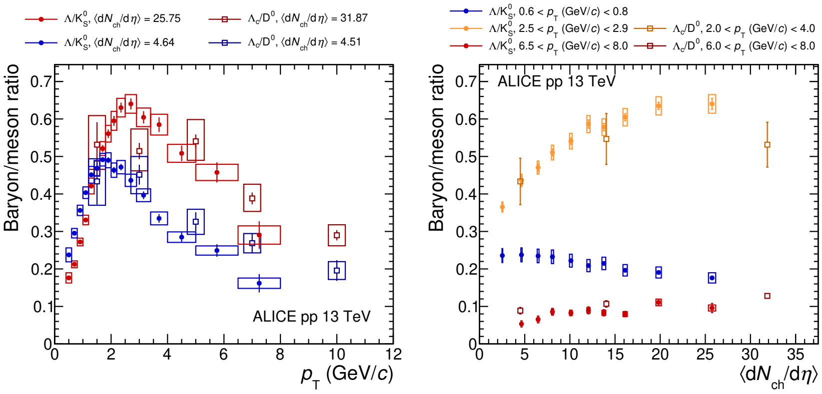

Figure 2.11: Baryon-to-meson ratios shown as the p_{T} differentials (left) and integrated yields in various p_{T} ranges as a function of multiplicity (right) for the $\Lambda/\mathrm{K}^0_{\mathrm{S}}$ and Λ_c/D^0 in pp collisions at $\sqrt{s} = 13\,\mathrm{TeV}$. [63, 96, 100]

Sequential suppression of Υ states

While defining R_{AA} to compare high-multiplicity and low-multiplicity events is unclear, and measuring yields as a function of N_{ch} is complicated by its biases related to the hardness of primary scatterings, it is worthwhile to investigate the ratio of excited-to-ground states of quarkonia as a function of N_{ch}.

Interestingly, these results [101] exhibit a decrease with increasing N_{ch}, resembling the pattern of sequential suppression due to QGP deconfinement. Even more remarkable, this dependence disappears in low-sphericity, jet-dominated, events (event shape observables such as sphericity are discussed in more detail in Chapter 6). These findings, reported in Fig. 2.12, suggest that the dependence on N_{ch} is solely influenced by the UE, rather than jets. As event multiplicity grows larger, excited Υ states become relatively less likely to be measured compared to the ground state.

These results indicate the need for a better understanding of Υ hadronisation and the role UE may play in it. They also raise the question of whether the ground state is enhanced rather than the excited states being suppressed. Additionally, the effects of the mass differences must also be considered. However, the fact that low-sphericity, jet-dominated events have the same ratios as high-sphericity, UE-dominated events at low N_{ch} argues against these ideas.

A hypothetically important caveat to note is that hadronic decays (which are dominant) of the heavy Υ states may result in tens of produced particles [102]. Therefore, not observing the excited states in the di-lepton channel (used in the measurements) might correlate with a substantial albeit trivial increase in the accompanying N_{ch}. To the author's knowledge, there are currently no available phenomenological descriptions of the observed behavior, which further limits potentially groundbreaking interpretations.

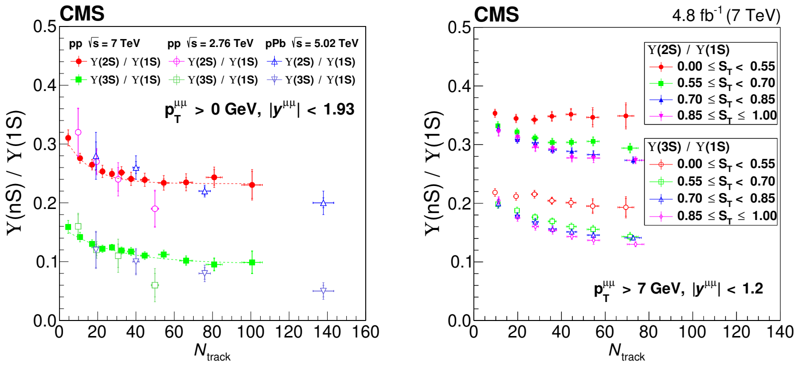

(a) (b)

Figure 2.12: The Υ(2S)/Υ(1S) and Υ(3S)/Υ(1S) ratios of measured yields in pp collisions as a function of **(a)** multiplicity, compared with p-Pb results, and **(b)** multiplicity and transverse sphericity, with the di-muon transverse momentum $p_{\mathrm{T}}^{\mu\mu} > 7$ GeV/c. [101]

Other QGP signatures

If a QGP is formed in small systems with sufficient volumes, the effect of jet quenching should be observed. One can also expect to observe it, due to the fact that in small systems, high-p_{T} hadrons have been measured to have finite flow v_2 [103], which could indicate that hard partons interact with an expanding medium. Whilst theoretical approaches do not provide unambiguous answers on whether this phenomenon can be observed [104] or not [105], experimental results on jet quenching in both pp and p-Pb collisions are consistent with no observable effect, within uncertainties [106]. These results are mostly based on measuring jet yields as a function of event activity, although such measurements are challenging due to fluctuations and interplays between jet characteristics and event activity.

2.3.1 Role of multiplicity

The observations made above highlight the significance of studying the role of multiplicity N_{ch}. In contrast to AA collisions, high-multiplicity events in pp collisions do not arise from a mere increase in the amount of colliding matter, as the values of N_{part} and N_{coll} are fixed:

$$N_{\text{part}} = 2\,, \qquad N_{\text{coll}} = 1\,. \tag{2.6}$$

Additionally, due to the relatively constant initial system volume, high-N_{ch} pp events may exhibit energy densities that exceed the threshold for QGP formation, given that the highest N_{ch} values are similar to those observed in peripheral AA collisions, where QGP formation is observed.

Clearly, the picture is more complex and despite its simplicity as an event activity classifier, N_{ch} poses challenges when it comes to relating data to theory since it cannot be directly linked to the initial state, and multiplicities in different events may originate from entirely different processes.

To address these issues and gain a better understanding of the evolution between low and high multiplicities and the potential for QGP formation, this dissertation focuses on transverse spherocity $S_{\text{O}}^{p_{\text{T}}=1.0}$ and underlying event activity R_{T} measurements. The goal of these studies is to provide a deeper insight into the relevant degrees of freedom involved.

2.4 Phenomenological models

The next parts of this thesis give an overview to phenomenological models and event generators pertinent to the measurements in Chapters 6 and 7. Other generators, such as Herwig 7 [107] or Sherpa [108], are not discussed here.

2.4.1 Pythia

Pythia is a Monte Carlo event generator used to simulate full events of high-energy particle collisions, based mostly on approximately perturbative QCD, with some important non-perturbative aspects. With more than four decades of development, only a brief overview is given in this thesis, whilst detailed descriptions can be found in

Ref. [29, 109]. Pythia has a modular structure to simulate different aspects of the collision process and includes the simulation of the initial kinematics, hard scattering, multiple parton interactions, parton showering, and hadronization, which were all discussed in Chapter 1. The various components of the event simulation, such as the matrix element for the primary scattering, or even the parton evolution, can also be replaced with external alternatives.

Its current and in ALICE most widely used version is Pythia 8, specifically its Monash tune [110], incorporating colour reconnections. Pythia has also included the implementation of Angantyr [111], a new model for the simulation of collisions of nuclei.

A pp collision event, as simulated by Pythia, can be seen in the illustration in Fig. 2.13 and crudely structured as:

1. Relevant parton kinematics are determined based on the PDFs of the beam particles and nature of the event is decided (e.g. Z^0 production). Produced resonances decay.
2. All subsequent partonic activity is simulated. This includes the initial- and final-state parton radiation, MPIs, and handling of the beam particle remnants. Eventually, after the full parton shower evolutions, a full partonic structure and string configuration is given.
3. Hadronisation occurs by the Lund string model fragmentation. This part is completely non-perturbative and fully phenomenological. Unstable particles decay and a full final-state particle collection is obtained. [112]

2.4.2 String interactions and Ropes

While some effects typically associated with QGP formation, such as radial flow, can be somewhat mimicked in Pythia by colour reconnection [31, 113], as touched upon in Sec. 1.6.1, it is not sufficient to describe the strangeness enhancement patterns observed in small systems.

Ideas that overlapping QCD strings in high-density environments interact and form higher-tension ropes date back to modelling AA collisions in 1984 [114] and have been explored further [115], specifically in the framework of the DIPSY model [116]. This “rope hadronisation” approach is also incorporated similarly in Pythia 8 and can be included in its simulations, which in the context of this dissertation will be referred to as the Pythia 8 Ropes tune.

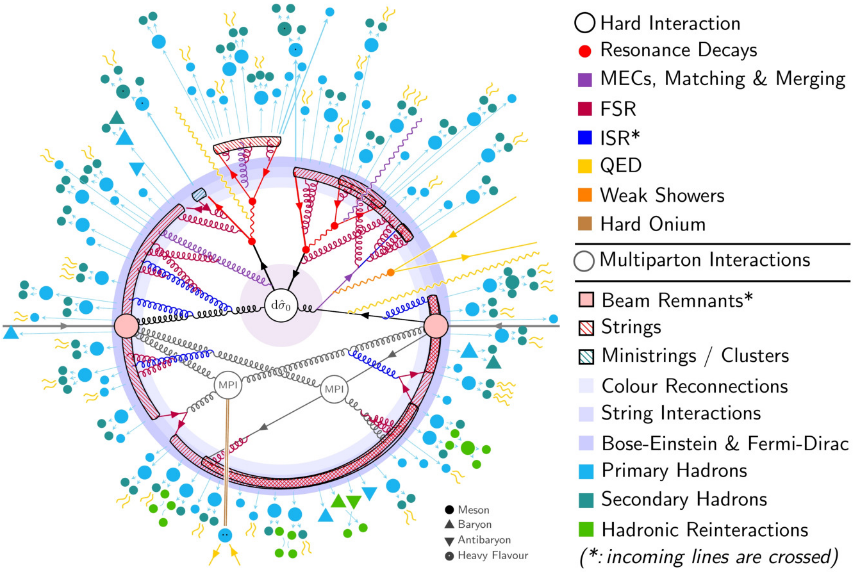

Figure 2.13: Diagram depicting a full simulation of pp collision event with its various components. For full description, see Ref. [29].

In Pythia, strings are considered overlapping on purely geometrical considerations and utilise a parameter α to quantify the size of strings relatively to the proton radius. Combining two strings follows an algebra based on the SU(3) group, described below, following a more detailed discussion in Ref. [116].

A $q\bar{q}$ string can be viewed as a SU(3) triplet, denoted $\mathbf{3}$. Stacking another string suggests adding another triplet and forming a multiplet with quantum numbers p, corresponding to the number of coherent triplets $\mathbf{3}$ (e.g. all red), and q, corresponding to the number of coherent anti-triplets $\bar{\mathbf{3}}$ (e.g. all anti-blue). Using a $\{p, q\}$ notation, the algebra for multiplets is as follows:

$$\{1,0\} \otimes \{1,0\} = \{2,0\} \oplus \{0,1\} \quad , \tag{2.7}$$

$$\{1,0\} \otimes \{0,1\} = \{1,1\} \oplus \{0,0\} \quad . \tag{2.8}$$

The first equation, physically, corresponds to merging of two colour strings with colour flows going in the same direction (same $q\bar{q}$ orientation), merging into a rope. When the colours are the same (e.g., both red), the result is a sextet rope $\mathbf{6}$, $\{2,0\}$. In other cases (e.g., red and blue), the result is an anti-triplet rope $\bar{\mathbf{3}}$, $\{0,1\}$ (corresponding to anti-green—green string). This algebra is illustrated in Fig. 2.14.

The second equation describes stacking a triplet $\mathbf{3}$ with an anti-triplet $\bar{\mathbf{3}}$ (opposite colour flows and $q\bar{q}$ orientation). This results either in a gluon octet $\mathbf{8}$, $\{1,1\}$, or a singlet **1**, $\{0,0\}$, with destructive interference and no colour flow.

The tension of the produced rope $\tilde{\kappa}$ is proportional to the quadratic Casimir operator C_2. When normalising to the tension of a single string κ, e.g., a $\{1,0\}$ triplet, the relative increase is given by

$$\frac{\tilde{\kappa}}{\kappa} = \frac{C_2(\{p,q\})}{C_2(\{1,0\})} = \frac{p^2+q^2+pq+3p+3q}{4} \quad , \tag{2.9}$$

so in the example of adding two red triplets, the resulting $\{2,0\}$ rope tension is $\tilde{\kappa} = 5/2$.

During hadronisation, the rope is assumed to break not entirely at once, but rather one string at a time. For the purpose of considering the probability of creating new quarks in (1.15), the effective tension from the $\{p,q\} \to \{p-1,q\}$ transition is given by (2.9) and corresponds to

$$\tilde{\kappa}_{\text{eff}} = \frac{2p+q+2}{4}\kappa \quad . \tag{2.10}$$

This means that in the example of the $\{2,0\}$ rope breaking, the first quark creation comes with relative effective tension $\tilde{\kappa}_{\text{eff}} = 3\kappa/2$, and the second one with the normal value of $\tilde{\kappa}_{\text{eff}} = \kappa$.

The strangeness production suppression factor in (1.16) then becomes modified as

$$\tilde{\rho} = \rho^{\frac{\kappa}{\tilde{\kappa}_{\text{eff}}}} \quad , \tag{2.11}$$

which makes it evident that overlapping many strings ($\tilde{\kappa}_{\text{eff}} \to \infty$) results in $\tilde{\rho} \to 1$ and strange quarks are produced at the same rate as up and down.

Furthermore, ideas for further interactions between strings, such as "string shoving", wherein overlapping strings may repel each other due to transverse pressure from their excess energy, have also been developed. Such mechanisms produce effects similar to a hydrodynamically expanding medium, e.g. long-range anisotropic flow. [117]

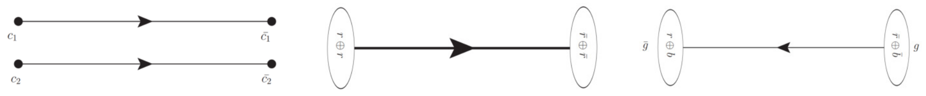

(a) (b) (c)

Figure 2.14: **(a)** Illustration of stacking two colour flow strings, triplets with colours c_1 and c_2. **(b)** Rope sextet resulting from adding two coherent triplets, $c_1 = c_2$, $\{2,0\}$. **(c)** Resulting rope anti-triplet coming from adding two incoherent triplets, $c_1 \neq c2$, $\{0,1\}$. Illustrations are by C. Bierlich.

2.4.3 EPOS LHC

EPOS is an event generator built on the Gribov-Regge theory [118], wherein several partons undergo multiple scatterings, each consisting of the hard scattering component as well as initial and final state linear parton emission. Together, they form a so-called parton ladder and correspond to a "cut" pomeron exchange [119]. The parton ladder represents a (mostly) longitudinally flowing colour field, a "flux tube", which may hadronise via pair production.

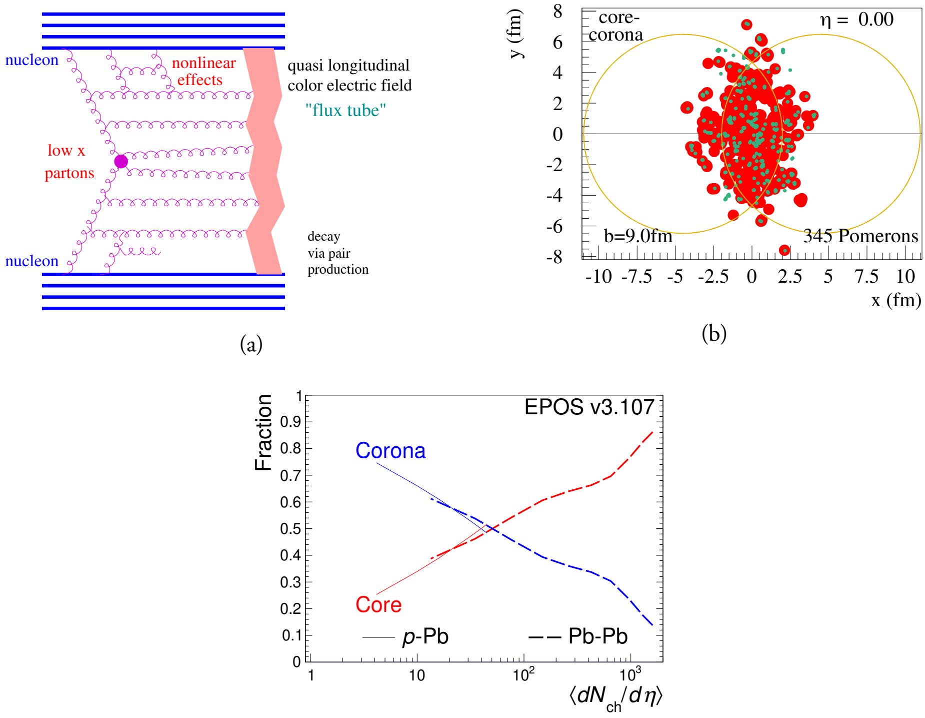

(a)

(b)

(c)

Figure 2.15: **(a)** Illustration of the partonic structure in the form of a parton ladder. [120] **(b)** Visualisation of the core (red) and corona (green) components in a peripheral $20 - 40\%$ collision of Pb-Pb with 345 initial multiple scatterings, modelled by EPOS3 [121] **(c)** Fractions of particle production associated with the core (red) and corona (blue) regions in p-Pb and Pb-Pb collisions, modelled by EPOS3. [122]

To model the full collision process, EPOS combines a two-component core-corona approach. When the density of flux tubes in a given volume exceeds a parameter ρ_0, the core is formed. Conversely, flux tubes escaping the volume (usually with higher p_T) make up the corona. The core is assumed to evolve hydrodynamically, corresponding to a QGP droplet, and then hadronises collectively, where smaller core segments form hadrons following a statistical ensemble. Since the relative amount of core- and corona-related particle production can vary continuously, EPOS models can be used to describe pp, pA, and AA collisions using a single paradigm. [120]

EPOS models have been successful particularly at modelling soft-QCD physics and, apart from collider physics, are also widely used in studies of cosmic rays [123]. Throughout this dissertation, an adaptation of EPOS called EPOS LHC [120] is mostly used and shown, which only parametrises the flow dynamics of the core instead of implementing a full hydrodynamic simulation. Diagrams illustrating the partonic structure and core-corona mixing can be seen in Fig. 2.15.

Part II

Experimental setup and methodology

Chapter 3

ALICE's adventures at the LHC

The experimental measurements conducted as part of this dissertation and described in Chapters 6 and 7 have been carried out using data from proton-proton collisions at the Large Hadron Collider (LHC) at CERN, collected with the ALICE detector. The aim of this chapter is to introduce these facilities.

3.1 CERN and the LHC

Conseil européen pour la recherche nucléaire (CERN) is a scientific institution dedicated to the study of particle physics, nuclear physics, and related fields. It was established in 1954 as a European collaborative endeavour and currently has 23 member states. The CERN laboratories employ almost 3000 on-site staff and host approx. 13000 users from universities and research institutions across the world. The biggest achievements of CERN include discoveries of the $W^{\pm}$, Z^{0}, [124] and Higgs bosons [4, 5], the first creation of anti-atoms, advancements to proton therapy and medical imaging technologies such as PET, and finally, being a birthplace to the World Wide Web.

The Large Hadron Collider (LHC) is the main particle accelerator at CERN. This synchrotron with circumference of almost 27 km can accelerate protons to energies up to 7 TeV, making it the world's most powerful particle accelerator. Apart from collisions of protons measured at $\sqrt{s} = 13\,\mathrm{TeV}$, it also studies collisions of nuclei, such as lead (Pb-Pb) at $\sqrt{s_{\mathrm{NN}}} = 5.02\,\mathrm{TeV}$, or proton-lead p-Pb at $\sqrt{s_{\mathrm{NN}}} = 8.16\,\mathrm{TeV}$. Particles in the synchrotron are accelerated by electric fields within RF cavities and kept on their semi-circular trajectory using magnetic dipoles. Magnets with higher number of poles are used for beam focusing and adjustment. The particles circulate in larger bunches (of $\sim 10^{11}$ protons or $\sim 7 \times 10^{7}$ Pb nuclei) in two separate rings, which intersect at the sites of four large experiments, detecting their collisions. Apart from ALICE, discussed in the next sections, these are:

- **ATLAS** (*A Toroidal LHC ApparatuS*) [125]: the LHC's largest experiment and a general purpose detector, with its foci including Higgs physics, scrutiny of the SM, and BSM searches.
- **CMS** (*Compact Muon Solenoid*) [126]: also a general purpose detector, with similar physics goals, but with a different technical design than ATLAS. It has also been a prominent contributor to QGP physics, particularly the study of small systems.
- **LHCb** (*Large Hadron Collider beauty*) [127]: a detector focused mostly on precise measurements of b physics and CP violation.

Table 3.1: Selection of parameters of the Large Hadron Colliders. [128]

Parameter	Value
Circumference	26.7 km
Energy at injection	450 GeV
Magnetic field at 7 TeV	~ 8.3 T
Number of magnets	~ 9300
Revolution frequency	~ 11 kHz
Number of bunches in a beam	2808
Bunch spacing	25 ns
Design luminosity	$\sim 10^{34}\,\mathrm{cm}^{-2}\mathrm{s}^{-1}$
Max. bunch crossing (BC) rate	~ 40 MHz
Number of inel. interactions per BC	$10 - 20$
Beam lifetime	~ 10 h

Some of the LHC parameters are summarised in Tab. 3.1 and an aerial photo of the LHC with locations of the Interaction Points (IPs) can be seen in Fig. 3.1.

3.2 The ALICE experiment

ALICE (A Large Ion Collider Experiment) [131, 132] is the detector at the LHC dedicated to studying collisions of heavy nuclei and the properties of QCD matter, such as quark-gluon plasma. Its biggest strengths are precise tracking and momentum determination all the way down to $p_{\mathrm{T}} > 0.15\,\mathrm{GeV}/c$ as well as superior particle identification (PID). Its sub-detectors are subjected to a magnetic field of 0.5 T to

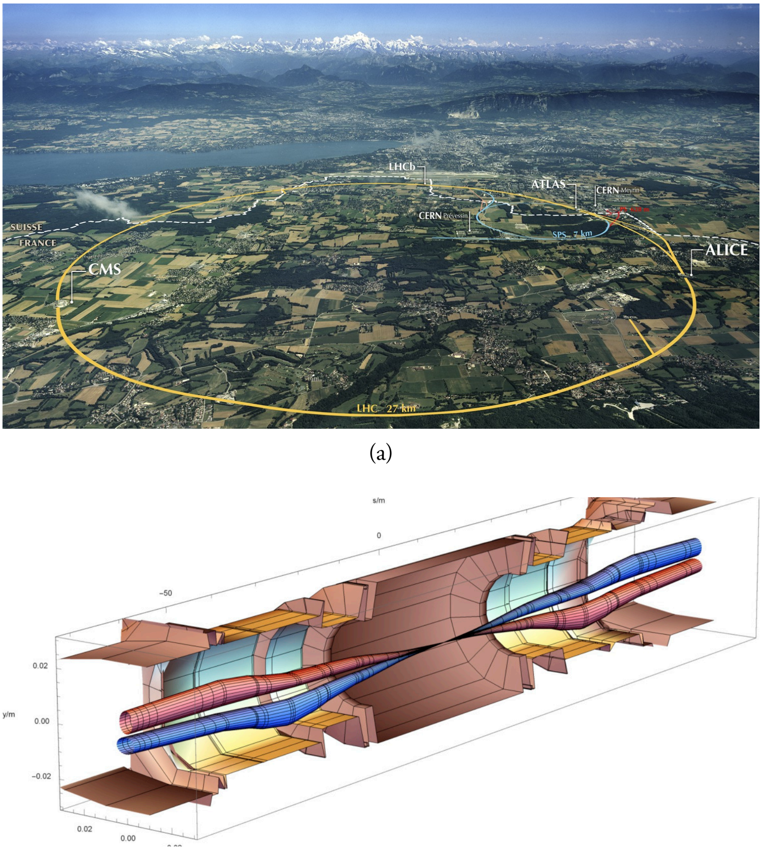

(a)

(b)

Figure 3.1: **(a)** Aerial photo of the LHC area, also depicting the location of the LHC tunnel (approx. 100 m underground), spanning over Switzerland and France. Geneva, Lac Léman, and the Mont Blanc can be seen in the background. [129] **(b)** Visualisation of the beam crossing at the ALICE experiment. Bunches of Beam 1 move from left to right in the blue beam envelope and bunches of Beam 2 move from right to left in the red beam envelope. The envelopes indicate the beam orbits and transverse size. [130]

allow momentum measurements from the track curvatures (in natural units, $p \approx 0.3Br$, $p \in [\,\mathrm{GeV}/c]$, $B \in [\mathrm{T}]$, $r \in [\mathrm{m}]$, for single-charged particles).

The ALICE detector, shown in Fig. 3.2, consists of several sub-systems, each fulfilling their function. Some of them which pertain to the measurements carried out within this dissertation are listed in Tab. 3.2. The following descriptions are based on their status when the data was collected, which corresponds to Run 2 (2015-2018).

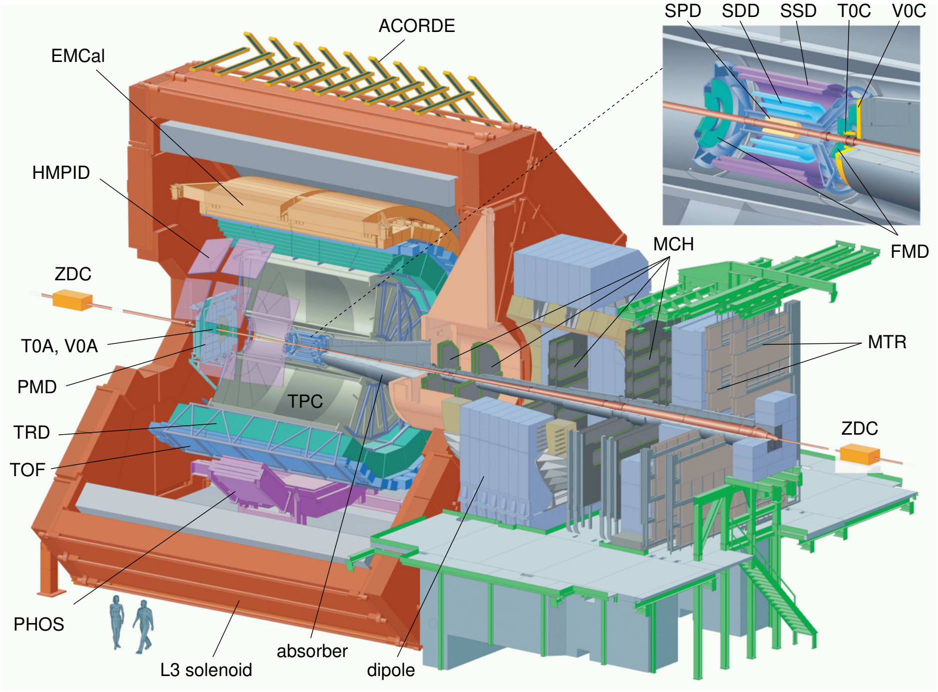

Figure 3.2: The ALICE experiment at the LHC, showing its sub-systems. The central barrel is subjected to a magnetic field from the solenoid (red). The ZDC detectors are approximately ± 113 m distant from the IP. [132]

Table 3.2: Selection of ALICE sub-detectors relevant to this thesis. Acceptance is given in terms of pseudorapidity, the azimuthal coverage for the detectors presented is full. The z-axis is defined anticlockwise to the LHC. [132]

Detector	Acceptance	Position (cm)	Technology	Main purpose
ITS SPD	$\|\eta\| < 2.0$	$r = 3.9$ cm	Si pixel	tracking, PV, triggering
ITS SPD	$\|\eta\| < 1.4$	$r = 7.6$ cm	Si pixel	tracking, PV, triggering
ITS SDD	$\|\eta\| < 0.9$	$r = 15.0$ cm	Si drift	tracking, PID
ITS SDD	$\|\eta\| < 0.9$	$r = 23.9$ cm	Si drift	tracking, PID
ITS SSD	$\|\eta\| < 1.0$	$r = 38.0$ cm	Si strip	tracking, PID
ITS SSD	$\|\eta\| < 1.0$	$r = 43.0$ cm	Si strip	tracking, PID
TPC	$\|\eta\| < 0.9$	$r = 85.0$ cm	Ne drift, MWPC	tracking, PV, PID
V0A	$2.8 < \|\eta\| < 5.1$	$z = 329.0$ cm	scintillator	centrality, triggering
V0C	$-3.7 < \|\eta\| < -1.7$	$z = -88.0$ cm	scintillator	centrality, triggering

3.3 Time Projection Chamber

The Time Projection Chamber (TPC) [133] is ALICE's primary tracking detector and investigation tool for hadronic observables. It is located in the central barrel. The cylinder, illustrated in Fig. 3.3 is filled with a mixture of gases and a central 100-kV high-voltage electrode subjects it to a longitudinal electric field. Charged particles traversing the gas medium ionise it and the electrons then drift to the end-caps with a drift time of around 90 μs. There, they are detected in Read-out Chambers (ROCs), using Multi-Wire Proportional Chambers (MWPC), and together with the drift duration time, a three-dimensional information can be determined. The ROCs are radially divided (inner IROCs and outter OROCs) and segmented into 18 sectors in azimuth. Each ROC has 159 rows and its signals are processed by attached Front-End Cards (FECs). The MWPC principle and the ROC design, visualised with a charged particle track crossing all its rows, can be seen in Fig. 3.4.

In addition to the tracking information, the TPC is also used in PID, by measuring the charged particles' specific ionisation loss $\mathrm{d}E/\mathrm{d}x$. Measurements of $\mathrm{d}E/\mathrm{d}x$ for different particle species as a function of the particle momentum and charge is displayed in Fig. 3.3. A selection of TPC parameters not discussed above is given in Tab. 3.3.

Table 3.3: Selection of parameters of the Time Projection Chamber. [131]

Parameter	Value
Radial position (active volume)	$84.8 < r < 246.6$ cm
Length (active volume)	2×250 cm
Detector gas	Ne/CO$_2$/N$_2$ or Ar/CO$_2$
Spatial resolution	$0.8 - 1.1$ mm in $r\phi$ $1.1 - 1.2$ mm in z
$\mathrm{d}E/\mathrm{d}x$ resolution	$\sim 5.0\%$
Material budget X/X_0	3.5% near $\eta = 0$

3.3.1 Upgrade for Run 3: GEM read-outs

In the Run 2 setup, to avoid build-up of space charge in the TPC due to backflow of ions from the amplification region in MWPCs, a gating grid is used. This limits the operating rate of the TPC to approximately 3.5 kHz. However, for the Run 3 operation, the TPC has been planned to enable a continous read-out mode of Pb-Pb collisions at the interaction rate 50 kHz. For this reason, a new read-out technology, the Gas Electron Multiplier (GEM), is used. The technology and upgrade are discussed in more detail in Ref. [135]. Uninstalling the original TPC read-out electronics and

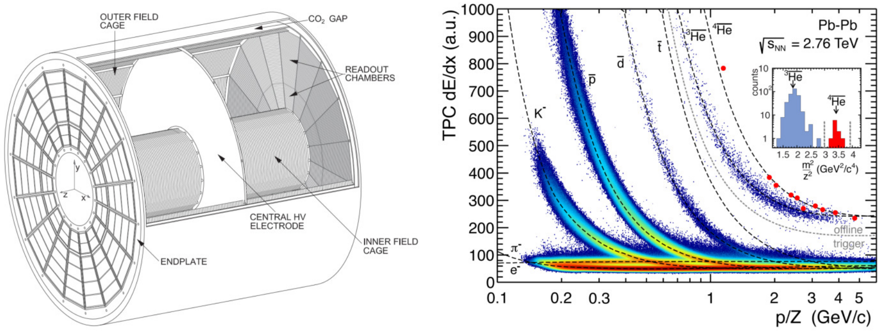

(a)

(b)

Figure 3.3: **(a)** Illustration of the TPC detector. [133]. **(b)** Ionisation energy loss of charged particles as a function of their momentum normalised by their charge as determined by the TPC. The dashed lines represent predictions from calculations. [132]

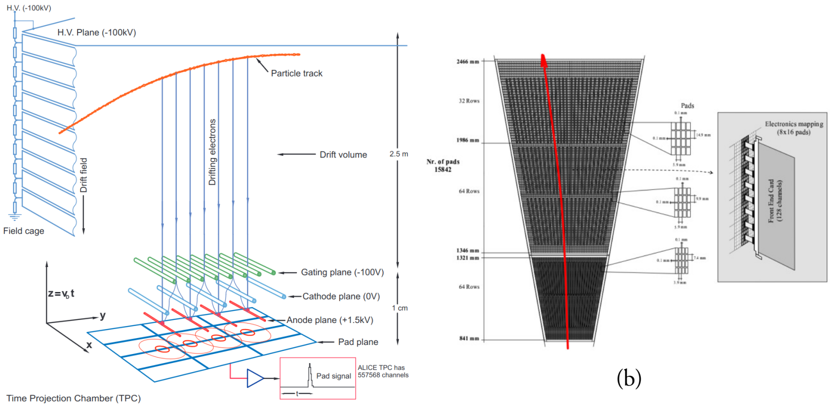

(a)

(b)

Figure 3.4: **(a)** Depiction of the operating principle at the ROCs, using MWPC. [134] **(b)** The IROC (bottom part) and OROC (top part) visualised with their number of rows and the signal-processing FECs. Also shown is a charged particle trajectory (red), which in this case crosses all 159 rows. [133] (*modified*)

commissioning of this upgraded TPC comprised the author's service (qualification) task.

The GEM uses 50-μm thin foils of insulating material, coated with conductive layers of thickness $2-5$ μm at each side, to which a potential difference of $200-400$ V is applied. The foil is perforated with double-conical holes of diameters ~ 70 and ~ 50 μm and a pitch of $\sim$ 140 or $\sim$ 280 μm. The electric field in the holes then causes avalanche multiplication. Four GEM layers are stacked on top of each other in a way, where the holes have different positions and densities, which reduces the ion backflow. Typically, for one electron, the gain is around 2000, with 20 ions flowing back into the drifting region. The GEM setup for the upgraded ALICE TPC is displayed in Fig. 3.5.

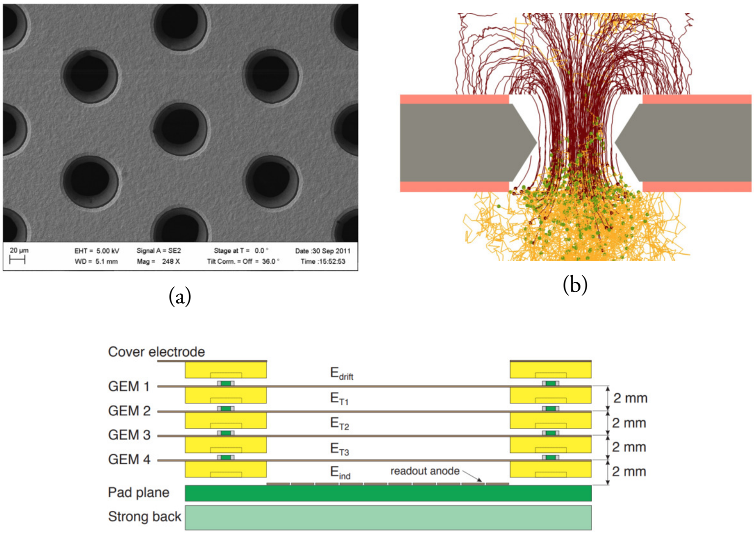

(a)

(b)

(c)

Figure 3.5: **(a)** Electron microscope photograph of a GEM foil with hole pitch 140 μm. [134] **(b)** Simulation of the charges in GEM holes. Dark lines represent ions and light lines electrons. Green dots mark multiplication site. **(c)** Schematic of the GEM setup at the upgraded ALICE TPC. [133]

3.4 Inner Tracking Systems

The Inner Tracking System [131, 136] is a set of semiconductor-based detectors also located in the central barrel, but much closer to the beam pipe. ALICE uses the ITS for its great spatial resolution, which complements the TPC tracking and allows for precise determination of the primary vertex (PV) as well as secondary vertices of short-lived particle decays. Moreover, thanks to its fast processing, it is also used for triggering. The ITS consists of three detectors, each of two layers, which use different silicon detector technologies:

- Silicon Pixel Detector (SPD): uses an extremely granular pixel matrix closest to the IP, where particle densities are the highest.
- Silicon Drift Detector (SDD): uses a similar technology based on drift cells. It is slightly less granular than the SPD but allows measuring of the deposited charge and thus PID based on $\mathrm{d}E/\mathrm{d}x$.

- Silicon Strip Detector (SSD): uses a silicon detector with two arrays of strips, misaligned with $\Delta\phi \approx 2\,\mathrm{deg}$, forming a lattice, on which a spatial coordinate can be determined. Similarly to the SDD, $\mathrm{d}E/\mathrm{d}x$ can also be measured.

Important parameters of the ITS sub-system can be found in Tab. 3.4 and the operating principles of the different silicon-based detector technologies used is discussed e.g. in Ref. [137, 138].

Table 3.4: Selection of parameters of the Inner Tracking System. [131]

Detector	SPD	SDD	SSD
Parameter			
Area (m^2)	0.07 and 0.14	0.42 and 0.89	2.09 and 2.68
Cell size (μm)	50×425	150×300	95×40000
Number of cells (M)	9.84	23	2.6
Spatial resolution (μm)	12 in $r\phi$, 100 in z	38 in $r\phi$, 28 in z	20 in $r\phi$, 830 in z
Mat. budget, layers X/X_0	1.14% and 1.14%	1.13% and 1.26%	0.83% and 0.86%
Mat. budget, supp. X/X_0	0.52%	0.25%	0.53%

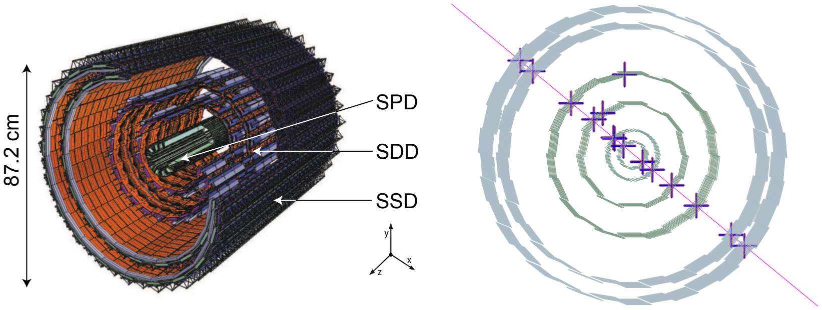

(a)

(b)

Figure 3.6: **(a)** Three-dimensional model of the ITS sub-system in ALICE detector simulations. **(b)** Display of a cosmic event detected by the ITS. [136]

3.5 V0A and V0C

The V0A and V0C[1] are two arrays of plastic scintillator counters, with PMT readouts, together forming the V0 sub-system [139]. They are placed asymmetrically on the z-axis with respect to the IP in order to accomodate the hadron absorber used in

---

[1] In ALICE, the "A-side" points in the counter-clockwise and the "C-side" in the clockwise direction of the LHC beam pipe, aligned with the z-axis. The C-side contains the muon system.

the muon tracking system of ALICE. Their inner and outer radii are 4.3 and 42.2 cm for the V0A and 4.5 and 32 cm for the V0C. Furthermore, they are segmented into 8 sectors azimuthally and 4 sectors radially. This is usually not granular enough for tracking, but sufficient for forward multiplicity estimation (combining amplitudes of both parts, referred to as V0M) or determination of the event plane.

Thanks to its speed, the V0 is also used for first-level (L0) triggering. Additionally, since the V0A and V0C can be used in coincidence, interactions of the protons/nuclei with residual gas in the beam pipe outside of the IP can be identified based on the different time information and rejected. The two detectors are visualised in Fig. 3.7.

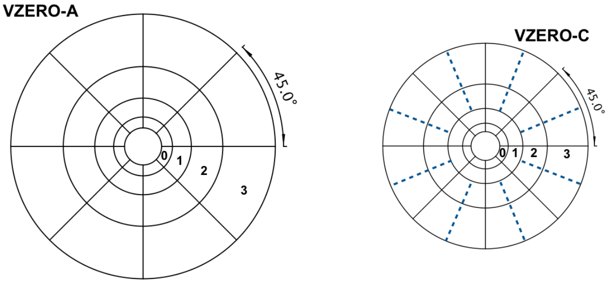

Figure 3.7: Schematic of the V0A and V0C scintillator arrays. [139]

Chapter 4

Events, tracks, vertices, and multiplicities

This Chapter provides an overview of the triggering and data preparation procedures at the ALICE experiment for Run 2. The aim is to give the reader an understanding of the process of obtaining final objects representing the particles produced in hadronic inelastic collisions at the interaction point of the LHC, utilizing the experimental apparatus that was described in the previous chapter.

4.1 Events and triggers

The ALICE experiment uses a trigger system [132, 140] to accommodate the different detector read-out times, limited data storage, and to select interesting physics events from collisions with rates of roughly 8 kHz for Pb-Pb collisions and up to 300 kHz for pp collisions. The Central Trigger Processor (CTP) collects input data from the trigger detectors and makes a decision about whether to take or reject the event, with the trigger decision split into three levels: L0, L1, and L2.

The L0 trigger level makes its decision based on the fastest detectors (e.g. the SPD and V0) and sends the decision back to detectors in $\sim 1.2\ \mu$s. The L1 trigger decision is based on all remaining fast detector inputs (also including e.g. the Zero Degree Calorimeters located 113 m far from the IP) and arrives back into detectors in 6.5 μs. The final L2 trigger level waits for all the detector readouts, including the slowest TPC detector, happening in about 105 μs time. Several trigger classes can be collected simultaneously during the data taking. Once an event passes the trigger decisions of the CTP, it is sent to the Data Acquisition System (DAQ) for more detailed processing and compression of the final data.

In ALICE measurements, the following names are commonly used for some of the triggered events:

- `kINT7` : the usual minimum bias (MB) class in pp collisions, based on a coincidence of the V0A and V0C detectors,
- `kINT1` : also a MB class, requiring at least two signals among V0A, V0C, and the SPD,
- |`INEL>0`| : requires a MB class and at least one SPD "tracklet" within $|\eta| < 1$, which is reconstructed in the two SPD layers.

4.2 Event and track reconstruction

Reconstruction of the event information in the central barrel follows a procedure discussed in Ref. [132] and summarised in Fig. 4.1. It begins with clusterisation, where the detector data is transformed into clusters, or *reconstruction points*, that include the spatial information, signal amplitude, signal time, and associated errors. The clusterisation is carried out locally for each detector. For instance, for the TPC, a cluster corresponds to a crossed row in the ROCs.

Next, a preliminary primary vertex (PV) position is determined by utilising clusters in the first two ITS layers (SPD). The Kalman filter technique is employed to perform track finding and fitting in TPC and ITS. The discovered tracks are then matched to other detectors in the central barrel and fitted. The reconstructed tracks are used to determine the final interaction vertex. The central-barrel tracking procedure concludes with a search for photon conversions and strange hadron decays (K^0_S, Λ, Ξ, and Ω). The steps are discussed in greater detail in this section.

4.2.1 First primary vertex determination

A preliminary primary vertex (PV) is determined using tracklets formed in the two SPD layers of the ITS. A three-dimensional reconstruction is performed in pp and pA collisions, iteratively, so that events with in-bunch pile-up can be treated. With each iteration, clusters with tracklets already pointing to a vertex are removed. By construction, the first found vertex has the highest number of corresponding tracklets

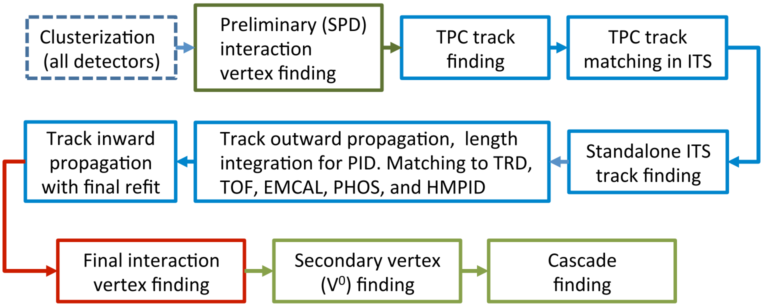

Figure 4.1: Work flow diagram of the event information reconstruction in the central barrel. [130]

and is defined as primary. If this method fails, the PV is determined only in the z-dimension. This is also the default in AA collisions. These methods are visualised in Fig. 4.2.

4.2.2 Tracking

Track finding (recognition) and track fitting (reconstruction) is carried out simultaneously using the Kalman filter technique in three steps: inwards, outwards, inwards [142]. The entire process is illustrated in Fig. 4.3.

First, for *primary* tracks, i.e. tracks hypothesised to originate from the PV, seeds are found from the preliminary SPD PV and pairs of TPC clusters at the highest radii, where track densities are the lowest. For *secondary* tracks, coming for instance from weak decays with displaced secondary vertices, three TPC clusters are used instead of considering the PV. The track seeds are then projected inwards, adding clusters fulfilling given proximity cuts, and updating the track parameters at each step, until the inner TPC radius is reached. Preliminary $\mathrm{d}E/\mathrm{d}x$ is also stored. Moreover, track candidates sharing multiple clusters (approximately more than 25%) are discarded in favour of their higher-quality doubles.

The TPC tracks are then extrapolated to the ITS, where the track parameters continue to get updated. The tracking efficiency in the TPC, displayed in Fig. 4.1, drops significantly below ≈ 200 MeV/c, where energy loss and multiple scatterings start playing a role. For this reason, the ITS also runs a standalone Kalman filter algorithm, using clusters that are not associated with the TPC track. There, similarly to the TPC, candidates are considered both with and without a PV constraint.

In the second step, tracks are extrapolated to the point of closest approach (PCA) with respect to the PV and back-propagated to the TPC outer radius, using the previously added clusters. Now, track lengths are also considered and an expected time-of-flight

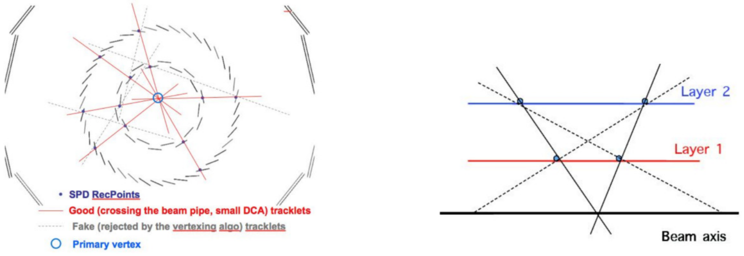

(a) (b)

Figure 4.2: **(a)** Preliminary three-dimensional reconstruction of the primary vertices, also depicting tracklets rejected by the algorithm. **(b)** Preliminary one-dimensional reconstruction of the PVs. [141]

(TOF) information is calculated based on the stored $\mathrm{d}E/\mathrm{d}x$. The tracks are then extrapolated to the Transition Radiation Detector (TRD), TOF, and possibly other detectors with clusters, where they can be matched with them. The ITS standalone tracks are propagated only to the ITS outer radius.

Finally, the tracks updated with the TRD and TOF (and possible other) information are re-fitted in each detector inwards again, starting at the TPC outer radii and propagating to the PV PCA. As a result of using the Kalmar filter, the track parameters are then finalised and given unambiguously, at the point of the primary vertex. More than 90% of the reconstructed tracks are primary tracks. This ratio can be significantly enhanced by imposing transverse and longitudinal cuts on the distance of closest approach (DCA) to the PV.

The ITS- and TPC-combined tracks enjoy the highest momentum resolution, which is plotted as a function of the track p_{T} in Fig. 4.4. It corresponds to values of about 1% at 1 GeV/c and then continues increasing as higher-p_{T} tracks are less curved, thus less constrained, and more likely to have a larger part in the detector's inactive regions. The disadvantage of the ITS-TPC tracks is their azimuthal non-uniformity due to gaps in the ITS acceptance, particularly the SPD.

Final PV determination

Subsequently, the ITS-TPC *global* tracks are used to determine the PV with a higher precision than when using the SPD tracklets alone. Tracks are also weighted to minimise the effect of outliers and the nominal beam position can also be used as a space point. In high pile-up runs, an iterative vertex finding process is performed. The standard deviation of the vertex position in the transverse region ranges from $\sim$ 1 mm in events with one track to $\sim$ 0.1 mm in events with five tracks and more.

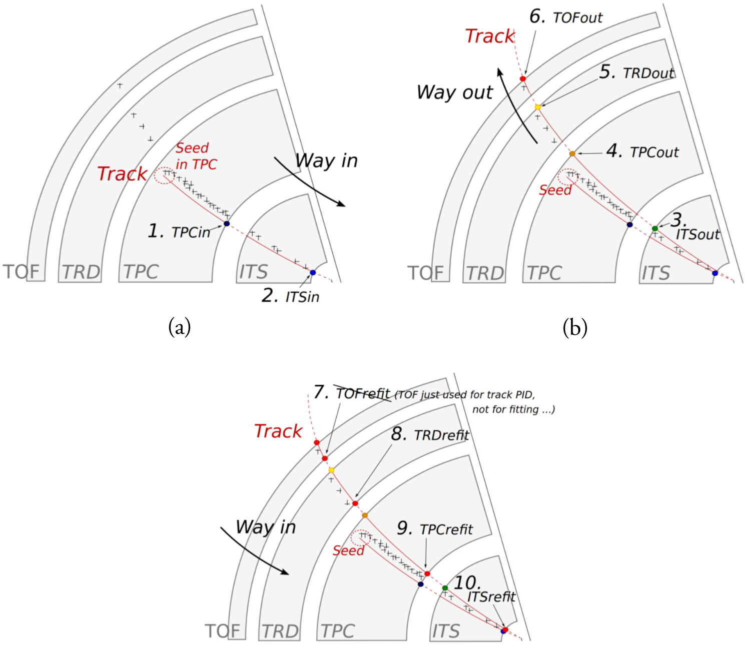

(a) (b)

(c)

Figure 4.3: Diagrams illustrating the inward-outward-inward approach in central barrel tracking. **(a)** First: track seeding and propagation to ITS and PV. **(b)** Second: back-propagation through ITS and TPC and extrapolation to TRD and TOF. **(c)** Third: final re-fit. [143]

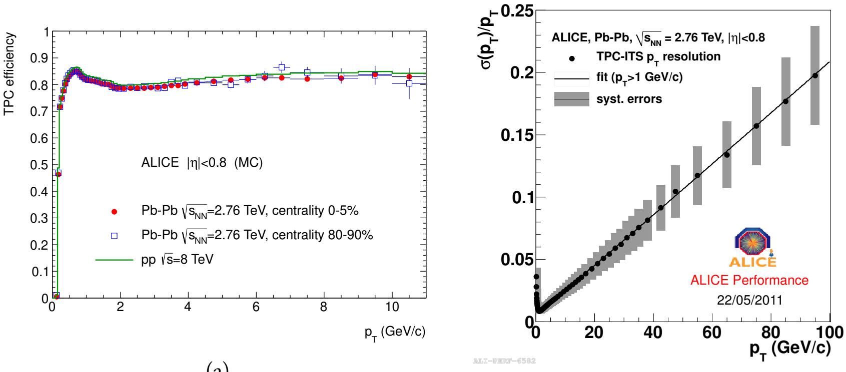

(a) (b)

Figure 4.4: **(a)** Efficiency of track finding in the TPC for primary particles in pp collisions (green) and Pb-Pb collisions at different centralities (blue and red), determined from simulations. [132] **(b)** Transverse momentum resolution of the combined ITS-TPC tracking in Pb-Pb collisions. [144]

4.2.3 Finding secondary vertices

After the track and primary vertex reconstruction, an algorithm finds secondary vertices corresponding to photon pair conversions, the so-called V^0s (weak decays of e.g.

the K^0_S and Λ) and the so-called *cascades* (Ξ and Ω), based on the topology shown in Fig. 4.5. First, pairs of unlike-signed tracks with a given DCA with respect to the PV are formed (more than 0.5 mm in pp or 1.0 mm in Pb-Pb). Furthermore, loose cuts on the topology of the decay (discussed in more detail in Chapter 5) are imposed. Specifically,

1. the PCA of the two tracks with respect to each other needs to be closer to the PV than the inner-most cluster of either of them, which corresponds to the case that the daughters are produced in the vertex,
2. the DCA of the two tracks needs to be smaller than 1.5 cm,
3. if the two-track momentum exceeds $p_T > 1.5\,\mathrm{GeV}/c$, cosine of the *pointing angle* (CPA) between the formed momentum vector and the straight line connecting the two-track PCA and the PV needs to be larger than 0.9.

The V^0s search can occur "online" during the tracking, using a full information of the clusters, or "offline", at a later stage, where it is based on the reconstructed tracks and can be re-configured. Subsequently, a search for cascades is performed: the found secondary vertices are matched with other secondary *bachelor* tracks if

1. the invariant mass of the found pair is consistent with that of a Λ, assuming a p and π mass hypothesis for the two tracks,
2. the bachelor DCA to the PV exceeds 0.2 cm.

4.3 Centrality and multiplicity measurements and their caveats

In Pb-Pb collisions, the experimentally measured multiplicity can be related to the centrality using the Glauber picture, as discussed in Chapter 2, which maps the final state to the percentage of the total hadronic cross section based on the collision geometry. This picture assumes that the multiplicity due to the different N_{part} dominates over contributions from specific event sub-structures (e.g. a hard jet), and that the effect of fluctuations is small enough to play a role. In ALICE, this procedure is performed typically using the V0M estimator (as it has the highest centrality resolution [132]). The V0M is a summed amplitude in the two V0A and V0C forward-rapidity scintillators, and the mapping procedure is discussed in detail in e.g. Ref. [145].

Apart from the V0M, multiplicity can also be estimated at mid-rapidity, using the SPD, which allows for taking into account particles with even very low momenta. This can be defined as either

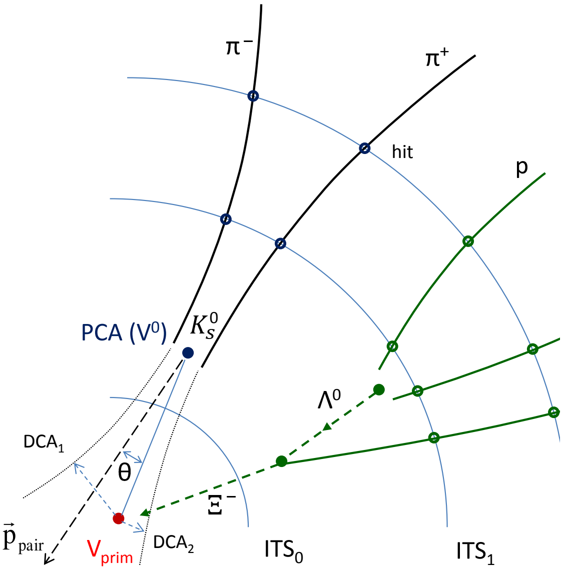

Figure 4.5: Diagram showing topology of a V^0 decay (in this case K^0_S) and a cascade decay (in this case Ξ) in the central barrel. Here, the decays occured within the ITS volume, but this is not a requirement for the reconstruction. The radii are not to scale. [132]

- the number of clusters in the first layer of the SPD, also known as `CL1`,
- or the number of formed tracklets in the SPD at $|\eta| < 0.8$. This is also used in the studies done in this thesis and is referred to as $N^{|\eta|<0.8}_{\mathrm{tracklets}}$.

In pp collisions, the choice of mid-rapidity estimators comes with an important caveat when measuring particle spectra. Since event classification and tracking are performed in the same coordinate space volume, and fluctuations are not negligible compared to the multiplicities, an auto-correlation bias occurs. This can be seen in Fig. 4.6, which compares the integrated yields of charged kaons to neutral K^0_S, scaled by a factor of two. As the multiplicity increases, the two yields become different, because requiring a large number of charged particles at mid-rapidity to classify the event as high-multiplicity biases the charged kaon yields to higher values. The figure also shows the result using the V0M estimator, where this effect does not occur.

Furthermore, it should be noted that apart from this auto-correlation bias, spectra measured as a function of mid-rapidity and forward-rapidity multiplicity may still exhibit differences, as the choice of rapidity also plays a role when accessing and classifying the underlying dynamics of particle production in the event. This is illustrated in Fig. 4.7, which shows a different dependence of the mean number of MPIs $\langle n_{\mathrm{MPI}} \rangle$ in Pythia 8 on the multiplicity selected by the two classifiers.

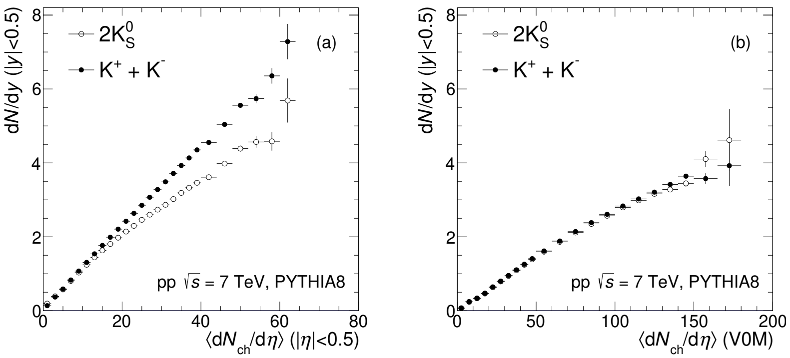

(a) (b)

Figure 4.6: Dependence of charged and neutral kaon yields in pp collisions on the multiplicity determined **(a)** at mid-rapidity using the $N_{\text{tracklets}}^{|\eta|<0.8}$ estimator and **(b)** at forward rapidity using the $\mathrm{V0M}$ estimator, as simulated by Pythia 8. [146]

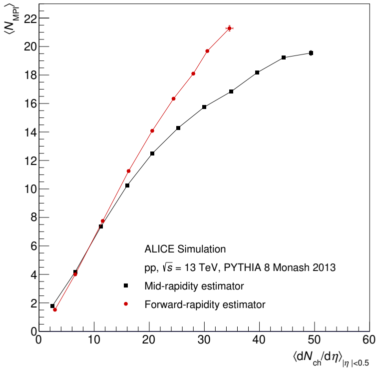

(a)

Figure 4.7: Mean number of MPIs as a function of multiplicity determined at mid-rapidity (black) and forward rapidity (red) in pp collisions at $\sqrt{s} = 13\,$TeV, as simulated by Pythia 8. [63]

4.4 Used tracks

The following tracks are often used in ALICE analyses and in the measurements within this dissertation:

- `ITSTPC2011`: The highest-quality ITS-TPC tracks, also referred to as “global” tracks. They require TPC and ITS re-fit, TPC goodness-of-fit $\chi^2/n_{\text{cluster}}^{\text{TPC}} < 4$, ITS goodness-of-fit $\chi^2/n_{\text{cluster}}^{\text{ITS}} < 36$, at least 70 crossed TPC rows, minimum 80% of findable clusters based on geometrical considerations, clusters in the SPD, longitudinal DCA to the PV within 2 cm, and no associated kink topology[1].

- `TPCOnly`: Tracks with better azimuthal uniformity, which require TPC goodness-of-fit $\chi^2/n^{\mathrm{TPC}}_{\mathrm{cluster}} < 4$, at least 50 crossed TPC rows, longitudinal DCA to the PV within 3.2 cm, transverse DCA to the PV within 2.4 cm, and no associated kink topology.

- `V0daughter`: Secondary tracks used to find candidates for weakly-decaying K^0_S and Λ (discussed further in Chapter 5), representing their charged daughters. They require a TPC re-fit, at least 70 crossed TPC rows, and no kink topology.

- Hybrid tracks: discussed below.

4.4.1 Hybrid tracks

For measurements requiring high track quality and momentum precision, such as for particle p_T spectra, the ITS-TPC tracks are usually used. As mentioned, these suffer from azimuthal non-uniformity due to the SPD acceptance. In situations where this is unacceptable, such as when using event shape observables or azimuthal topology classifications, "hybrid tracks" can be used instead. These correspond to a union of ITS-TPC tracks and *complementary tracks*, which are subjected to identical requirements save for the SPD cluster information. Furthermore, they must be constrained to the PV. A track can be classified as complementary only if it does not pass the ITS-TPC cuts first.

This union significantly improves the azimuthal uniformity, as displayed in Fig. 4.8.

4.4.2 Geometrical cuts on tracks

In measurements using a high-momentum trigger particle, additional geometrical constraints can be utilised to ensure the low-curvature particle trajectory does not significantly cover an inactive sector of the TPC.

In order to have just one set of requirements independent of the magnetic polarity and the particle charge, the modified azimuthal ϕ' is assigned using the following steps:

1. $\phi' = \phi$: the starting angle is the default azimuthal angle of the track.

---

[1] In ALICE, decays of charged particles into one charged and one neutral daughter, e.g. $\pi^- \to \mu^- \bar{\nu_\mu}$, can be identified in the TPC from a characteristic "kink" topology.

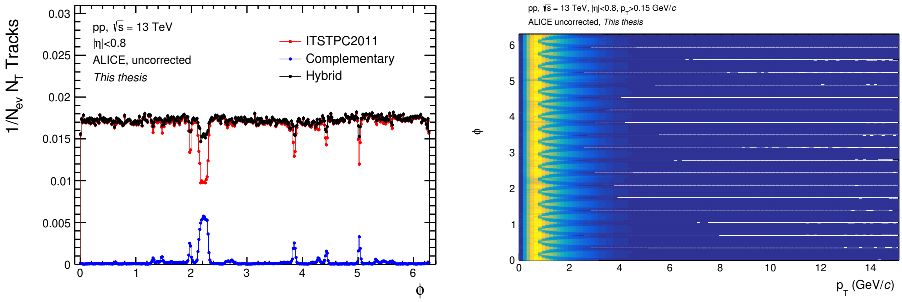

(a) (b)

Figure 4.8: **(a)** Azimuthal distributions of the standard ITS-TPC tracks (red), complementary tracks (blue), and their union: hybrid tracks (black), in events used for measurements presented in this thesis. **(b)** Two-dimensional distribution of the track azimuthal angle and transverse momentum, showing the effect of applying geometrical constraints to avoid boundaries between two adjacent TPC sectors.

2. $\phi' = 2\pi - \phi'$, if the polarity of magnetic field is negative ($B < 0$).
3. Then $\phi' = 2\pi - \phi'$, if the charge of the particle is negative ($q < 0$).
4. Finally, $\phi' = \phi' + \frac{\pi}{18}$, to off-set the angle to the mid-point between two sector boundaries.

Subsequently, a p_{T}-dependent constraint is applied in each sector, which corresponds to considering the following cuts on the remainder of ϕ' divided by the sector length $\frac{\pi}{9}$:

1. the track is rejected if $(\phi' \bmod \frac{\pi}{9}) < 0.12/p_{\mathrm{T}} + \frac{\pi}{18} + 0.035$, which means it exceeds the region of the boundary between two sectors from one side,
2. AND if $(\phi' \bmod \frac{\pi}{9}) > 0.1/p_{\mathrm{T}}^2 + \frac{\pi}{18} - 0.025$, when it exceeds the boundary region from the other side.

The effect is visualised in Fig. 4.8.

Part III

Author’s measurements

Chapter 5

Reconstruction of neutral strange particles with ALICE

The $\mathrm{K^0_S}$ and Λ ($\overline{\Lambda}$) hadrons are unstable neutral primary particles that usually decay within the volume of the detector through the weak interaction. Their mean lifetimes are $\sim 2.7\,\mathrm{cm}/c$ and $\sim 7.9\,\mathrm{cm}/c$, respectively [147]. Their dominant decay channels, which are also used for their measurement, are:

$$\mathrm{K^0_S} \rightarrow \pi^+\,\pi^- \tag{5.1}$$

$$\Lambda \rightarrow \mathrm{p}\,\pi^- \tag{5.2}$$

$$\overline{\Lambda} \rightarrow \bar{\mathrm{p}}\,\pi^+ \ . \tag{5.3}$$

Because of how these hadrons' decay topologies appear in the detector (an undetectable neutral particle decaying into a V-shaped pair of detectable tracks), they are commonly nicknamed $\mathrm{V^0}$s[1].

5.1 Analysed datasets

The analysed data used in the measurements presented in this dissertation were collected with ALICE in pp collisions at $\sqrt{s} = 13\,\mathrm{TeV}$ during the Run 2 program in years 2016 and 2017. For the spherocity analysis in Chapter 6, data from year 2018 were also used. This corresponds to the following number of minimum bias (MB) events:

---

[1] Not to be confused with V0A and V0C—the forward calorimeters in ALICE, or V0M—the related multiplicity estimator using the scintillators' signal.

- 2016+2017+2018: approximately 1.3B events,
- 2016+2017: approximately 630M events.

Events classified as $|$`INEL>0`$|$, discussed in Chapter 4, were analysed. Furthermore, events with incomplete data acquisition were rejected (which can happen due to failures of detector sub-systems during data collection). The reconstructed primary vertex (PV) also must have its spatial resolution less than 0.25 cm in the z-direction, and dispersion less than 0.04 cm in the transverse direction. To ensure consistent performance of ALICE detectors among all events, the vertex is also required to be within 10 cm of then nominal interaction point in the z-direction. Finally, events with multiple reconstructed PVs or inconsistent timing information from the V0 and SPD detectors were rejected to minimise in-bunch and out-of-bunch pile-up, respectively. These requirements reduce the number of analysed MB events by roughly 8%.

To estimate reconstruction effects, Monte Carlo (MC) simulations based on Pythia 8 [29] of the ALICE detector, modelled by GEANT3 [148], were utilised. These simulations are linked to individual data collection periods to match their specifics, such as the TPC gas mixture and calibrations.

5.2 Identification of $\mathrm{V^0s}$ using ALICE

A centrally developed ALICE algorithm, the ALICE $\mathrm{V^0}$ finder (discussed in Chapter 4), is used to collect suitable $\mathrm{V^0}$ candidates from pairs of oppositely charged tracks with the relevant topology. This typical topology and its characterising quantities are illustrated in Fig. 5.1. Additional selection criteria ("cuts") are further applied to suppress the background among those candidates. These include:

- cuts on kinematics of the mother and the daughters,
- constraints on the topology of the decay,
- constraints on the reconstruction quality of the daughter tracks,
- cuts on the specific ionisation energy loss $\mathrm{d}E/\mathrm{d}x$ of the daughter tracks in the TPC gas (expressed as the number of standard deviations σ_{TPC} away from the expected value),
- rejection of contributions from pile-up using "fast detector" information (at least one daughter must have TOF information or ITS re-fit),

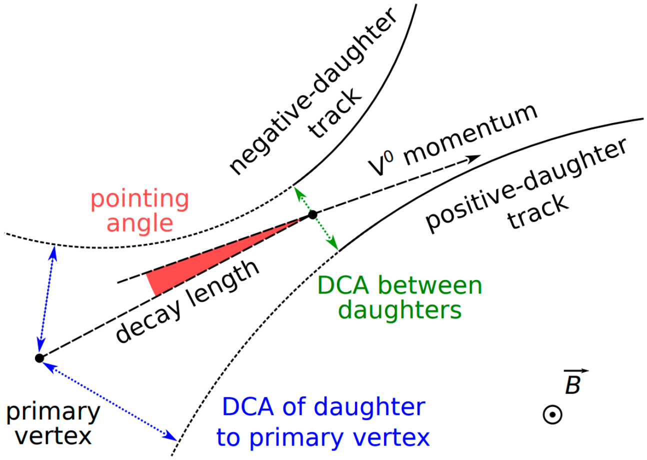

Figure 5.1: Typical topology of V^0 decay. PV stands for primary vertex, SV for secondary vertex. [149]

- rejection of V^0 candidates with invariant mass calculated under competing hypotheses of daughter masses too close to the mass of the competing V^0 species (e.g., a V^0 with $M_{\pi\pi} \approx m_{\mathrm{K}^0_\mathrm{S}}$ will not be considered as a Λ or $\overline{\Lambda}$ candidate).

The full list of used cuts is listed in Tab. 5.1. The TPC track quality cuts are also discussed in Chapter 4.

5.3 Signal extraction

The determination of the actual particle species that is the reconstructed V^0 is based on calculating its invariant mass, which is then used to statistically extract the signal from the background. The invariant mass is calculated individually for all three V^0 species as

$$M^2_{\mathrm{inv}} = (p_1 + p_2)^2 \quad , \tag{5.4}$$

where p_1 and p_2 are the daughter four-momentum vectors and one assumes the daughter masses based on the V^0 species hypothesis, i.e., $M_{\pi\pi} \equiv M_{\mathrm{K}^0_\mathrm{S}}$, $M_{p\pi} \equiv M_\Lambda$, and $M_{\pi p} \equiv M_{\overline{\Lambda}}$.

The V^0 signal is separated from the background in distributions of $\Delta M_{V^0} \equiv M_{\mathrm{inv}} - m_{\mathrm{V}^0}$, where m_{V^0} is the mass of the V^0 species taken from Ref. [6]. This is performed in individual p_T intervals and uses the so-called sideband method. Assuming the signal peaks around $\Delta M_{V^0} = 0$ and approximating the background in this region as being linear, the subsequent procedure is followed:

Table 5.1: Cuts used in the identification of the $\mathrm{K^0_S}$, Λ, and $\overline{\Lambda}$ particles. Decay radius corresponds to the decay length in the xy-plane. The fast detector requirement indicates the minimum number of ITS or TOF signals among the $\mathrm{V^0}$ daughters. The standard deviations in the competing mass cut denote the invariant mass peak widths, as defined in the signal extraction procedure.

Cut Variable	Cut Value for $\mathrm{K^0_S}$ (Λ, $\overline{\Lambda}$)
Topology	
V^0 DCA	$\mathrm{DCA^{d-d}} < 1.0$ cm
Pointing angle	$\cos\mathrm{PA} > 0.97(0.995)$
Decay radius	0.5 cm $< R_{xy}$
Daughter Tracks Selection	
DCA of daughters to PV	$\mathrm{DCA}_{xy}^{\mathrm{d-PV}} > 0.06$ cm
TPC PID of daughters	$< 5\,\sigma_{\mathrm{TPC}}$
Track pseudorapidity	$-0.8 < \eta < 0.8$
TPC crossed rows	$N_{\mathrm{cr}} > 70$
TPC crossed rows to findable ratio	$N_{\mathrm{cr}}/N_{\mathrm{f}} > 0.8$
Candidate Selection	
V^0 pseudorapidity	$-0.8 < \eta < 0.8$
Transverse momentum	$0.4 < p_{\mathrm{T}} < 8.0\ \mathrm{GeV}/c$
Proper lifetime (transverse)	$(\,R_{xy} \times m_{(\Lambda,\overline{\Lambda})}/p_{\mathrm{T}} < 30$ cm$\,)$
Competing mass	$> 4\,\sigma$
Fast detector information	> 1 detector

1. The sideband regions are defined. The ΔM_{V^0} spectra are fitted in the $-0.03 < \Delta M_{V^0} < -0.03\,\mathrm{GeV}/c^2$ interval using a χ^2-fit with the seven-parameter function

$$f(\Delta M_{V^0}) = \{0\} + \{1\} \cdot \Delta M_{V^0} + \{2\} \cdot \mathcal{N}(\Delta M_{V^0}, \mu, \sigma_1^2) \tag{5.5}$$

$$+ \{3\} \cdot \mathcal{N}(\Delta M_{V^0}, \mu, \sigma_2^2)\ , \tag{5.6}$$

   where $\mathcal{N}$ is a Gaussian distribution and $\{\cdot\}$ represent four free parameters. Thus, this function represents a linear background component and two Gaussians, with a common mean μ and widths σ_1 and σ_2, respectively. This procedure is followed for all p_{T} bins and illustrated in Fig. 5.2.

2. In each p_{T} bin, a common parameter σ is obtained from the two Gaussians. It is calculated as the RMS of the $\{2\} \cdot \mathcal{N}(\mu, \sigma_1^2) + \{3\} \cdot \mathcal{N}(\mu, \sigma_2^2)$ distribution, sampled 10^5 times.

3. The variables $\mu_{\mathrm{V^0}}$ and $\sigma_{\mathrm{V^0}}$ as functions of p_{T} are interpolated using a χ^2-fit

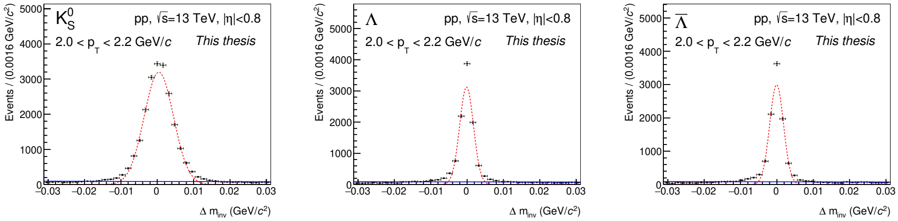

Figure 5.2: Determination of the signal peak mean and width for $\mathrm{K^0_S}$, Λ, and $\overline{\Lambda}$ invariant mass spectra using a function fit including a signal component using two con-centric Gaussian distributions and a linear background component, here illustrated on $\mathrm{V^0}$s within $2.0 < p_\mathrm{T} < 2.2$ GeV/c. Only the main Gaussian (red line) and background (blue line) components are displayed. The data sample shown does not represent the entire dataset.

and the parametrisations:

$$\mu_{\mathrm{K^0_S}}(p_\mathrm{T}) = \begin{cases} \{0\} + \{1\} \cdot p_\mathrm{T} + \{2\} \cdot p_\mathrm{T}^2 & \text{if } p_\mathrm{T} < 1.6\,\mathrm{GeV}/c, \\ \{3\} & \text{if } p_\mathrm{T} \geq 1.6\,\mathrm{GeV}/c, \end{cases} \tag{5.7}$$

$$\mu_{\Lambda,\overline{\Lambda}}(p_\mathrm{T}) = \begin{cases} \{0\} + \{1\} \cdot p_\mathrm{T} + \{2\} \cdot p_\mathrm{T}^2 & \text{if } p_\mathrm{T} < 1.9\,\mathrm{GeV}/c, \\ \{3\} + \{4\} \cdot p_\mathrm{T} & \text{if } p_\mathrm{T} \geq 1.9\,\mathrm{GeV}/c, \end{cases} \tag{5.8}$$

$$\sigma_{\mathrm{V^0}}(p_\mathrm{T}) = \{0\} + \{1\} \cdot p_\mathrm{T} + \frac{\{2\}}{p_\mathrm{T}} \;. \tag{5.9}$$

The fitted parametrisations can be seen in Fig. 5.3.

4. In each p_T bin, one defines the signal region **N** as $(\mu_{\mathrm{V^0}} - 6\sigma_{\mathrm{V^0}}; \mu_{\mathrm{V^0}} + 6\sigma_{\mathrm{V^0}})$ and the sidebands **A** and **B** as $(\mu_{\mathrm{V^0}} - 12\sigma_{\mathrm{V^0}}; \mu_{\mathrm{V^0}} - 6\sigma_{\mathrm{V^0}})$ and $(\mu_{\mathrm{V^0}} + 6\sigma_{\mathrm{V^0}}; \mu_{\mathrm{V^0}} + 12\sigma_{\mathrm{V^0}})$. In these regions, the data entries are summed together to acquire N, A, B. The choice of $6\sigma_{\mathrm{V^0}}$ is rather cautious to avoid biases from incorrect determination of the $\mu_{\mathrm{V^0}}$ or the imperfect description of the signal peak width $\sigma_{\mathrm{V^0}}$

5. If the background is assumed to be linear, the sum of the two sideband integrals is an accurate estimation of the background in the signal region. Particle yields Y and the corresponding statistical uncertainties σ_Y are calculated as

$$Y = N - A - B \tag{5.10}$$

$$\sigma_Y = \sqrt{N + A + B} \;, \tag{5.11}$$

due to the fact that the statistical uncertainties in the signal and sideband regions are fully uncorrelated. Illustrations of this step can be seen in Fig. 5.4.

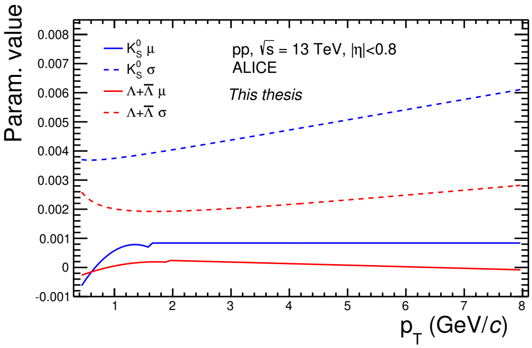

Figure 5.3: Parametrisation of the signal peak means and widths for the K^0_S and Λ ($\overline{\Lambda}$) as a function of p_T.

5.3.1 Validation using simulations

The accuracy of the sideband method is tested with a “MC closure”: in MC-simulated data, the raw p_T-spectra reconstructed blindly from the V^0 candidates are compared with raw p_T-spectra of reconstructed, labelled V^0, which showed a $\sim 5\%$ effect at high-p_T. This is caused by the fact that in ALICE MC simulations, the V^0 mass peaks have somewhat longer tails than in data and thus, the signal can enter the background regions. This has to be taken into account when defining reconstruction efficiency using MC simulations.

Alternative approach

Originally, methods involving a likelihood fit and an unbinned likelihood fit of two Gaussian distributions as well as other background descriptions were tested. However, although more sophisticated, these methods proved considerably less precise. This is due to the fact that the signal peaks cannot be accurately described by the two Gaussian distributions, particularly in highly populated p_T bins. In spite of that, they are still found to be sufficient to determine the signal and background region parametrisation for the above-stated purposes.

Mass resolution of secondary Λ and $\overline{\Lambda}$ particles

Approximately 20% of the measured Λ yields are produced as secondary particles, also called feeddown. Most of these come from decays of the Ξ baryon. Investigations of the simulated data revealed that the invariant mass of these secondaries suffers from a worse resolution (circa 3 times higher σ_{V^0}). Subsequently, this gives the sideband

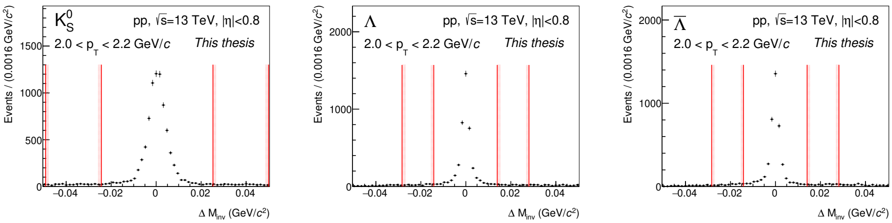

Figure 5.4: Visualisation of the sideband regions (red), from which the background is estimated, in invariant mass spectra of the $\mathrm{K^0_S}$, Λ, and $\overline{\Lambda}$ particles. Here illustrated on $\mathrm{V^0}$s within $2.0 < p_{\mathrm{T}} < 2.2\,$GeV/$c$. The data sample shown does not represent the entire dataset.

extraction about 75% efficiency for secondaries, and approximately 95% efficiency for inclusive Λ yields at intermediate p_{T}. This has to be taken into consideration when calculating corrections for the feeddown yields. This effect can be seen in Fig. 5.5.

5.4 Normalisation

The reconstructed $\mathrm{K^0_S}$, Λ, and $\overline{\Lambda}$ yields $Y(\eta, p_{\mathrm{T}})$ are normalised according to

$$\frac{\mathrm{d}^2 N^{\mathrm{raw}}}{\mathrm{d}y \mathrm{d}p_{\mathrm{T}}} = \frac{1}{N_{\mathrm{ev}}} J \frac{1}{\Delta\eta} \frac{1}{\Delta p_{\mathrm{T}}} Y(\eta, p_{\mathrm{T}}) \quad , \tag{5.12}$$

where N_{ev} is the number of selected events corrected for no vertex reconstruction, J the Jacobian of the $\eta \to y$ transformation, and $\Delta\eta$ and Δp_{T} the widths of the pseudorapidity and transverse momentum intervals, respectively. The Jacobian is given as follows,

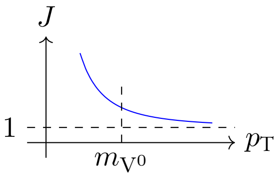

$$J(p_{\mathrm{T}}) \equiv \sqrt{1 + \left(\frac{m_{\mathrm{V^0}}}{p_{\mathrm{T}} \cosh \eta_0}\right)^2} \quad , \tag{5.13}$$

and is used to compare measurements reported in $|\eta| < \eta_0$ to those in $|y| < y_0 = \eta_0$.

The correction to include events with no good reconstructed vertex is performed in a data-driven way according to:

$$N_{\mathrm{ev}} = N_{|\mathrm{v.}|<10} \times \left(1 + \frac{N_{\mathrm{no\,v.}}}{N_{\mathrm{good\,v.}}}\right) \quad , \tag{5.14}$$

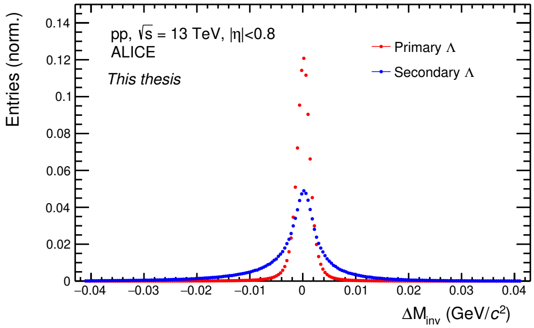

Figure 5.5: Invariant mass distributions of primary Λ (red) and secondary Λ (blue) in ALICE MC simulations of pp collisions at $\sqrt{s} = 13\,\text{TeV}$

where $N_{|\text{v.}|<10}$ is the number of events with a good reconstructed vertex within 10 cm of the nominal IP in the z-direction, $N_{\text{no v.}}$ the number of all events with no good vertex, and $N_{\text{good v.}}$ the number of all events with a good vertex.

5.5 Corrections to the reconstructed production

To acquire results with scientific relevance, the raw yields of V^0s observed with ALICE need to be corrected for geometrical acceptance, detector effects, and, in the case of Λ ($\overline{\Lambda}$), also for secondary contribution.

5.5.1 Secondary contribution correction

Only approximately 80% of the measured inclusive Λ and $\overline{\Lambda}$ yields are produced directly in the pp collision or near-instantanously in non-weak decays of resonances, as primary particles. The remainder is produced secondarily, as products of weak decays of heavier baryons. The dominant, and the only relevant, reactions are:

$$\Xi^- \to \Lambda\,\pi^- \;, \tag{5.15}$$

$$\Xi^0 \to \Lambda\,\pi^0 \;, \tag{5.16}$$

$$\Xi^+ \to \overline{\Lambda}\,\pi^+ \;, \tag{5.17}$$

$$\overline{\Xi}^0 \to \overline{\Lambda}\,\pi^0 \;. \tag{5.18}$$

For the K^0_S, the secondary production (such as from ϕ mesons) is negligible.

The primary Λ yields can be estimated using the following equation,

$$\begin{aligned}\Lambda^{\mathrm{raw}}(p_{\mathrm{T}}^{i}) &= \Lambda^{\mathrm{raw}}_{\mathrm{measured}}(p_{\mathrm{T}}^{i}) - \Lambda^{\mathrm{raw}}_{\mathrm{secondary}}(p_{\mathrm{T}}^{i}) &\quad (5.19)\\ &= \Lambda^{\mathrm{raw}}_{\mathrm{measured}}(p_{\mathrm{T}}^{i}) - \sum_{j} F^{\Lambda}_{ij} \int_{p_{\mathrm{T}}^{j}} \frac{dN}{dp_{\mathrm{T}}}(\Xi^{-}) \quad , &\quad (5.20)\end{aligned}$$

where F_{ij} is the so-called feeddown matrix giving the probabilities of a produced Ξ^{-} or Ξ^{0} particle in a p_{T} interval j decaying into a reconstructed Λ in a p_{T} interval i, and $\frac{dN}{dp_{\mathrm{T}}}(\Xi^{-})$ the measured transverse momentum Ξ^{-} spectra. This approach assumes that the Ξ^{0} decay contribution is identical to Ξ^{-} and is used because Ξ^{0} baryons are challenging to measure. For the $\overline{\Lambda}$, the equation is analogous but uses Ξ^{+} .

The feeddown matrix is calculated in ALICE MC simulations of MB events, using the relation

$$F^{\Lambda}_{ij} = 2 \cdot \frac{N_{\mathrm{rec.}}(\Lambda)\big|^{p_{\mathrm{T}}^{\Xi}=j}_{p_{\mathrm{T}}^{\Lambda}=i}}{N_{\mathrm{gen.}}(\Xi)\big|_{p_{\mathrm{T}}^{\Xi}=j}} \quad , \qquad (5.21)$$

where Ξ represent both Ξ^{-} and Ξ^{0}. There is an assumption that the probabilities, and thus, the matrix, do not depend on multiplicity of the event. This assumption is taken into account in systematic uncertainties.

An alternative approach is to construct the F^{Λ}_{ij} from charged Ξ solely, and then multiply the $\Lambda^{\mathrm{raw}}_{\mathrm{secondary}}$ by a factor of two. It was used to determine the systematic uncertainty of the method.

As discussed previously, due to the worse mass resolution of secondary Λ, a $\Delta M_{V^{0}}$ cut of $5\sigma_{\mathrm{V}^{0}}$ (determined in the sideband definition procedure) is considered, to account for the fact that a large amount of secondaries enter the background regions. Since they subsequently reduce the signal, a negative weight of -1 has to be applied when constructing the feeddown matrix for those decays where the Λ mass enters the background regions. This method results in the best MC closure validation, but other configurations (a $6\sigma_{\mathrm{V}^{0}}$ cut and -1 weight, a $4\sigma_{\mathrm{V}^{0}}$ cut and 0 weight) were also tested.

The feeddown matrices F^{Λ}_{ij}, $F^{\overline{\Lambda}}_{ij}$ are displayed in Fig. 5.6.

Ξ spectra

In order to obtain the feeddown contribution from the above-stated method, Ξ transverse momentum spectra measured in the same collisions need to be provided. Fully corrected Ξ spectra from pp collisions at $\sqrt{s} = 13\,\mathrm{TeV}$ measured within $0.6 < p_{\mathrm{T}} < 6.5$ GeV/c in ALICE were used.

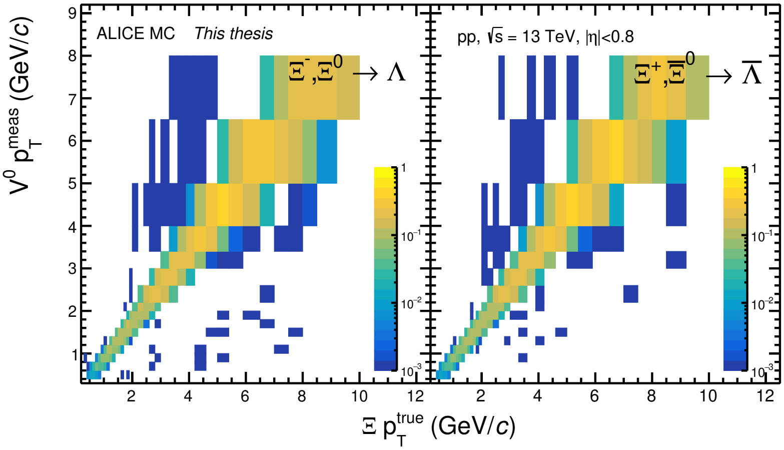

Figure 5.6: Feeddown matrices F_{ji}^{Λ} (left) and $F_{ji}^{\overline{\Lambda}}$ (right) from Ξ baryons, calculated using ALICE MC simulations of pp collisions at $\sqrt{s} = 13$ TeV.

Moreover, as the feeddown method requires the Ξ spectra to be extrapolated down to zero, they were fitted with a Lévy-Tsallis function, which is defined as

$$f(p_\mathrm{T}) = N \cdot p_\mathrm{T} \cdot \frac{(n-1)(n-2)}{nC(nC+m(n-2))} \cdot \left[1 + \frac{\sqrt{p_\mathrm{T}^2 + m^2} - m}{n \cdot C}\right]^{-n}, \quad (5.22)$$

where m is the mass of the particle (in this case Ξ), n, C, and N are the fit parameters. The fitted spectra as well as the estimated fraction of secondary Λ can be seen in Fig. 5.7

5.5.2 Reconstruction efficiency

The total reconstruction efficiency for V^0s, including the acceptance, can be determined using the Monte Carlo simulations. The η-integrated efficiency $\epsilon(p_\mathrm{T})$ is calculated as

$$\epsilon(p_\mathrm{T}) = \text{acceptance} \times \epsilon_\mathrm{rec} \quad (5.23)$$

$$= \frac{\#\,\text{associated reconstructed } \mathrm{V}^0\text{s}}{\#\,\text{generated } \mathrm{V}^0\text{s within } |\eta| < 0.8}, \quad (5.24)$$

in events that passed the selection criteria. The association is done by comparing the mother's and daughters' particle species label, as well as the MC generator indices. Particles in the numerator have to satisfy all selection cuts. The reconstruction efficiency for K^0_S, Λ, and $\overline{\Lambda}$ determined from this method is plotted in Fig. 5.8.

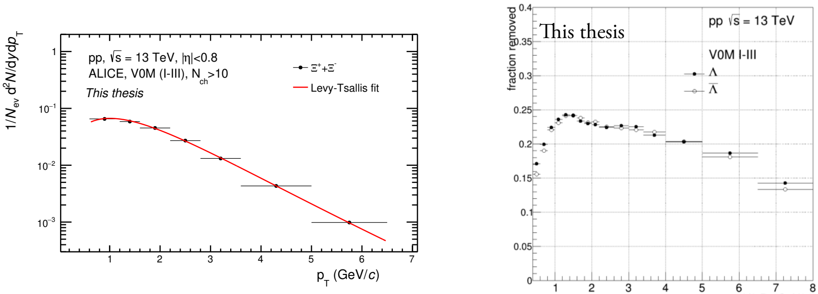

(a)

(b)

Figure 5.7: **(a)** Transverse momentum spectrum of Ξ baryons in $\mathrm{V0M}$ I-III events, fitted with a Lévy-Tsallis function. The Ξ spectra were measured by co-author P. Christiansen. **(b)** Fraction of the secondary Λ and $\overline{\Lambda}$ in the inclusive yields as a function of transverse momentum of the V^0, here calculated in high-multiplicity $\mathrm{V0M}$ I-III events.

As mentioned before, in ALICE simulations, the M_{inv} resolution worsens with increasing p_{T}; in high-p_{T} bins, the simulated V^0s are sometimes reconstructed with a M_{inv} that lies in the heavily dominated background region. This would lead to a lower efficiency as these V^0s are not extracted, and, subsequently, an overestimation of the corrected spectra. For this reason, a $4\sigma_{\mathrm{V}^0}$ cut on ΔM_{V^0} is required for particles in the numerator. Alternatively, one could use a cut of $6\sigma_{\mathrm{V}^0}$ and add the particle with a negative weight -1 to the numerator in the cases where the cut is not satisfied.

The reconstruction efficiency is defined in MB events, assuming the reconstruction in pp collisions does not largely depend on multiplicity, geometrical event classification, or event sub-structure. This assumption is taken into account in the systematic uncertainties.

5.6 Transverse momentum spectra

Using the corrections on the normalised yields and the η-integrated reconstruction efficiency, one acquires the measured transverse momentum spectra as follows

$$\frac{\mathrm{d}^2 N}{\mathrm{d}y\mathrm{d}p_{\mathrm{T}}} = \frac{1}{\epsilon(p_{\mathrm{T}})} \times \frac{\mathrm{d}^2 N^{\mathrm{raw}}_{\mathrm{primary}}}{\mathrm{d}y\mathrm{d}p_{\mathrm{T}}} \quad . \tag{5.25}$$

These spectra are now comparable with production cross sections and thus theoretical predictions.

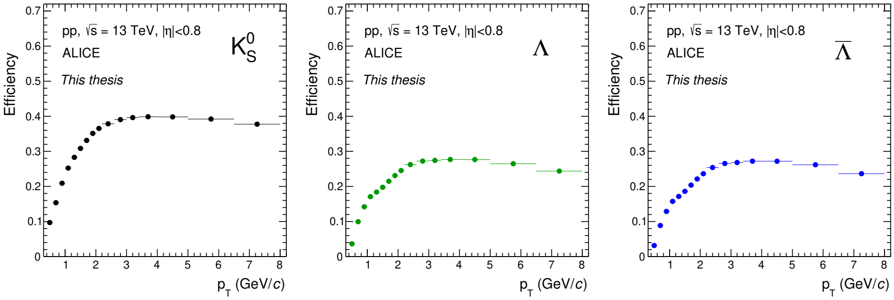

Figure 5.8: Reconstruction efficiency of the $\mathrm{K^0_S}$, Λ, and $\overline{\Lambda}$ particles as a function of transverse momentum in pp collisions at $\sqrt{s} = 13\,$TeV with ALICE.

5.6.1 Comparisons with previously published results

The acquired results were tested against previously published measurements of $\mathrm{K^0_S}$, Λ, and $\overline{\Lambda}$ transverse momentum spectra at the ALICE experiment in MB as well as high-multiplicity (V0M I and V0M III) events in pp collisions at $\sqrt{s} = 13$ TeV.

$\mathrm{K^0_S}$

The published $\mathrm{K^0_S}$ results using the 2015 data [150] were measured in `kINT7` events (see Chapter 4 for definition) . Thus, in order to compare on an equal footing, a |`INEL>0`| trigger efficiency scaling factor, $\epsilon_{\mathrm{trig}} = 0.7448$ [150], was applied to this analysis.

The comparison of this analysis to the published results can be seen in Fig. 5.9. In high-multiplicity events, the spectra are in a good agreement across the entire p_{T} range (most points lie within $\sim 5\%$ difference). In MB events, there is a difference ($\sim 10\%$) at the lowest p_{T} values. This is understood as a loss of signal in events with no reconstructed charged tracks and is usually corrected for. Since the correction plays a role only in MB events – which are of a limited interest to this thesis' work – it is not taken into account here.

$\Lambda + \overline{\Lambda}$

The published $\Lambda + \overline{\Lambda}$ results using the 2015 data [100] were measured in events with the same selection as this analysis, (|`INEL>0`|), therefore, ϵ_{trig} was not applied. They are compared to this analysis in Fig. 5.9 and show a satisfactory agreement (most points lie within $\sim 5\%$ difference).

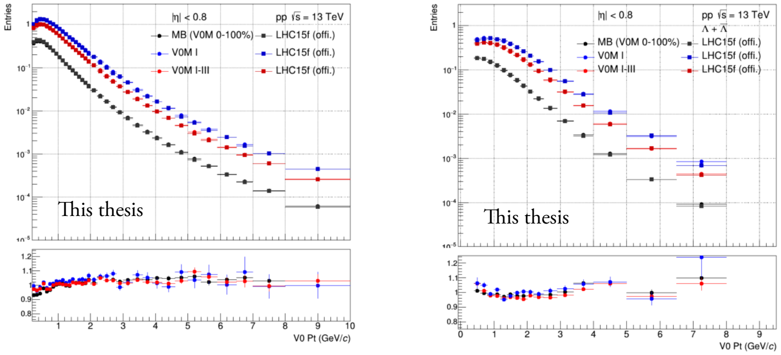

(a) (b)

Figure 5.9: Cross-checks of this analysis' p_{T} spectra of **(a)** $\mathrm{K}^0_{\mathrm{S}}$ and **(b)** $\Lambda + \overline{\Lambda}$ in MB, $\mathrm{V0M}$ I, and $\mathrm{V0M}$ I-III events in pp collisions at $\sqrt{s} = 13$ TeV (circles) against results previously published by ALICE, using data from 2015 (squares).

5.7 Systematic uncertainties

Experimentally measured values always come with uncertainties – statistical and systematic. Whereas statistical uncertainties are caused by the limited number of measurements and can be decreased by increasing the statistical sample analyzed, systematic uncertainties represent the imprecision or the bias of the experimental methodology itself. Calculation of statistical uncertainties is given directly from frequentist statistics. Definition of systematic uncertanties, however, is not always straightforward – one cannot simply re-do the measurement with several completely different experimental setups and data analysis techniques. Therefore, a lot of effort needs to go into identifying all possible sources of systematic uncertainties and estimating reasonable method variations.

In this measurement, the following sources of systematic uncertainty were identified as relevant:

- **Variation of selection criteria**
  In determining the reconstruction efficiency, it is assumed that in ALICE MC simulations, all observables used for the identification of V^0s and for assuring the quality of daughter tracks represent reality. Their inaccurate description, however, results in a bias. This bias is estimated by testing the sensitivity of the final results to varying the selection criteria on these observables and is discussed in the text below.

- **Signal extraction method**

The biases of the sideband background estimation procedure are tested against increasing and reducing the signal and background regions, by varying the number of σ_{V^0}. Variations of 5 and 7 σ_{V^0} were used.

- **Multiplicity dependence of $\epsilon(p_{\mathrm{T}})$**
  Studies of the reconstruction efficiency in pp collisions reveal a small, albeit significant dependence on the collision final state. A constant uncertainty of 2% is applied on the spectra to account for this.

- **Feeddown correction**
  Three sources of uncertainty on the contribution of secondary particles were identified – variation of the Ξ yields determined from the Lévy-Tsallis extrapolation, multiplicity dependence of the feeddown matrix (assumed 2%), and an alternative method, using a feeddown matrix constructed solely from charged Ξ, as discussed in Sec. 5.5.1.

- **Material budget**
  This uncertainty reflects that implementing ALICE's material composition in simulations comes with limitations. Previous studies in ALICE [132] which varied parameters of the description of the apparatus showed that this effect ranges between $3 - 5\%$, depending on the particle species. Here, a constant, overall normalisation, uncertainty of 4% was used on the measured spectra.

When testing the default method A against an alternative method B, one can implement the deviation of the ratio of their measured values $\Delta = B/A$ from unity as an uncertainty. To ensure that this difference is statistically significant and not just an effect of a limited data sample, the deviation is considered only if it exceeds its own uncertainty, defined as

$$\sigma_{\Delta} = \frac{\sqrt{|\sigma_B^2 - \sigma_A^2|}}{A} \quad , \tag{5.26}$$

where σ_A and σ_B are the uncertainties of the results from methods A and B, respectively. This procedure is based on the discussion in Ref. [151].

5.7.1 Variation of selection criteria

To investigate the differences between description of variables in measured data and ALICE simulations, and determine sensible cut variations λ_i, raw yield loss F was studied. It was measured in MB events and defined as

$$F(\lambda) = 1 - \frac{Y(\lambda)}{Y(\lambda_{\mathrm{LOOSEST}})} \quad , \tag{5.27}$$

where $Y(\lambda)$ is the raw yield as a function of the cut value λ and $\lambda_{\mathrm{LOOSEST}}$ the loosest variation (corresponding to the highest yield).

For most observables, the systematic effect can be estimated from alternative methods using $\lambda_{\mathrm{LOOSEST}}$ and $\lambda_{\mathrm{TIGHTEST}}$. To ensure the stability and possible non-linearity, less strict λ_{LOOSE} and λ_{TIGHT} are also tested. If applicable, it is reasonable to choose the strictest λ_i such that $F(\lambda_i)$ does not exceed approximately 10%.

The $F(\lambda)$ for the different selection critera, and with the chosen λ_i are studied and shown in Fig. 5.10, Fig. 5.11, and Fig. 5.12 for $\mathrm{K}^0_{\mathrm{S}}$, Λ, and $\overline{\Lambda}$, respectively. The pile-up rejection cut, which requires "fast detector" information for at least one daughter is of a binary nature. Therefore, its variation was tested by requiring a different amount of fast detector signals shared between the two daughters. The values of λ_i, selected based on this raw yield loss study, are summarised in Tab. 5.2.

Following the approach described above, measurements with a cut parameter λ_i, and corrected with a reconstruction efficiency also using λ_i, are considered as the alternative method B. Similarly, measurements with the default cut value and reconstruction efficiency are considered as the default method A. The systematic uncertainty is then calculated as the deviation of Δ from unity, if statistically significant according to Eq. (5.26).

Table 5.2: Cut variation parameters λ_i for the $\mathrm{K}^0_{\mathrm{S}}$ (Λ and $\overline{\Lambda}$). Dashes represent that given cut variation is not applicable and a less strict value is used instead.

Variation λ_i	loosest	loose	default	tight	tightest
Quality					
radius (cm)	0.3	0.4	0.5	0.6	0.7
$\mathrm{DCA}_{\mathrm{d-d}}$ (cm)	1.5	1.25	1.0	0.75	0.5
cos PA	0.95 (0.993)	0.96 (0.994)	0.97 (0.995)	0.98 (0.996)	0.99 (0.997)
fast detector signals	-	-	1	2	-
comp. mass of $n\sigma$	2.5	3.0	4.0	5.0	5.5
lifetime (cm)	-	(35.0)	(30.0)	(25.0)	-
TPC PID $n\sigma^{\mathrm{TPC}}$	6.5	6.0	5.0	4.0	3.5
$\mathrm{DCA}_{\mathrm{PV-d+}}$ (cm)	0.05	0.055	0.06	0.07	0.08
$\mathrm{DCA}_{\mathrm{PV-d-}}$ (cm)	0.05	0.055	0.06	0.07	0.08
TPC crossed rows	-	-	70	75	80
TPC find. ratio	-	-	0.8	0.95	-

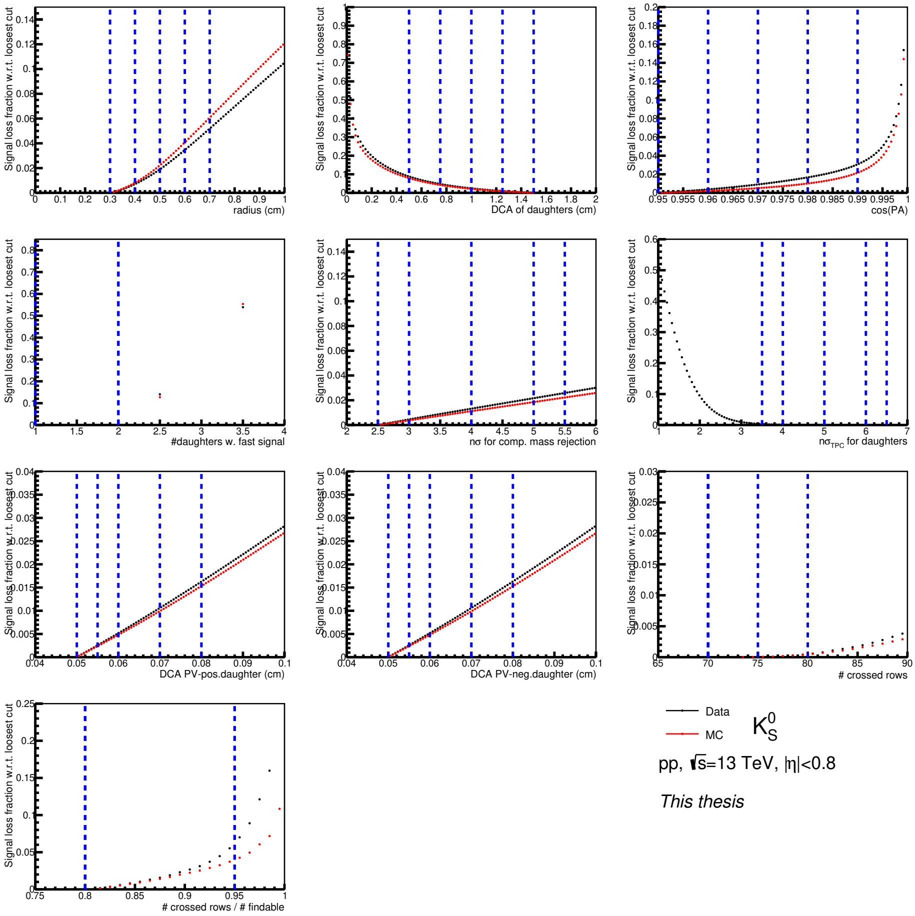

Figure 5.10: Study of the K^0_S raw signal loss due to individual cuts, shown as a function of the chosen cut value, comparing data (black) and simulations (red). Blue dashed lines represent the selected λ_i.

5.7.2 Feeddown correction uncertainty

As mentioned before, first, the Ξ yields, from which the feeddown is calculated, are varied within the extrapolation uncertainties of using the Lévy-Tsallis fit. Second, similarly to $\epsilon(p_\mathrm{T})$, the assumption of no multiplicity dependence of the feeddown matrix is accompanied by a constant uncertainty of 2% on the secondary yields (corresponding to roughly 0.6% uncertainty on the primary yields).

Lastly, an alternative method of estimating the feeddown just from charged Ξ baryons, and multiplying by a factor of two, was also tested and contributes a systematic uncertainty. It is considered statistically significant and applied only when $|\Delta - 1| > \sigma_\Delta$, following Eq. (5.26). It should be noted that whilst the secondary yields suffer from

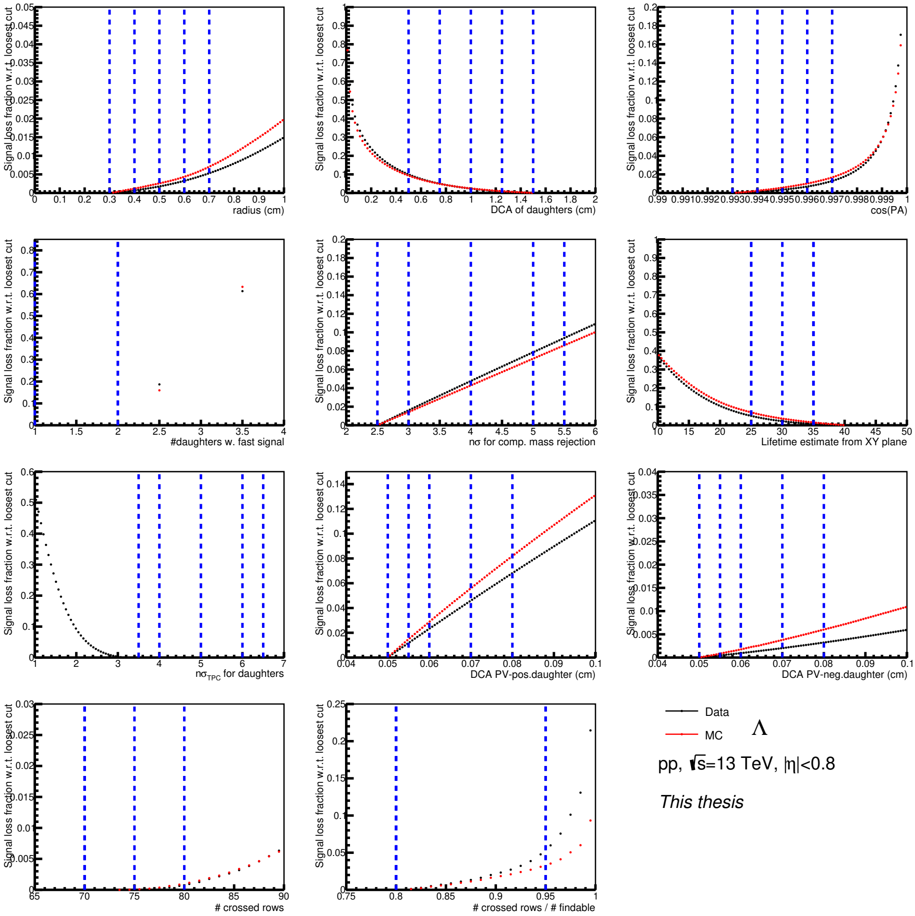

Figure 5.11: Study of the Λ raw signal loss due to individual cuts, shown as a function of the chosen cut value, comparing data (black) and simulations (red). Blue dashed lines represent the selected λ_i.

a rather large systematic uncertainty (up to $\sim 7\%$), the effect on the primary spectra is significantly smaller, as the uncertainties enter as $\frac{1-B}{1-A}$ and the secondary yields do not exceed $\sim 30\%$.

5.7.3 Determination of uncorrelated uncertainties

When comparing the measurement of an observable in two different event types, a and b, it is important to avoid overestimating the uncertainties in the ratio, as one should not include correlated uncertainties between a and b, which need to be determined. For instance, in this dissertation, p_{T} spectra are measured in events with (a) and without a selection on transverse spherocity (b) and reported as ratio of the two.

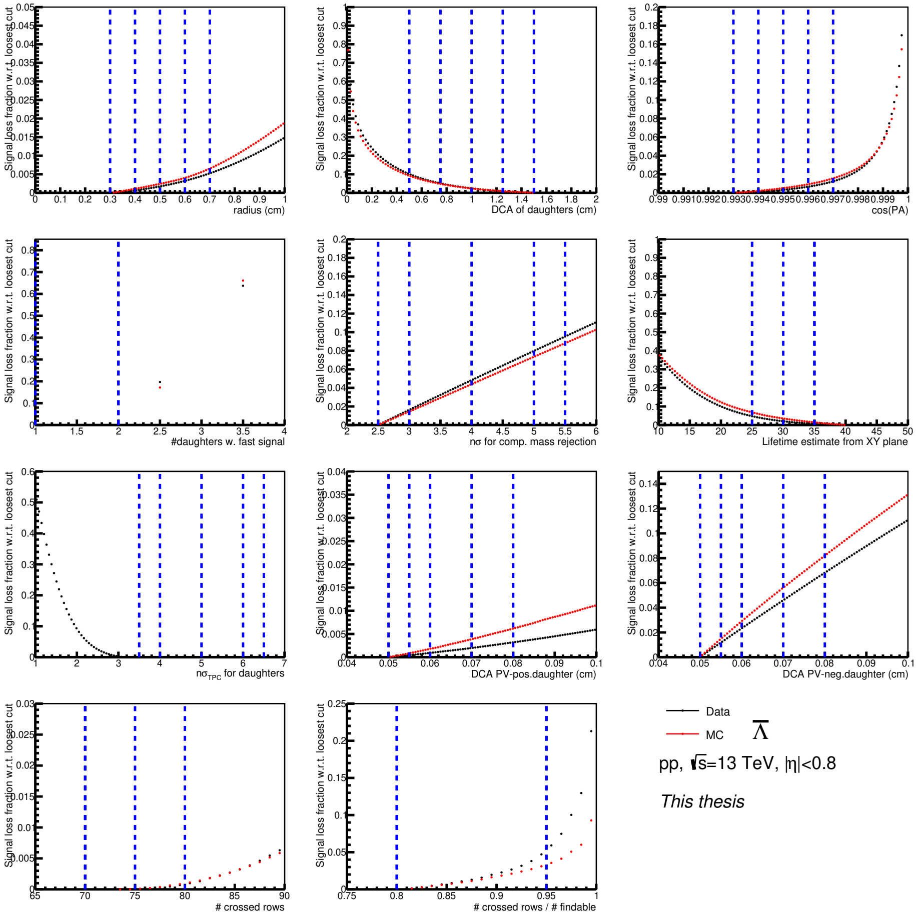

Figure 5.12: Study of the $\overline{\Lambda}$ raw signal loss due to individual cuts, shown as a function of the chosen cut value, comparing data (black) and simulations (red). Blue dashed lines represent the selected λ_i.

In this case, the aim is to identify which uncertainties are affected by the spherocity selection (uncorrelated) and which are correlated with it, and exclude them from the ratio result.

To calculate the uncorrelated uncertainties, one can consider the following double ratio ρ

$$\rho = \frac{\Delta_a}{\Delta_b} \quad , \tag{5.28}$$

where Δ_a and Δ_b are the ratios of the alternative to default methods in event types a and b, respectively. Similarly, the deviation is deemed statistically significant only if it exceeds its own uncertainty, which for this ratio is given as

$$\sigma_\rho = \frac{\sqrt{|\sigma^2_{\Delta,a} - \sigma^2_{\Delta,b}|}}{\Delta_b} \quad , \tag{5.29}$$

where $\sigma_{\Delta,a}$ and $\sigma_{\Delta,b}$ are the statistical uncertainties defined in Eq. (5.26) for event types a and b, respectively.

Chapter 6

Transverse spherocity

In this chapter, measurements of $\mathrm{K^0_S}$, Λ, and $\overline{\Lambda}$ transverse momentum spectra and yields are reported as a function of transverse spherocity $S_{\mathrm{O}}^{p_{\mathrm{T}}=1.0}$, a measure of the event's topology in the transverse $xy-$plane.

6.1 Transverse spherocity

6.1.1 Motivation for studying event topology

As explained in Sec. 2.3, there is overwhelming evidence that some phenomena associated with QGP, such as collective flow and strangeness enhancement, also arise in pp and pA collisions at LHC energies, particularly in events with high multiplicity. This challenges the conventional assumption that the hadron densities and densities of colour fields between partons are too low in these collisions to interact with each other and form a hydrodynamic medium. Consequently, high-multiplicity pp (and pA) collisions cannot be treated as superpositions of mostly independent parton-parton (or parton-hadron) scatterings and a more in-depth approach is required to fully understand these phenomena.

Event shape observables have been used historically in lepton-lepton scattering experiments to study fundamental QCD properties such as the gluon spin [152], and also at the Tevatron and the LHC in events with very high p_{T} ($\gtrsim$ 100 GeV/c) jets to further test pQCD predictions [153]. There are various observables, including the sphericity S_{T}, spherocity S_{O}, thrust T, F-parameter, and Ellis-Karliner angle, most of which are collinear- and infrared-safe and therefore moderately easily calculable [154]. An

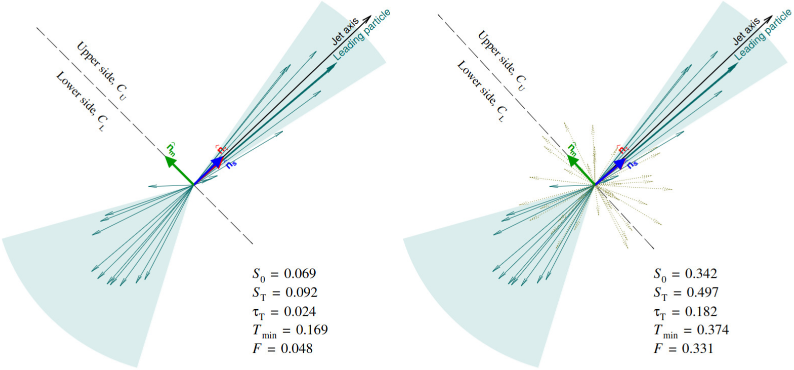

Figure 6.1: Visualisation of two events in the azimuthal plane: **(left)** more "jetty" and **(right)** more isotropic. Values for the transverse spherocity S_O are given as well as for some other event shape observables: sphericity, thrust, thrust-minor, and F-parameter. The vector minimising the S_O calculation is denoted as a blue arrow. [153]

illustration of two events with different topologies and calculated values of selected observables can be seen in Fig. 6.1.

With the discoveries of QGP-like phenomena in high-multiplicity collisions of small systems, event shape observables become attractive for different reasons. This is because pQCD ("hard") processes are responsible for a significant fraction of particle production and are likely to impact the character of QGP phenomena in non-trivial ways. Moreover, the role of non-perturbative ("soft") processes is particularly interesting to study as the underlying production mechanisms are not fully understood and their interpretation relies on phenomenological models that require clear experimental measurements with high discriminatory power.

Event shape observables allow events to be classified according to the dominant contributing processes and thus be studied in more detail. For instance, collisions with a single large p_T transfer scattering are likely to lead to events with two back-to-back, highly collimated showers, which create a pencil-like shape in the transverse plane. Conversely, collisions with multiple lower p_T transfer partonic interactions will exhibit a high degree of azimuthal isotropy. Therefore, event shape measurements help deliver a deeper understanding of events and a better control over the magnitudes of the hard and soft contributions. Ultimately, these measurements may help determine whether QGP formation is observed in small systems or uncover new physical behaviours.

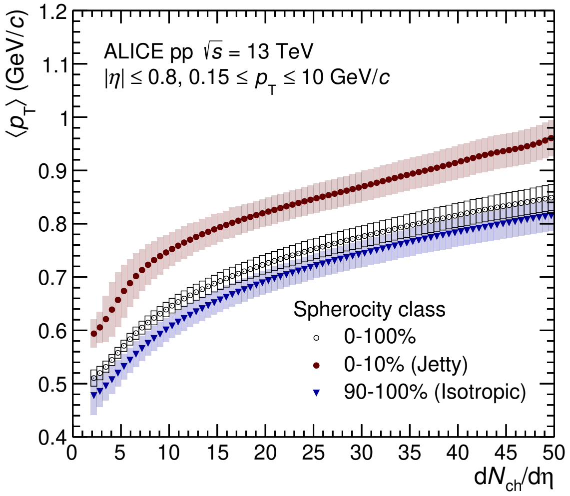

Figure 6.2: Dependence of the average transverse momentum of charged particles on the event multiplicity at mid-rapidity. Results for jetty, isotropic, and spherocity-unbiased events are displayed. Systematic uncertainties are indicated by the boxes and shaded areas. [155]

6.1.2 S_O and $S_O^{p_T=1.0}$ as experimental observables

Traditionally [154], transverse spherocity S_O is defined as:

$$S_O = \frac{\pi^2}{4} \min_{\hat{n}} \left(\frac{\sum_i |p_{T,i} \times \hat{n}|}{\sum_i |p_{T,i}|} \right)^2 \quad , \tag{6.1}$$

where $p_{T,i}$ represents the vector of transverse momentum of a particle i and $\hat{n}$ is the event-dependent unit vector that minimises the sum. The sum runs over all charged particles in the event within the detector acceptance.

Previous ALICE measurements [155] studied characteristics of charged particles produced in pp collisions and discovered the strong dependence of $\langle p_T \rangle$ on spherocity S_O, which agrees with the previously discussed motivation. This relationship is shown in Fig. 6.2 and shows that low-spherocity events have higher average p_T than high-spherocity events. Additionally, phenomenological studies of S_O in Pythia 8 further demonstrate its classifying power by finding a strong dependence of $\langle n_{MPI} \rangle$ as well as the mean number of reconstructed jets $\langle n_j \rangle$ on S_O [156, 157]. These results can be seen in Fig. 6.3.

This work uses a modified definition of this observable, *unweighted* transverse spherocity $S_O^{p_T=1.0}$, defined as follows:

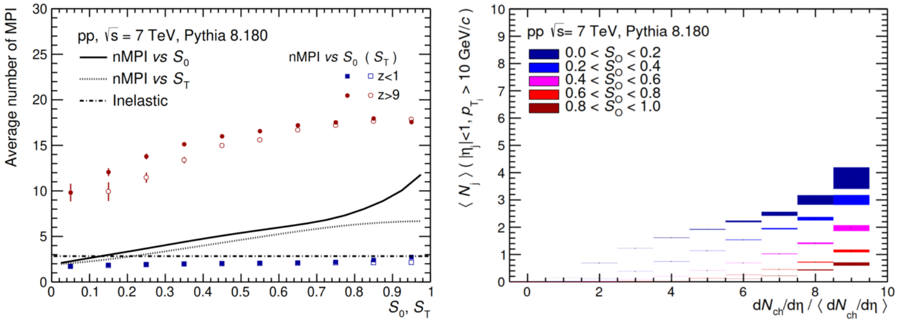

(a) (b)

Figure 6.3: **(a)** Correlation between the mean number of MPIs and transverse spherocity (and sphericity) in pp collisions at $\sqrt{s} = 7\,\text{TeV}$ predicted by Pythia 8, shown as solid and dotted lines. The horizontal line shows the average for minimum bias inelastic events. Events with high (red) and low (blue) self-normalised event multiplicity z are also studied and depicted as datapoints. [156] **(b)** Average number of reconstructed jets as a function of self-normalised event multiplicity in pp collisions at $\sqrt{s} = 7\,\text{TeV}$ with varying values of spherocity, as predicted by Pythia 8. [157]

$$S_{\mathrm{O}}^{p_{\mathrm{T}}=1.0} = \frac{\pi^2}{4} \min_{\hat{n}} \left(\frac{\sum_i |\hat{p}_{\mathrm{T},i} \times \hat{n}|}{N_{\mathrm{trks}}} \right)^2 , \tag{6.2}$$

where $\hat{p}_{\mathrm{T},i}$ represents the unit vector of transverse momentum of a particle i and N_{trks} the number of charged particles entering the sum.

In this thesis, unless stated otherwise, the terms transverse spherocity and spherocity are both used to refer to this unweighted transverse spherocity $S_{\mathrm{O}}^{p_{\mathrm{T}}=1.0}$.

Applying the spherocity $S_{\mathrm{O}}^{p_{\mathrm{T}}=1.0}$, events in two geometrical limits can be studied:

- $S_{\mathrm{O}}^{p_{\mathrm{T}}=1.0} \to 0$: the "**jetty**" limit, where a pencil-like topology is selected. These events are dominated by hard pQCD processes. In this limit, with perfectly collimated back-to-back particles, $\hat{n}$ aligns with them. Thus, the sum of vector products in Eq. 6.2 contains only zero values as $\sin 0 = \sin \pi = 0$.
- $S_{\mathrm{O}}^{p_{\mathrm{T}}=1.0} \to 1$: the "**isotropic**" limit, where a circular topology is selected. Such events are dominated by multiple softer non-perturbative processes[1]. In this limit of $N \to \infty$ uniformly distributed unit vectors within $(0, 2\pi)$, the

---

[1] However, it is important to mention that anisotropic collective flow such as v_2, a non-perturbative phenomenon, reduces the event isotropy.

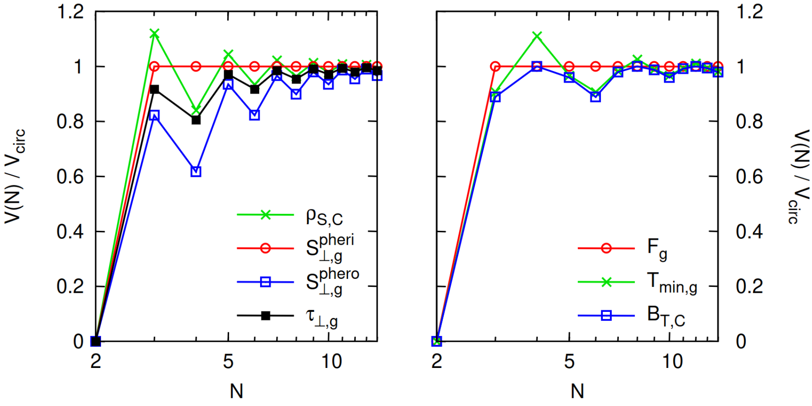

Figure 6.4: Graphs showing how rapidly the different event shape observables approach the circular limit $V_{\rm circ}$ corresponding to $N \rightarrow \infty$, based on the number of perfectly isotropically distributed particles N. Transverse spherocity, here denoted as $S_{\perp,g}^{\rm phero}$, exhibits the slowest rise, and never exceeds unity.[154]

choice of $\hat{n}$ becomes arbitrary and calculation of the sum in Eq. (6.2) leads to:

$$\frac{1}{N}\sum_{n=1}^{N}|\sin\frac{2\pi n}{N}| \approx \frac{1}{N}\int_0^N |\sin\frac{2\pi x}{N}|{\rm d}x \tag{6.3}$$

$$= \frac{2}{N}\int_0^{N/2}\sin\frac{2\pi x}{N}{\rm d}x = \frac{1}{\pi}\int_0^{\pi}\sin u{\rm d}u \tag{6.4}$$

$$= \frac{1}{\pi}\left[-\cos x\right]_0^{\pi} = \frac{2}{\pi} \tag{6.5}$$

and therefore $S_{\rm O}^{p_{\rm T}=1.0} = 1$.

Figure 6.4 illustrates how spherocity slowly approaches the circular limit value with increasing N compared to other event shape observables. This makes spherocity the most sensitive to the underlying physics in high-multiplicity isotropic events.

6.1.3 Relationship between $S_{\rm O}^{p_{\rm T}=1.0}$ and $S_{\rm O}$

In ALICE, only charged particles are considered when calculating spherocities. This introduces biases when measuring charged and neutral species of hadrons. For instance, even topologically identical events with dominant high-$p_{\rm T}$ leading π^{+} and π^{0} can yield significantly different values of the traditional $p_{\rm T}$-weighted spherocity $S_{\rm O}$, despite being comparable in all relevant aspects. In contrast, unweighted spherocity $S_{\rm O}^{p_{\rm T}=1.0}$ offers a more similar quantification of the two events, as shown in Fig. 6.5.

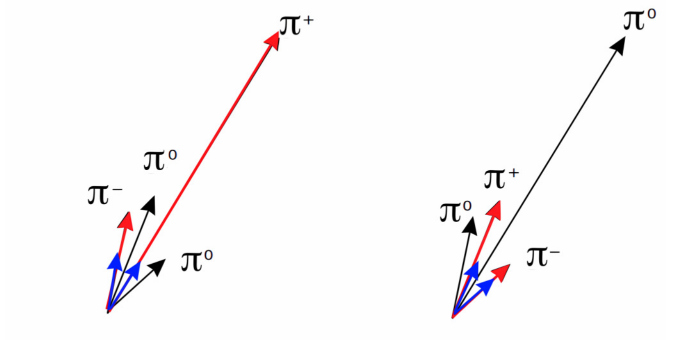

Figure 6.5: Illustration of two topologically identical events with swapped charged and neutral particles. Momentum vectors entering the p_{T}-weighted spherocity (red) and p_{T}-unweighted (blue) calculations are displayed, showing a larger difference between the two scenarios for the former than the latter. [158]

This modified definition thus describes the measured topology more accurately and makes it easier to compare with models. However, it should be noted that it is only applicable to events with many tracks (i.e., $N_{\mathrm{trks}} > 10$).

In addition, while not a large concern in high-multiplicity collisions [155], $S_{\mathrm{O}}^{p_{\mathrm{T}}=1.0}$ also offers improved resolution compared to S_{O}, as the failure to reconstruct a high-p_{T} track has a smaller impact. Overall, S_{O} and $S_{\mathrm{O}}^{p_{\mathrm{T}}=1.0}$ exhibit similar values and interpretations, with a strong correlation between the two, as illustrated in Fig. 6.6.

6.1.4 Track and event selection

The measurements are carried out on MB events with |`INEL>0`|, requiring at least one hit in the V0A or V0C scintillators and one charged particle reconstructed within $|\eta| < 1$. The primary vertex is reconstructed using hits in the SPD and is required to be within 10 cm of the nominal interaction point. The fast read-out time of the SPD allows rejection of out-of-bunch pile-up. In-bunch pile-up is further removed by excluding events with multiple reconstructed vertices. The presented results are based on high-multiplicity events, selected by the classifiers V0M (forward rapidity) and $N_{\mathrm{tracklets}}^{|\eta|<0.8}$ (mid-rapidity), and require a minimum of 10 reconstructed tracks within $|\eta| < 0.8$ and with $p_{\mathrm{T}} > 0.15\,\mathrm{GeV}/c$.

To ensure a high level of azimuthal acceptance uniformity, which is important for event shape measurements, the following, rather loose, track selection criteria are employed in the calculation of $S_{\mathrm{O}}^{p_{\mathrm{T}}=1.0}$:

1. The SPD layers are not used due to inactive sectors, at the expense of a lower momentum resolution.

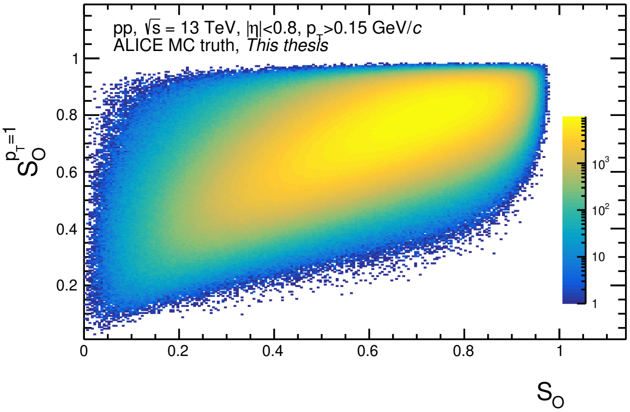

Figure 6.6: Two-dimensional histogram showing the correlation between the traditional transverse spherocity S_{O} and the unweighted transverse spherocity $S_{\mathrm{O}}^{p_{\mathrm{T}}=1.0}$ employed in this measurement, obtained from ALICE MC simulations.

2. A track is required to have at least 50 clusters in the TPC and be matched to clusters in the ITS to improve tracking precision and further reject pile-up.

3. DCA cuts are applied in both the longitudinal ($|\mathrm{DCA}_z| < 3.2$ cm) and transverse ($|\mathrm{DCA}_{xy}| < 2.4$ cm) planes to ensure that the reconstructed TPC track points to the primary vertex.

It should be noted that charged decay products of V^0s with small decay radii may enter and influence $S_{\mathrm{O}}^{p_{\mathrm{T}}=1.0}$ determination. At low p_{T} of the V^0, the momentum vectors of the daughters and the mother may be too different. This causes a bias for measurements of V^0 spectra below $p_{\mathrm{T}} \lesssim 1$ GeV/c, thus, they are excluded.

6.1.5 Multiplicity selection and its interplay with $S_{\mathrm{O}}^{p_{\mathrm{T}}=1.0}$

Spherocity exhibits a twofold correlation with multiplicity that is not particularly informative. First, the definition of $S_{\mathrm{O}}^{p_{\mathrm{T}}=1.0}$ results in higher values for events with more particles that are uniformly distributed, as shown in Fig. 6.4. Second, in models such as Pythia, high multiplicity is often associated with more MPI, which tend to lead to higher isotropy due to the increased number of emission sources. To gain a more nuanced understanding of the relationship between spherocity and multiplicity, the effect of $S_{\mathrm{O}}^{p_{\mathrm{T}}=1.0}$ on measured particles was analysed in high-multiplicity events determined in two distinct rapidity regions, as described above. Specifically, the top 1% (10%) quantiles are used, denoted as V0M I and $N_{\mathrm{tracklets}}^{|\eta|<0.8}$ I (V0M I-III and $N_{\mathrm{tracklets}}^{|\eta|<0.8}$ I-III).

Figure 6.7 shows the effect of $S_{\mathrm{O}}^{p_{\mathrm{T}}=1.0}$ on the pion yields and $\langle p_{\mathrm{T}} \rangle$. Pions are measured in the high-multiplicity events and in top and bottom 10% and 1% quantiles of $S_{\mathrm{O}}^{p_{\mathrm{T}}=1.0}$. The result reveals that when measuring multiplicity in forward rapidity (V0M I), the effect of $S_{\mathrm{O}}^{p_{\mathrm{T}}=1.0}$ causes a change of approximately 100% in the yields when going from jetty to isotropic limits, whereas the difference in $\langle p_{\mathrm{T}} \rangle$ is only about 10%. Conversely, when determining the multiplicity in mid-rapidity ($N_{\mathrm{tracklets}}^{|\eta|<0.8}$ I), the same region where the pion spectra are reconstructed, the change in the yields is only approximately 10% while the change in $\langle p_{\mathrm{T}} \rangle$ is approximately 25%.

For this reason, the following combinations of multiplicity and $S_{\mathrm{O}}^{p_{\mathrm{T}}=1.0}$ selections are presented:

1. $N_{\mathrm{tracklets}}^{|\eta|<0.8}$ I and $S_{\mathrm{O}}^{p_{\mathrm{T}}=1.0}$ top and bottom 10% quantiles: This selection emphasises the impact of extreme event topologies on the QCD processes whilst minimising the effect of multiplicity dependence.
2. $N_{\mathrm{tracklets}}^{|\eta|<0.8}$ I-III and $S_{\mathrm{O}}^{p_{\mathrm{T}}=1.0}$ top and bottom 1% quantiles: This selection shows the effect of even more extreme event topologies but with overall less and somewhat varying multiplicity.
3. V0M I and $S_{\mathrm{O}}^{p_{\mathrm{T}}=1.0}$ top and bottom 10% quantiles: This selection highlights the effect of extreme event topologies with highly varying mid-rapidity multiplicity. It also allows for a comparison with $N_{\mathrm{tracklets}}^{|\eta|<0.8}$ I-III and $S_{\mathrm{O}}^{p_{\mathrm{T}}=1.0}$ 1% selection, as the mid-rapidity multiplicity and the $\langle p_{\mathrm{T}} \rangle$ variations are more similar.

The measured $S_{\mathrm{O}}^{p_{\mathrm{T}}=1.0}$ distributions in $N_{\mathrm{tracklets}}^{|\eta|<0.8}$ I, $N_{\mathrm{tracklets}}^{|\eta|<0.8}$ I-III, and V0M I-III are shown in Fig. 6.8. They are treated with Bayesian unfolding to account for reconstruction effects [159, 160]. They are also compared with theoretical predictions from Pythia 8 (Monash [110] and Ropes [116] tunes), EPOS LHC [120], and Herwig 7 [107]. Table 6.1 provides the $S_{\mathrm{O}}^{p_{\mathrm{T}}=1.0}$ cut values associated with the quantile selections in data.

6.1.6 Comparison of V^0 production with MC generators

Further on in this chapter, the spectra of $\mathrm{K}_{\mathrm{S}}^0$, Λ, and $\overline{\Lambda}$ as a function of $S_{\mathrm{O}}^{p_{\mathrm{T}}=1.0}$ are presented and compared with predictions from the phenomenological MC models Pythia 8 [29], EPOS LHC [120], and Herwig 7 [107]. To mitigate the effect of reconstruction on the experimental results and make the comparison with these predictions as comparable as possible, the following strategies were employed based on findings using the ALICE MC simulations:

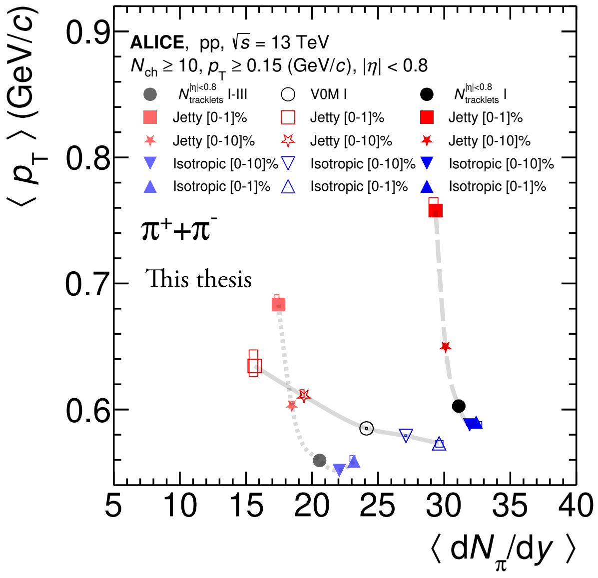

Figure 6.7: Relationship between the mean transverse momentum of charged pions and their yields in events with different $S_{\rm O}^{p_{\rm T}=1.0}$ values and event multiplicity determined at mid-rapidity ($N_{\rm tracklets}^{|\eta|<0.8}$) and forward rapidity (VOM). Events in the same multiplicity classes are connected with lines for clarity's sake. Plot co-produced with co-authors O. Vazquez and R. Rath.

Table 6.1: Cut values of the different quantiles of the uncorrected $S_{\rm O}^{p_{\rm T}=1.0}$ distribution used for the event selections in this analysis.

Event class	$N_{\rm tracklets}^{|\eta|<0.8}$ I	$N_{\rm tracklets}^{|\eta|<0.8}$ I-III	V0M I
Jetty			
$S_{\rm O}^{p_{\rm T}=1.0}$ 0–1%	< 0.487	< 0.408	< 0.433
$S_{\rm O}^{p_{\rm T}=1.0}$ 0–10%	< 0.624	< 0.561	< 0.589
Isotropic			
$S_{\rm O}^{p_{\rm T}=1.0}$ 90–100%	> 0.892	> 0.871	> 0.882
$S_{\rm O}^{p_{\rm T}=1.0}$ 99–100%	> 0.942	> 0.930	> 0.936

- The results were compared using the same quantiles of the $S_{\rm O}^{p_{\rm T}=1.0}$ distributions in both the MC and the data, instead of relying on the experimental $S_{\rm O}^{p_{\rm T}=1.0}$ ranges determined by the absolute cut values. This approach reduced the effects of $S_{\rm O}^{p_{\rm T}=1.0}$ resolution.

- In the MC simulations, the $S_{\rm O}^{p_{\rm T}=1.0}$ calculations included neutral particles $\rm K_S^0$, Λ, and $\overline{\Lambda}$, despite their neutral charge. This helped minimize differences between the true and reconstructed/corrected MC results, due to the potential contribution of charged daughters to the $S_{\rm O}^{p_{\rm T}=1.0}$ calculation.

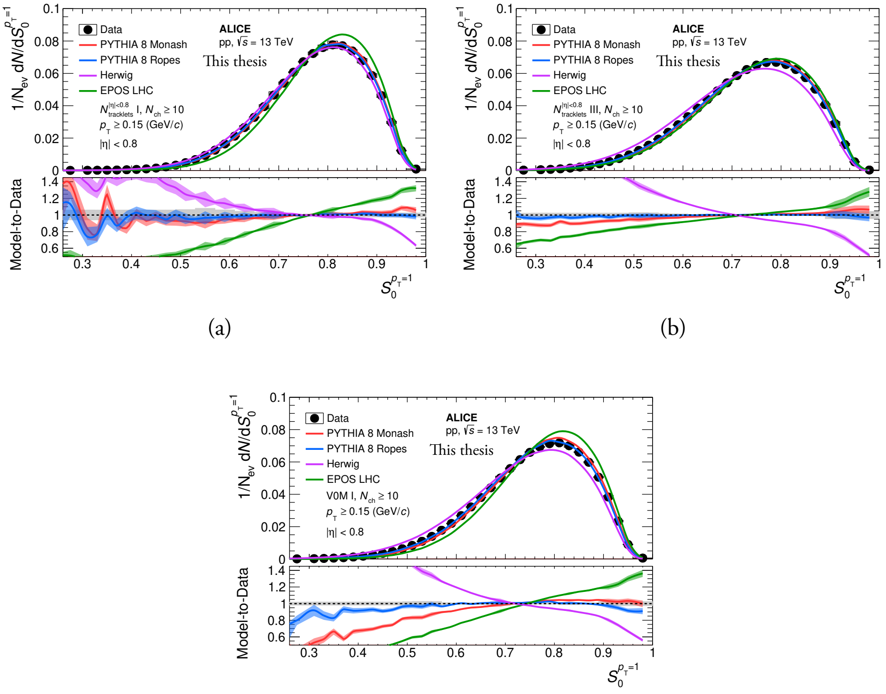

(a)

(b)

(c)

Figure 6.8: The measured and fully corrected $S_{\mathrm{O}}^{p_{\mathrm{T}}=1.0}$ distributions for both **(a)** $N_{\mathrm{tracklets}}^{|\eta|<0.8}$ 0–1%, **(b)** 0–10% and **(c)** V0M 0–1% . The curves represent different model prediction, where the shaded area represents the statistical uncertainty of the models. Plots co-produced with co-author O. Vazquez.

Any discrepancies that still persisted between the true and reconstructed/corrected transverse momentum spectra were accounted for as systematic uncertainties.

6.2 Systematic uncertainties

The systematic uncertainties associated with the p_{T} spectra of $\mathrm{K_S^0}$, Λ, and $\overline{\Lambda}$ were evaluated separately for $N_{\mathrm{tracklets}}^{|\eta|<0.8}$ I and V0M I events with no $S_{\mathrm{O}}^{p_{\mathrm{T}}=1.0}$ selection, as well as for the top and bottom 10% isotropic and jetty quantiles, using the methodology described in Sec. 5.7. The relative systematic uncertainties obtained from these configurations were also applied to the $N_{\mathrm{tracklets}}^{|\eta|<0.8}$ I-III and V0M I-III event classes with different jetty/isotropic quantiles.

Figure 6.9 illustrates an example of the cut variations and the resulting maximal deviations.

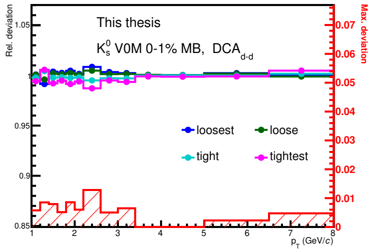

(a)

(b)

Figure 6.9: Variations on the corrected transverse momentum spectra due to using different cut values, relative to the default method. Here, the $\mathrm{DCA}_{\mathrm{d-d}}$ cut is presented for **(a)** $\mathrm{K^0_S}$ in spherocity-unbiased (denoted as MB) $\mathrm{V0M}$ I events and **(b)** $\overline{\Lambda}$ in isotropic $\mathrm{V0M}$ I events.

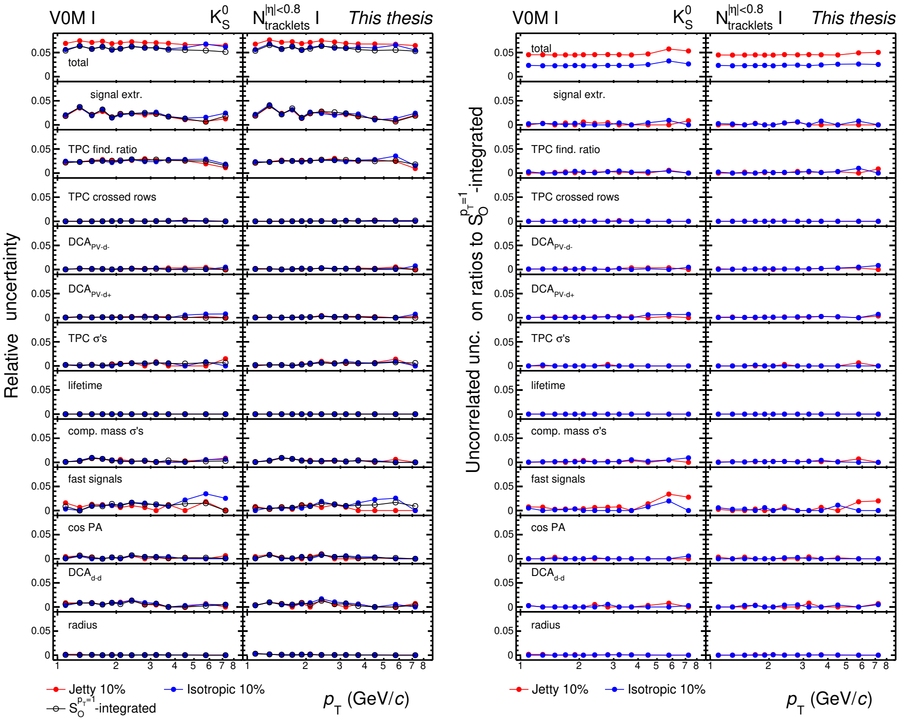

(a)

(b)

Figure 6.10: **(a)** Summary of the relative systematic uncertainties on transverse momentum spectra and the individual contributions for $\mathrm{K^0_S}$ in the $\mathrm{V0M}$ I (left) and $N^{|\eta|<0.8}_{\mathrm{tracklets}}$ I (right) event class for the different spherocity selections. Here, the total uncertainty also includes the experimental bias (see text for details). **(b)** Uncorrelated components of the systematic uncertainties on the ratio of spherocity-biased spectra to those with no spherocity selection.

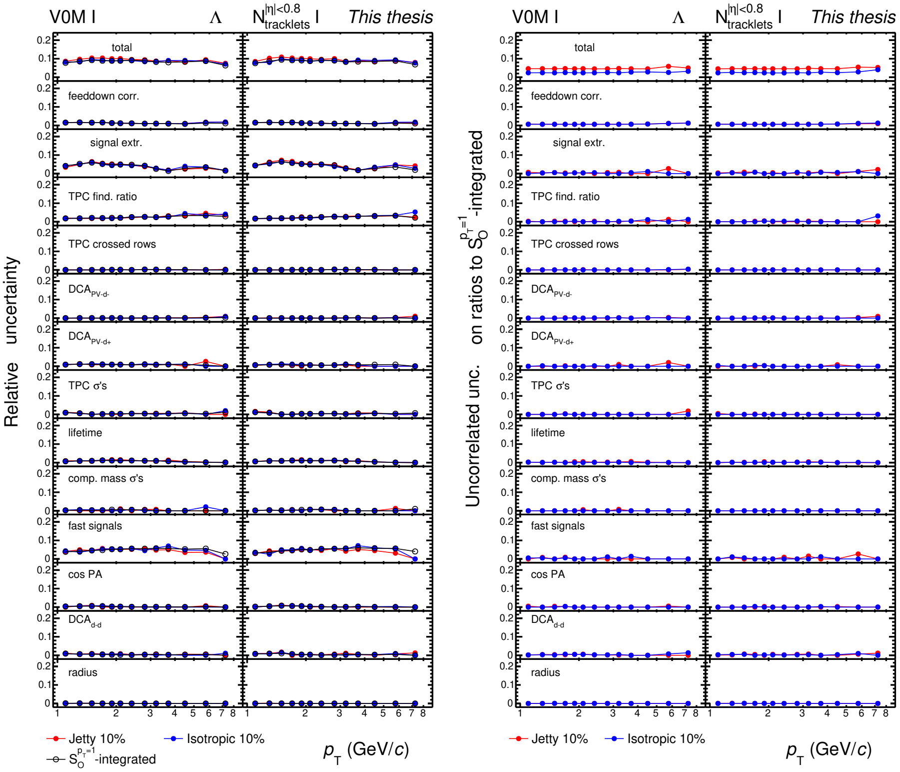

(a) (b)

Figure 6.11: **(a)** Summary of the relative systematic uncertainties on transverse momentum spectra and the individual contributions for Λ in the $\mathrm{V0M}$ I (left) and $N_{\text{tracklets}}^{|\eta|<0.8}$ I (right) event class for the different spherocity selections. Here, the total uncertainty also includes the experimental bias (see text for details). **(b)** Uncorrelated components of the systematic uncertainties on the ratio of spherocity-biased spectra to those with no spherocity selection.

6.2.1 Experimental bias

To estimate the experimental bias of the $S_{\text{O}}^{p_{\text{T}}=1.0}$ selection, Monte Carlo closure tests were used, studying the ratios of true p_{T} spectra in jetty/isotropic quantiles of the true $S_{\text{O}}^{p_{\text{T}}=1.0}$ distribution to the measured and corrected p_{T} spectra in quantiles of the measured $S_{\text{O}}^{p_{\text{T}}=1.0}$ distribution.

Due to the loose DCA cuts used in the $S_{\text{O}}^{p_{\text{T}}=1.0}$ determination, it is expected that the V^0 daughters may enter its calculation. Thus, to make the predictions from simulations more comparable to the data, the K_{S}^0, Λ, and $\overline{\Lambda}$ particles were included in the true $S_{\text{O}}^{p_{\text{T}}=1.0}$ calculation. Although insufficient below $p_{\text{T}} < 1$ GeV/c, this works well

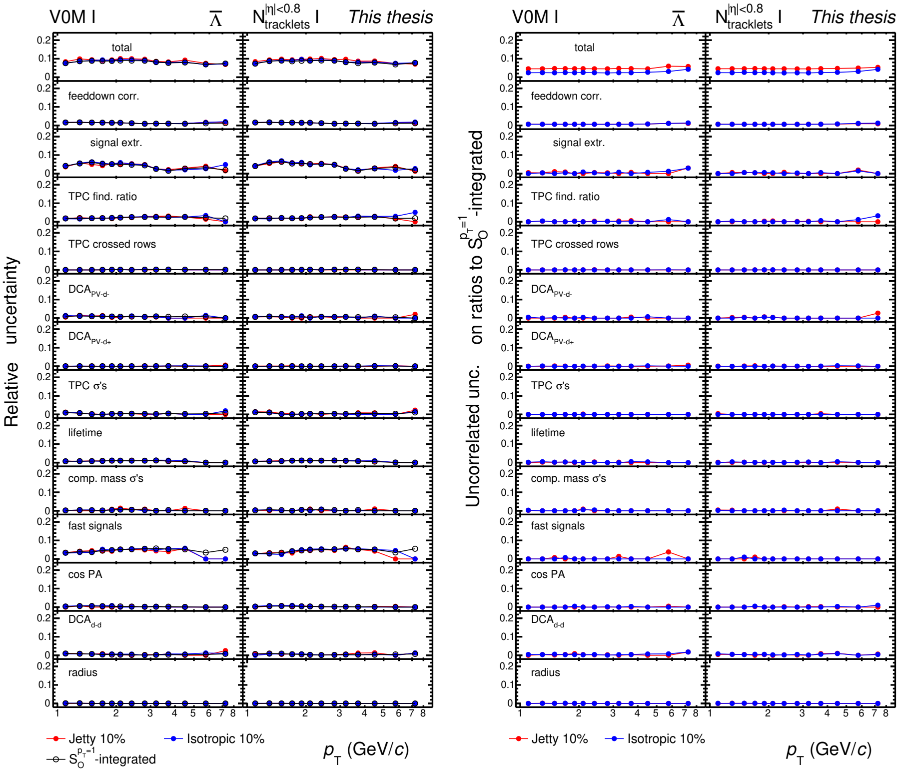

(a)

(b)

Figure 6.12: **(a)** Summary of the relative systematic uncertainties on transverse momentum spectra and the individual contributions for $\overline{\Lambda}$ in the $\mathrm{V0M}$ I (left) and $N_{\mathrm{tracklets}}^{|\eta|<0.8}$ I (right) event class for the different spherocity selections. Here, the total uncertainty also includes the experimental bias (see text for details). **(b)** Uncorrelated components of the systematic uncertainties on the ratio of spherocity-biased spectra to those with no spherocity selection.

and corresponds to 1% and 4% discrepancies for isotropic and jetty events, respectively [158].

Alternatively, as discussed further in this dissertation in the R_T measurements in Chapter 7, but not employed here, this effect could be accounted for experimentally, by making the two track sets (spherocity and V^0 daughters) explicitly disjunct by enforcing a DCA cut.

6.2.2 Correlation of uncertainties with $S_{\mathrm{O}}^{p_{\mathrm{T}}=1.0}$

Correlations of several systematic uncertainties with respect to the $S_{\mathrm{O}}^{p_{\mathrm{T}}=1.0}$ selection are expected. Since the ratios of jetty/isotropic results to $S_{\mathrm{O}}^{p_{\mathrm{T}}=1.0}$-unbiased ones provide important insights, it is necessary to account for these correlations in order to not overestimate the uncertainties, following the methodology described in Sec. 5.7.3.

The systematic uncertainty associated with the material budget is treated as fully correlated between $S_{\mathrm{O}}^{p_{\mathrm{T}}=1.0}$-biased and unbiased events, and assuming the reconstruction efficiency is independent of multiplicity leads to an uncorrelated uncertainty. The latter assumption would normally lead to a factor of $\sqrt{2}$ in the ratios of jetty/isotropic to $S_{\mathrm{O}}^{p_{\mathrm{T}}=1.0}$-unbiased for this uncertainty. However, in ALICE, this assumption is generally considered too conservative [146], and thus this factor is omitted. The same approach is used for the uncertainty associated with the multiplicity independence of the feeddown matrix.

6.2.3 Summary

The systematic uncertainties of $\mathrm{K}_{\mathrm{S}}^{0}$, Λ, and $\overline{\Lambda}$, as well as their uncorrelated components for the ratios, are reported in Fig. 6.10, Fig. 6.11, and Fig. 6.12, respectively. Furthermore, the p_{T}-independent normalisation uncertainties (material budget and MB reconstruction efficiency) are also added, and together summarised in Tab. 6.2 for the V0M I case. The dominant contributions are, in no specific order, track quality cuts, experimental bias, signal extraction, and the enforcement of signals from fast detectors to prevent track pile-up.

6.3 Transverse momentum spectra vs. $S_{\mathrm{O}}^{p_{\mathrm{T}}=1.0}$

The corrected spectra in V0M and $N_{\mathrm{tracklets}}^{|\eta|<0.8}$ high-multiplicity events and the dependence on spherocity for the $\mathrm{K}_{\mathrm{S}}^{0}$ and $\Lambda + \overline{\Lambda}$ can be seen in Fig. 6.13 and Fig. 6.14, respectively. The trends observed in the spectra are consistent between $\mathrm{K}_{\mathrm{S}}^{0}$ and Λ and indicate a significant hardening (softening) in the low (high) spherocity selection, relative to the inclusive high-multiplicity event class. These trends are qualitatively generally well captured by the included model predictions, favouring Pythia 8 Ropes. Particularly, Pythia 8 Monash fails in describing the Λ p_{T} spectra.

The separation between jetty and isotropic events is more pronounced in the $N_{\mathrm{tracklets}}^{|\eta|<0.8}$ high-multiplicity events, and shows a significant difference in the spectra slopes. The

Table 6.2: The most relevant systematic uncertainties for the long-lived particles $\mathrm{K^0_S}$ and Λ ($\overline{\Lambda}$) as a function of $S_{\mathrm{O}}^{p_{\mathrm{T}}=1.0}$. "HM" in this table represents the high-multiplicity $\mathrm{V0M}$ I, $S_{\mathrm{O}}^{p_{\mathrm{T}}=1.0}$-unbiased spectra. Uncertainties are p_{T}-dependent, and the ranges listed represents the minimum-maximum values presented in the final spectra (see text for details).

Topology:	Jetty	Iso	HM	Jetty/HM	Iso/HM
$\mathrm{K^0_S}$					
Selection cuts	3%	3–4%	3–4%	Negl.	1%
Track pile–up	1%	1–3%	1%	0–2%	0–2%
Signal extraction	1–3%	1–3%	1–3%	Negl.	Negl.
Efficiency	2%	2%	2%	2%	2%
Material budget	4%	4%	4%	–	–
Experimental bias	4%	1%	–	4%	1%
Total uncertainty	7%	6–7%	5–6%	5%	2–3%
$\Lambda(\overline{\Lambda})$					
Selection cuts	1–5%	2–6%	4–5%	0–1%	0–3%
Track pile–up	4–5%	5%	3–5%	0–1.5%	0–1%
Signal extraction	2–6%	2–6%	2–6%	0–2%	0–1%
Feed-down correction	1.0–1.5%	1.0–1.5%	1.0–1.5%	Negl.	Negl.
Efficiency	2%	2%	2%	2%	2%
Material budget	4%	4%	4%	–	–
Experimental bias	4%	1%	–	4%	1%
Total uncertainty	8–10%	8–9%	7–9%	5%	3–4%

V0M events exhibit a much weaker difference in the slopes and rather show a more general offset.

6.3.1 Ratios of neutral kaons to charged kaons

To verify the robustness of $S_{\mathrm{O}}^{p_{\mathrm{T}}=1.0}$ as an event observable, the p_{T} spectra of neutral and charged kaons are compared in the $N_{\mathrm{tracklets}}^{|\eta|<0.8}$ I and V0M I classes. The ratios exhibit no dependence on $S_{\mathrm{O}}^{p_{\mathrm{T}}=1.0}$ and are consistent with unity, according to expectations. The slight depletion of $\mathrm{K^0_S}$ in the $N_{\mathrm{tracklets}}^{|\eta|<0.8}$ I class is interpreted as the multiplicity selection bias due to requiring a large number of charged tracks at midrapidity, and is also reproducible by simulations. The ratios are shown in Fig. 6.15.

6.4 Mean transverse momenta and integrated yields

The $\langle p_{\mathrm{T}}\rangle$ and particle yields $\langle \mathrm{d}N/\mathrm{d}y\rangle$ in different $S_{\mathrm{O}}^{p_{\mathrm{T}}=1.0}$ bins for the $N_{\mathrm{tracklets}}^{|\eta|<0.8}$ I class are reported in Fig. 6.16 and Fig. 6.17, respectively. The measured values of $\langle p_{\mathrm{T}}\rangle$ quantify the observations in the spectra: there is a significant p_{T}-hardening in jet-like events, consistently seen in both $\mathrm{K^0_S}$ and Λ. Furthermore, the $\langle p_{\mathrm{T}}\rangle$ of the

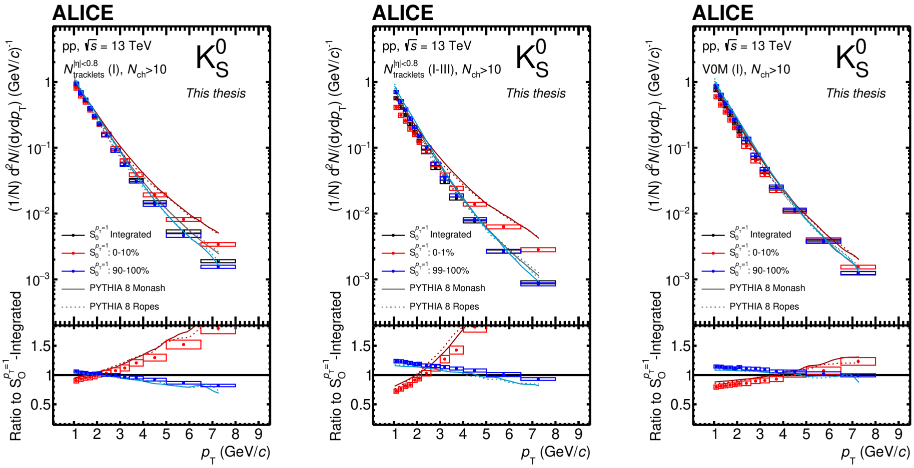

(a) (b) (c)

Figure 6.13: Transverse momentum spectra of K^0_S in high-multiplicity jetty (red) and isotropic (blue) events of pp collisions at $\sqrt{s} = 13$ TeV measured in the **(a)** $N_{\mathrm{tracklets}}^{|\eta|<0.8}$ I, **(b)** $N_{\mathrm{tracklets}}^{|\eta|<0.8}$ I-III, and **(c)** $\mathrm{V0M}$ I event classes. The bottom panels display ratios to the $S_\mathrm{O}^{p\mathrm{T}=1.0}$-unbiased spectra. Statistical and systematic uncertainties are indicated with error bars and boxes, respectively.

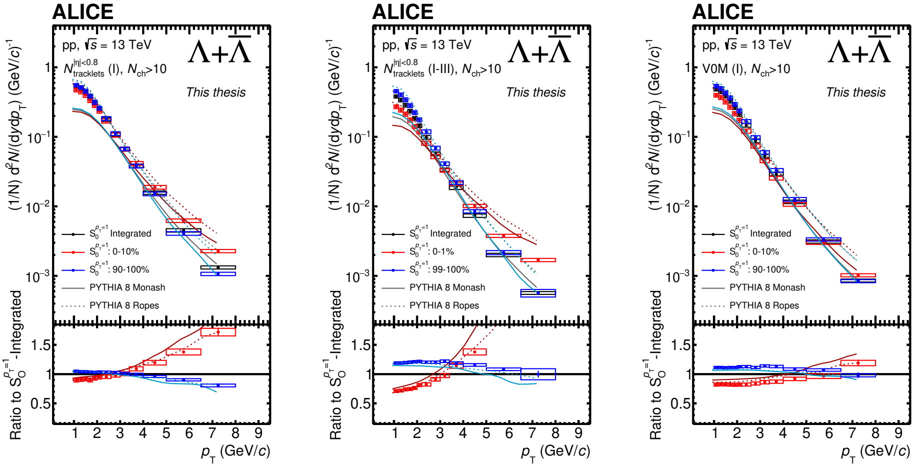

(a) (b) (c)

Figure 6.14: Transverse momentum spectra of Λ +$\overline{\Lambda}$ in high-multiplicity jetty (red) and isotropic (blue) events of pp collisions at $\sqrt{s} = 13$ TeV measured in the **(a)** $N_{\mathrm{tracklets}}^{|\eta|<0.8}$ I, **(b)** $N_{\mathrm{tracklets}}^{|\eta|<0.8}$ I-III, and **(c)** $\mathrm{V0M}$ I event classes. The bottom panels display ratios to the $S_\mathrm{O}^{p\mathrm{T}=1.0}$-unbiased spectra. Statistical and systematic uncertainties are indicated with error bars and boxes, respectively.

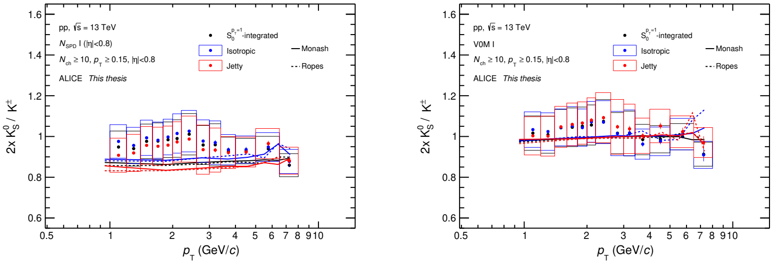

(a) (b)

Figure 6.15: Ratios of transverse momentum spectra of $\mathrm{K^0_S}$ to $K^{\pm}$ in **(a)** $N^{|\eta|<0.8}_{\mathrm{tracklets}}$ I and **(b)** $\mathrm{V0M}$ I high-multiplicity events, also showing the effect of spherocity selection. The results are compared with MC predictions of Pythia 8 tunes.

inclusive high-multiplicity events is consistent with that of the isotropic subsample. This result suggests that the average high-multiplicity events and $S_{\mathrm{O}}^{p_{\mathrm{T}}=1.0}$-selected isotropic events are dominated by similar underlying physics processes.

Furthermore, the $S_{\mathrm{O}}^{p_{\mathrm{T}}=1.0}$-integrated event class is not simply the arithmetic average of the jetty and isotropic subsamples. This implies that jetty events are rare outliers of a much more homogeneous group of high-multiplicity events, which will be further focused on in the next sections.

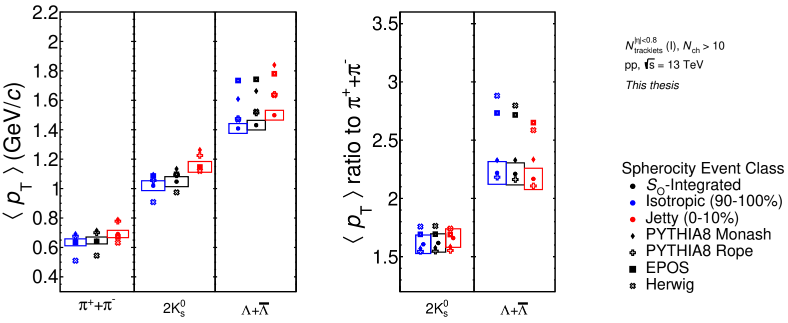

Figure 6.16: Mean transverse momentum of $\pi^{+}+\pi^{-}$, $\mathrm{K^0_S}$, and $\Lambda+\overline{\Lambda}$ in jetty, isotropic, and $S_{\mathrm{O}}^{p_{\mathrm{T}}=1.0}$-unbiased high-multiplicity events determined at mid-rapidity, and the ratios of $\mathrm{K^0_S}$ and $\Lambda+\overline{\Lambda}$ to pions.

The results indicate that not only charged pions but also neutral $\mathrm{K^0_S}$ and Λ show little variation in multiplicity between the different $S_{\mathrm{O}}^{p_{\mathrm{T}}=1.0}$ extremes in the $N^{|\eta|<0.8}_{\mathrm{tracklets}}$ I class, although more so for the latter two. This could be because of their smaller correlation with $S_{\mathrm{O}}^{p_{\mathrm{T}}=1.0}$ as they are neutral, or it may suggest strangeness enhancement. The models generally provide good agreement with the measured $\langle p_{\mathrm{T}} \rangle$ of $\mathrm{K^0_S}$, while the results for Λ are best described by the Pythia Ropes model. The yields for $\mathrm{K^0_S}$ are

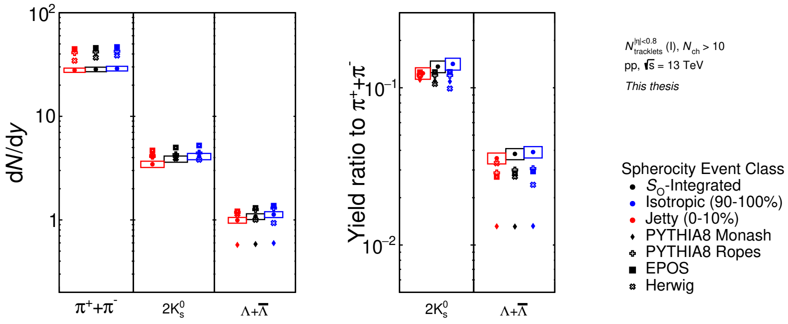

Figure 6.17: Integrated yields of $\pi^+ + \pi^-$, $\mathrm{K^0_S}$, and $\Lambda + \overline{\Lambda}$ in jetty, isotropic, and $S_{\mathrm{O}}^{p_{\mathrm{T}}=1.0}$-unbiased high-multiplicity events determined at mid-rapidity, and the ratios of $\mathrm{K^0_S}$ and $\Lambda + \overline{\Lambda}$ to pions.

also largely consistent with the models presented, whereas the Pythia Monash model does not match the Λ yields.

6.5 Ratios to pions

Rather than focusing on the models' inability to match the absolute yields, this measurement can provide an opportunity to study the underlying dynamics that affect the heavier and stranger particles. To achieve this, the $\mathrm{K^0_S}$ and $\Lambda + \overline{\Lambda}$ p_{T} spectra are divided by the $\pi^+ + \pi^-$ spectra. The results are presented in Fig. 6.18 and Fig. 6.19.

The data reveals overall suppression of $\mathrm{K^0_S}$ in jetty events and enhancement in isotropic events in the measured p_{T} range. The effect is observed, although in different ways (referring back to the discussion in Sec. 6.1.5), in all three event classes: $N^{|\eta|<0.8}_{\mathrm{tracklets}}$ I (where spherocity is assumed to affect mostly the $\langle p_{\mathrm{T}} \rangle$), $N^{|\eta|<0.8}_{\mathrm{tracklets}}$ I-III (where spherocity is assumed to impact both the $\langle p_{\mathrm{T}} \rangle$ and multiplicity), and V0M I (where spherocity is assumed to change mostly the multiplicity). The Λ ratios behave similarly but a small depletion in low-p_{T} is observed in the V0M I isotropic case, resembling typical radial flow signatures.

The presented models cannot describe the ratios to pions, although the trends relative to the $S_{\mathrm{O}}^{p_{\mathrm{T}}=1.0}$-unbiased case are reproduced well.

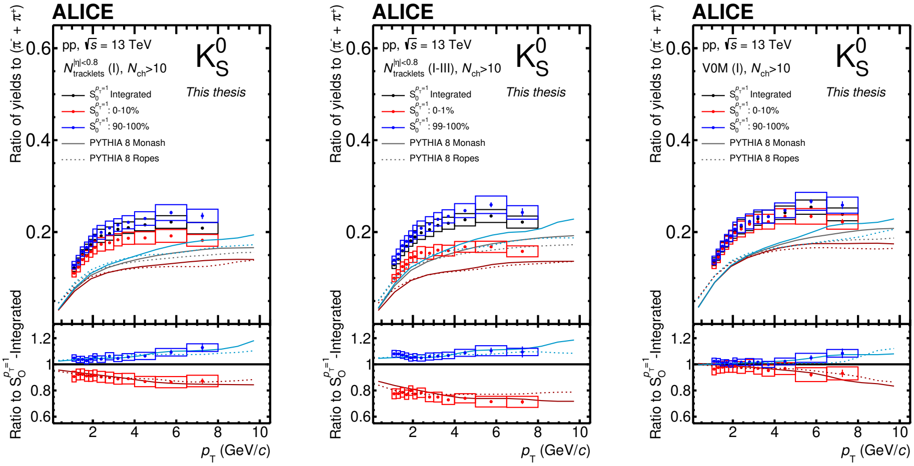

(a)

(b)

(c)

Figure 6.18: Ratios of transverse momentum spectra of K^0_S to $\pi^+ + \pi^-$ in jetty, isotropic, and $S_\mathrm{O}^{p_\mathrm{T}=1.0}$-unbiased in events with high-multiplicity classes **(a)** $N_\mathrm{tracklets}^{|\eta|<0.8}$ I, **(b)** $N_\mathrm{tracklets}^{|\eta|<0.8}$ I-III, and **(c)** $\mathrm{V0M}$ I. Statistical and systematic uncertainties are depicted as error bars and boxes, respectively.

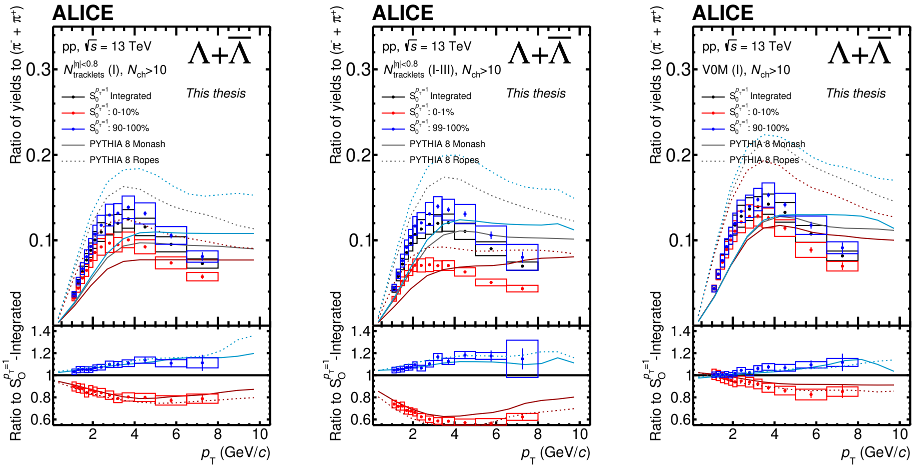

(a)

(b)

(c)

Figure 6.19: Ratios of transverse momentum spectra of $\Lambda + \overline{\Lambda}$ to $\pi^+ + \pi^-$ in jetty, isotropic, and $S_\mathrm{O}^{p_\mathrm{T}=1.0}$-unbiased in events with high-multiplicity classes **(a)** $N_\mathrm{tracklets}^{|\eta|<0.8}$ I, **(b)** $N_\mathrm{tracklets}^{|\eta|<0.8}$ I-III, and **(c)** $\mathrm{V0M}$ I. Statistical and systematic uncertainties are depicted as error bars and boxes, respectively.

6.6 Baryon-to-meson ratio

The baryon-to-meson ratio $(\Lambda + \overline{\Lambda})/(2\mathrm{K}^0_\mathrm{S})$ was investigated in this study, as it is a common observable used to measure the effects of radial flow, as discussed in Chapter 2. To focus on the different functions of $S_{\mathrm{O}}^{p_{\mathrm{T}}=1.0}$ selection in the different high-multiplicity classes, the results for the $N_{\mathrm{tracklets}}^{|\eta|<0.8}$ I and V0M I events are shown in Fig. 6.20. They are also juxtaposed with the p/π ratios [159]. The ratios reveal a significant increase when transitioning from jetty to isotropic events, indicating that the production of heavier Λ is systematically more suppressed in jetty events than $\mathrm{K_S^0}$. Similar observations have been made in other ALICE measurements studying jets (discussed further in 7.8) [161].

Although the increase in the ratio is consistent with the typical signatures of radial flow, the $N_{\mathrm{tracklets}}^{|\eta|<0.8}$ I results do not reveal the depletion at low p_{T} and neither result shows the shift of the peak to higher p_{T}, both of which are also its characteristic features. Additionally, the data are compared with the two tunes of Pythia 8, favouring the Ropes configuration.

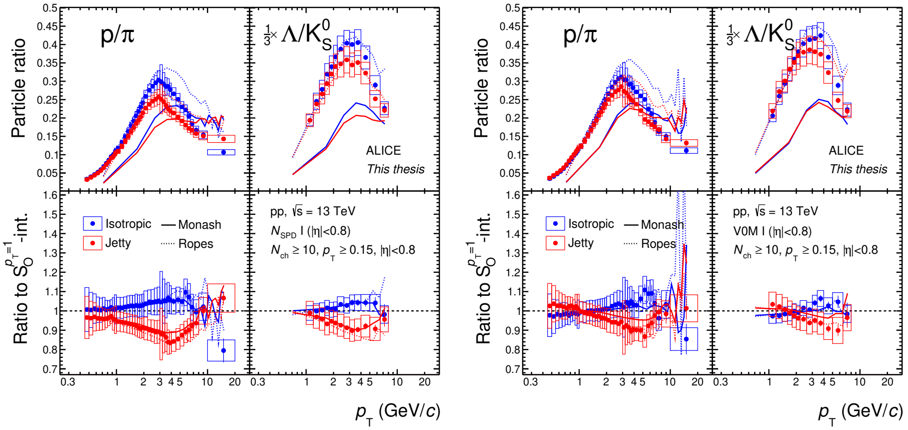

(a) (b)

Figure 6.20: Baryon-to-meson ratios of jetty ($0-10\%$) and isotropic ($90-100\%$) transverse momentum spectra of p to π (measured by co-author O. Vazquez) and $\Lambda+\overline{\Lambda}$ to $\mathrm{K_S^0}$ in the **(a)** $N_{\mathrm{tracklets}}^{|\eta|<0.8}$ I and **(b)** $\mathrm{V0M}$ I high-multiplicity events of pp collisions at $\sqrt{s}=13\,\mathrm{TeV}$. The bottom panels display the ratios to the $S_{\mathrm{O}}^{p_{\mathrm{T}}=1.0}$-unbiased case. MC predictions are denoted as lines, statistical uncertainties as error bars, and systematic uncertainties as error boxes.

6.7 Ratio of integrated yields vs. $S_{\mathrm{O}}^{p_{\mathrm{T}}=1.0}$

A key contribution of this study is the investigation of strangeness production as a function of $S_{\mathrm{O}}^{p_{\mathrm{T}}=1.0}$. Yields of the Λ baryon were determined in $N_{\mathrm{tracklets}}^{|\eta|<0.8}$ I and V0M I classes in the following intervals of $S_{\mathrm{O}}^{p_{\mathrm{T}}=1.0}$: $0-1\%$, $1-5\%$, $5-10\%$, $10-20\%$, $20-80\%$, $80-90\%$, $90-95\%$, $95-99\%$, and $99-100\%$. The integration was done in the measured p_{T} range rather than extrapolated to $p_{\mathrm{T}} = 0$. The $S_{\mathrm{O}}^{p_{\mathrm{T}}=1.0}$-dependent Λ yields are then divided by $S_{\mathrm{O}}^{p_{\mathrm{T}}=1.0}$-dependent pion yields as a reference. The effects of not extrapolating were studied and found to be unimportant, and while the extrapolation confirms the physics message of the default method, it also increases systematic uncertainties.

The results, together also with p ($|S| = 0$) and Ξ ($|S| = 2$) are reported in Fig. 6.21. For the $N_{\mathrm{tracklets}}^{|\eta|<0.8}$ I events, there is a clear strangeness- and/or mass-dependent enhancement with increasing $S_{\mathrm{O}}^{p_{\mathrm{T}}=1.0}$. It is important to emphasize that in this event class, the N_{ch} multiplicity is basically fixed. Therefore, these effects are results of the different underlying dynamics of the collisions, specifically the varying hardness of involved scatterings, rather than merely an effect of increased N_{ch}.

Conversely, the V0M I events show no such dependence, and jetty and isotropic events appear to produce the same relative amount of strangeness. This goes against intuition that varying N_{ch} between jetty ($N_{\mathrm{ch}} \to 15$) and isotropic events ($N_{\mathrm{ch}} \to 30$, according to Fig. 6.7) should introduce an effect, in accordance with traditional studies of strangeness enhancement in pp collisions as a function of N_{ch}. This observation is not fully understood, but it suggests that the decrease in strangeness in jetty events due to the decrease in N_{ch} and increase in $\langle p_{\mathrm{T}} \rangle$ is not trivial and counterbalanced by some other factors of the collision.

Finally, the results were compared with MC predictions, and only Pythia 8 Ropes accurately captures the observed trends and, to some extent, the magnitudes.

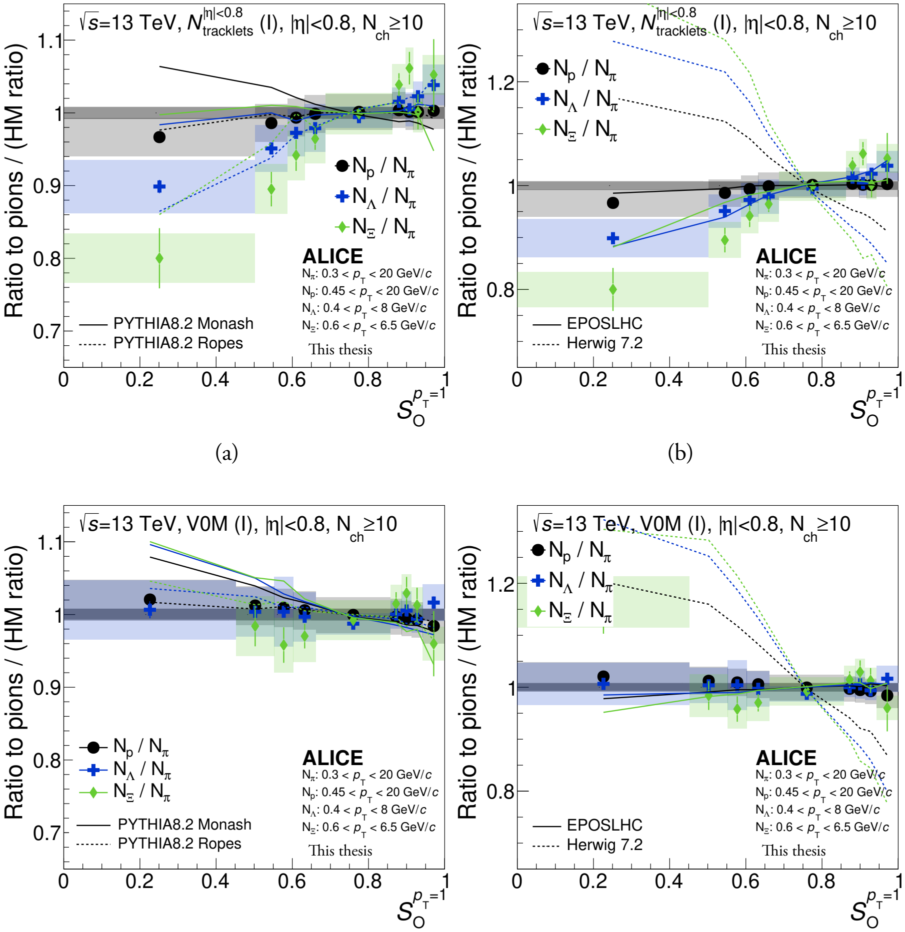

(a)

(b)

(c)

(d)

Figure 6.21: Double-ratios of integrated yields with respect to pions as a function of $S_O^{p_T=1.0}$ in the $N_{\text{tracklets}}^{|\eta|<0.8}$ I and $\mathrm{V0M}$ I events. Statistical and total systematic uncertainties are shown by bars and boxes, respectively. The curves represent different model predictions of the same measurement: **(a,c)** Pythia Monash and Ropes, **(b,d)** EPOS LHC and Herwig, where the y-axis range has been extended to accomodate the predictions. Plots co-created with co-author A. Nassirpour.

Chapter 7

Underlying event activity

In this chapter, measurements of $\mathrm{K_S^0}$, Λ, and $\overline{\Lambda}$ transverse momentum spectra and yields are reported as a function of the underlying event activity classifiers R_{T}, $R_{\mathrm{T,min}}$, and $R_{\mathrm{T,max}}$. These observables quantify the magnitude of the underlying event and are an experimental proxy of the number of Multiple Partonic Interactions, n_{MPI}.

7.1 Motivation for studying event sub-structure

7.1.1 Underlying event

As discussed in Section 1.7, the underlying event is composed of particles that are not directly related to the primary hard scattering and its related fragmentation. Typically, it can be studied in order to subtract it from the hard scattering process and learn more about jet properties in precision measurements. Moreover, since it is a manifestation of the proton substructure and the parton interactions, it can give an insight into the parton dynamics in the non-perturbative QCD region.

7.1.2 Hard process–multiplicity bias

Studying QGP phenomena in small systems as a function of event activity is challenging due to selection biases that arise when analyzing the data. It is known that selecting events with large momentum transfer leads to a bias towards higher multiplicities (and underlying event) [106], and conversely, selecting events with higher multiplicities (and UE) enhances the hard processes [160]. This bias can be under-

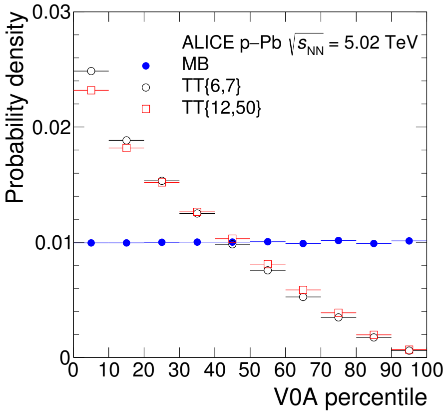

(a)

Figure 7.1: Distribution of event activity measured at forward rapidity (V0A percentile) for minimum bias events (blue points) and for events requiring a high-p_T trigger in the intervals $6 < p_T < 7$ GeV/c (black points) and $12 < p_T < 50$ GeV/c (red points), determined in p–Pb collisions. Lower V0A percentile represent higher event activity. The MB distribution is trivally uniform by construction. [106]

stood in several ways. Firstly, a harder process tends to occur with lower impact parameters, which in turn leads to higher particle multiplicities. Secondly, an event with n partonic interactions has n chances of containing a hard process. Lastly, harder processes fragment into more particles, further contributing to higher event activity. As an example, Figure 7.1 shows how the requirement of a high p_T track can skew the forward-rapidity centrality distribution to lower values (higher event activity), as observed in a result from p-Pb collisions at ALICE [106].

7.1.3 Azimuthal regions and transverse activity

A simple way to study the bias of the hard process on the UE is to investigate the magnitude of the UE as a function of the transferred momentum, which can be proxied by the momentum of the "leading", highest-p_T track in the event. The UE magnitude quickly saturates for moderate momentum transfers, which indicates that the hard process biases the UE in a similar way, independent of the hardness [162]. This saturation effect can be observed when studying particle production in three topological regions defined with respect to the azimuthal angle of the leading track, which approximates the axis of the primary scattering process. The three regions are defined as follows:

1. Toward (also known as "Near"), where $|\phi - \phi^{\text{leading}}| < \frac{\pi}{3}$,

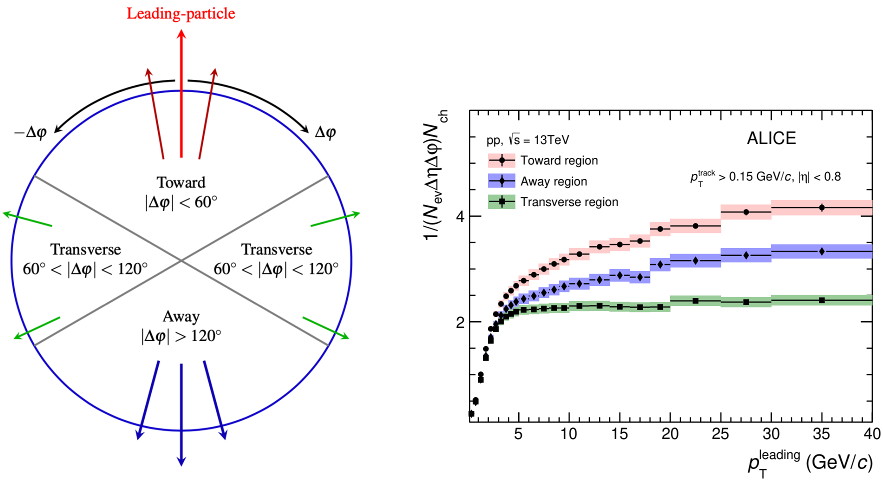

(a) (b)

Figure 7.2: **(a)** Illustration of the three azimuthal regions: Toward, Away, Transverse; defined with respect to the highest-p_T track. [162] **(b)** Charged particle density distributions as a function of p_T of the leading track in the three azimuthal regions. Error bars indicate statistical uncertainties and shaded areas represent systematic uncertainties. [162]

2. Away, where $|\phi - \phi^{\text{leading}}| > \frac{2\pi}{3}$, and
3. Transverse, where $\frac{\pi}{3} < |\phi - \phi^{\text{leading}}| < \frac{2\pi}{3}$.

Here, ϕ^{leading} is the azimuthal angle of the leading track. This definition is illustrated in Figure 7.2.

Studying particle multiplicity (or sum of their p_T) in these regions as a function of the transverse momentum of the leading track p_T^{leading} reveals that in the regions Toward and Away, the multiplicity continues to increase with the hardness of the primary process [162, 163]. These regions contain the leading and the recoil jet, respectively. In contrast, in the Transverse region, the multiplicity (further denoted as N_T in this thesis but $N_{\text{ch}}^{\text{trans}}$ is also used in cited literature) reaches a plateau at around $p_T^{\text{leading}} \sim$ 5 GeV/c. In this region, the underlying event becomes independent of the strength of the primary process, and the selection bias is minimized. Notably, this phenomenon is universal regardless of the system size or collision energy [162, 163, 164, 165]. As an example, measurements from ALICE are shown in Fig. 7.2.

7.2 R_{T} as an experimental observable

The magnitude of the underlying event can be quantified using the self-normalized ratio:

$$R_{\mathrm{T}} = \frac{N_{\mathrm{T}}}{\langle N_{\mathrm{T}} \rangle}, \tag{7.1}$$

which is often referred to as the underlying event activity, transverse activity, or relative transverse activity in various literature [162, 166, 167], and also in this thesis. This observable and its uses were suggested in Ref. [166].

By selecting events based on R_{T}, two limits can be studied:

- $R_{\mathrm{T}} \to 0$: the "**ee**" limit, where events with minimal UE are selected. These events are dominated by a single hard scattering and can be compared to LEP fragmentation models.
- $R_{\mathrm{T}} \to \infty$: the "**AA**" limit, where events with very high transverse activity are selected, which can come from many MPIs and/or from transverse jets. These events may exhibit features similar to pA and AA collisions.

7.2.1 Proxy to n_{MPI}

As could be intuitively expected, R_{T} serves as an experimental proxy for $\langle n_{\mathrm{MPI}} \rangle$. Phenomenological models that incorporate MPIs provide an illustration of this relationship. As shown in Fig. 7.3, Pythia 8 predicts a strong dependence of $\langle n_{\mathrm{MPI}} \rangle$ on R_{T} until $R_{\mathrm{T}} \lesssim 5$. Similarly, Herwig 7 predicts a dependence until $R_{\mathrm{T}} \lesssim 3$, albeit weaker. Pythia's prediction for the relationship between R_{T} and the event multiplicity, which is affine, is also shown in Fig. 7.3.

7.2.2 Extension to $R_{\mathrm{T,min}}$, $R_{\mathrm{T,max}}$

Upon closer inspection of Fig. 7.2, it can be observed that the charged particle multiplicity does not completely plateau in the Transverse region either. The plateauing was an important factor in motivating R_{T} measurements, as it suggests an independence of the UE activity on the hardness of the primary process and separation of the softer and harder components of particle production. Instead, there is a slight increase with $p_{\mathrm{T}}^{\mathrm{leading}}$, although the effect is small. This rise can be attributed to harder, wide-angle ISR and FSR [169].

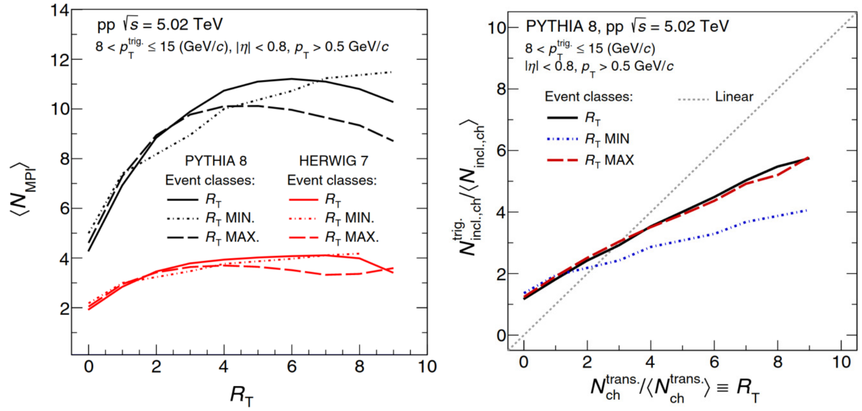

(a)

(b)

Figure 7.3: **(a)** Dependence of the mean number of MPIs on the underlying event activity classifiers R_{T}, $R_{\mathrm{T,min}}$, and $R_{\mathrm{T,max}}$ in pp collisions at $\sqrt{s} = 5.02$ TeV, as predicted by Pythia 8 (black) and Herwig 7 (red). [168] **(b)** Pythia 8 prediction for the correlation of the self-normalised charged particle multiplicity measured at mid-rapidity in events with a high-p_{T} trigger and the underlying event activity classifiers R_{T}, $R_{\mathrm{T,min}}$, $R_{\mathrm{T,max}}$. [168]

To separate the soft and hard components of the underlying event – namely, the MPIs from wide-angle ISR/FSR – the definition of R_{T} can be extended. The two transverse sub-regions can be further classified as Transverse-min or Transverse-max, based on which sub-region has fewer or more particles. Softer contributions from MPIs will enter both sub-regions, whereas harder radiation should affect mainly the Transverse-max sub-region. This makes Transverse-min more sensitive to particle production from MPIs. Figure 7.4 illustrates how the Transverse-max region captures most of the rise of $\langle N_{\mathrm{ch}} \rangle$ and $\langle p_{\mathrm{T}} \rangle$, whereas the Transverse-min region is much closer to plateauing.

Analogously, the following underlying event activity classifiers can be defined:

$$R_{\mathrm{T,min}} = \frac{N_{\mathrm{T,min}}}{\langle N_{\mathrm{T,min}} \rangle} \quad , \tag{7.2}$$

$$R_{\mathrm{T,max}} = \frac{N_{\mathrm{T,max}}}{\langle N_{\mathrm{T,max}} \rangle} \quad , \tag{7.3}$$

where $N_{\mathrm{T,min}}$ and $N_{\mathrm{T,max}}$ are the particle multiplicities in the Transverse-min and Transverse-max sub-regions, respectively. This approach follows measurements developed at UE studies at the Tevatron [169] and has been suggested to use in searches for QGP phenomena in small systems based on investigations in phenomenological models [168]. In the rather rare situations with $N_{\mathrm{T,min}} = N_{\mathrm{T,max}}$, the classification is based on the sum of p_{T} instead, with the Transverse-min region being the region with the smaller sum.

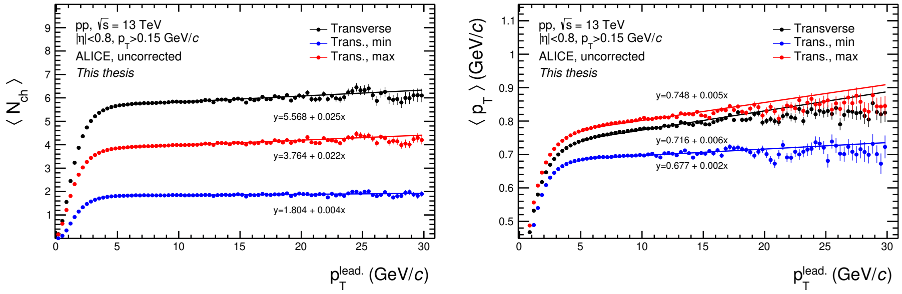

(a) (b)

Figure 7.4: **(a)** Mean number of particles in the Transverse region (black) **(b)** and their average momentum, measured in pp collisions at $\sqrt{s} = 13$ TeV as a function of the leading track momentum. The Transverse-min (blue) and Transverse-max (red) regions are also shown. The solid lines represent linear fits in the range above $p_{\mathrm{T}}^{\mathrm{leading}} > 5$ GeV/c. Their parameters values are indicated. The results are not corrected and show only statistical uncertainties.

According to Pythia 8, as shown in Fig. 7.3, $R_{\mathrm{T,min}}$ and $R_{\mathrm{T,max}}$ follow different relationships with $\langle n_{\mathrm{MPI}} \rangle$. Whereas $\langle n_{\mathrm{MPI}} \rangle$ starts falling as a function of $R_{\mathrm{T,max}}$ (due to the inclusion of mini-jets) at $R_{\mathrm{T,max}} \approx 5$, it continues rising as a function of $R_{\mathrm{T,min}}$ across the entire range. Furthermore, compared to R_{T}, $R_{\mathrm{T,min}}$ also shows some degree of decorrelation with event multiplicity.

Charged particle p_{T} spectra

Phenomenological models also reveal a different evolution of transverse momentum spectra of inclusive charged particles based on $R_{\mathrm{T,min}}$ and $R_{\mathrm{T,max}}$, as shown in Fig. 7.5. For the highest reported ranges of $R_{\mathrm{T,max}}$ and R_{T}, a significant hardening of the spectrum is observed in both Pythia 8 and Herwig 7, similarly to multiplicity studies [146], indicating a strong auto-correlation. In contrast, $R_{\mathrm{T,min}}$ exhibits a Cronin-like enhancement[1] at intermediate p_{T} and a plateau at $p_{\mathrm{T}} \gtrsim 6$ GeV/c, even in the highest $R_{\mathrm{T,min}}$ bin [168]. So far, this behaviour has not been observed in data.

7.2.3 Track and event selection

The event selection follows the same criteria as the $S_{\mathrm{O}}^{p_{\mathrm{T}}=1.0}$ measurement discussed in Section 6.1.4, which conform to the standard analysis of light flavour hadrons versus multiplicity in pp collisions conducted in ALICE [100]. The |`INEL>0`| events, which

---

[1] The Cronin effect refers to the modification of p_{T} spectra in nuclear collisions as a result of partonic scattering in the nuclear medium and can be observed as a characteristic peak in nuclear modification factors at intermediate p_{T} [170].

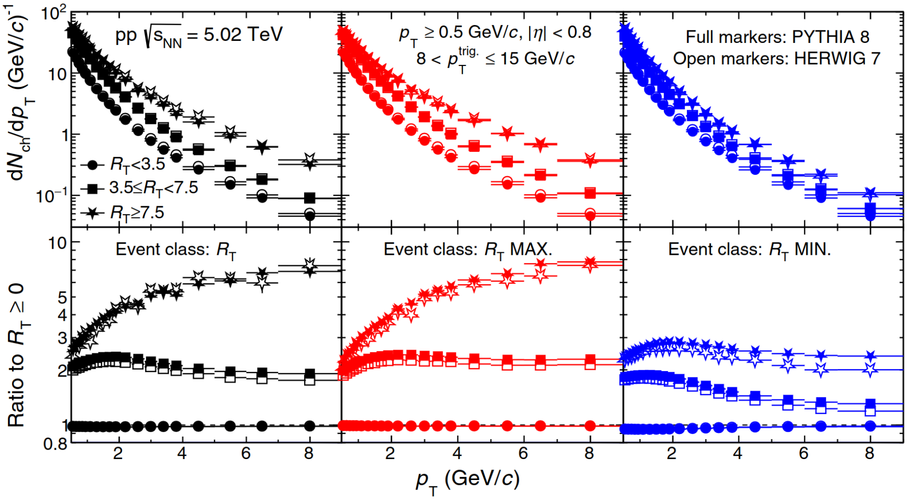

Figure 7.5: Transverse momentum spectra of charged particles produced in three azimuthal regions: **(left)** Transverse, **(middle)** Transverse-max, **(right)** Transverse-min, as a function of the underlying event activity $R_T/R_{T,\max}/R_{T,\min}$ in pp collisions at $\sqrt{s} = 5.02$ TeV. The bottom row displays the ratios to the UE-activity integrated cases. The predictions are based on Pythia 8 and Herwig 7 simulations. [168]

require at least one hit in either V0A or V0C scintillators and a track reconstructed within $|\eta| < 1$, are used. The SPD is used for the reconstruction of the primary vertex, which is further required to be close to the nominal vertex ($|\Delta z| < 10$ cm) to reject out-of-bunch pile-up. To remove in-bunch pile-up, events with multiple reconstructed vertices are excluded.

Events are required to have a leading track with reconstructed momentum $5 < p_T^{\text{leading}} < 40$ GeV/c[2]. These values were chosen to access the plateau in transverse activity and isolate the UE while retaining a large data sample. Maintaining a high momentum and spatial resolution of the leading track is crucial in this measurement. However, this can be compromised at high p_T when a significant portion of the track curvature can fall between two sectors of the TPC. To address this issue, geometrical cuts are used, as discussed in Sec. 4.4.2.

For both the leading particle as well as the particles entering N_T and R_T calculations, tracks are required to be within $|\eta| < 0.8$ and have $p_T > 0.15$ GeV/c, and must satisfy the following:

1. "Hybrid tracks", described in more detail in Sec. 4.4.1, are used for both leading and N_T tracks to ensure a high level of azimuthal acceptance uniformity. These

---

[2] Note that p_T spectrum is falling very steeply, at an approximately exponential rate, making the upper bound negligibly restrictive compared to the lower bound.

tracks consist of high-quality “global track” requirements, including the SPD information, which leads to azimuthal non-uniformity, and “complementary track” cuts, a looser set requiring only ITS and TPC in cases where the first are not satisfied.

2. For the leading track, strict p_{T}-dependent DCA cuts are applied in the transverse direction ($|\mathrm{DCA}_{xy}| < 0.0182 + \frac{0.0350}{p_{\mathrm{T}}^{1.01}}$ cm, $p_{\mathrm{T}} \in$ [GeV/c]), to ensure good momentum resolution and that the track is a primary one.

3. For the N_{T} tracks, a DCA cut ($|\mathrm{DCA}_{xy}| < 0.06$ cm) is required to avoid biases in V^0 measurements, as explained in the text below.

7.2.4 R_{T} measurements of neutral particles vs. charged particles

The V^0s are neutral particles and thus, they cannot be leading tracks nor enter N_{T} ($N_{\mathrm{T,min}}$, $N_{\mathrm{T,max}}$) and R_{T} ($R_{\mathrm{T,min}}$, $R_{\mathrm{T,max}}$) calculations. This has several implications:

1. V^0s suffer from auto-correlation biases much less than $\pi/\mathrm{K}/\mathrm{p}$, which can be seen in azimuthal distributions and in $\mathrm{K}^0_{\mathrm{S}}/\mathrm{K}^{\pm}$ ratios. Requiring high/low $N_{\mathrm{T}}/R_{\mathrm{T}}$ can lead to an increase/decrease of charged particles in the Transverse region due to selecting fluctuations in addition to the UE scaling. However, this effect is significantly smaller for neutral V^0s. This behaviour is shown in Fig. 7.6. It is important to bear this caveat in mind when comparing p_{T} spectra and yields of $\pi/\mathrm{K}/\mathrm{p}$ and V^0s.

2. While N_{T} is always at least 1 for $\pi/\mathrm{K}/\mathrm{p}$ in the Transverse region, for V^0s it can be equal to 0. Similar logic applies to the Transverse-min/max sub-regions and $N_{\mathrm{T,min}}/N_{\mathrm{T,max}}$.

3. The maximum p_{T} measurable for $\pi/\mathrm{K}/\mathrm{p}$ in the Toward region is limited to $p_{\mathrm{T}} < 5\,\mathrm{GeV}/c$, at which point the trigger requirement would lead to a trivial increase. For V^0s, however, this limitation does not apply and their measured p_{T} range does not need to be restricted.

4. The charged daughters of V^0s could sometimes enter N_{T}, leading to significant biases at low p_{T} in the Toward and Away regions of $\mathrm{K}^0_{\mathrm{S}}/\mathrm{K}^{\pm}$ ratios.

In this thesis, the behaviour described in the last point was rectified by making N_{T} track candidates and V^0 daughter tracks two disjunct sets. This was achieved by applying the $|\mathrm{DCA}_{xy}| > 0.06$ cm cut, used in the V^0 reconstruction as discussed

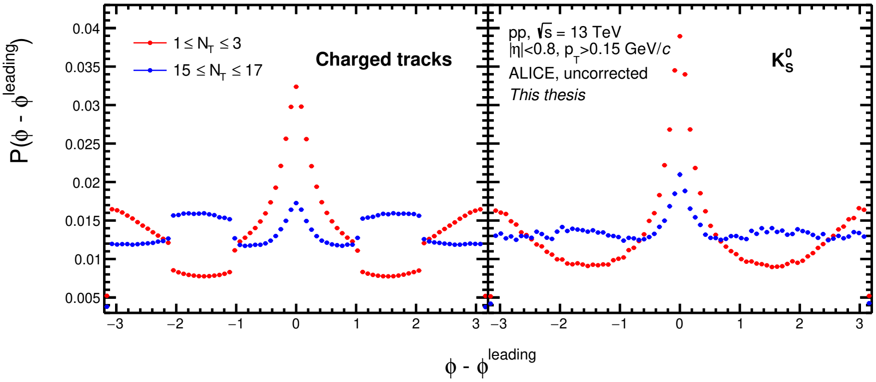

Figure 7.6: Probability distributions of the azimuthal angle of **(left)** charged tracks and **(right)** the neutral K^0_S. Events with low N_T (red) and high N_T (blue) are compared. The results are uncorrected for reconstruction effects and acceptance and show only statistical uncertainties.

in Section 5.2, in opposite ways. This reduces the N_T track candidates by less than 5%. The effect of this solution can be seen in Fig. 7.7, which shows a disappearance of the bias in the ratios of neutral to charged kaons in the Toward and Away regions at low p_T, caused by the V^0 daughters "leaking" into the Transverse region and the N_T calculation.

7.3 Bayesian unfolding procedure

The measurements of V^0s are conducted as a function of the number of measured tracks N_T^m within the detector acceptance. The measured multiplicity N_T^m includes a fraction of the true primary charged-particle multiplicity N_T^t not lost due to acceptance, efficiency, or track selection, as well as contributions from secondary particles or particles smeared into the measurement's kinematic acceptance due to detector resolution (i.e., from $p_\mathrm{T} < 0.15\,\mathrm{GeV}/c$). These effects fluctuate on an event-by-event basis and thus there is no unique correlation between N_T^m and N_T^t. This means that events with true multiplicity N_T^t can be measured with different N_T^m, contributing to V^0 measurements in multiple N_T^m bins. Therefore, each spectrum contains particles from events with many true multiplicities N_T^t.

This thesis uses a Bayesian unfolding procedure, as discussed in Ref. [171], to convert V^0 measurements as a function of N_T^m into measurements as a function of N_T^t and thus correct for the mentioned effects.

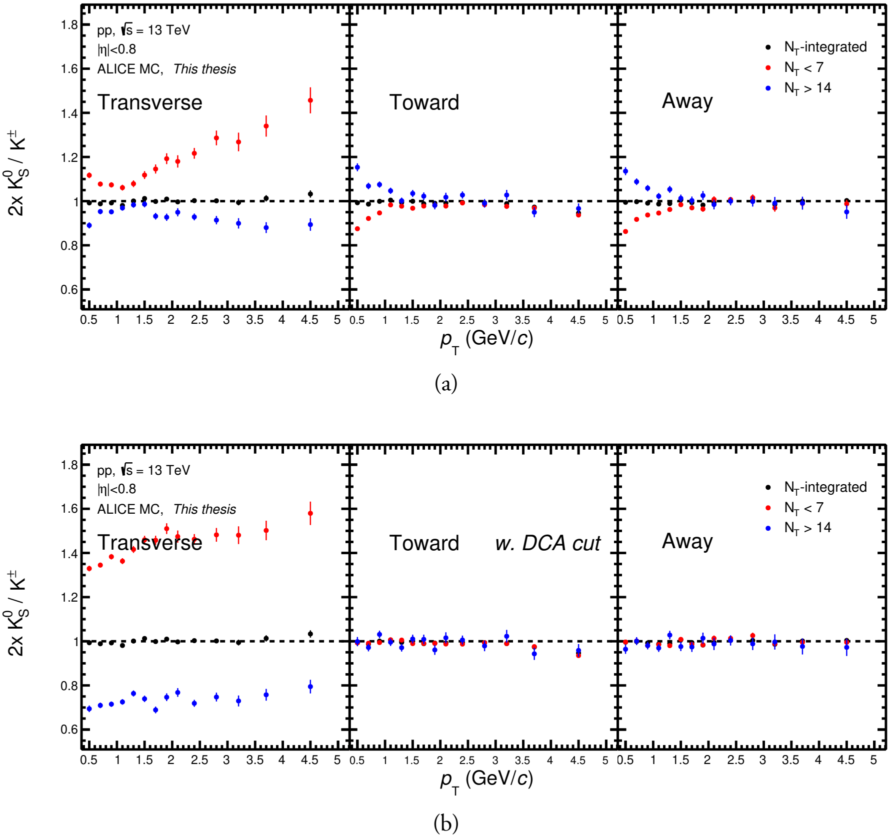

Figure 7.7: Transverse momentum spectra ratios of the neutral $\mathrm{K^0_S}$ to the charged $K^\pm$ without enforcing the DCA cut (top) and after its inclusion (bottom) in the three azimuthal regions. Events with low N_T (red) and high N_T (blue) are compared. The results come from ALICE detector simulations, are uncorrected for reconstruction effects and acceptance, and show only statistical uncertainties.

7.3.1 One-dimensional unfolding

The measured multiplicity distribution $n_\mathrm{ev}(N_\mathrm{T}^m)$ can be mathematically represented as the result of convolving (or "folding") the true multiplicity distribution produced by the collisions, $n_\mathrm{ev}(N_\mathrm{T}^t)$, with the detector's response function. The response matrix S_{mt}, which represents the conditional probability $P(N_\mathrm{T}^m|N_\mathrm{T}^t)$ of an event with multiplicity N_T^t being measured with multiplicity N_T^m, can be obtained from MC simulations of the apparatus. Using this matrix, also shown in Fig. 7.8, $n_\mathrm{ev}(N_\mathrm{T}^m)$ can be expressed in terms of $n_\mathrm{ev}(N_\mathrm{T}^t)$ as follows:

$$n_\mathrm{ev}(N_\mathrm{T}^m) = \sum_t \mathrm{S}_{mt} \cdot n_\mathrm{ev}(N_\mathrm{T}^t) \quad . \tag{7.4}$$

To obtain the true multiplicity distribution from the measured distribution, the inverse of S_{mt} could be used, hypothetically, as shown below:

$$n_{\mathrm{ev}}(N_{\mathrm{T}}^{t}) = \sum_{m} \mathrm{S}_{mt}^{-1} \cdot n_{\mathrm{ev}}(N_{\mathrm{T}}^{m}) \quad . \tag{7.5}$$

However, the inverse S_{mt}^{-1} may have multiple or zero solutions, making this approach unfeasible. Alternatively, S_{mt}^{-1} could be obtained directly from MC simulations, just like the detector response. However, this matrix would then strongly depend on the generated N_{T}^{t} distribution and be significantly model-dependent, as physics generators vary in their N_{T}^{t} predictions. In contrast, the detector response is mostly affected by the accuracy of the particle propagation simulations, which is a lot better understood. Therefore, an iterative numerical procedure based on Bayes' theorem is used to obtain the unfolding matrix M_{mt}, which represents the conditional probabilities $P(N_{\mathrm{T}}^{t}|N_{\mathrm{T}}^{m})$ [171].

In this application, Bayes' theorem can be expressed in terms of N_{T}^{m} and N_{T}^{t} as follows,

$$P(N_{\mathrm{T}}^{t}|N_{\mathrm{T}}^{m}) = \frac{P(N_{\mathrm{T}}^{m}|N_{\mathrm{T}}^{t})P(N_{\mathrm{T}}^{t})}{P(N_{\mathrm{T}}^{m})} \quad , \tag{7.6}$$

where $P(N_{\mathrm{T}}^{t})$ and $P(N_{\mathrm{T}}^{m})$ are probability distributions for an event occurrence with N_{T}^{t} and N_{T}^{m}, respectively. Assuming that $P(N_{\mathrm{T}}^{t})$ is known, $P(N_{\mathrm{T}}^{m})$ can be calculated as follows:

$$P(N_{\mathrm{T}}^{m}) = \sum_{t} P(N_{\mathrm{T}}^{m}|N_{\mathrm{T}}^{t})P(N_{\mathrm{T}}^{t}) \quad . \tag{7.7}$$

Therefore, using Eq. 7.6, the conditional probability in the unfolding matrix can be written as follows:

$$P(N_{\mathrm{T}}^{t}|N_{\mathrm{T}}^{m}) = \frac{P(N_{\mathrm{T}}^{m}|N_{\mathrm{T}}^{t})P(N_{\mathrm{T}}^{t})}{\sum_{t'} P(N_{\mathrm{T}}^{m}|N_{\mathrm{T}}^{t'})P(N_{\mathrm{T}}^{t'})} \quad . \tag{7.8}$$

However, $P(N_{\mathrm{T}}^{t})$ (the "prior") is, actually, initially unknown and must be arbitrarily chosen. The unfolding matrix can be calculated using this prior, and the unfolded distribution can be obtained as follows:

$$\hat{n}_{\mathrm{ev}}(N_{\mathrm{T}}^{t}) = \sum_{m} P(N_{\mathrm{T}}^{t}|N_{\mathrm{T}}^{m}) n_{\mathrm{ev}}(N_{\mathrm{T}}^{m}) \quad . \tag{7.9}$$

This unfolded multiplicity can subsequently be used to update the prior as follows:

$$\hat{P}(N_{\mathrm{T}}^{t}) = \frac{\hat{n}_{\mathrm{ev}}(N_{\mathrm{T}}^{t})}{\sum_{t'} \hat{n}_{\mathrm{ev}}(N_{\mathrm{T}}^{t'})} \quad , \tag{7.10}$$

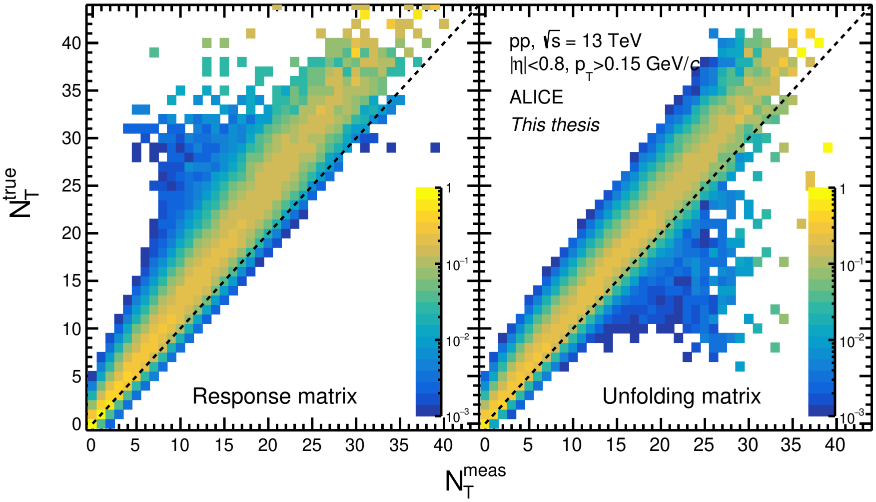

Figure 7.8: **(left)** Response matrix S_{mt} showing the correlation between measured and true track multiplicity in the Transverse region determined from ALICE MC simulations based on Pythia 8. The matrix is row-wise normalised. **(right)** Unfolding matrix $P(N_{\mathrm{T}}^{t}|N_{\mathrm{T}}^{m})$ calculated from the iterative Bayesian unfolding procedure.

starting a new iteration. The updated $\hat{P}(N_{\mathrm{T}}^{t})$ is closer to the true $P(N_{\mathrm{T}}^{t})$ than the initial guess because the arbitrarily chosen prior is constrained by the $n_{\mathrm{ev}}(N_{\mathrm{T}}^{m})$ observable, which contains information about $P(N_{\mathrm{T}}^{t})$. The statistical uncertainties are propagated according to the discussion in Ref. [171].

Multiple approaches can be taken to choose the prior: a uniform distribution, the N_{T}^{t} distribution generated by a model, or the N_{T}^{m} distribution acquired from data. In this thesis, the prior choice was found to not play a role and the N_{T}^{m} distribution was used.

The χ^2/ndf is calculated to determine the validity of the correction and the stopping point for the iterative process. It is calculated by comparing the N_{T}^{t} distribution – known a priori in the simulations – and the unfolded $\hat{n}_{\mathrm{ev}}(N_{\mathrm{T}}^{t})$ distribution, where ndf refers to the number of degrees of freedom, in this case the number of data points in the distribution. The process is stopped when χ^2/ndf reaches a minimum value or the iterations take a maximum number of steps n_{iter}. This is imposed to avoid overfitting and overestimation of statistical uncertainties, which increase with n_{iter}.

In this dissertation, the $N_{\mathrm{T,min}}$ and $N_{\mathrm{T,max}}$ distributions are unfolded analogously to the N_{T} case. The selected n_{iter} values are reported in Tab. 7.1. The entire iterative process is summarised in a diagram shown in Fig. 7.9.

The used response matrix, as well as the resulting unfolding matrix, can be seen in

Fig. 7.8. The method still exhibits some degree of model dependence due to the generation of the response matrix. Previous studies in ALICE have compared the response matrix for N_{T} acquired from Pythia 8 and from EPOS LHC MC simulations, which revealed that the effect is less than 1% [159]. This effect is taken into consideration as a source of systematic uncertainty.

Table 7.1: The number of iterations in the Bayesian unfolding process for N_{T} (capped at maximum n_{iter}), $N_{\mathrm{T,min}}$, and $N_{\mathrm{T,max}}$.

Unfolding observable	N_{T}	$N_{\mathrm{T,min}}$	$N_{\mathrm{T,max}}$
n_{iter}	20 (max.)	10	18

7.3.2 Unfolding of $\mathrm{K}^0_{\mathrm{S}}$, Λ, and $\overline{\Lambda}$ p_{T} spectra

In the unfolding treatment of the Λ and $\overline{\Lambda}$, the particle and the anti-particle p_{T} spectra were combined to reduce statistical uncertainties and increase the method's robustness. For the Toward and Away regions, the spectra can be unfolded in a similar fashion to the N_{T} activity, assuming that they are completely decoupled from the production in the Transverse region. This implies mere reshuffling of V^0s in individual p_{T} bins $n^{\mathrm{V}^0}_{p_{\mathrm{T}}=i}$ between different events, based on the unfolding recipe established above:

$$\hat{n}^{\mathrm{V}^0}_{p_{\mathrm{T}}=i}(N^t_{\mathrm{T}}) = \sum_m P(N^t_{\mathrm{T}}|N^m_{\mathrm{T}})\, n^{\mathrm{V}^0}_{p_{\mathrm{T}}=i}(N^m_{\mathrm{T}}) \quad . \tag{7.11}$$

Closure tests using MC simulations were conducted to compare the unfolded p_{T} spectra as a function of unfolded-reconstructed N_{T} to the generated p_{T} spectra as a function of generated N_{T}– and showed the plausibility of this approach. The closure tests are presented in Fig. 7.10, indicating mostly consistent results within 5%, with the deviations observed more in the R_{T} extremes.

For the treatment of the Transverse regions, two approaches were considered:

1. Similarly to how this unfolding method was applied in other multiplicity and N_{T} measurements in ALICE for charged particles [159], one assumes correlations between the p_{T} spectra and the event activity. This approach requires multiplying the response matrix with number of tracks in each column, modifying the unfolding matrix to make it p_{T}-dependent, and applying different unfolding recipes to V^0s based on their p_{T}, which approximates reshuffling on a particle-by-particle basis.

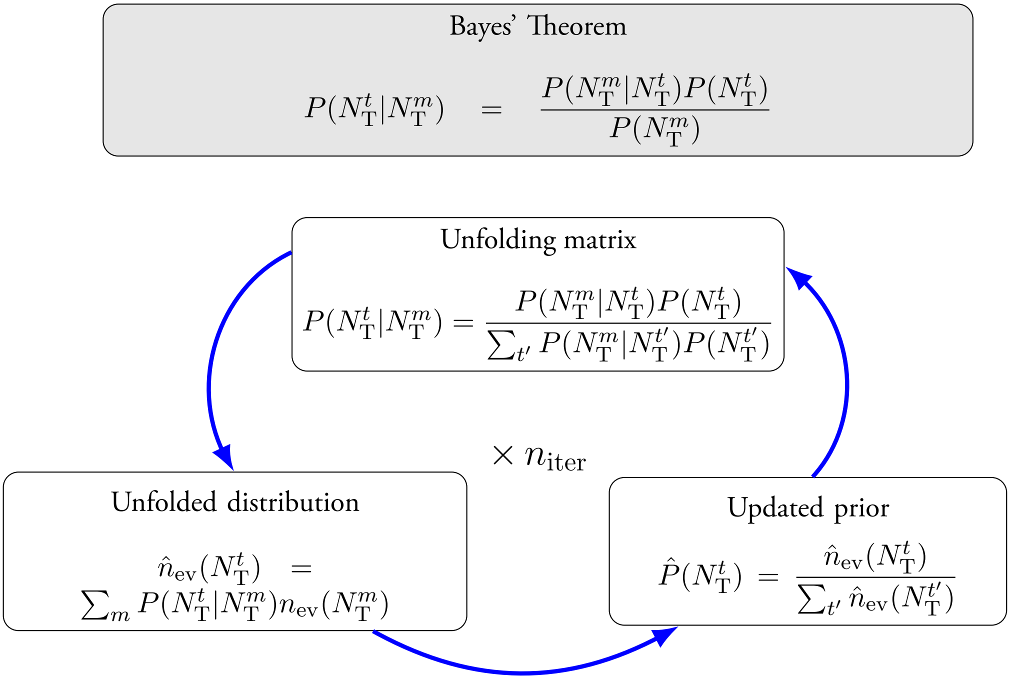

Figure 7.9: Diagram showing the iterative process of Bayesian unfolding.

2. Given the fact that the N_{T} tracks and the V^0 daughters were made two disjunct sets in this measurement by separating them with a $|\mathrm{DCA}_{xy}|$ boundary, one may assume complete de-correlation between the V^0 p_{T} spectra and the measured N_{T}. Subsequently, the Transverse region would be treated like the Toward and Away.

In this study, both approaches were tested and the second method was chosen for the measurement. Although the first method generally produced somewhat smaller non-closure discrepancies, the second method is more logically sound. Additionally, modifying the response matrix in the first method resulted in an empty zeroth bin by construction. As a consequence, events with $N_{\mathrm{T}} = 0$ but the number of V^0s $n^{\mathrm{V}^0} > 0$ could not be treated since the unfolding matrix cannot recover this scenario. While this is not a limitation in charged particle analyses since such cases cannot occur, it posed a problem here.

The closure tests for the Transverse region are shown in Fig. 7.10, but it should be noted that they exhibit somewhat larger deviations (up to 10%) in the most extreme bins of R_{T} compared to the Toward/Away regions. One possible explanation for this is the simplicity of the unfolding method used here, as well as the fact that the closure tests were conducted on Pythia simulations, which due to the local string breakings may exhibit strongly correlated particle production in phase space, leading to somewhat of a coupling between N_{T} and V^0s.

Unfolding of the V^0s spectra in the Transverse-min and Transverse-max regions as a function of $N_{\mathrm{T,min}}$ and $N_{\mathrm{T,max}}$, respectively, was performed in an identical manner. Although the results close well in MC tests in the central $R_{\mathrm{T,min}}/R_{\mathrm{T,max}}$ intervals, deviations of up to around 20% are observed in the most extreme bins, as depicted in Fig. 7.10. This is likely due to low statistics samples, the simplicity of the method, and the fact that the individual $R_{\mathrm{T,min}}/R_{\mathrm{T,max}}$ intervals cover even smaller ranges of $N_{\mathrm{T,min}}/N_{\mathrm{T,max}}$, making the process highly sensitive to fluctuations.

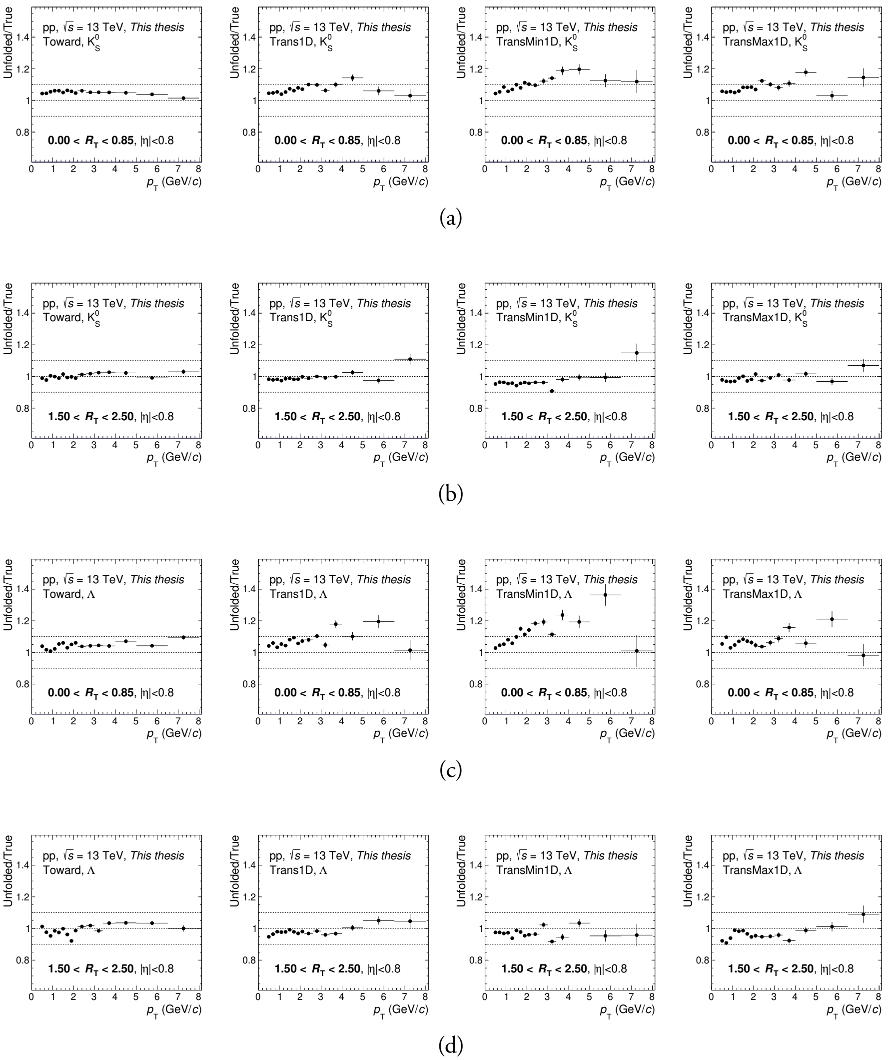

Figure 7.10: Transverse momentum Monte Carlo closure tests between true spectra and reconstructed, corrected, and unfolded spectra for **(a)** $\mathrm{K^0_S}$ low-R_T/$R_{\mathrm{T,min}}$/$R_{\mathrm{T,max}}$ events, **(b)** $\mathrm{K^0_S}$ high-R_T/$R_{\mathrm{T,min}}$/$R_{\mathrm{T,max}}$ events, **(c)** $\Lambda + \overline{\Lambda}$ low-R_T/$R_{\mathrm{T,min}}$/$R_{\mathrm{T,max}}$ events, and **(d)** $\Lambda + \overline{\Lambda}$ high-R_T/$R_{\mathrm{T,min}}$/$R_{\mathrm{T,max}}$ events. The columns show the regions in this order: Toward, Transverse, Transverse-min, and Transverse-max. A 10%-effect band is indicated.

7.4 R_T, $R_{\mathrm{T,min}}$, $R_{\mathrm{T,max}}$ distributions

The unfolded N_T, $N_{\mathrm{T,min}}$, and $N_{\mathrm{T,max}}$ distributions were self-normalised to obtain the R_T, $R_{\mathrm{T,min}}$, and $R_{\mathrm{T,max}}$ distributions, respectively. The mean values used for self-normalisation are reported in Tab. 7.2. They are shown in Fig. 7.11 and compared with predictions from Pythia 8 (Monash tune [110] and Ropes tune [116]) as well as EPOS LHC [120].

Table 7.2: Mean number of transverse multiplicities used in the definition of R_{T}, $R_{\mathrm{T,min}}$, and $R_{\mathrm{T,max}}$.

Event classifier	R_{T}	$R_{\mathrm{T,min}}$	$R_{\mathrm{T,max}}$
Average $N_{\mathrm{T}}/N_{\mathrm{T,min}}/N_{\mathrm{T,max}}$	7.345	2.470	4.869

The results can be described by the predictions quite accurately, favouring EPOS LHC, but show deviations in high-UE-activity events. The different quantiles corresponding to the $R_{\mathrm{T}}/R_{\mathrm{T,min}}/R_{\mathrm{T,max}}$ ranges used in this measurement are highlighted. They are also summarised in Tab. 7.3. It should be noted that since the transverse multiplicities are non-negative integers, $N_{\mathrm{T}}, N_{\mathrm{T,min}}, N_{\mathrm{T,max}} \in \mathbb{N}_0$, the $R_{\mathrm{T}}/R_{\mathrm{T,min}}/R_{\mathrm{T,max}}$ distributions are not continuous observables.

Table 7.3: The intervals for UE activity classifier selected in this measurement and the corresponding average values.

Average values	$\langle R_{\mathrm{T}} \rangle$	$\langle R_{\mathrm{T,min}} \rangle$	$\langle R_{\mathrm{T,max}} \rangle$
Intervals			
0–0.85	0.49	0.42	0.53
0.85–1.5	1.19	1.21	1.20
1.5–2.5	1.92	1.90	1.91
2.5–5.0	2.97	3.27	3.01

7.5 Systematic uncertainties

The systematic uncertainties on the p_{T} spectra were determined individually for each R_{T} interval and azimuthal region, following the procedures discussed in more detail in Sec. 5.7 and Sec. 6.2. They are reported in Fig. 7.12, Fig. 7.13, and Fig. 7.14 for the $\mathrm{K}^0_{\mathrm{S}}$, Λ, and $\overline{\Lambda}$, respectively. Furthermore, they are added together with the p_{T}-independent uncertainties, as well as uncertainties from the unfolding (discussed below) and summarised in Tab. 7.4. The dominant contributions to the systematic uncertainties, in no specific order, come from signal extraction, selection cuts related to TPC tracking and topological reconstruction, and the requirement of signals from fast detectors to reject track pile-up.

As there are no reasons to believe the relative systematic uncertainties should differ when using the more specific UE activity classifiers in the two Transverse sub-regions, they are also assigned to the results in the $R_{\mathrm{T,min}}$ and $R_{\mathrm{T,max}}$ measurements.

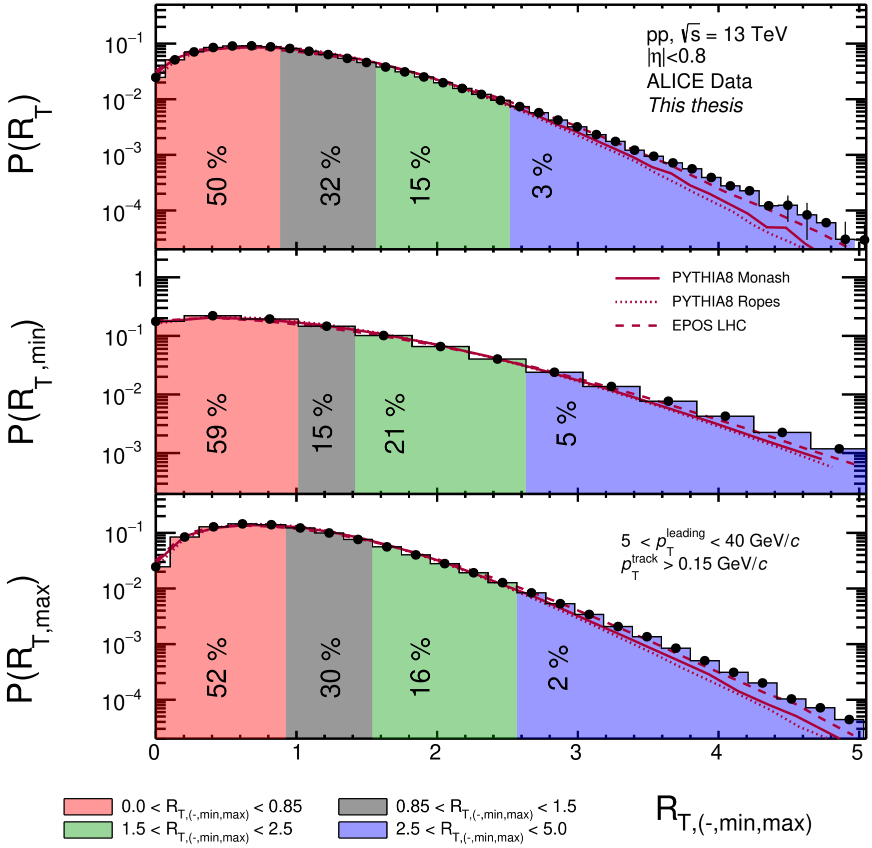

(a)

Figure 7.11: Probability distribution function of the underlying event activity classifiers R_{T} (top), $R_{\mathrm{T,min}}$ (middle), and $R_{\mathrm{T,max}}$ (bottom) in pp collisions at $\sqrt{s} = 13$ TeV in events with a high-p_{T} track $5 < p_{\mathrm{T}} < 40$ GeV/c. The results are treated with Bayesian unfolding and compared with predictions from Pythia 8 Monash, Pythia 8 Ropes, and EPOS LHC. The R_{T}/$R_{\mathrm{T,min}}$/$R_{\mathrm{T,max}}$ intervals used in this dissertation are shown along with the corresponding quantile values. Only statistical uncertainties are shown.

7.5.1 Uncertainties from the unfolding procedure

The deviations between the generated p_{T} spectra and the reconstructed, corrected, and unfolded p_{T} spectra displayed in Fig. 7.10 were used to determine the systematic uncertainties associated with the unfolding procedure. To isolate the effect of unfolding from other reconstruction effects, the "non-closures" in each $R_{\mathrm{T}}/R_{\mathrm{T,min}}/R_{\mathrm{T,max}}$ interval were divided by the non-closure in the $R_{\mathrm{T}}/R_{\mathrm{T,min}}/R_{\mathrm{T,max}}$-integrated bin.

The unfolding systematic uncertainties exhibited a large amount of correlation be-

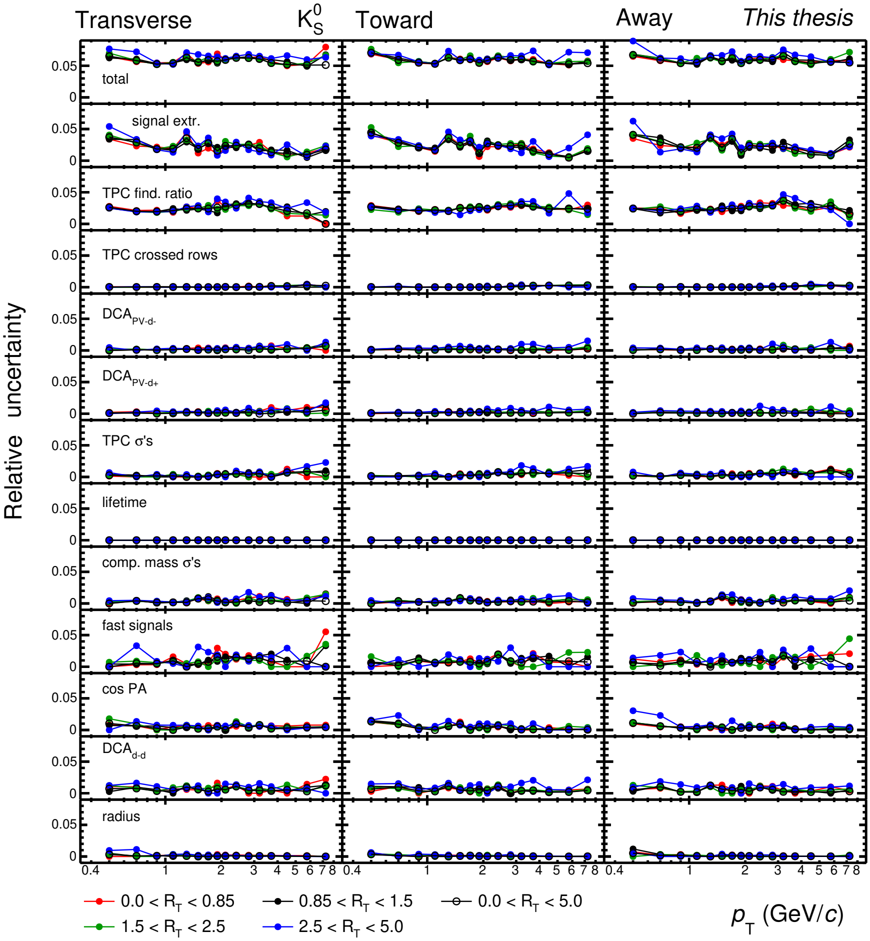

Figure 7.12: Summary of the relative systematic uncertainties on transverse momentum spectra and the individual contributions for K^0_S in the **(left)** Transverse, **(middle)** Toward, and **(right)** Away in the different R_T intervals.

tween K^0_S and Λ. This correlation was expected, as the V^0 species should unfold in similar patterns. Therefore, the systematic uncertainty on the baryon-to-meson ratio was also calculated independently to avoid these correlations and reduce the systematic uncertainty on those results.

Moreover, in the most extreme bins, the non-closures sometimes exhibited unrealistic deviations from unity due to limited statistics and fluctuations. To address this issue, a smoothing procedure was applied by fitting the resulting uncertainties with first- and second-order polynomials. The results are shown in Fig. 7.15.

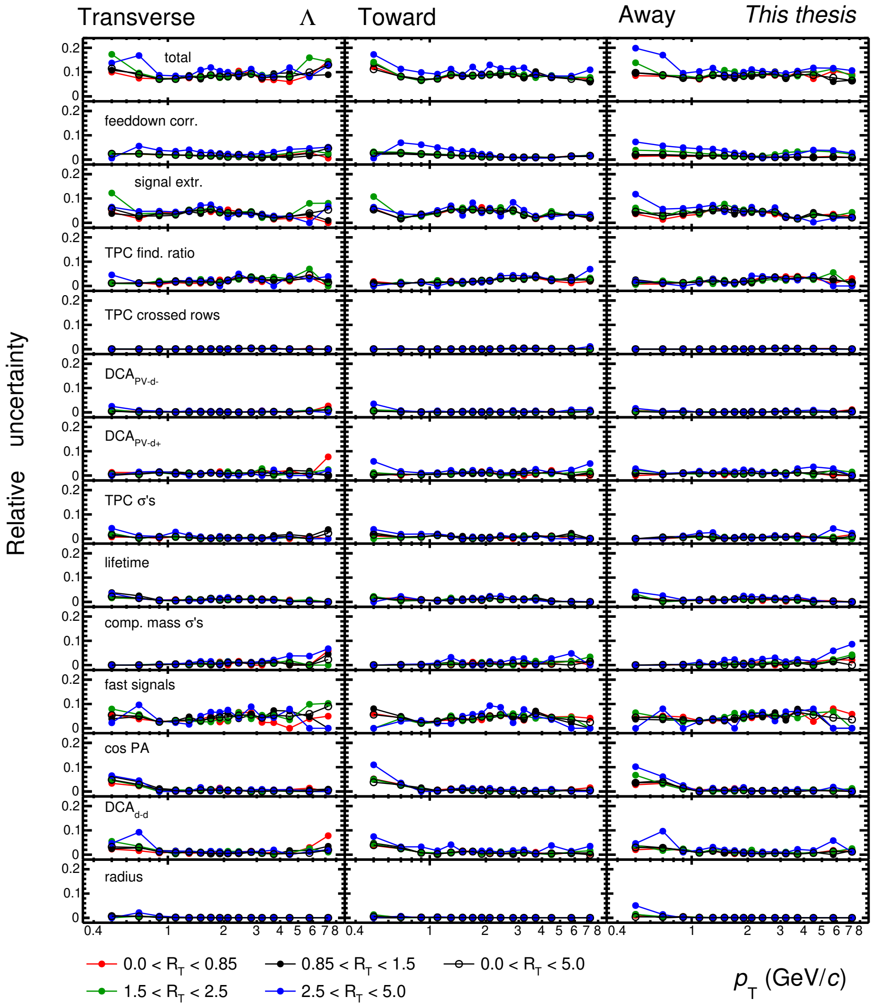

Figure 7.13: Summary of the relative systematic uncertainties on transverse momentum spectra and the individual contributions for Λ in the **(left)** Transverse, **(middle)** Toward, and **(right)** Away in the different R_T intervals.

7.5.2 Uncorrelated uncertainties

Systematic uncertainties may be largely correlated between the different R_T intervals and thus cancel to some degree when reporting ratios of p_T spectra in given R_T bins to the R_T-integrated case. To determine the uncorrelated part, the procedure outlied in Sec. B is followed, in the same fashion as in the $S_\mathrm{O}^{p_\mathrm{T}=1.0}$ measurement. They are reported in Appendix B and summarised in Tab. 7.4.

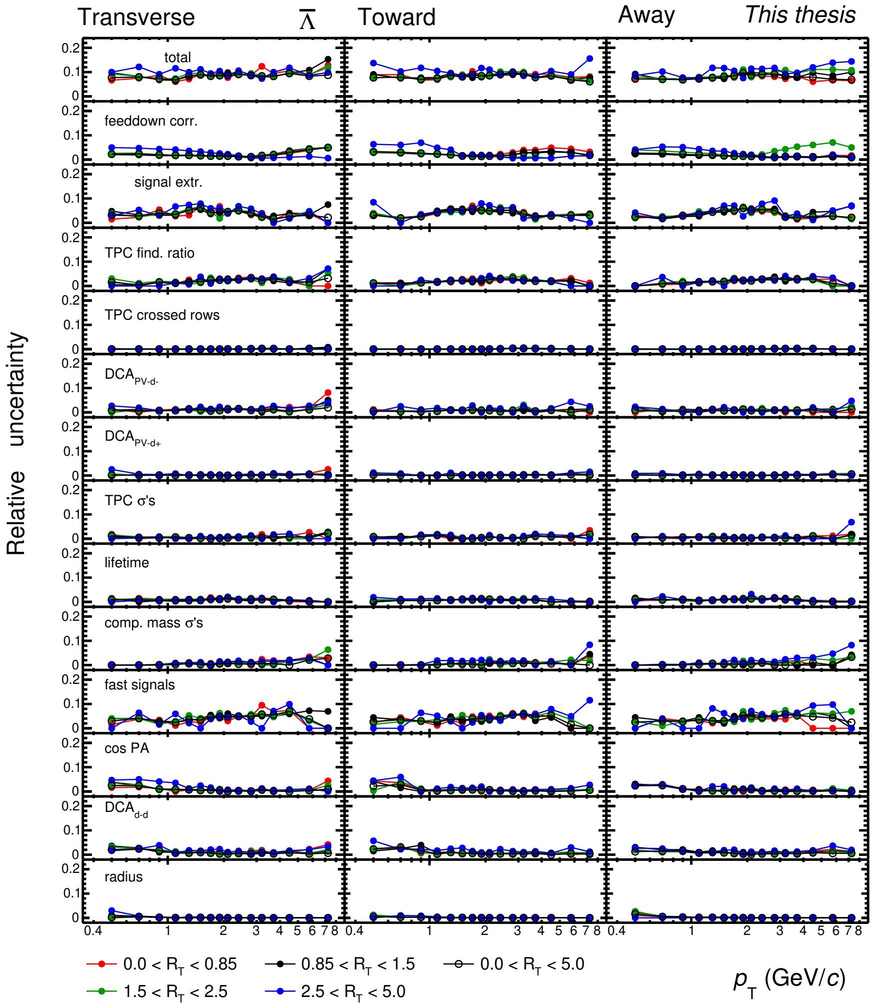

Figure 7.14: Summary of the relative systematic uncertainties on transverse momentum spectra and the individual contributions for $\overline{\Lambda}$ in the **(left)** Transverse, **(middle)** Toward, and **(right)** Away in the different R_{T} intervals.

7.6 Description of regions and mean transverse momentum

After unfolding, the average transverse momenta $\langle p_{\mathrm{T}} \rangle$ of $\mathrm{K^0_S}$ and Λ were studied in the Toward, Away, Transverse, Transverse-min, and Transverse-max regions as a function of N_{T}, $N_{\mathrm{T,min}}$, and $N_{\mathrm{T,max}}$. To guide the focus of the analysis, according to MC paradigms as well as previous UE measurements [169, 172], the following

Table 7.4: The most relevant systematic uncertainties for the long-lived particles $\mathrm{K^0_S}$ and Λ ($\overline{\Lambda}$) as a function of R_T in the Transverse region. "Low" and "high" in this table represent the $0.0 < R_\mathrm{T} < 0.85$ and $2.5 < R_\mathrm{T} < 5.0$ intervals, respectively. Uncertainties are p_T-dependent, and the ranges listed represents the minimum-maximum values presented in the final spectra (see text for details).

R_T selection	Low	High	Unbiased	Low/Unbiased	High/Unbiased
$\mathrm{K^0_S}$					
Selection cuts	2–3%	3–4%	3–4%	0–1%	0–2%
Track pile–up	1–3%	1–3%	1–2%	0–1%	0–2%
Signal extraction	2–3%	1–4%	1–4%	0–1%	0–2%
Efficiency	2%	2%	2%	2%	2%
Material budget	4%	4%	4%	–	–
Unfolding	4–6%	4–8%	–	4–6%	4–8%
Total uncertainty	7–9%	7–10%	6–8%	5–7%	6–7%
$\Lambda(\overline{\Lambda})$					
Selection cuts	1–4%	2–6%	3–5%	1–6%	1–6%
Track pile–up	2–6%	2–7%	2–7%	0–4%	0–5%
Signal extraction	2–5%	2–6%	2–5%	0–3%	0–3%
Feed-down correction	1.0–2%	2–4%	2–3%	Negl.	0–3%
Efficiency	2%	2%	2%	2%	2%
Material budget	4%	4%	4%	–	–
Unfolding	5–10%	2–10%	–	5–10%	2–10%
Total uncertainty	10–13%	11–14%	8–10%	8–11%	8–13%

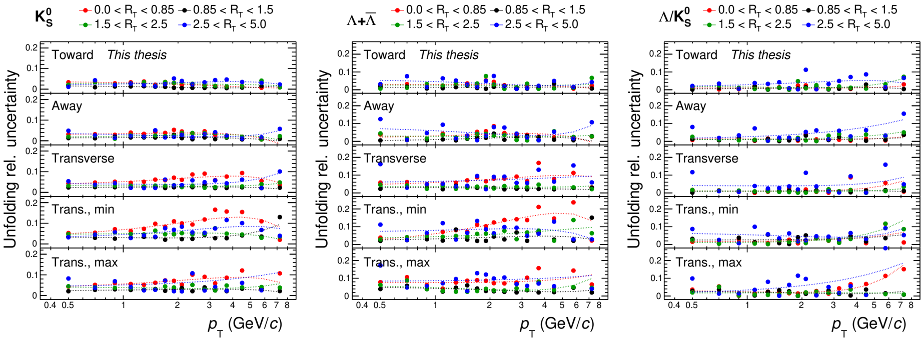

(a) (b) (c)

Figure 7.15: Relative systematic uncertainties on transverse momentum spectra resulting from the Bayesian unfolding treatment for the **(a)** $\mathrm{K^0_S}$, **(b)** $\Lambda + \overline{\Lambda}$, **(c)** and the $(\Lambda+\overline{\Lambda})/(2\mathrm{K^0_S})$ ratio. The smoothened results obtained from first- and second-order polynomial fits are shown as dotted lines.

expectations were considered on the origin of the particles:

1. *Toward and Away regions*: particles from jet fragmentation and underlying event.
2. *Transverse region*: particles from UE, which includes contributions from softer

MPIs and harder wide-angle initial- and final-state radiation.

3. *Transverse-min region*: particles from UE, where the softer MPI contribution dominates.
4. *Transverse-max region*: particles from UE biased towards higher amounts of harder ISR/FSR.

The choice of the independent observable is then expected to focus on the effects of:

1. *Toward and Away regions*: for all N_{T}, $N_{\mathrm{T,min}}$, and $N_{\mathrm{T,max}}$, mixing the relative contributions of UE and jet fragmentation.
2. *Transverse(-min,max) regions*: for N_{T}, the magnitude of the inclusive UE, for $N_{\mathrm{T,min}}$, the magnitude of the softer-MPIs-enhanced UE, and for $N_{\mathrm{T,max}}$, the magnitude of the harder-ISR/FSR-biased UE.

Fig. 7.16 shows the $\mathrm{K^0_S}$ $\langle p_{\mathrm{T}} \rangle$ results for different configurations, obtained from the unfolded spectra.[3] In the Toward and Away regions, the dependence on N_{T}, $N_{\mathrm{T,min}}$, and $N_{\mathrm{T,max}}$ appears comparable, exhibiting a "jet peak" at low N_{T} and a flow-like boost from the underlying event at high N_{T} values. In the Transverse, Transverse-min, and Transverse-max regions, $\langle p_{\mathrm{T}} \rangle$ steeply increases with N_{T}, with an ordering in terms of absolute values, although the slopes are similar. These results suggest that the choice of particle region does not have a significant impact on its dynamical properties.

Additionally, the increase in $\langle p_{\mathrm{T}} \rangle$ with $N_{\mathrm{T,max}}$ is much steeper in the Transverse-max region compared to the Transverse-min region's increase with $N_{\mathrm{T,min}}$, indicating that the choice of independent variable plays the more important role. Together with the choice of particle region, it has the potential to isolate distinct behaviors between the two activity extremes.

Given these findings, this dissertation focuses on the following measurements: Toward/Away/Transverse versus R_{T} (N_{T}), Transverse-min versus $R_{\mathrm{T,min}}$ ($N_{\mathrm{T,min}}$), and Transverse-max versus $R_{\mathrm{T,max}}$ ($N_{\mathrm{T,max}}$).

---

[3] Alternatively, the $\langle p_{\mathrm{T}} \rangle$ values can be calculated by a re-weighting procedure, which determines $\langle p_{\mathrm{T}} \rangle$ on the pre-unfolded spectra and then sums them together with weights obtained from the smearing matrix [162]. However, this method was not pursued in this dissertation.

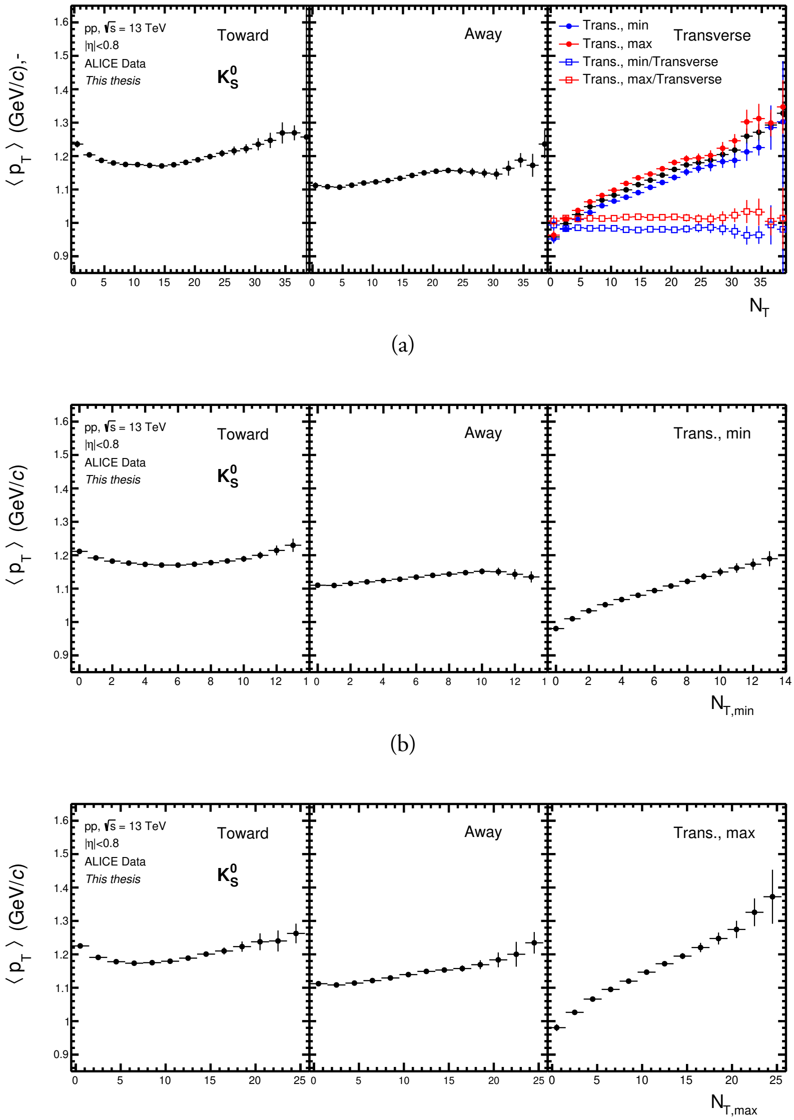

(a)

(b)

(c)

Figure 7.16: Mean transverse momentum for $\mathrm{K^0_S}$ as a function of **(a)** N_T, **(b)** $N_\mathrm{T,min}$, **(c)** $N_\mathrm{T,max}$ in the different azimuthal regions. The x-axis ranges were chosen such that they represent comparable quantiles of the distributions of their variables, to facilitate a more direct comparison. Only statistical uncertainties are presented and systematic biases on $\langle p_\mathrm{T} \rangle$ from the unfolding treatment were not considered.

7.7 Transverse momentum spectra

The measured p_T spectra for $\mathrm{K^0_S}$ and Λ, after applying all corrections and accounting for systematic uncertainties, are presented in Fig. 7.17 and Fig. 7.19, respectively.

In addition, these spectra are compared with model predictions in Fig. 7.18 and Fig. 7.20.

In the Toward and Away regions, there is a dependence on R_{T} at intermediate p_{T}, followed by a convergence ”to a jet” at high p_{T}. This suggests that high-momentum particles solely originating from jets are independent of the UE, as expected. The Transverse region exhibit an increase and hardening with increasing R_{T}, indicating that events with higher UE activity are more likely to contain higher-p_{T} particles. This trend is similar to studies of charged particles at mid-rapidity as a function of N_{ch} measured at mid-rapidity [100], where the auto-correlation bias is an important factor in interpretation.

The behavior of the Transverse-max region is similar to that of the Transverse region, indicating the selection of harder wide-angle ISR/FSR. However, the Transverse-min region seems to plateau, suggesting that at higher p_{T}, $R_{\mathrm{T,min}}$ does not impact the particle p_{T} spectral shapes.

When compared with MC predictions including Pythia Monash, Pythia Ropes, and EPOS LHC, all models reproduce the data qualitatively very well, although quantitative differences can be noticed.

Finally, it is also interesting to remember Pythia and Herwig predictions for inclusive charged particles shown in Fig. 7.5, which showed a steady hardening in high-UE events in the Transverse and Transverse-max regions, whereas a Cronin-like peak was observed for the Transverse-min case. The data reported here offer some support to these expectations but do not explicitely confirm them, suggesting that even higher $R_{\mathrm{T,min}}$ values are needed.

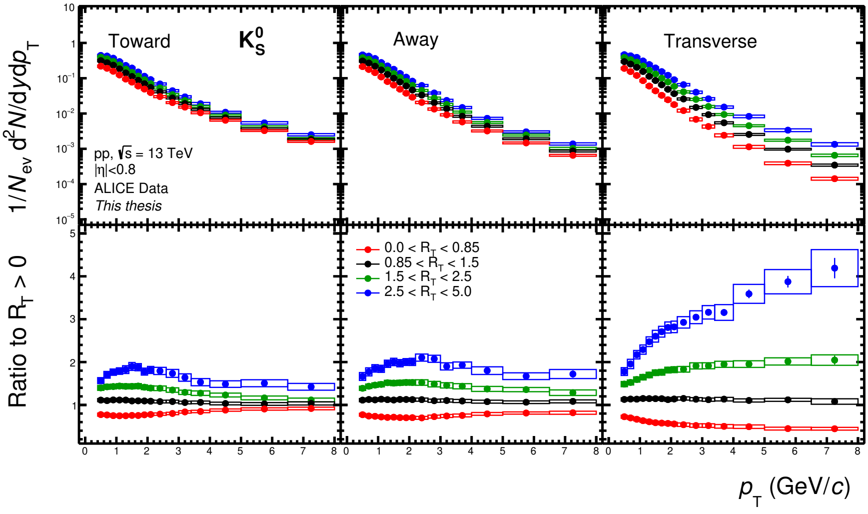

(a)

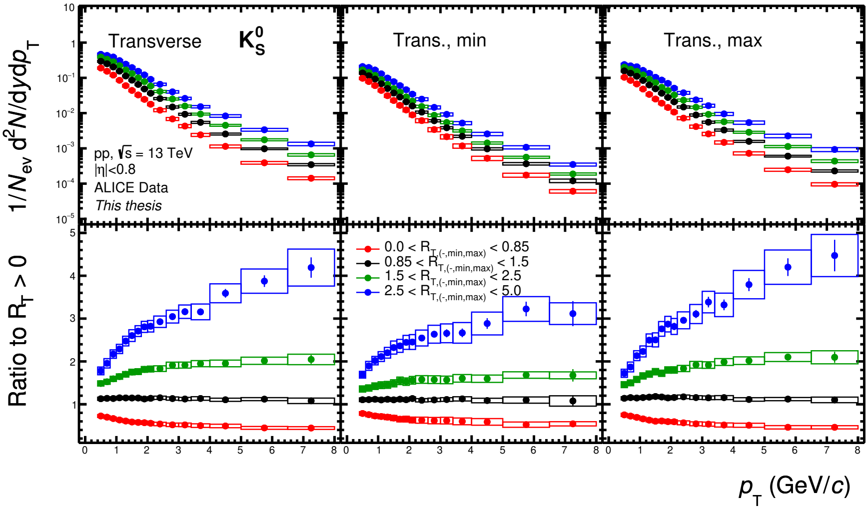

(b)

Figure 7.17: Transverse momentum spectra of K^0_S for different R_T/$R_{\mathrm{T,min}}$/$R_{\mathrm{T,max}}$ intervals in pp collisions at $\sqrt{s} = 13$ TeV in **(a)** Toward, Away, and Transverse, **(b)** Transverse, Transverse-min, and Transverse-max regions. The bottom panels display ratios to the R_T/$R_{\mathrm{T,min}}$/$R_{\mathrm{T,max}}$-integrated cases. The error bars represent statistical uncertainties and the rectangles show the systematic uncertainties.

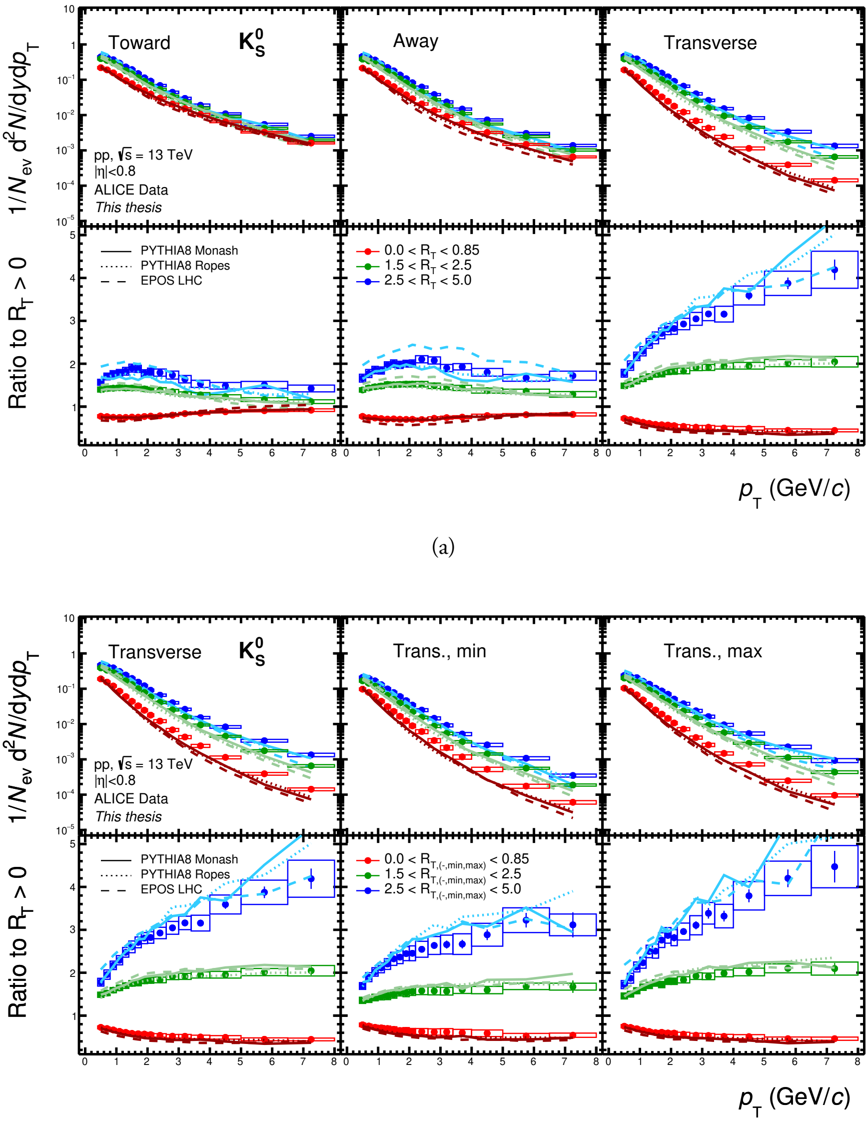

(a)

(b)

Figure 7.18: Transverse momentum spectra of K^0_S for different $R_\mathrm{T}/R_{\mathrm{T,min}}/R_{\mathrm{T,max}}$ intervals in pp collisions at $\sqrt{s} = 13\,\mathrm{TeV}$ compared with MC predictions in **(a)** Toward, Away, and Transverse, **(b)** Transverse, Transverse-min, and Transverse-max regions. The bottom panels display ratios to the $R_\mathrm{T}/R_{\mathrm{T,min}}/R_{\mathrm{T,max}}$-integrated cases. The error bars represent statistical uncertainties and the rectangles show the systematic uncertainties.

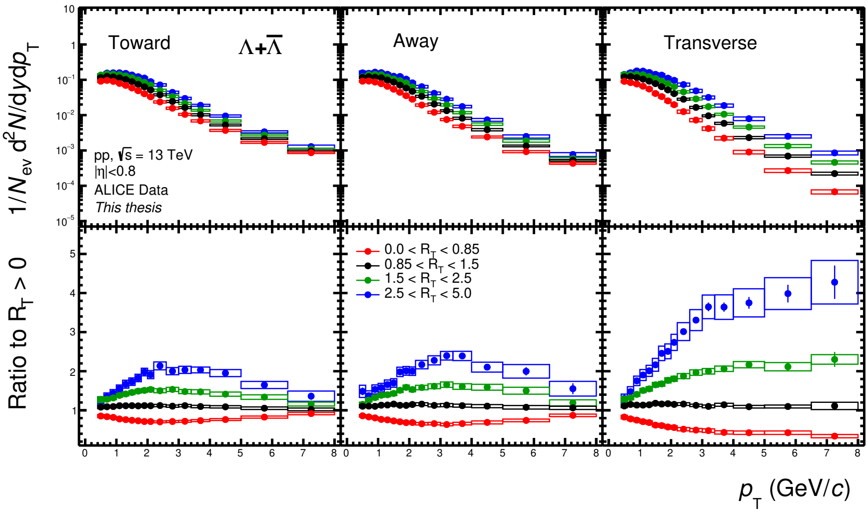

(a)

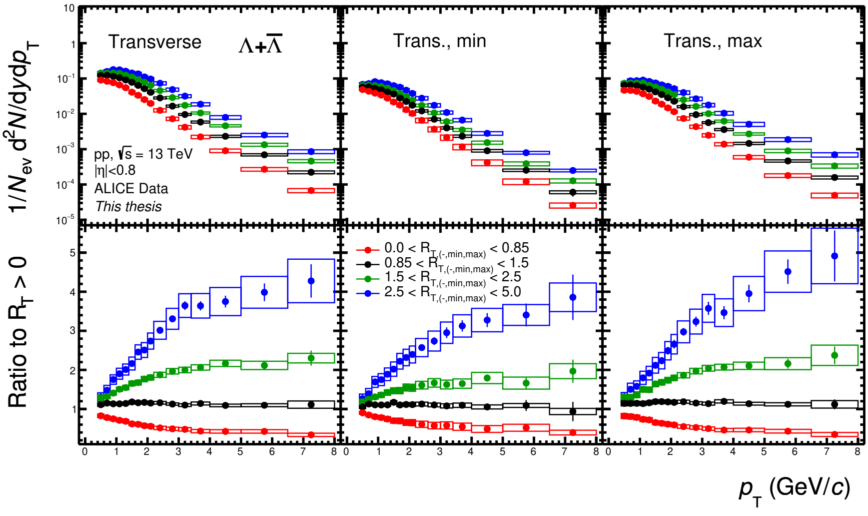

(b)

Figure 7.19: Transverse momentum spectra of $\Lambda + \overline{\Lambda}$ for different R_{T}/$R_{\mathrm{T,min}}$/$R_{\mathrm{T,max}}$ intervals in pp collisions at $\sqrt{s} = 13$ TeV in **(a)** Toward, Away, and Transverse, **(b)** Transverse, Transverse-min, and Transverse-max regions. The bottom panels display ratios to the R_{T}/$R_{\mathrm{T,min}}$/$R_{\mathrm{T,max}}$-integrated cases. The error bars represent statistical uncertainties and the rectangles show the systematic uncertainties.

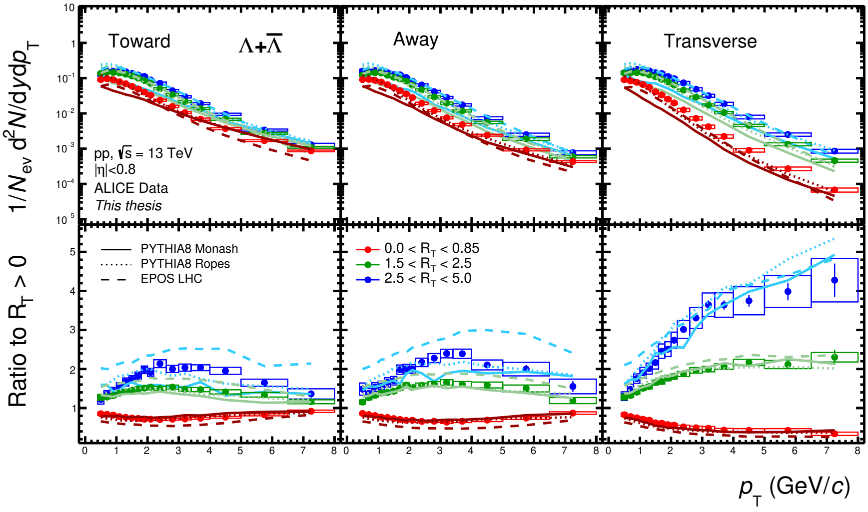

(a)

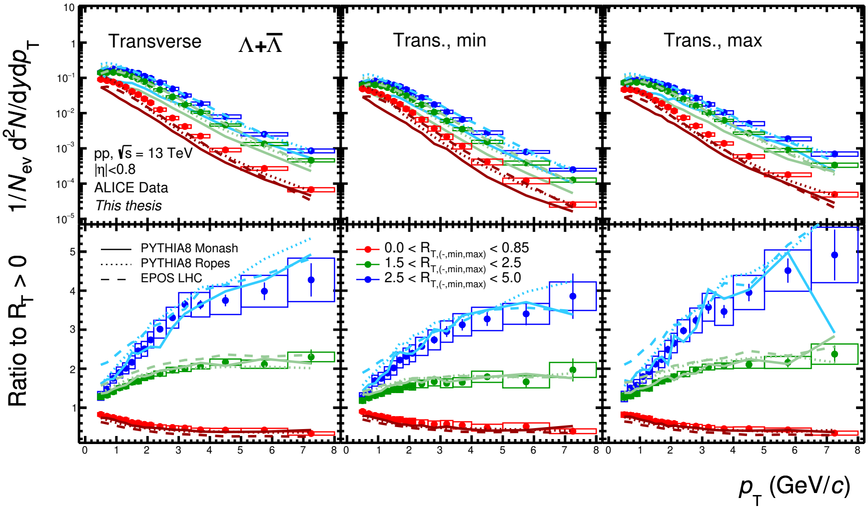

(b)

Figure 7.20: Transverse momentum spectra of $\Lambda + \overline{\Lambda}$ for different $R_{\mathrm{T}}/R_{\mathrm{T,min}}/R_{\mathrm{T,max}}$ intervals in pp collisions at $\sqrt{s} = 13$ TeV compared with MC predictions in **(a)** Toward, Away, and Transverse, **(b)** Transverse, Transverse-min, and Transverse-max regions. The bottom panels display ratios to the $R_{\mathrm{T}}/R_{\mathrm{T,min}}/R_{\mathrm{T,max}}$-integrated cases. The error bars represent statistical uncertainties and the rectangles show the systematic uncertainties.

7.8 Baryon-to-meson ratio

To investigate the observable most directly linked to radial flow studies, the baryon-to-meson ratios, the $(\Lambda + \overline{\Lambda})/(2\mathrm{K}^0_\mathrm{S})$ results are presented in Fig. 7.22, and model predictions are compared in Fig. 7.23.

Noteworthily, the biggest dependence on UE activity can be observed in the Toward and Away regions. Although this may not be immediately intuitive, as one may naively expect these regions to be dominated by jets and thus insensitive to softer phenomena like radial flow, there is a somewhat straightforward interpretation. In this region, R_T controls the amount of interplay between jet-related and UE-related production, which may differ for the K^0_S and Λ. Indeed, ALICE measurements of $(\Lambda+\overline{\Lambda})/(2\mathrm{K}^0_\mathrm{S})$ ratios inside reconstructed jet cones and outside of them [161] reveal a drastic difference, shown in Fig. 7.21, further suggesting that the difference in production regime plays a significant role here, rather than any collective-flow-like behavior due to increased n_MPI.

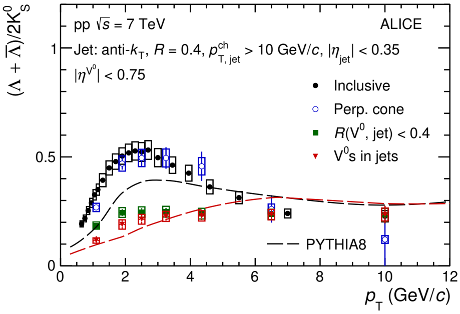

Figure 7.21: The $(\Lambda+\overline{\Lambda})/(2\mathrm{K}^0_\mathrm{S})$ ratio measured with ALICE in pp collisions at $\sqrt{s} = 7$ TeV in events with high-p_T jets, based on the particle origin: inclusive (black), inside the jet cone (green), perpendicular to the jet (blue), and in jets with the UE subtracted (red). [161]

In contrast to the $S_\mathrm{O}^{p_\mathrm{T}=1.0}$ findings, the Transverse region exhibits typical radial flow patterns: enhancement of the ratio at intermediate p_T, corresponding depletion at low p_T, and an overall shift of the peak by about 1 GeV/c. Moreover, despite the fact that the Toward region results and the results in Fig. 7.21 show a significant difference between the “hard” and “soft” productions, the Transverse-min and Transverse-max regions appear to behave very similarly, with small hints of the Transverse-min exhibiting a slightly bigger effect than the Transverse-max, although the results suffer from significant statistical uncertainties. Therefore, more precise measurements are needed to confirm this observation.

Based on the selected models, the Pythia Ropes predictions are the most consistent with the data, whereas EPOS LHC exhibits a much larger dependence on R_{T}, and Pythia Monash significantly underestimates the ratios. The latter two models also demonstrate smaller variations of $(\Lambda+\overline{\Lambda})/(2\mathrm{K}^0_{\mathrm{S}})$ across different regions than the experimental data. Nevertheless, all the model predictions are generally consistent with describing the ratios to the R_{T}-integrated case. Overall, these results suggest that mechanisms that account for interactions between MPI, such as the Pythia Ropes model's implementation of increasing tension strength of many overlapping strings, are a step in the right direction.

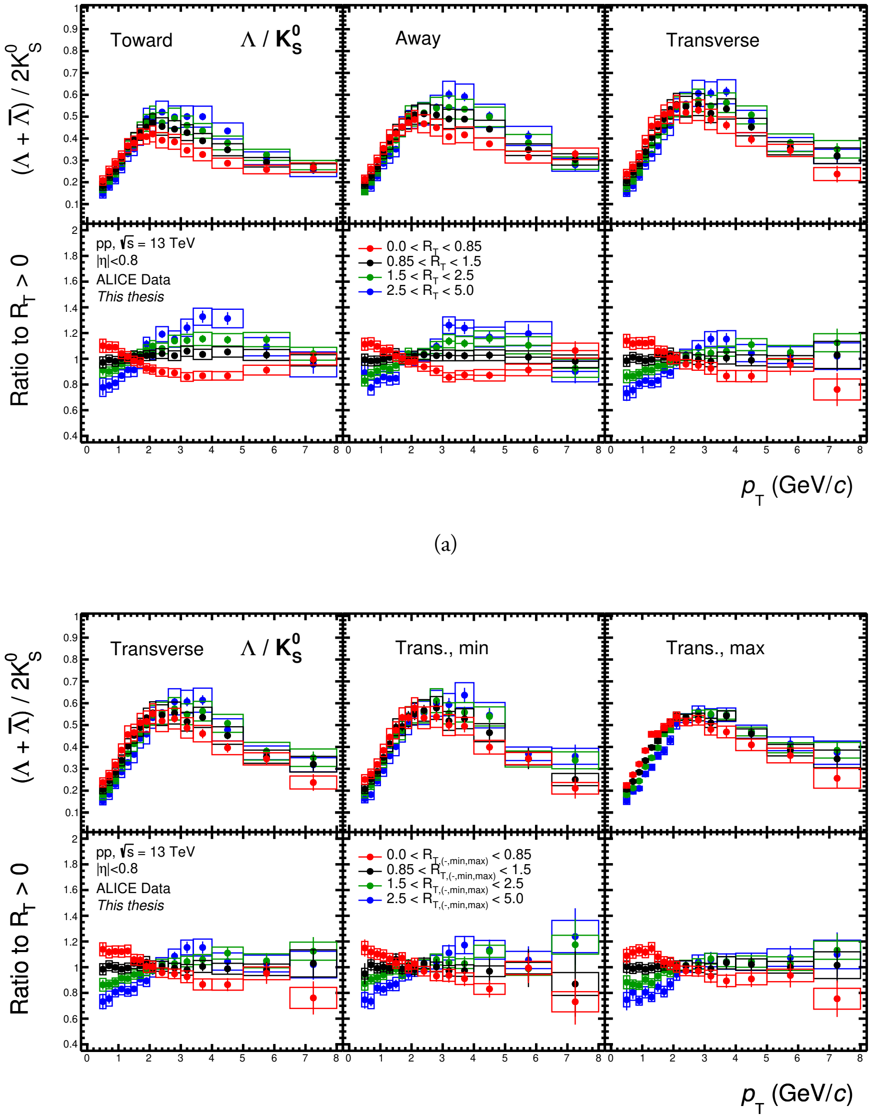

(a)

(b)

Figure 7.22: Baryon-to-meson ratios of p_T spectra $(\Lambda + \overline{\Lambda})/(2\mathrm{K}^0_\mathrm{S})$ for different R_T/$R_{\mathrm{T,min}}$/$R_{\mathrm{T,max}}$ intervals in pp collisions at $\sqrt{s}$ = 13 TeV in **(a)** Toward, Away, and Transverse, **(b)** Transverse, Transverse-min, and Transverse-max regions. The bottom panels display ratios to the R_T/$R_{\mathrm{T,min}}$/$R_{\mathrm{T,max}}$-integrated cases. The error bars represent statistical uncertainties and the rectangles show the systematic uncertainties.

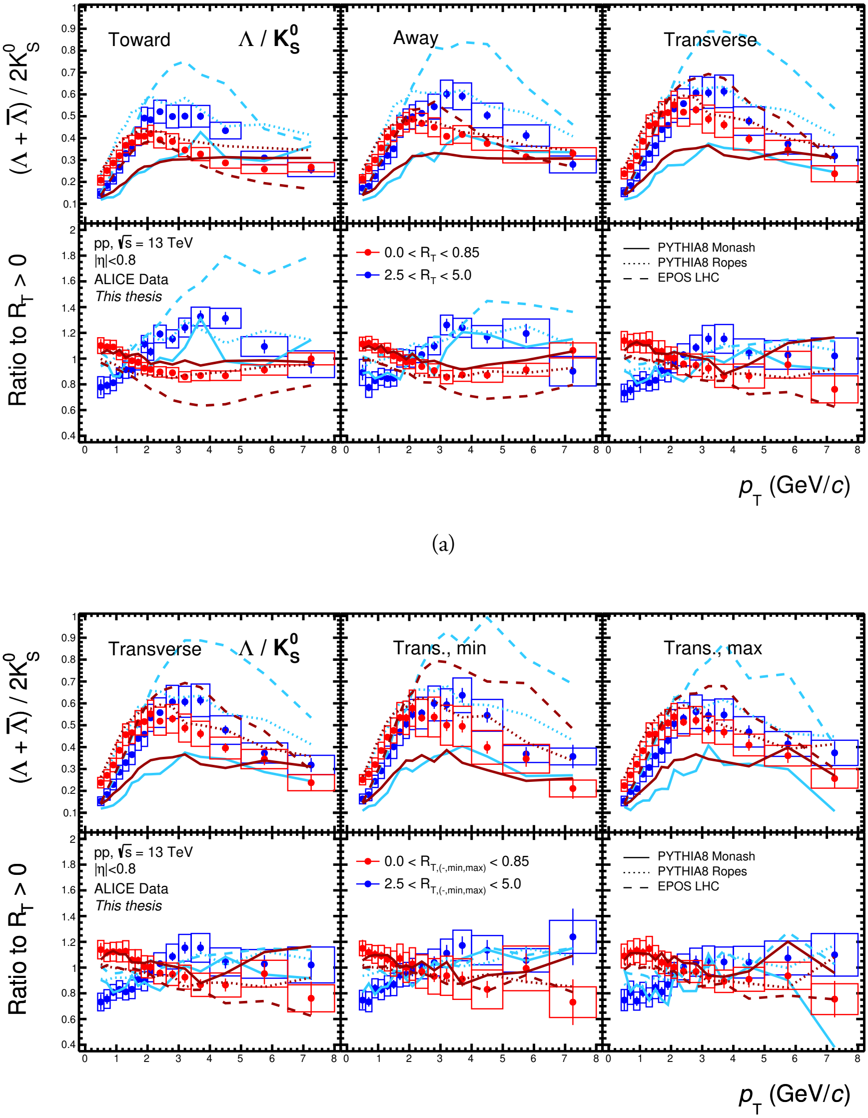

(a)

(b)

Figure 7.23: Baryon-to-meson ratios of p_T spectra $(\Lambda+\overline{\Lambda})/(2K^0_S)$ for different $R_T/R_{T,\min}/R_{T,\max}$ intervals in pp collisions at $\sqrt{s} = 13$ TeV in **(a)** Toward, Away, and Transverse, **(b)** Transverse, Transverse-min, and Transverse-max regions, compared with MC predictions. The bottom panels display ratios to the $R_T/R_{T,\min}/R_{T,\max}$-integrated cases. The error bars represent statistical uncertainties and the rectangles show the systematic uncertainties.

7.9 Integrated yields

Finally, in Fig. 7.24, the integrated yields of K^0_S and Λ are shown as a function of R_T, $R_\mathrm{T,min}$, and $R_\mathrm{T,max}$. The yields are self-normalised, similar to other multiplicity-dependent particle production measurements by ALICE [94, 100]. Using the same approach as in the $S_\mathrm{O}^{p_\mathrm{T}=1.0}$ measurement, for the V^0s, the reported p_T range is used to integrate the yields, rather than extrapolating. The yields are then compared to data on pions and protons, as well as model predictions.

The yields of K^0_S and Λ increase with R_T, but at a slower rate than the underlying UE activity (same rate would correspond to $y = x$). The increase of Λ with R_T appears to be somewhat faster than K^0_S, which is in contrast to similar measurements using forward-rapidity event activity classifier [94]. The largest increase in yields is observed in the Transverse and Transverse-max regions, with the Transverse-min region showing a slightly slower increase. In the Toward and Away regions, the increase in yields appears to be slower than linear.

When comparing the yields of charged particles [159], the effect of decoupling the neutral K^0_S and Λ from the N_T in the Transverse region is evident. There is also slight, albeit systematic evidence for strangeness enhancement in the Toward and Away regions, with K^0_S increasing slightly faster than π and Λ slightly faster than p. However, the uncertainties are significant, and strong conclusions cannot be drawn.

Based on the selected models, Pythia Monash and Pythia Ropes predict values that are consistent with the experimental data. EPOS LHC is also consistent in the Transverse regions but exhibits a faster rise with R_T than what is observed. In addition, it is less sensitive to the choice of regions compared to the other models.

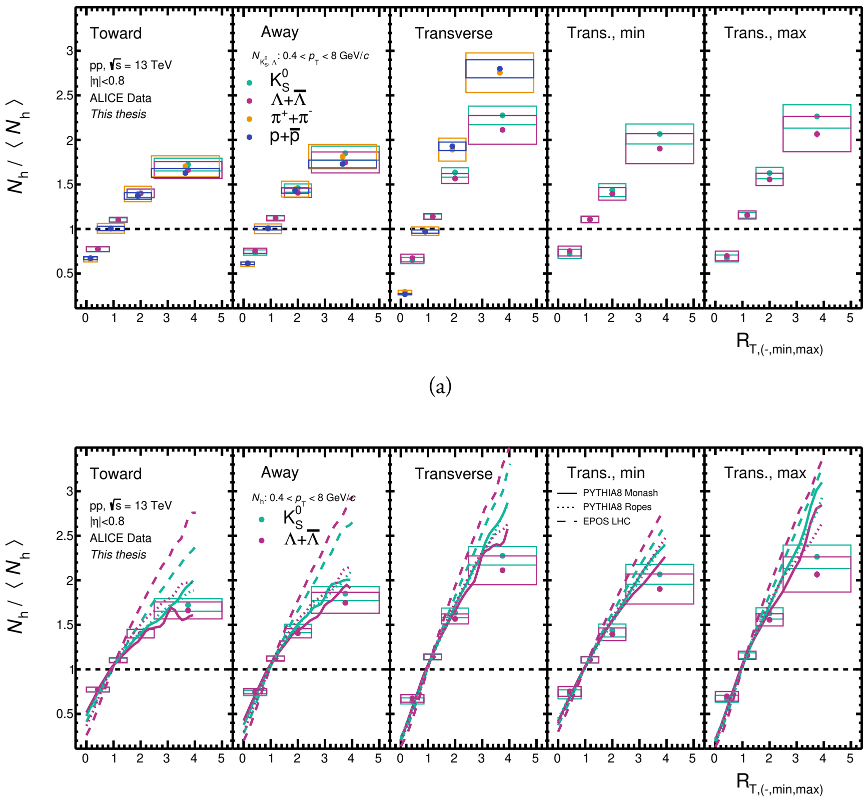

(a)

(b)

Figure 7.24: Self-normalised yields of $\mathrm{K^0_S}$ and $\Lambda + \overline{\Lambda}$ as a function of R_T/$R_{\mathrm{T,min}}$/$R_{\mathrm{T,max}}$, the self-normalised mid-rapidity underlying event activity, compared with **(a)** charged particles [159] and **(b)** MC predictions. The $\mathrm{K^0_S}$ and $\Lambda + \overline{\Lambda}$ yields are determined by integration in the reported p_T range. Datapoints are centered to the median R_T values, and not $\langle R_\mathrm{T} \rangle$, of the given intervals. Statistical and systematic uncertainties are indicated by vertical error bars and boxes, respectively.

Chapter 8

Discussion of results, conclusions, and outlook

8.1 Summary of the research goals

The first part of this dissertation provides an introduction to quantum chromodynamics (QCD), a theory of the fundamental strong force of the Universe, and explains why QCD interactions involving low-momentum (soft) transfers cannot be calculated from first principles, unlike hard processes, which can be computed using perturbation theory. Next, the importance of studying QCD matter at extreme conditions is discussed, specifically the plasma of deconfined quarks and gluons QGP.

Furthermore, the dissertation presents an overview of experimental studies that investigate the properties and signatures of the QGP in AA collisions and their dependence on collision centrality, which can be related to energy densities as well as final-state multiplicities in the system. Special attention is given to the phenomena of strangeness enhancement, where strange particles are produced more abundantly in collisions with larger event activity, and collective flow, where the hydrodynamic behavior of the plasma affects the kinematics of final-state hadrons.

The dissertation also describes the challenges to traditional paradigms, i.e., that pp collisions were thought to be incapable of producing extremes of QCD matter, and lists the observations resembling traditional QGP phenomena in these small system collisions. Moreover, it explains the intricacies of isolating the physics behind these phenomena, given that event multiplicity arises from non-perturbative (softer) as well as perturbative (harder) processes, is susceptible to large fluctuations, and cannot be directly linked to the energy density.

The goal of this dissertation is to provide a clearer and more differential study of QGP phenomena, namely strangeness enhancement and radial flow, and to elucidate the roles played by both soft and hard processes. The aim is to identify and utilise observables that isolate events with extreme activity resulting from non-perturbative processes, where novel physics may be at play, such as the formation of a QGP-like state or complex interactions of overlapping QCD fields. Two state-of-the-art phenomenological models are used to represent these paradigms: EPOS LHC, which includes QGP droplets, and the Ropes tune of Pythia 8, which allows for the merging of strings into higher-tension fields. These observables should also be capable of isolating event activity extremes dominated by perturbative physics at the other end of the spectrum.

Given the complexity of the physics picture and its need to be studied from various angles, these measurements are unlikely to single-handedly confirm or reject the "big hypothesis" of whether QGP is formed in pp collisions. Nevertheless, they are expected to provide valuable insight into the underlying physics processes in hadronic and partonic interactions and their deeper understanding. Furthermore, the measurements have the potential to significantly discriminate between different phenomenological models.

8.2 Highlights of the $S_{\mathrm{O}}^{p_{\mathrm{T}}=1.0}$ measurement

Chapter 6 introduces measurements of the neutral, weakly decaying $\mathrm{K}^0_{\mathrm{S}}$, Λ, and $\overline{\Lambda}$ as a function of transverse spherocity $S_{\mathrm{O}}^{p_{\mathrm{T}}=1.0}$ in pp collisions at $\sqrt{s} = 13\,\mathrm{TeV}$ using the ALICE detector at the LHC. This observable describes the geometrical shape of the charged particles produced in the collision and provides a simple, albeit effective discriminator between pencil-like events, dominated by a di-jet coming from a single hard partonic scattering, and isotropic events, where particles are produced from multiple sources involving lower momentum transfers.

These measurements provide the first ever experimental results of these strange particles as a function of an event shape observable. Moreover, they develop and utilise the so-called unweighted spherocity, a modification from its traditional form S_{O}, which is easier to compare with phenomenological models. The results are fully corrected and come with a thorough inverstigation of their experimental uncertainties.

In this dissertation, the following results are presented: transverse momentum p_{T} spectra, average $\langle p_{\mathrm{T}} \rangle$, ratios of p_{T} spectra to pions, baryon-to-meson ratios, and integrated production yields as a function of $S_{\mathrm{O}}^{p_{\mathrm{T}}=1.0}$ in high-multiplicity events. The following findings can be highlighted:

1. Figure 6.7 shows that $S_{\mathrm{O}}^{p_{\mathrm{T}}=1.0}$ has interplays with the event multiplicity:
    - If high multiplicity is determined at forward-rapidity (V0M), $S_{\mathrm{O}}^{p_{\mathrm{T}}=1.0}$ varies mostly the mid-rapidity multiplicity, leading to more p_{T}-independent increases and decreases in particle spectra between jetty and isotropic events (Fig. 6.14).
    - If high multiplicity is determined at mid-rapidity ($N_{\text{tracklets}}^{|\eta|<0.8}$), $S_{\mathrm{O}}^{p_{\mathrm{T}}=1.0}$ varies mostly the $\langle p_{\mathrm{T}} \rangle$, leading to similar yields but significant hardening and softening between jetty and isotropic events (Fig. 6.14 and Fig. 6.16).

2. Generally, the isotropic spectra are closer to the $S_{\mathrm{O}}^{p_{\mathrm{T}}=1.0}$-unbiased spectra than the jetty are, suggesting that average high-multiplicity collisions are somewhat isotropic, whereas jetty events are outliers. This is a key finding, as it reveals that particle yields in high-multiplicity events are dominated by soft physics, which gives support to comparing measurements as a function of multiplicity across different collision systems.

3. Ratios to pions in Fig. 6.19 reveal that relatively to pions, $\mathrm{K}_{\mathrm{S}}^{0}$ and Λ are consistently suppressed in jetty events and enhanced in isotropic events in $N_{\text{tracklets}}^{|\eta|<0.8}$ classes. This effect is different in the V0M class.

4. The baryon-to-meson ratios $(\Lambda + \overline{\Lambda})/(2\mathrm{K}_{\mathrm{S}}^{0})$ in Fig. 6.20 display an enhancement of Λ in intermediate p_{T} in isotropic events. This is expected with observing radial flow, however, its other characteristic features, such as shift of the peak, are not seen.

5. Ratios of integrated yields to pions in Fig. 6.21 show a characteristic strangeness enhancement behaviour for the $N_{\text{tracklets}}^{|\eta|<0.8}$ class and the effect increases with increasing the mass and strangeness content. This result is the first observation ever of strangeness enhancement that occurs with (mostly) constant multiplicity and suggests that multiplicity alone does not drive strangeness production. In the V0M class, the effect is not observed.

6. Results are compared with selected MC predictions, mostly favouring Pythia 8 Ropes and EPOS LHC over Pythia 8 Monash, although with varying degrees of success.

8.3 Highlights of the R_{T} measurements

Chapter 7 presents measurements of the production of $\mathrm{K}_{\mathrm{S}}^{0}$, Λ, and $\overline{\Lambda}$ in pp collisions at $\sqrt{s} = 13\,\mathrm{TeV}$ and their dependence on the relative underlying event activity R_{T}.

This quantity controls the magnitude of the underlying event, which consists of many softer particles produced through multiple partonic interactions (MPIs) and other sources, and is unrelated to the primary hard partonic scatterings and its fragmentation. It acts as a dial, selecting events resembling ee collisions ($R_{\mathrm{T}} \to 0$, $n_{\mathrm{MPI}} \to 1$) and AA collisions ($R_{\mathrm{T}} \to \infty$, $n_{\mathrm{MPI}} \to \infty$). Particle production is studied in three azimuthal regions based on the highest-p_{T} track, which serves as a proxy for the primary scattering axis: Toward, Away, and Transverse.

Moreover, to distinguish between the contributions to the underlying event from softer (MPIs) and harder (wide-angle radiation ISR/FSR) interactions, this approach is extended to divide the Transverse region further into Transverse-min and Transverse-max based on the number of particles, and define the classifiers $R_{\mathrm{T,min}}$ and $R_{\mathrm{T,max}}$, accordingly. At the time of conducting this measurement, the $R_{\mathrm{T,min}}$ observable is expected to be among the cleanest probes of the $\langle n_{\mathrm{MPI}} \rangle$ available, as the harder contributions are captured in the $R_{\mathrm{T,max}}$ quantity.

The measurements presented in this dissertation are the first ever experimental results of $\mathrm{K^0_S}$, Λ, and $\overline{\Lambda}$ as a function of R_{T}, as well as the first use ever of $R_{\mathrm{T,min}}$ and $R_{\mathrm{T,max}}$ on identified particles. Considerable effort has been required to experimentally use and understand these observables, particularly in the choice of tracks used, the treatment with Bayesian unfolding, and the quantification of systematic uncertainties.

The following results are focused on: p_{T} spectra, $\langle p_{\mathrm{T}} \rangle$, baryon-to-meson ratios, and self-normalised yields. Key outcomes of this study are:

1. Figure 7.16 implies a much steeper increase of $\langle p_{\mathrm{T}} \rangle$ of $\mathrm{K^0_S}$ with $R_{\mathrm{T,max}}$ than $R_{\mathrm{T,min}}$.
2. The transverse momentum spectra in Fig. 7.17 and Fig. 7.19 show:
    - In the Toward region, the spectra in different R_{T} events converge at high p_{T} to the R_{T}-integrated values, corresponding to the dominance of jet.
    - In the Transverse region, p_{T} spectra continue hardening with increasing R_{T}, similarly to the picture in multiplicity measurements.
    - In contrast, the Transverse-min region seems to plateau.
3. The baryon-to-meson ratios in Fig. 7.22 reveal typical radial flow features in high-R_{T} events, including the enhancement of intermediate-p_{T} baryons, their depletion at low-p_{T}, as well as shifts of the peaks. Moreover,
    - In the Toward region, the effect is the largest. This is due to the mixing of jet- and UE-related particle production, which shows largely different $(\Lambda + \overline{\Lambda})/(2\mathrm{K^0_S})$ ratios.

  - The effect is comparable among the Transverse, Transverse-min, and Transverse-max regions, with only small hints of being slightly bigger in the Transverse-min case. This suggests that the harder and softer components of the UE affect the relative production of Λ and K^0_S in a similar fashion.
  - The fact that the Transverse-min and Transverse-max regions show similar behaviour somewhat contrasts the Toward region results, which displayed a large difference between the harder (jet) and softer (UE) components of particle production.

4. The self-normalised yields in Fig. 7.24 of K^0_S and Λ are consistent with π and p, respectively, in the Toward and Away regions, although more experimental precision is needed. In the Transverse region, the effect of auto-correllation is apparent for the charged particles. Moreover, the K^0_S and Λ yields rise more slowly in the Transverse-min cases than the Transverse-max.

5. The experimental data favour the Pythia 8 Ropes predictions. EPOS LHC does not display the right amount of sensitivity to the azimuthal region and the Pythia 8 Monash tune underestimates the effects of radial flow. This implies that Colour Reconnection is somewhat insufficient to describe the flow-like behaviour.

6. Generally, higher values of $R_\mathrm{T}/R_{\mathrm{T,min}}/R_{\mathrm{T,max}}$ observables need to be reached in order to isolate the different behaviours of softer MPIs and harder ISR/FSR and further test the MC predictions.

8.4 Outlook

There are several directions in which the measurements in this dissertation could be expanded. To begin with, one possibility would be to extend the $S_\mathrm{O}^{p_\mathrm{T}=1.0}$ and R_T measurements to the charm sector. Charm quarks cannot be produced through string breakings, and must instead come directly from the scattering process. Therefore, this would be a rigorous test of models that simulate QGP-like signatures in pp collisions by either forming QGP droplets or through complex interactions of colour strings.

Some evidence for QGP-like behaviour in the heavy flavour sector has already been observed, such as the suppression of excited Υ states with increasing multiplicity in events with high sphericity, discussed in Sec. 2.3. However, the much heavier $\mathrm{b\bar{b}}$ system is somewhat difficult to juxtapose with light-flavour measurements since hadronisation is modelled in completely different ways [173, 174] and the significant momentum transfer required further biases event observables. Therefore, studying the D meson might be a better way to bridge and contextualise the light- and heavy-flavour sectors. As an example, one could measure and compare the production of D^0 and D_s. Apart from providing an additional way to investigate strangeness enhancement, this measurement also directly studies the effect of the early-produced charm quark forming colour fields with the abundant up and down quarks, also present in beam remnants, or the suppressed strange quark. This can further test CR and string interaction mechanisms.

These ideas also align with the upgrades at ALICE. Measuring the open-charm hadrons is statistically and experimentally demanding, nonetheless, the Run 3 upgrade of ALICE increased its capabilities for charm reconstruction. This is thanks to the implementation of new tracking detectors that significantly improve the estimation of secondary vertices and increase the signal to background ratio.

Part IV

Appendices

Appendix A

List of acronyms

AA	nucleus-nucleus collisions
A side	ATLAS side
ALICE	A Large Ion Collider Experiment
ATLAS	A Toroidal LHC Apparatus
BK	The Balitsky-Kovchegov equation
C side	CMS side
CERN	European Organisation for Nuclear Research
CMS	Compact Muon Solenoid
CP	Charge-Parity
CR	Colour Reconnection
DCA	Distance of Closest Approach
DGLAP	The Dokshitzer–Gribov–Lipatov–Altarelli–Parisi equation
FSR	Final State Radiation
GEANT	Geometry And Tracking
GEM	Gas Electron Multiplier
HM	High Multiplicity
HRG	Hadron Resonance Gas
IP	Interaction Point
ISR	Initial State Radiation

ITS	Inner Tracking System
LHC	The Large Hadron Collider
LHCb	LHC beauty
LQCD	Lattice QCD
MB	Minimum Bias
MC	Monte Carlo
MPIs	Multiple Partonic Interactions
MWPC	Multiwire Proportional Chambers
pA	proton-nucleus collisions
PA	Pointing Angle
Pb-Pb	lead-lead collisions
PCA	Point of Closest Approach
PID	Particle Identification
pp	proton-proton collisions
pQCD	perturbative QCD
PV	Primary Vertex
QCD	Quantum Chromodynamics
QED	Quantum Electrodynamics
QFT	Quantum Field Theory
QGP	Quark-Gluon Plasma
RHIC	Relativistic Heavy Ion Collider
ROC	Read-Out Chamber
SM	Standard Model
SPD	Silicon Pixel Detector
SPS	Super Proton Synchrotron
TOF	Time-Of-Flight detector
TPC	Time Projection Chamber
UE	Underlying Event

Appendix B

Uncorrelated systematic uncertainties in the R_T measurement

This appendix presents the uncorrelated components of systematic uncertainties with respect to R_T selection that are used for the ratios of R_T-biased transverse momentum spectra to R_T-integrated one. See text in Sec. for details and Sec. for the methodology used for their calculation. The results can be seen in Fig. B.1, Fig. B.2, and Fig. B.3 for the K^0_S, Λ, and $\overline{\Lambda}$, respectively.

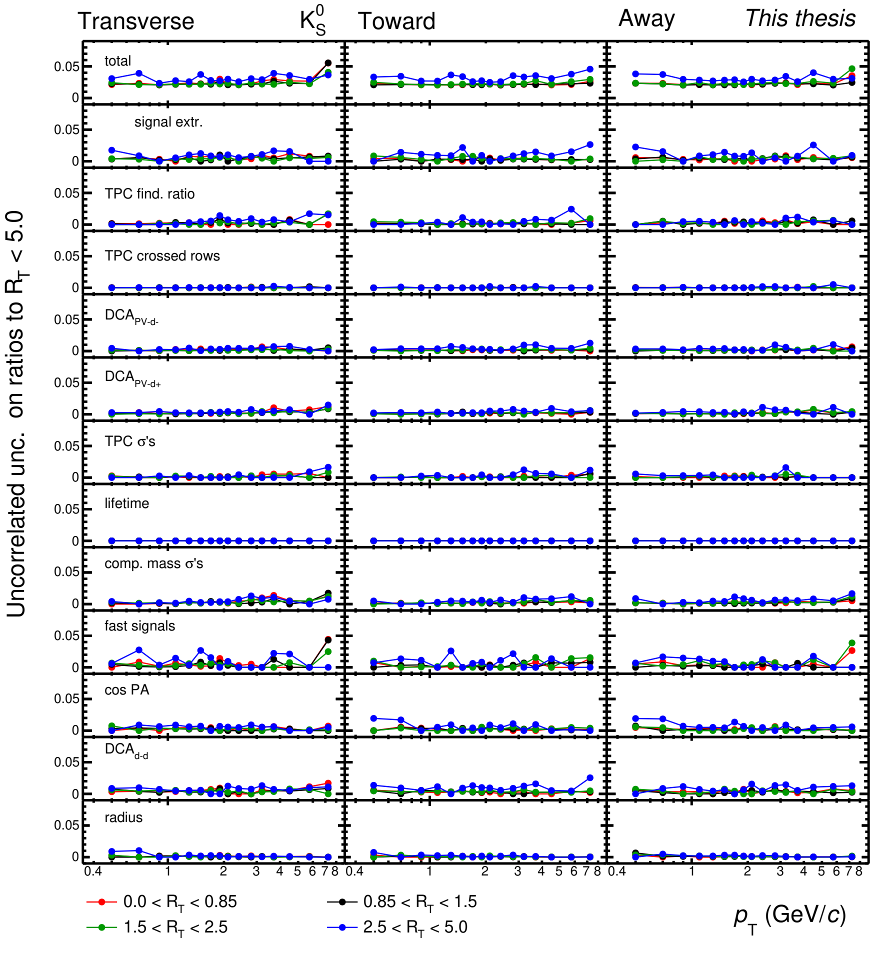

Figure B.1: Summary of the uncorrelated relative systematic uncertainties on ratios of transverse momentum spectra with an R_{T} selection to R_{T}-integrated ones for $\mathrm{K}^0_{\mathrm{S}}$ in the **(left)** Transverse, **(middle)** Toward, and **(right)** Away in the different R_{T} intervals.

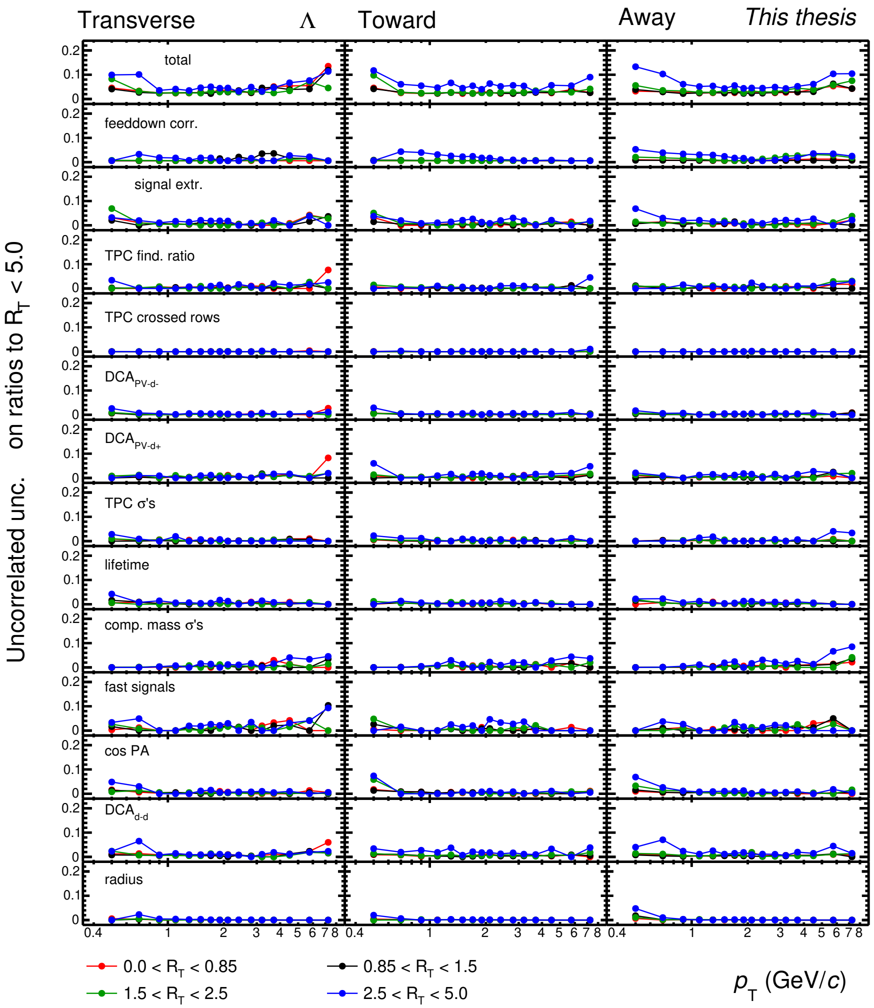

Figure B.2: Summary of the uncorrelated relative systematic uncertainties on ratios of transverse momentum spectra with an R_{T} selection to R_{T}-integrated ones for Λ in the **(left)** Transverse, **(middle)** Toward, and **(right)** Away in the different R_{T} intervals.

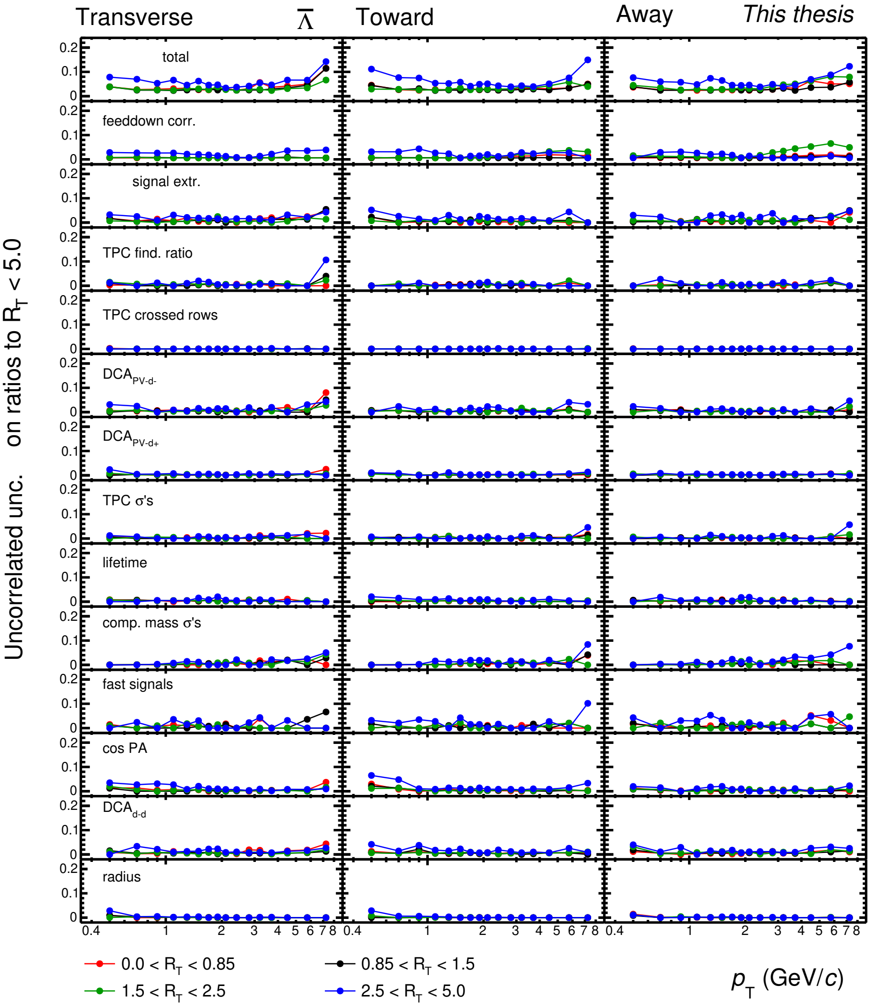

Figure B.3: Summary of the uncorrelated relative systematic uncertainties on ratios of transverse momentum spectra with an R_T selection to R_T-integrated ones for $\overline{\Lambda}$ in the **(left)** Transverse, **(middle)** Toward, and **(right)** Away in the different R_T intervals.

References

[1] M. Tanabashi *et al.*, “Review of Particle Physics,” *Phys. Rev. D*, vol. 98, no. 3, p. 030001, 2018.

[2] P. W. Higgs, “Broken Symmetries and the Masses of Gauge Bosons,” *Phys. Rev. Lett.*, vol. 13, no. 16, pp. 508–509, Oct. 1964.

[3] F. Englert and R. Brout, “Broken Symmetry and the Mass of Gauge Vector Mesons,” *Phys. Rev. Lett.*, vol. 13, no. 9, pp. 321–323, Aug. 1964.

[4] The ATLAS Collaboration, “Observation of a new particle in the search for the Standard Model Higgs boson with the ATLAS detector at the LHC,” *Physics Letters B*, vol. 716, no. 1, pp. 1–29, Sep. 2012.

[5] The CMS Collaboration, “Observation of a new boson at a mass of 125 GeV with the CMS experiment at the LHC,” *Physics Letters B*, vol. 716, no. 1, pp. 30–61, Sep. 2012.

[6] Particle Data Group *et al.*, “Review of Particle Physics,” *Progress of Theoretical and Experimental Physics*, vol. 2022, no. 8, p. 083C01, Aug. 2022.

[7] H. Fritzsch, “Fundamental Constants at High Energy,” *Fortschr. Phys.*, vol. 50, no. 5-7, pp. 518–524, May 2002.

[8] B. Delamotte, “A hint of renormalization,” *American Journal of Physics*, vol. 72, no. 2, pp. 170–184, Feb. 2004.

[9] B. Odom *et al.*, “New Measurement of the Electron Magnetic Moment Using a One-Electron Quantum Cyclotron,” *Phys. Rev. Lett.*, vol. 97, no. 3, p. 030801, Jul. 2006.

[10] G. Altarelli, “A QCD Primer,” in *AIP Conference Proceedings*, vol. 631, 2002, pp. 70–111.

[11] H. D. Politzer, "Reliable Perturbative Results for Strong Interactions?" *Phys. Rev. Lett.*, vol. 30, no. 26, pp. 1346–1349, Jun. 1973.

[12] A. Deur, S. J. Brodsky, and G. F. de Teramond, "The QCD Running Coupling," *Progress in Particle and Nuclear Physics*, vol. 90, pp. 1–74, Sep. 2016.

[13] D. J. Gross and F. Wilczek, "Asymptotically Free Gauge Theories. I," *Phys. Rev. D*, vol. 8, no. 10, pp. 3633–3652, Nov. 1973.

[14] G. Dissertori, "The Determination of the Strong Coupling Constant," in *Advanced Series on Directions in High Energy Physics*, Oct. 2016, vol. 26, pp. 113–128.

[15] S. Prestel, "Lecture notes: Particle Physics Phenomenology," https://canvas.education.lu.se/courses/14231, Lund University, 2022.

[16] G. Altarelli and G. Parisi, "Asymptotic freedom in parton language," *Nuclear Physics B*, vol. 126, no. 2, pp. 298–318, Aug. 1977.

[17] J. C. Collins, D. E. Soper, and G. Sterman, "Factorization of Hard Processes in QCD," http://arxiv.org/abs/hep-ph/0409313, Sep. 2004.

[18] A. M. Cooper-Sarkar, "Extraction of the proton parton density functions using a NLO-QCD fit of the combined H1 and ZEUS inclusive DIS cross sections," http://arxiv.org/abs/0808.1854, Aug. 2008.

[19] C. Marquet and G. Soyez, "The Balitsky-Kovchegov equation in full momentum space," *Nuclear Physics A*, vol. 760, no. 1-2, pp. 208–222, Oct. 2005.

[20] STAR Collaboration *et al.*, "Evidence for Nonlinear Gluon Effects in QCD and Their Mass Number Dependence at STAR," *Phys. Rev. Lett.*, vol. 129, no. 9, p. 092501, Aug. 2022.

[21] S. Ferreres-Solé and T. Sjöstrand, "The Space-Time Structure of Hadronization in the Lund Model," *Eur. Phys. J. C*, vol. 78, no. 11, p. 983, Nov. 2018.

[22] T. Sjostrand, "QCD for BSM in PYTHIA," http://home.thep.lu.se/~torbjorn/talks/kyoto11bsm.pdf, IMPU-YITP Workshop, Kyoto, 2011.

[23] T. Åkesson *et al.*, "Double Parton Scattering in p p Collisions at \sqrts=63-GeV," *Z. Phys. C*, vol. 34, p. 163, 1987.

[24] Z. Koba, H. B. Nielsen, and P. Olesen, "Scaling of multiplicity distributions in high energy hadron collisions," *Nuclear Physics B*, vol. 40, pp. 317–334, Jan. 1972.

[25] G. J. Alner *et al.*, "Scaling violation favouring high multiplicity events at 540 GeV CMS energy," *Physics Letters B*, vol. 138, no. 4, pp. 304–310, Apr. 1984.

[26] R. E. Ansorge *et al.*, "Charged particle multiplicity distributions at 200 and 900 GeV c.m. energy," *Z. Phys. C - Particles and Fields*, vol. 43, no. 3, pp. 357–374, Sep. 1989.

[27] T. Sjöstrand, "The Development of MPI Modelling in PYTHIA," http://arxiv.org/abs/1706.02166, Jun. 2017.

[28] "Electroweak measurements in electron–positron collisions at W-boson-pair energies at LEP," *Physics Reports*, vol. 532, no. 4, pp. 119–244, Nov. 2013.

[29] C. Bierlich *et al.*, "A comprehensive guide to the physics and usage of PYTHIA 8.3," http://arxiv.org/abs/2203.11601, Mar. 2022.

[30] G. Gustafson, "Multiple Interactions, Saturation, and Final States in pp Collisions and DIS," http://arxiv.org/abs/0905.2492, May 2009.

[31] A. Ortiz *et al.*, "Color reconnection and flow-like patterns in pp collisions," *Phys. Rev. Lett.*, vol. 111, no. 4, p. 042001, Jul. 2013.

[32] CDF Collaboration *et al.*, "Charged jet evolution and the underlying event in proton-antiproton collisions at 1.8 TeV," *Phys. Rev. D*, vol. 65, no. 9, p. 092002, Apr. 2002.

[33] G. Arnison *et al.*, "Hadronic jet production at the CERN proton-antiproton collider," *Physics Letters B*, vol. 132, no. 1, pp. 214–222, Nov. 1983.

[34] H. Caines, "Underlying Event Studies at RHIC," http://arxiv.org/abs/0910.5203, Oct. 2009.

[35] C. E. DeTar and J. F. Donoghue, "BAG MODELS OF HADRONS," *Ann.Rev.Nucl.Part.Sci.*, vol. 33, pp. 235–264, 1983.

[36] O. Matonoha, "Upsilon meson production in heavy-ion collisions at the STAR experiment," Diploma Thesis (Monograph), Czech Technical University in Prague, 2018.

[37] C. Wong, *Introduction to High-Energy Heavy-Ion Collisions.* United States: World Scientific Pub Co, 1990.

[38] J. McGreevy, "Lecture Notes: Quantum Ideal Gases," https://mcgreevy.physics.ucsd.edu/s12/lecture-notes/chapter09.pdf, University of California San Diego.

[39] H. B. Meyer, “Lattice QCD: A Brief Introduction,” in *Lattice QCD for Nuclear Physics*, ser. Lecture Notes in Physics, H.-W. Lin and H. B. Meyer, Eds. Cham: Springer International Publishing, 2015, pp. 1–34.

[40] E. Bennett *et al.*, “BSMBench: A flexible and scalable HPC benchmark from beyond the standard model physics,” in *2016 International Conference on High Performance Computing & Simulation (HPCS)*, Jul. 2016, pp. 834–839.

[41] K. Nagata, “Finite-density lattice QCD and sign problem: Current status and open problems,” *Progress in Particle and Nuclear Physics*, vol. 127, p. 103991, Nov. 2022.

[42] S. Dürr *et al.*, “Ab Initio Determination of Light Hadron Masses,” *Science*, vol. 322, no. 5905, pp. 1224–1227, Nov. 2008.

[43] P. Petreczky, “Lattice QCD at non-zero temperature,” *J. Phys. G: Nucl. Part. Phys.*, vol. 39, no. 9, p. 093002, Aug. 2012.

[44] A. Bazavov *et al.*, “The equation of state in (2+1)-flavor QCD,” *Phys. Rev. D*, vol. 90, no. 9, p. 094503, Nov. 2014.

[45] R. Pasechnik and M. Šumbera, “Phenomenological Review on Quark–Gluon Plasma: Concepts vs. Observations,” *Universe*, vol. 3, no. 1, p. 7, Jan. 2017.

[46] H. Sazdjian, “Introduction to chiral symmetry in QCD,” *EPJ Web Conf.*, vol. 137, p. 02001, 2017.

[47] S. Gottlieb *et al.*, “Estimating the chiral-symmetry–restoration temperature in two-flavor QCD,” *Phys. Rev. Lett.*, vol. 59, no. 14, pp. 1513–1516, Oct. 1987.

[48] Y.-Z. Xu, S.-X. Qin, and H.-S. Zong, “Chiral symmetry restoration and properties of Goldstone bosons at finite temperature,” *Chinese Phys. C*, vol. 47, no. 3, p. 033107, Mar. 2023.

[49] STAR Collaboration *et al.*, “Search for the Chiral Magnetic Effect with Isobar Collisions at $\sqrt{s_{NN}}$ = 200 GeV by the STAR Collaboration at RHIC,” http://arxiv.org/abs/2109.00131, Aug. 2021.

[50] P. M. Hohler and R. Rapp, “Is ρ-meson melting compatible with chiral restoration?” *Physics Letters B*, vol. 731, pp. 103–109, Apr. 2014.

[51] M. L. Miller *et al.*, “Glauber Modeling in High Energy Nuclear Collisions,” *Annu. Rev. Nucl. Part. Sci.*, vol. 57, no. 1, pp. 205–243, Nov. 2007.

[52] D. Kharzeev and M. Nardi, “Hadron production in nuclear collisions at RHIC and high density QCD,” *Physics Letters B*, vol. 507, no. 1-4, pp. 121–128, May 2001.

[53] B. Schenke, P. Tribedy, and R. Venugopalan, “Fluctuating Glasma Initial Conditions and Flow in Heavy Ion Collisions,” *Phys. Rev. Lett.*, vol. 108, no. 25, p. 252301, Jun. 2012.

[54] C. Loizides, “Glauber modeling of high-energy nuclear collisions at subnucleon level,” *Phys. Rev. C*, vol. 94, no. 2, p. 024914, Aug. 2016.

[55] S. Borsányi, “Thermodynamics of the QCD transition from lattice,” *Nuclear Physics A*, vol. 904–905, pp. 270c–277c, May 2013.

[56] I. Arsene *et al.*, “Quark–gluon plasma and color glass condensate at RHIC? The perspective from the BRAHMS experiment,” *Nuclear Physics A*, vol. 757, no. 1, pp. 1–27, Aug. 2005.

[57] J. Adams *et al.*, “Experimental and theoretical challenges in the search for the quark–gluon plasma: The STAR Collaboration’s critical assessment of the evidence from RHIC collisions,” *Nuclear Physics A*, vol. 757, no. 1, pp. 102–183, Aug. 2005.

[58] T. Niida and Y. Miake, “Signatures of QGP at RHIC and the LHC,” http://arxiv.org/abs/2104.11406, Apr. 2021.

[59] U. Heinz and M. Jacob, “Evidence for a New State of Matter: An Assessment of the Results from the CERN Lead Beam Programme,” http://arxiv.org/abs/nucl-th/0002042, Feb. 2000.

[60] CMS Collaboration, “Measurement of nuclear modification factors of $\Upsilon(1S)$, $\Upsilon(2S)$, and $\Upsilon(3S)$ mesons in PbPb collisions at $\sqrt{s_{\mathrm{NN}}} = 5.02$ TeV,” *Physics Letters B*, vol. 790, pp. 270–293, Mar. 2019.

[61] L. Adamczyk *et al.*, “Global Λ hyperon polarization in nuclear collisions,” *Nature*, vol. 548, no. 7665, pp. 62–65, Aug. 2017.

[62] D. E. Kharzeev, L. D. McLerran, and H. J. Warringa, “The effects of topological charge change in heavy ion collisions: ”Event by event P and CP violation”,” *Nuclear Physics A*, vol. 803, no. 3-4, pp. 227–253, May 2008.

[63] ALICE Collaboration, “The ALICE experiment – A journey through QCD,” http://arxiv.org/abs/2211.04384, Nov. 2022.

[64] S. Sarkar, H. Satz, and B. Sinha, Eds., *The Physics of the Quark-Gluon Plasma: Introductory Lectures*, ser. Lecture Notes in Physics. Berlin, Heidelberg: Springer, 2010, vol. 785.

[65] T. Matsui and H. Satz, "J/ψ suppression by quark-gluon plasma formation," *Physics Letters B*, vol. 178, no. 4, pp. 416–422, Oct. 1986.

[66] H. Satz, "Probing the States of Matter in QCD," *Int. J. Mod. Phys. A*, vol. 28, no. 27, p. 1330043, Oct. 2013.

[67] B. Krouppa and M. Strickland, "Predictions for bottomonia suppression in 5.023 TeV Pb-Pb collisions," *Universe*, vol. 2, no. 3, p. 16, Aug. 2016.

[68] J. Rafelski and B. Müller, "Strangeness Production in the Quark-Gluon Plasma," *Phys. Rev. Lett.*, vol. 48, no. 16, pp. 1066–1069, Apr. 1982.

[69] P. Koch, B. Müller, and J. Rafelski, "Strangeness in relativistic heavy ion collisions," *Physics Reports*, vol. 142, no. 4, pp. 167–262, Sep. 1986.

[70] ALICE Collaboration, "Multi-strange baryon production in p-Pb collisions at $\sqrt{s_{\mathbf{NN}}} = 5.02$ TeV," http://arxiv.org/abs/1512.07227, Jan. 2016.

[71] A. Andronic, P. Braun-Munzinger, and J. Stachel, "Thermal hadron production in relativistic nuclear collisions: The hadron mass spectrum, the horn, and the QCD phase transition," *Physics Letters B*, vol. 673, no. 2, pp. 142–145, Mar. 2009.

[72] S. Wheaton, J. Cleymans, and M. Hauer, "THERMUS—A thermal model package for ROOT," *Computer Physics Communications*, vol. 180, no. 1, pp. 84–106, Jan. 2009.

[73] S. Hamieh, K. Redlich, and A. Tounsi, "Canonical Description of Strangeness Enhancement from p-A to Pb-Pb Collisions," *Physics Letters B*, vol. 486, no. 1-2, pp. 61–66, Jul. 2000.

[74] ALICE Collaboration, "Centrality dependence of π, K, p production in Pb-Pb collisions at $\sqrt{s_{\mathrm{NN}}}$ = 2.76 TeV," *Phys. Rev. C*, vol. 88, no. 4, p. 044910, Oct. 2013.

[75] ALICE Collaboration, "K^0_S and Λ production in Pb-Pb collisions at $\sqrt{s_{\mathrm{NN}}}$ = 2.76 TeV," *Phys. Rev. Lett.*, vol. 111, no. 22, p. 222301, Nov. 2013.

[76] ALICE Collaboration, "K*(892)^0 and Φ(1020) production in Pb-Pb collisions at $\sqrt{s_{\mathrm{NN}}}$ = 2.76 TeV," *Phys. Rev. C*, vol. 91, no. 2, p. 024609, Feb. 2015.

[77] C. M. Hung and E. Shuryak, “Equation of State, Radial Flow and Freeze-out in High Energy Heavy Ion Collisions,” *Phys. Rev. C*, vol. 57, no. 4, pp. 1891–1906, Apr. 1998.

[78] E. Schnedermann, J. Sollfrank, and U. Heinz, “Thermal phenomenology of hadrons from 200 AGeV S+S collisions,” *Phys. Rev. C*, vol. 48, no. 5, pp. 2462–2475, Nov. 1993.

[79] K. Werner *et al.*, “Analysing radial flow features in p-Pb and p-p collisions at several TeV by studying identified particle production in EPOS3,” *Phys. Rev. C*, vol. 89, no. 6, p. 064903, Jun. 2014.

[80] S. Voloshin and Y. Zhang, “Flow Study in Relativistic Nuclear Collisions by Fourier Expansion of Azimuthal Particle Distributions,” *Zeitschrift fr Physik C Particles and Fields*, vol. 70, no. 4, pp. 665–671, May 1996.

[81] B. Alver and G. Roland, “Collision geometry fluctuations and triangular flow in heavy-ion collisions,” *Phys. Rev. C*, vol. 82, no. 3, p. 039903, Sep. 2010.

[82] ALICE Collaboration, “Higher harmonic anisotropic flow measurements of charged particles in Pb-Pb collisions at 2.76 TeV,” *Phys. Rev. Lett.*, vol. 107, no. 3, p. 032301, Jul. 2011.

[83] M. Luzum, “Flow fluctuations and long-range correlations: Elliptic flow and beyond,” *J. Phys. G: Nucl. Part. Phys.*, vol. 38, no. 12, p. 124026, Dec. 2011.

[84] ALICE Collaboration, “Elliptic flow of identified hadrons in Pb-Pb collisions at $\sqrt{s_{\mathrm{NN}}}$ = 2.76 TeV,” *J. High Energ. Phys.*, vol. 2015, no. 6, p. 190, Jun. 2015.

[85] K. Schade, “Applications of Holography to Strongly Coupled Plasmas,” Ph.D. dissertation, University of Heidelberg, 2012.

[86] M. Gyulassy and M. Plümer, “Jet quenching in dense matter,” *Physics Letters B*, vol. 243, no. 4, pp. 432–438, Jul. 1990.

[87] X.-N. Wang, “Effect of Jet Quenching on High-p_T Hadron Spectra in High-energy Nuclear Collisions,” *Phys. Rev. C*, vol. 58, no. 4, pp. 2321–2330, Oct. 1998.

[88] M. Gyulassy, P. Levai, and I. Vitev, “Non-Abelian Energy Loss at Finite Opacity,” *Phys. Rev. Lett.*, vol. 85, no. 26, pp. 5535–5538, Dec. 2000.

[89] K. Zapp *et al.*, “A Monte Carlo Model for ’Jet Quenching’,” *Eur. Phys. J. C*, vol. 60, no. 4, p. 617, Apr. 2009.

[90] Collaboration CMS, “CMS collision events: From lead ion collisions,” http://cdsweb.cern.ch/record/1309898, 2010.

[91] R. Vogt, “Shadowing Effects on J/ψ and Υ Production at the LHC,” *Phys. Rev. C*, vol. 92, no. 3, p. 034909, Sep. 2015.

[92] J. W. Cronin *et al.*, “Production of hadrons at large transverse momentum at 200, 300, and 400 GeV,” *Phys. Rev. D*, vol. 11, no. 11, pp. 3105–3123, Jun. 1975.

[93] E. G. Ferreiro, “Excited charmonium suppression in proton–nucleus collisions as a consequence of comovers,” *Physics Letters B*, vol. 749, pp. 98–103, Oct. 2015.

[94] J. Adam *et al.*, “Enhanced production of multi-strange hadrons in high-multiplicity proton–proton collisions,” *Nature Phys*, vol. 13, no. 6, pp. 535–539, Jun. 2017.

[95] ALICE Collaboration, “Multiplicity dependence of J/ψ production at midrapidity in pp collisions at $\sqrt{s}$ = 13 TeV,” *Physics Letters B*, vol. 810, p. 135758, Nov. 2020.

[96] ALICE Collaboration, “Observation of a multiplicity dependence in the p_{T}-differential charm baryon-to-meson ratios in proton-proton collisions at $\sqrt{s} =$ 13 TeV,” *Physics Letters B*, vol. 829, p. 137065, Jun. 2022.

[97] CMS Collaboration, “Evidence for collectivity in pp collisions at the LHC,” *Physics Letters B*, vol. 765, pp. 193–220, Feb. 2017.

[98] R. D. Weller and P. Romatschke, “One fluid to rule them all: Viscous hydrodynamic description of event-by-event central p+p, p+Pb and Pb+Pb collisions at $\sqrt{s} = 5.02$ TeV,” *Physics Letters B*, vol. 774, pp. 351–356, Nov. 2017.

[99] ALICE Collaboration, “Investigations of anisotropic flow using multi-particle azimuthal correlations in pp, p-Pb, Xe-Xe, and Pb-Pb collisions at the LHC,” *Phys. Rev. Lett.*, vol. 123, no. 14, p. 142301, Oct. 2019.

[100] ALICE Collaboration, “Multiplicity dependence of (multi-)strange hadron production in proton-proton collisions at $\sqrt{s}$ = 13 TeV,” *Eur. Phys. J. C*, vol. 80, no. 2, p. 167, Feb. 2020.

[101] CMS Collaboration, “Investigation into the event-activity dependence of Υ(nS) relative production in proton-proton collisions at $\sqrt{s} = 7$ TeV,” *J. High Energ. Phys.*, vol. 2020, no. 11, p. 1, Nov. 2020.

[102] S. Behrends *et al.*, "Inclusive Hadron Production in Upsilon Decays and in Nonresonant electron-Positron Annihilation at 10.49-GeV," *Phys.Rev.D*, vol. 31, p. 2161, 1985.

[103] CMS Collaboration, "Elliptic flow of charm and strange hadrons in high-multiplicity pPb collisions at $\sqrt{s_{\mathrm{NN}}} = 8.16$ TeV," *Phys. Rev. Lett.*, vol. 121, no. 8, p. 082301, Aug. 2018.

[104] B. G. Zakharov, "Parton energy loss in the mini quark-gluon plasma and jet quenching in proton-proton collisions," *J. Phys. G: Nucl. Part. Phys.*, vol. 41, no. 7, p. 075008, Jul. 2014.

[105] S.-Y. Chen *et al.*, "Centrality Dependence of Productions for Single Hadrons and Inclusive Jets in High-Energy p + A Collisions with NLO QCD*," *Commun. Theor. Phys.*, vol. 64, no. 1, p. 95, Jul. 2015.

[106] ALICE Collaboration, "Constraints on jet quenching in p-Pb collisions at $\sqrt{\mathbf{s_{NN}}}$ = 5.02 TeV measured by the event-activity dependence of semi-inclusive hadron-jet distributions," *Physics Letters B*, vol. 783, pp. 95–113, Aug. 2018.

[107] J. Bellm *et al.*, "Herwig 7.2 Release Note," *Eur. Phys. J. C*, vol. 80, no. 5, p. 452, May 2020.

[108] E. Bothmann *et al.*, "Event Generation with Sherpa 2.2," *SciPost Phys.*, vol. 7, no. 3, p. 034, Sep. 2019.

[109] T. Sjöstrand, "The PYTHIA Event Generator: Past, Present and Future," *Computer Physics Communications*, vol. 246, p. 106910, Jan. 2020.

[110] P. Skands, S. Carrazza, and J. Rojo, "Tuning PYTHIA 8.1: The Monash 2013 tune," *Eur. Phys. J. C*, vol. 74, no. 8, p. 3024, Aug. 2014.

[111] C. Bierlich *et al.*, "The Angantyr model for Heavy-Ion Collisions in PYTHIA8," *J. High Energ. Phys.*, vol. 2018, no. 10, p. 134, Oct. 2018.

[112] T. Sjöstrand, S. Mrenna, and P. Skands, "A Brief Introduction to PYTHIA 8.1," *Computer Physics Communications*, vol. 178, no. 11, pp. 852–867, Jun. 2008.

[113] C. Bierlich and J. R. Christiansen, "Effects of Colour Reconnection on Hadron Flavour Observables," *Phys. Rev. D*, vol. 92, no. 9, p. 094010, Nov. 2015.

[114] T. S. Biro, H. B. Nielsen, and J. Knoll, "Colour rope model for extreme relativistic heavy ion collisions," *Nuclear Physics B*, vol. 245, pp. 449–468, Jan. 1984.

[115] H. Sorge *et al.*, "Colour rope formation and strange baryon production in ultrarelativistic heavy ion collisions," *Physics Letters B*, vol. 289, no. 1, pp. 6–11, Sep. 1992.

[116] C. Bierlich *et al.*, "Effects of Overlapping Strings in pp Collisions," http://arxiv.org/abs/1412.6259, Feb. 2015.

[117] C. Bierlich, G. Gustafson, and L. Lönnblad, "A shoving model for collectivity in hadronic collisions," http://arxiv.org/abs/1612.05132, Dec. 2016.

[118] H. J. Drescher *et al.*, "Parton-Based Gribov-Regge Theory," *Physics Reports*, vol. 350, no. 2-4, pp. 93–289, Sep. 2001.

[119] K. Werner, F.-M. Liu, and T. Pierog, "Parton Ladder Splitting and the Rapidity Dependence of Transverse Momentum Spectra in Deuteron-Gold Collisions at RHIC," *Phys. Rev. C*, vol. 74, no. 4, p. 044902, Oct. 2006.

[120] T. Pierog *et al.*, "EPOS LHC : Test of collective hadronization with LHC data," *Phys. Rev. C*, vol. 92, no. 3, p. 034906, Sep. 2015.

[121] A. G. Knospe *et al.*, "Hadronic resonance production and interaction in partonic and hadronic matter in EPOS3 with and without the hadronic afterburner UrQMD," *Phys. Rev. C*, vol. 93, no. 1, p. 014911, Jan. 2016.

[122] A. G. Knospe *et al.*, "Hadronic resonance production and interaction in p-Pb collisions at LHC energies in EPOS3," *Phys. Rev. C*, vol. 104, no. 5, p. 054907, Nov. 2021.

[123] T. Pierog and K. Werner, "EPOS Model and Ultra High Energy Cosmic Rays," *Nuclear Physics B - Proceedings Supplements*, vol. 196, pp. 102–105, Dec. 2009.

[124] R. Cashmore, L. Maiani, and J.-P. Revol, Eds., *Prestigious Discoveries at CERN*. Berlin, Heidelberg: Springer, 2003.

[125] The ATLAS Collaboration *et al.*, "The ATLAS Experiment at the CERN Large Hadron Collider," *J. Inst.*, vol. 3, no. 08, p. S08003, Aug. 2008.

[126] The CMS Collaboration *et al.*, "The CMS experiment at the CERN LHC," *J. Inst.*, vol. 3, no. 08, p. S08004, Aug. 2008.

[127] The LHCb Collaboration *et al.*, "The LHCb Detector at the LHC," *J. Inst.*, vol. 3, no. 08, p. S08005, Aug. 2008.

[128] R. Schmidt *et al.*, "Protection of the CERN Large Hadron Collider," *New J. Phys.*, vol. 8, no. 11, p. 290, Nov. 2006.

[129] M. Brice, "Aerial View of the CERN taken in 2008." https://cds.cern.ch/record/1295244, 2008.

[130] "LHC report: Make way for the heavy ions," https://home.cern/news/news/accelerators/lhc-report-make-way-heavy-ions, Mar. 2023.

[131] The ALICE Collaboration *et al.*, "The ALICE experiment at the CERN LHC," *J. Inst.*, vol. 3, no. 08, p. S08002, Aug. 2008.

[132] ALICE Collaboration, "Performance of the ALICE Experiment at the CERN LHC," *Int. J. Mod. Phys. A*, vol. 29, no. 24, p. 1430044, Sep. 2014.

[133] V. Peskov, M. Planicic, and F. García, *Technical Design Report for the Upgrade of the ALICE Time Projection Chamber*, Mar. 2014.

[134] A. Kalweit, "Production of light flavor hadrons and anti-nuclei at the LHC," Doctoral Thesis (Monograph), Technische Universitat Darmstadt, 2012.

[135] J. Adolfsson *et al.*, "The upgrade of the ALICE TPC with GEMs and continuous readout," *JINST*, vol. 16, no. arXiv:2012.09518, 2021.

[136] ALICE Collaboration, "Alignment of the ALICE Inner Tracking System with cosmic-ray tracks," *J. Inst.*, vol. 5, no. 03, pp. P03 003–P03 003, Mar. 2010.

[137] M. Krammer, "Silicon detectors in High Energy Physics experiments," *Scholarpedia*, vol. 10, no. 10, p. 32486, 2015.

[138] S. Masciocchi, "Lecture notes: Semiconductor detectors," https://www.physi.uni-heidelberg.de/~sma/teaching/ParticleDetectors2/sma_Semiconductors_3.pdf, University of Heidelberg, 2017.

[139] ALICE Collaboration, "Performance of the ALICE VZERO system," *J. Inst.*, vol. 8, no. 10, pp. P10 016–P10 016, Oct. 2013.

[140] M. Krivda *et al.*, "The ALICE trigger system performance for p-p and Pb-Pb collisions," *J. Inst.*, vol. 7, no. 01, p. C01057, Jan. 2012.

[141] ALICE Data Preparation Group, "ALICE Data Flow," https://indico.cern.ch/event/752367/contributions/3116617/attachments/1704565/2858687/DPG_AnalysisTutorial_20181129.pdf, Nov. 2018.

[142] M. Arslandok *et al.*, "Track Reconstruction in a High-Density Environment with ALICE," *Particles*, vol. 5, no. 1, pp. 84–95, Mar. 2022.

[143] A. Maire, "Production des baryons multi-étranges au LHC dans les collisions proton-proton avec l'expérience ALICE," Ph.D. dissertation, Strasbourg U., 2011.

[144] G. Contin, “Performance of the present ALICE Inner Tracking System and studies for the upgrade,” *J. Inst.*, vol. 7, no. 06, p. C06007, Jun. 2012.

[145] ALICE Collaboration, “Centrality determination of Pb-Pb collisions at $\sqrt{s_{\mathrm{NN}}}$ = 2.76 TeV with ALICE,” *Phys. Rev. C*, vol. 88, no. 4, p. 044909, Oct. 2013.

[146] ALICE Collaboration, “Multiplicity dependence of light-flavor hadron production in pp collisions at $\sqrt{s}$ = 7 TeV,” *Phys. Rev. C*, vol. 99, no. 2, p. 024906, Feb. 2019.

[147] ALICE Collaboration, “The ALICE definition of primary particles,” https://cds.cern.ch/record/2270008, 2017.

[148] R. Brun *et al.*, *GEANT: Detector Description and Simulation Tool; Oct 1994*, ser. CERN Program Library. Geneva: CERN, 1993.

[149] V. Kučera, “Study of strange particle production in jets with the ALICE experiment at the LHC,” Monograph, Charles University, Nov. 2016.

[150] S. Acharya *et al.*, “Production of light-flavor hadrons in pp collisions at $\sqrt{s}$ = 7 and $\sqrt{s}$ = 13 TeV,” *Eur. Phys. J. C*, vol. 81, no. 3, p. 256, Mar. 2021.

[151] R. J. Barlow, “Practical Statistics for Particle Physics,” *CERN Yellow Reports: School Proceedings*, vol. Vol. 5, p. 149 Pages, Sep. 2020.

[152] R. Brandelik *et al.*, “Evidence for a spin-1 gluon in three-jet events,” *Physics Letters B*, vol. 97, no. 3, pp. 453–458, Dec. 1980.

[153] A. Ortiz, “Experimental results on event shapes at hadron colliders,” in *Multiple Parton Interactions at the LHC*, Dec. 2018, vol. 29, pp. 343–357.

[154] A. Banfi, G. P. Salam, and G. Zanderighi, “Phenomenology of event shapes at hadron colliders,” *J. High Energ. Phys.*, vol. 2010, no. 6, p. 38, Jun. 2010.

[155] ALICE Collaboration, “Charged-particle production as a function of multiplicity and transverse spherocity in pp collisions at $\sqrt{s}$ = 5.02 and 13 TeV,” *Eur. Phys. J. C*, vol. 79, no. 10, p. 857, Oct. 2019.

[156] E. Cuautle *et al.*, “Disentangling the soft and hard components of the pp collisions using the sphero(i)city approach,” http://arxiv.org/abs/1404.2372, Apr. 2014.

[157] E. Cuautle, A. Ortiz, and G. Paic, “Mid-rapidity charged hadron transverse spherocity in pp collisions simulated with Pythia,” *Nuclear Physics A*, vol. 941, pp. 78–86, Sep. 2015.

[158] A. Nassirpour, “The Shape of Strangeness: Transverse Spherocity and Underlying Event studies of φ and its relation to Ξ in $\sqrt{\text{s}}$ = 13 TeV pp collisions,” Doctoral Thesis (Monograph), Lund University (Media-Tryck), Nov. 2022.

[159] O. Vazquez Rueda, “Study of the production of π, K and p in pp collisions at $\sqrt{\text{s}}$ = 13 TeV as a function of the Transverse Spherocity and the Relative Transverse Activity,” Doctoral Thesis (Monograph), Lund University (Media-Tryck), 2022.

[160] ALICE Collaboration, “Multiplicity dependence of charged-particle production in pp, p-Pb, Xe-Xe and Pb-Pb collisions at the LHC,” http://arxiv.org/abs/2211.15326, Nov. 2022.

[161] S. Acharya *et al.*, “Production of Λ and KS0 in jets in p–Pb collisions at sNN=5.02 TeV and pp collisions at s=7 TeV,” *Physics Letters B*, vol. 827, p. 136984, Apr. 2022.

[162] ALICE Collaboration, “Underlying Event properties in pp collisions at $\sqrt{s}$ = 13 TeV,” *J. High Energ. Phys.*, vol. 2020, no. 4, p. 192, Apr. 2020.

[163] ATLAS Collaboration, “Measurement of charged-particle distributions sensitive to the underlying event in $\sqrt{s} = 13$ TeV proton-proton collisions with the ATLAS detector at the LHC,” *J. High Energ. Phys.*, vol. 2017, no. 3, p. 157, Mar. 2017.

[164] ALICE collaboration, “Underlying Event measurements in pp collisions at $\sqrt{s}$ = 0.9 and 7 TeV with the ALICE experiment at the LHC,” *J. High Energ. Phys.*, vol. 2012, no. 7, p. 116, Jul. 2012.

[165] ALICE Collaboration, “Underlying-event properties in pp and p−Pb collisions at $\sqrt{s_{\mathrm{NN}}} = 5.02$ TeV,” http://arxiv.org/abs/2204.10389, Apr. 2022.

[166] T. Martin, P. Skands, and S. Farrington, “Probing collective effects in hadronisation with the extremes of the underlying event,” *Eur. Phys. J. C*, vol. 76, no. 5, p. 299, May 2016.

[167] ALICE Collaboration, “Production of pions, kaons and protons as a function of the transverse event activity in pp collisions at $\sqrt{s} = 13$ TeV,” http://arxiv.org/abs/2301.10120, Jan. 2023.

[168] G. Bencédi, A. Ortiz, and A. Paz, “Disentangling the hard gluon bremsstrahlung effects from the relative transverse activity classifier in p p collisions,” *Phys. Rev. D*, vol. 104, no. 1, p. 016017, Jul. 2021.

[169] R. Field, “The Underlying Event in Hadronic Collisions,” *Annual Review of Nuclear and Particle Science*, vol. 62, no. 1, pp. 453–483, 2012.

[170] B. Z. Kopeliovich *et al.*, “Cronin Effect in Hadron Production off Nuclei,” *Phys. Rev. Lett.*, vol. 88, no. 23, p. 232303, May 2002.

[171] G. D’Agostini, “A multidimensional unfolding method based on Bayes’ theorem,” *Nuclear Instruments and Methods in Physics Research Section A: Accelerators, Spectrometers, Detectors and Associated Equipment*, vol. 362, no. 2, pp. 487–498, Aug. 1995.

[172] A. Ortiz, “Energy dependence of underlying-event observables from RHIC to LHC energies,” *Phys. Rev. D*, vol. 104, no. 7, p. 076019, Oct. 2021.

[173] C.-Y. Wong, “The Soft Gluon Emission Process in the Color-Octet Model for Heavy Quarkonium Production,” *Phys. Rev. D*, vol. 60, no. 11, p. 114025, Nov. 1999.

[174] Y.-Q. Ma and R. Vogt, “Quarkonium Production in an Improved Color Evaporation Model,” *Phys. Rev. D*, vol. 94, no. 11, p. 114029, Dec. 2016.